Processes of felsic melt migration through the mid-crust: evidence from field relations in the Central Zone of the Damara Belt, Namibia

Carly Faber

a thesis submitted for the degree of
Master of Science
at the University of Cape Town, Cape Town,
South Africa.

2012

Abstract

The migration of granitic melt is the main mechanism that facilitates upward movement of heat and mass, and the chemical differentiation of the continental crust. Whereas the processes of melt segregation and emplacement are relatively well understood, melt ascent mechanisms are more speculative. Specific outstanding questions include the structure of melt conduits, the driving forces of melt ascent, and the timescales involved.

The Central Zone of the Damara Belt presents a snapshot of melt migration through subsolidus, mid-crustal rocks. Outcrops selected for detailed investigation are representative of a variety of mestasedimentary rock types and strain environments, and all contain pervasive and interconnected leucosome networks representative of melt movement through, and emplacement into these rocks. Leucosome networks consist of melt-bearing bedding and foliation planes, shears, tensile fractures and boudin necks. The type of structures that constitute the networks are predominantly controlled by the dominant strain regime, and subordinately by rock types and melt volume. The presence of multiple, overprinting melt phases within the same structures shows that migration is episodic and long-lived, and preferentially re-uses existing permeability networks. The nature of the networks suggests that melt movement is predominantly driven by pressure gradients created between sites of localized dilation and compaction. These transient sites are formed through heterogeneous deformation of inhomogeneous rocks, and melt is actively expelled from sites undergoing compaction, and drawn into sites that are experiencing dilation. These examples highlight the fundamental influence of progressive deformation on all aspects of the melt migration process.

Acknowledgements

This research project would not have been possible without student funding from the National Research Foundation (NRF), and without the permission of Bannerman Resources, Swakopmund. I owe my deepest gratitude to my supervisor Dr Johann Diener, whose encouragement, guidance and support have been invaluable. I am grateful to Prof. Alex Kisters for guidance and advice, and to Dr Åke Fagereng for helpful discussions. I would also like to thank the reviewers of this thesis for their time and effort, and my family and friends for all their support and encouragement during the completion of the project.

Carly Faber

Contents

List of Tables

List of Figures

Chapter 1

Introduction

The generation, segregation, migration/ascent, and emplacement of felsic melt in the continental crust are the principal mechanisms by which heat and mass are transferred from the lower to the upper crust (Sawyer *et al.*, 2011). The combination of these processes are central to the internal differentiation of the continental crust; however, many of the details of these processes are not well-constrained. In particular, the mechanisms, rates and scales involved in the large-scale migration of melt from its source region in the mid- to lower crust to its emplacement level in the upper crust are not adequately documented or understood (Sawyer, 1994; Brown & Solar, 1998a; Simakin & Talbot, 2001; Sawyer, 2001; Kisters *et al.*, 2009). Most of the research performed on granite plutons is geochemical, and focuses on the roles of chemical differentiation and fractionation on the origin of these rocks. Conversely, migmatite terranes are primarily used to investigate the processes of melt generation and segregation, and only more recently have studies begun to focus on the relationship between migmatite terrains and granite intrusions in the upper crust (Sawyer, 2001; Nex *et al.*, 2001; Brown, 2004; Weinberg & Mark, 2008).

The spatial and temporal association of regional tectonism, high-grade metamorphism and granite magmatism suggests that they are interrelated and that the formation and transfer of granite melt is largely a syntectonic process (e.g. Brown & Solar, 1998a, 1999; Brown, 2007). The growing understanding of the feedback relationship between crustal melting and tectonic deformation highlights the importance of the process of crustal melting and melt movement, as well as the influence such a relationship has on crustal deformation (Sawyer *et al.*, 2011).

Estimates for the scale and rate of the entire granitic magmatism process, from melt generation to emplacement, show that the process spans more than 21 orders of magnitude

in size, and anywhere from 10^4 to 10^7 years (Petford *et al.*, 2000; Brown, 2007). Part of the reason for the lack of relative understanding of melt migration is that mid-crustal orogenic terranes do not often preserve evidence for the large-scale or pervasive movement of melt through these rocks (Clemens, 1998; Brown, 2007). This could be because melt migration occurs in selective and isolated structures that are not readily exposed, or because melt migration is a highly effective and transient process that does not readily preserve fossil melt transfer networks (Weinberg, 1999; Sawyer, 2001).

The volume of the lower-crustal region in which melt is generated and sourced is around an order of magnitude larger than the volume of the resulting pluton, suggesting that crustal-scale melt transfer networks have a branching-downwards structure (e.g. Sawyer, 2001, Fig. 1.1), where flow is achieved through a connected network of melt-filled fractures (Brown & Solar, 1998a; Weinberg, 1999). Fossil melt transfer networks can therefore be expected to be common in mid-crustal terranes, but are either not readily preserved, or easily observed. Because of this lack of observational data, important aspects of mid-crustal melt migration, such as the mechanisms involved, the architecture of the melt transfer network, the driving forces and the timing, rate and duration of melt movement, as well as the various factors that influence and control these aspects, remain speculative.

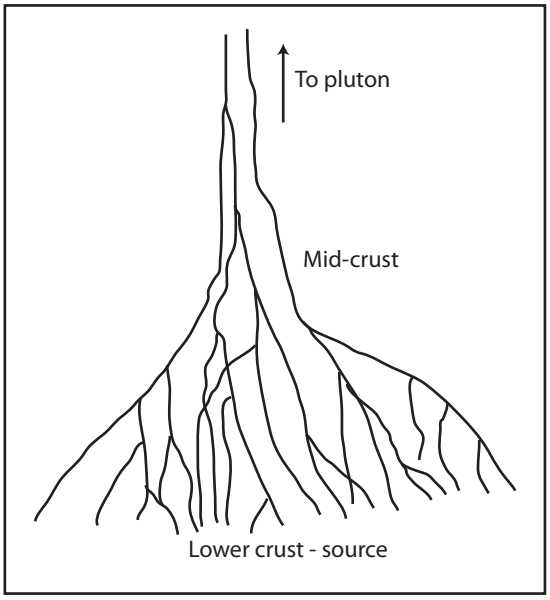

Figure 1.1: Sketch figure showing the likely branching-downwards nature of melt migration networks.

This thesis will examine and elucidate on many of these aspects through the investigation

of medium- to large-scale leucogranite-bearing structures preserved in a variety of structural settings in well-exposed mid-crustal rocks from the Damara Belt, Namibia. In this study, the leucogranite structures are interpreted as previous melt pathways or emplacement structures, and the rocks occur above the level of the source rocks, within the zone where migration can still be expected to be pervasive (Fig. 1.1). These rocks therefore provide a rare opportunity to elucidate and strengthen our understanding of the connection between the source region and emplacement level of crustal melts.

1.1 Melt generation and segregation

The generation, segregation and accumulation of melt within the lower crust occur during the early stages of magma evolution. These processes occur on a centimetre to decimetre scale and evidence of them are preserved in most high grade metamorphic terranes. These terranes include migmatitic rocks that show field evidence for anatexis and the associated processes of melt segregation (Sawyer, 2001; Vernon & Paterson, 2001; Marchildon & Brown, 2003). In addition, melt generation in crustal rocks has also been investigated through experiments (Vielzeuf & Holloway, 1988; Rushmer, 1991; Stevens *et al.*, 1997), and mineral equilibria modelling calculations (e.g. White *et al.*, 2001; White & Powell, 2002), allowing our understanding of the initial parts of the melt cycle to be relatively well-constrained.

Most felsic melt is generated by partial melting of crustal rocks (Clemens, 1998). When temperatures in excess of 700 to 800°C are reached, and depending on the composition and presence of H_2O-rich volatile phases, melting begins (Brown, 2010). Initial melting occurs at grain triple junctions, and proceeds along the grain boundaries around peritectic minerals (Vanderhaeghe, 2001). As melt volume increases, the grain boundary melt films begin to link up to form small, grain-scale interconnected networks (Petford *et al.*, 2000; Sawyer, 2001; Brown, 2007). The initiation of mechanical melt movement occurs when permeability is achieved as the rock weakens, and typically when melt reaches a few volume percent. The networks become interconnected and melt can move away from the volume in which it was generated to accumulate in larger dilatant structures, such as shown in Figure 1.2A. This process is cyclic and often comprises several melt generation, segregation and accumulation events (Brown, 2007). The structures that contain segregated melt are preserved as the leucosome components of migmatites, whereas the melt-depleted, residual and dehydrated rock becomes the mesosome.

Field evidence suggests that the segregation and removal of melt from their source rocks requires deformation, as most melt-bearing features are structurally-controlled. Melt-filled shears and tensile fractures are observed in migmatite terranes and contribute towards the movement of melts further away from their source (Brown, 2007; Sawyer, 2001). Migmatites typically contain both in situ leucosome, formed through primary melt segregation and recognized by its diffuse contacts with surrounding mesosome (Fig. 1.2A), as well as injected leucosome, formed through the movement of already-segregated melt and which can be distinguished by its sharp contacts with the surrounding rock, larger size, general lack of peritectic phases, the presence of wall-rock xenoliths and crosscutting relationship with in situ leucosome (Fig. 1.2B; Kisters *et al.*, 2009). These injected leucosomes represent the first small-scale occurrences of melt migration.

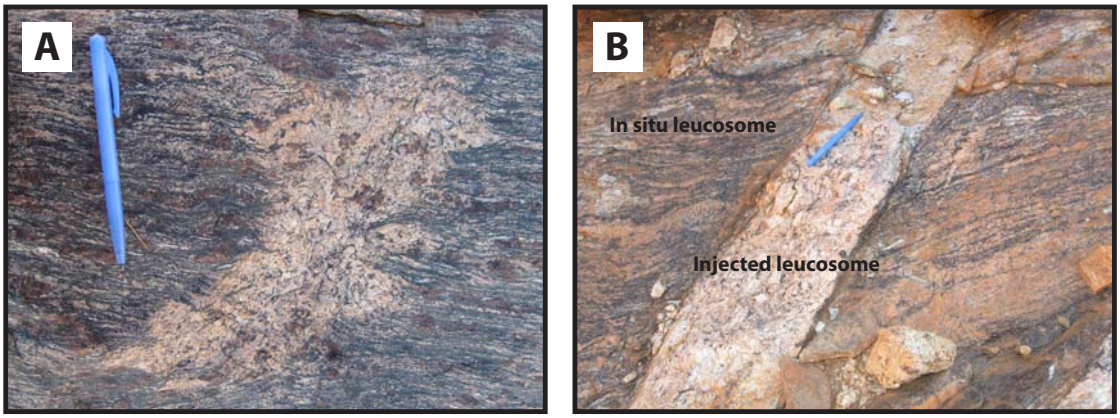

Figure 1.2: A) Photograph of a typical structure related to initial melt segregation and accumulation. B) Photograph of a migmatite that shows both in situ and injected leucosome. In situ leucosome has slightly diffuse boundaries, whereas boundaries of injected leucosome are sharp.

1.2 Melt migration and ascent

Migration occurs on a much larger range of scales than segregation, and over greater distances. It describes the process whereby melt moves away from its lower crustal anatectic source, ascending several 10's of kilometres through the mid-crust, to where it is emplaced as granite intrusions in the upper crust. Diapirism, dyking and pervasive migration are the three main mechanisms that are currently favoured to explain melt migration processes through the crust (Fig. 1.3).

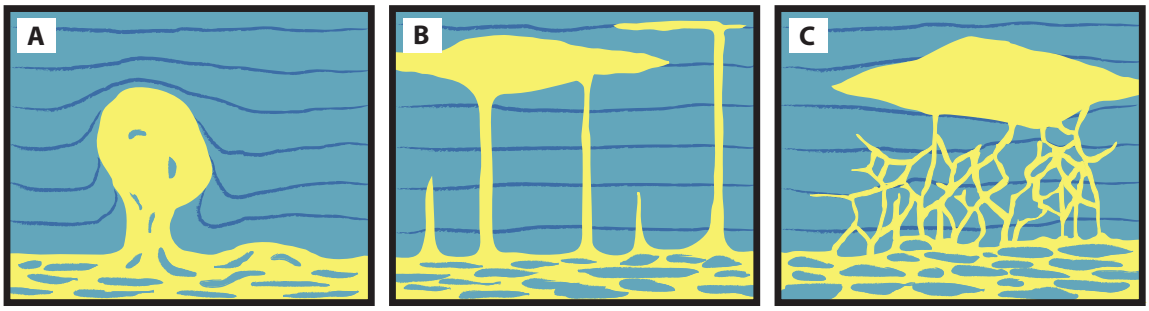

Figure 1.3: The three main melt migration mechanisms. A) Diapiric rise of melt from the source rocks. B) Migration through dykes which either connect the source to a pluton, or freeze in the middle and upper crust. C) Migration from the source to emplacement level via an interconnected network of fractures known as pervasive migration. Figure after Bons & van Milligen (2004).

1.2.1 Diapirism

Diapirism is the rise of large, single buoyant bodies through the crust while the surrounding rocks deform viscously to accommodate them (Weinberg & Podladchikov, 1994; Paterson, 1995; Weinberg, 1999). It was a popular model for melt migration and emplacement in the 1970's and 1980's (Sweeney, 1975; Batemen, 1984; Weinberg & Podladchikov, 1994) because it explained the assumed shape of plutons, and because it easily explained how magmas moved through the crust without freezing. However, it has since been largely refuted as a general mechanism owing to our increasing ability to seismically image batholiths, which shows that many are more tabular and have relatively flat bottom surfaces (either laccolith and lopolith-shaped), as opposed to the typically assumed rounded batholith shape (Clemens, 1998; Vanderhaeghe, 1999; Benn *et al.*, 1999).

1.2.2 Dyking

Dyking has long been the accepted mechanism for the ascent of low-viscosity mafic magma (Weertman, 1971; McLeod & Tait, 1999). Dyking has also been shown to be an effective mechanism to move large volumes of felsic melt at high velocity through the upper crust where viscosity contrasts are sufficiently high, provided they reach a width sufficient to avoid freezing (Clemens & Mawer, 1992; Brown, 1994; Petford *et al.*, 1993; Clemens & Petford, 1999). A few examples of plutons with exposed root zones show evidence of large feeder dykes, e.g. in the Chemehuevi Mountains (John, 1988), and in the Gangotri pluton (Scaillet

et al., 1995), confirming that dyking is the likely mechanism for melt movement through the brittle upper crust.

However, there is less evidence of large felsic feeder dykes in the more ductile mid-crust. It has also been argued that dyking is an inefficient mechanism during the initial stages of melt migration because in order to maintain a critical width and prevent freezing, a dyke requires a steady flow of melt, which is not always readily available in a slowly melting source. In addition, felsic magmas are predicted to have a high viscosity (relative to mafic magmas), although this can vary with magma composition and water content. This likely higher viscosity could make the infilling of dykes very slow (Weinberg, 1999). Also, a predominant tectonic environment in which felsic magmas occur are orogenic belts (Brown & Solar, 1998a, 1999; Marchildon & Brown, 2003), an environment typically associated with horizontal maximum compressive stress, a situation that is not amenable to the formation of vertical dykes (Brown & Solar, 1998a).

1.2.3 Pervasive migration

Pervasive melt migration appears the most likely mechanism for melt movement in the mid- to lower crust (Brown & Solar, 1999; Vanderhaeghe, 1999; Weinberg, 1999), and describes flow through a connected network of melt-filled fractures. Pervasive migration has been previously overlooked because it was believed that melt would freeze once it began moving through subsolidus rocks unless it was in conduits of a critical thickness. If melt has the same solidus temperature as its source rock, pervasive migration would be restricted to the zone of melting, and melt would never leave the source. However, melt has a lower solidus temperature relative to its source because the process of melting separates fertile minerals and water into melt, leaving behind refractory minerals (higher solidus) in the source. This was pointed out by Weinberg (1999), who showed that this difference in solidus temperature gives melt the capability to remain liquid at shallower crustal levels up to $\sim$5 km above its source. This difference in solidus temperature, together with the pervasive structure of the melt networks, can heat the crustal rocks through which the melt migrates, thereby making pervasive migration feasible to even shallower crustal levels (Brown & Solar, 1999).

The orientation of the fractures that compose the networks is determined by pre-existing high permeability zones, such as bedding and foliation planes, shear zones and dilational structures (Collins & Sawyer, 1996; Weinberg, 1999; Sawyer, 2001). The presence of fractures

in lower-crustal rocks that are at ductile deformation conditions has been attributed to a process of melt-enhanced embrittlement by cataclastic flow. This occurs as melt volume increases and pore fluid pressures become equal to the mean stress or confining pressure, allowing brittle failure to occur in otherwise ductile rock (Davidson *et al.*, 1994). This kind of deformation is integral in creating the requisite pathways to allow pervasive migration (Weinberg, 1999). These hydrofractures are likely to be transient, and will only remain open as long as they are melt-bearing and could re-seal once melt has passed through them (Bons *et al.*, 2001; Bons & van Milligen, 2004; Brown, 2007; Kisters *et al.*, 2009).

Pervasive melt networks have been described at outcrop scale, particularly in migmatite terranes, where the leucosomes are interpreted as evidence of melt movement out of the source. However, much of the details of the internal architecture of dyke networks that occur above the source, and the factors that control the orientation, shape and size of individual structures as well as the interconnectivity of the network are not well known. Given observations of small-scale melt networks, and networks in anatectic migmatite terranes, the structure of larger-scale melt transfer networks is likely to be a function of the complex interplay between a number of factors. These factors include: melt volume (which has a direct effect on melt pressure), rock strength and competency contrasts between rock types, melt viscosity, melt driving forces, and regional deformation that determines the style and intensity of pre-existing planar and linear fabrics, and anisotropies (Brown & Solar, 1999; Sawyer, 2001; Basson & Greenway, 2004).

1.2.4 Driving forces and rates of melt movement

Melt movement through the crust is ultimately driven by buoyancy of the melt, but at mid-crustal depths the local pressure and hydraulic gradients that control melt movement are the result of the interplay of lithostatic and tectonic forces and the melt pressure (Brown & Solar, 1998a), so that migration is driven by both pushing and pulling of melts along pressure and hydraulic gradients (Petford *et al.*, 2000; Sawyer, 2001; Kisters *et al.*, 2009). Tectonic forces create such gradients by forming dilational spaces which become melt accumulation sites when melt is drawn towards them, and by compaction which forces melt away from high pressure sites (Weinberg, 1999). Therefore, melt can locally move upwards, laterally, or even downwards.

Models for the rates of melt migration suggest that felsic magma, depending on the

viscosity (considered to be $10^3 - 10^8$ Pa s; Clemens, 1998; Clemens & Petford, 1999) and relative density contrast with the surrounding wallrock, can travel in dykes at a rate of 3×10^{-3} to 1 m s^{-1} (Petford *et al.*, 1993; Clemens, 1998). This would suggest that the duration of migration from source to emplacement, purely using the dyke model, is relatively fast, on the order of $10^{-1} - 10^2$ years (Clemens & Mawer, 1992; Petford *et al.*, 1993). Pervasive flow is thought to be much slower as it involves smaller melt bodies, resulting in lower buoyancy stresses. Estimates of ascent rates are closer to tectonic deformation rates, with ascent taking about 10^6 years (Collins & Sawyer, 1996; Brown & Solar, 1999; Weinberg, 1999).

It is also unclear whether migration is continuous, or whether it occurs in a stepwise manner with episodic batches of melt migrating through the crust in cycles of accumulation and migration (Brown & Solar, 1998a), and whether later melt batches exploit the same pre-existing structures and networks utilised by earlier batches of melt (Brown & Solar, 1999; Bons *et al.*, 2001). Observations of the layered internal nature of plutons and dykes suggests that emplacement occurs in a stepwise manner (Petford *et al.*, 2000; Bons *et al.*, 2001; Kisters *et al.*, 2009), implying that either migration paths must be used multiple times by multiple batches of magma, or migration paths should be more abundant. However, field evidence to support either possibility is relatively rare.

1.3 Melt emplacement

The termination of melt migration is marked either by eruption, or by the beginning of emplacement in the upper crust, which mark two possible final stages in the granitic magmatism process. Melt emplacement occurs when melt movement changes from moving in a predominantly vertical to predominantly horizontal direction and begins to accumulate in its final site of emplacement (Clemens, 1998). The space problem of how rocks accommodate large volumes of incoming magma is one of the most researched and debated stages in the melt cycle. It is now generally accepted that emplacement occurs during active regional deformation (Brown & Solar, 1998a; Brown, 2007). Furthermore, the increasing accuracy of seismic imaging has allowed for a better description of the three-dimensional shapes of plutons and batholiths, and has clarified much about their emplacement mechanisms (Petford *et al.*, 2000). The growing acceptance that most batholiths are flat-lying or funnel-shaped features has led to greater consensus about their emplacement mechanisms, and the most widely accepted method of emplacement involves the sheeted intrusion of multiple discrete

pulses of magma, giving batholiths an internally layered and composite nature (Brown, 2007).

1.4 Aims of this study

Pervasive migration is generally considered to be a lower-crustal melt movement mechanism and is more closely associated with segregation processes than pure migration through the crust. The rocks of the field area show that pervasive migration occurred through subsolidus rocks, and suggests that pervasive migration is a more effective and general mechanism than typically suggested. In addition, our understanding of the position and shape of melt pathways in heterogeneous and anisotropic systems is incomplete, because deformation alters original geometries of leucosome structures. Similarly, we know little about the amount of deformation required to form an interconnected network of melt pathways that would allow effective movement through otherwise impermeable rocks. Our understanding around the interplay between deformation and melt migration is slowly expanding, and contributions by field studies and experimental work continuously develop a better picture of the relationship. However, questions around whether melt can move easily through an already set up melt network, and the level of assistance it requires by tectonic deformation remain, and the level of connectivity of the source to the sink, and whether melt migration is continuous or episodic with time are more speculative.

Figure 1.4 is a schematic diagram of the crust illustrating what are currently the preferred structures for granitic melt in various parts of the crust, taken from Sawyer *et al.* (2011). This diagram has a large question mark at the transition from migmatite terranes into subsolidus ductile crust, clearly illustrating the current gap in our understanding of the melt migration process. The exposed melt networks in the study area preserve a snapshot of frozen migration pathways that fall within this zone: close to, but above the level of the melt source. Nearly all leucosome described in this study is injected, and interpreted to have formed from partially melted rocks at a lower stratigraphic level. This area therefore provides an ideal opportunity to examine the initial stages of pure migration through subsolidus rocks (with small emplaced bodies interpreted as failed migration), without the complexity that arises from having to distinguish between in situ segregation structures and injected migration structures that complicate migration studies in migmatite terranes that include suprasolidus rocks that record anatexis. In this thesis, the term subsolidus, used in reference to the metasediments, describes the unmelted/liquid-absent nature of the host rocks at the time of leucogranite intrusion. It

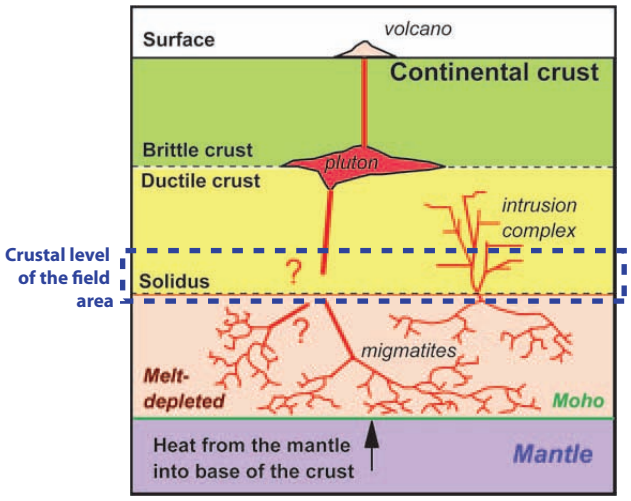

Figure 1.4: Schematic diagram from Sawyer *et al.* (2011) illustrating processes associated with granitic magmatism in the crust. The blue box indicates the level of the rocks described in the study area.

does not refer to the temperature at which the intruding leucogranites crystallized, which is here termed the crystallization temperature.

This study examines aspects of pervasive mid-crustal melt migration by characterising the nature of medium- to large-scale leucogranite-bearing structures and networks in subsolidus metasedimentary rocks of the Damara Belt, Namibia. Several different localities of the type and size shown in Figure 1.5 are used to investigate how variations in rock type (specifically with respect to differences in rock strength), local structural setting (such as planar/linear fabric orientation and differences in strain type and intensity), and melt volume influence and control the style and mechanisms of melt migration through the rocks. All maps produced in this work were obtained by detailed field mapping and are ground-truthed where rocks are accessible without a rope. They are mapped on outcrop photographs (Chapters 4, 5 (High Strain Cliff), and 7), metre by metre grids (Chapter 5 (Etusis Pavement)), and Google Earth^{TM} images (Chapters 3, 4, and 7). Map and structural data from these outcrops are then integrated and discussed to provide general conclusions and implications for the behaviour of the mid-crust during orogenic melt movement.

Pervasive melt movement and segregation into and through shears, tensile fractures and melt networks is well documented from migmatite terrains for stages which represent melt segregation and early melt movement out of anatectic rocks (e.g. Kisters *et al.*, 1998; Sawyer, 2001; Brown *et al.*, 2003; Vanderhaeghe, 2009). This thesis will confirm that pervasive migra-

Figure 1.5: Photographs showing examples of the medium- to large-scale pervasive leucogranite networks investigated during this study.

tion and the utilisation of pre-existing structural weaknesses such as shears, and anisotropies are effective melt ascent and migration mechanisms through subsolidus rocks within several kilometres above the source, and that it can occur at higher levels in the crust than typically speculated. It will show the similarity of the structures to those described for melt segregation in actively melting rocks (suprasolidus), and highlight the importance of melt embrittlement in the creation of pathways for melt migration through subsolidus rocks. This thesis will also discuss the similarity of migration through rocks outside of the source to melt movement within a suprasolidus source terrain, as both are structurally controlled.

In addition, it will compare which strain regimes display the best ability to accommodate effective melt migration, and will also examine the driving forces of melt migration, which are likely to be slightly different to those driving segregation and during anatexis (Brown, 2007). It will describe melt migration driven by changing pressure gradients created during heterogenous progressive deformation (thus transient stress fields) in the crust, combined with pressures created by the buoyancy of the melt. The multiple granite phases present in the field area, together with the varying degrees of deformation experienced by each phase, also allows for discussions of the rates and timescales of melt migration.

Chapter 2

Geological Setting

2.1 Regional geology

The study area is located approximately 45 km east of Swakopmund in western Namibia, within the southern Central Zone of the Damara Belt (Fig. 2.1). The Damara Belt is one of the major Pan-African (550–480 Ma) orogenic belts in southern Africa that records the oblique north-directed collision between the Congo and Kalahari Cratons (Prave, 1996; Poli & Oliver, 2001). The orogen consists of two branches; the Kaoko belt, a north-trending coastal branch, and the Damara belt, a NE-trending intracontinental branch (Martin & Porada, 1977; Miller, 1983, Fig. 2.1).

The orogen consists of a several thousand metre thick succession of Neoproterozoic to Paleozoic metasedimentary rocks of the Damara Supergroup. The sequence documents early rifting between 780–760 Ma, marine sedimentation from 740–580 Ma, and continental collision from 580 Ma (Miller, 1983; Henry *et al.*, 1990). The belt is internally subdivided into four zones based on stratigraphy, metamorphic grade, structural style, and geochronology (Miller, 1983). The main subdivisions include the low-grade metamorphic Northern Platform, which consists of a thick sequence of Otavi Group carbonates, and the Northern and Southern Zones that are separated by the high-grade metamorphic Central Zone (Fig. 2.1). The Northern Zone consists of low-grade metamorphic volcanic and sedimentary rocks and intrusive bodies that experienced folding and thrusting towards the north, whereas the Southern Zone consists almost exclusively of pelitic sedimentary rocks that were thrust to the south-east. (Miller, 1983; Martin & Porada, 1977). The Central Zone is comprised of mainly pelite and shelf-type carbonate metasedimentary rock (Miller, 1983; Kisters *et al.*, 2004).

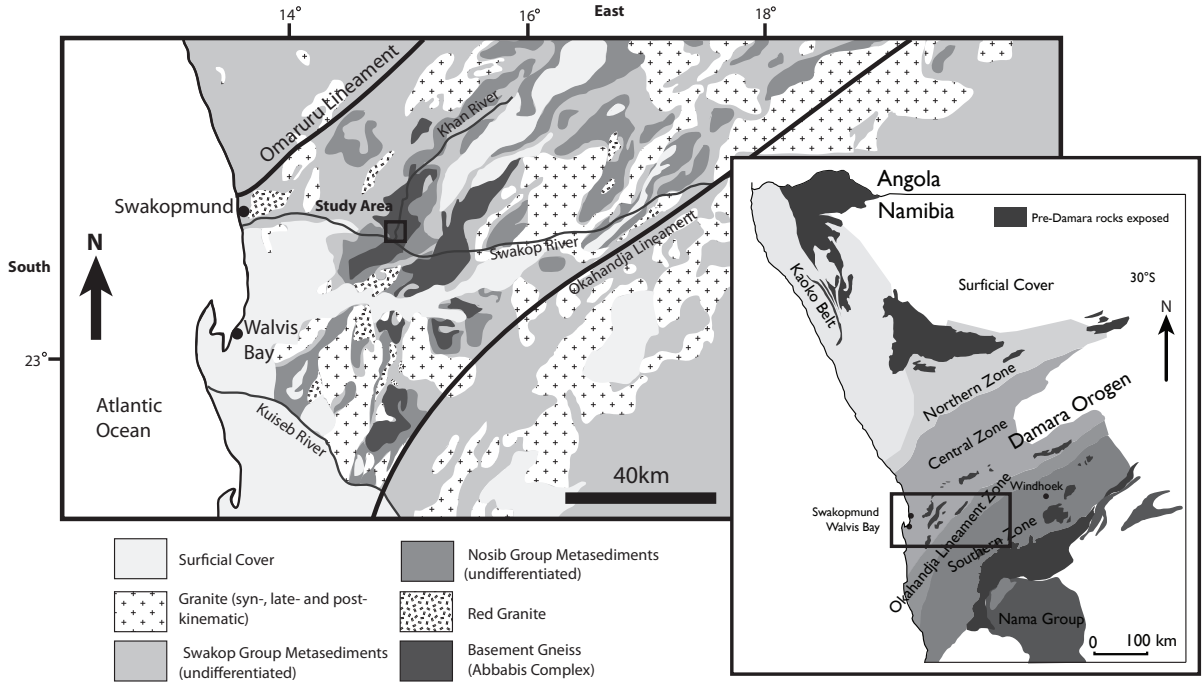

Figure 2.1: Location map of the study area in the southern Central Zone along the Khan River, near its intersection with the Swakop River, after Jung *et al.* (1999) and Basson & Greenway (2004). Inset: A map of Namibia showing the zones of the Damara Orogen, after Miller (1983) and Viola *et al.* (2006).

The Central Zone is separated from Northern and Southern Zones by the Otjihorongo thrust and Okahandja Lineament, respectively (Fig. 2.1). The Central Zone is further separated into northern and southern sections by the Omaruru lineament, with the upper stratigraphic formations of the Damara sequence exposed in the northern Central Zone, and the southern Central Zone comprising of its lower formations (Miller, 1983; Nex *et al.*, 2001). The current exposure level of the Central Zone provides an oblique cross section through the orogen, such that greenschist facies rocks at structurally higher levels are exposed inland towards the eastern region of the orogen, with higher-grade rocks from progressively deeper structural levels exposed closer to the coast in the west (Fig. 2.1).

The area around Swakopmund and Walvis Bay falls within the southern Central Zone and exposes mid-crustal, upper-amphibolite and granulite facies rocks (Miller, 1983; Jung *et al.*, 2002). Here the base of these Damara Group rocks overlie the gneisses of the Abbabis Complex, a sequence of 2.0–1.1 Ga-old quartzofeldspathic augen gneisses with minor amphi-

bolite and pelitic biotite schist, that are considered to represent the margins of the Congo and Kalahari cratons (Jacob *et al.*, 1978; Kröner *et al.*, 1991; Nex *et al.*, 2001; Jung *et al.*, 2002). Within the Southern Central Zone, these basement rocks occur as a series of NE–SW trending antiformal elongate domes (Fig. 2.1), and typically display high strain zones occur along their basement–metasediment contacts (Tack & Bowden, 1999).

2.1.1 Stratigraphy

The Damaran metasediments, which overlie the basement in the southern Central Zone, form part of the Nosib and Swakop Groups (Fig. 2.2). The Nosib Group consists of fluviatile sediments, interpreted as an early rifting sequence, and includes arkoses and quartzites of the Etusis Formation that are overlain by hornblende–biotite schists, various metapsammitic gneisses and calc-silicate rocks of the Khan Formation (Nex *et al.*, 2001; Basson & Greenway, 2004). The lower Swakop Group rocks are thought to be associated with the change from rifting to spreading. The Swakop Group includes marbles and schists of the Rössing Formation, glaciogenic diamictites, metapsammitic gneisses, and minor banded-iron formation of the Chuos Formation, and marbles, calc-silicate rocks, and metapelites of the Karibib Formation (Miller, 1983; Nex *et al.*, 2001; Basson & Greenway, 2004). The Chuos Formation diamictites (746 ± 2 Ma; Hoffman *et al.*, 1996) represent a period of glaciation, and are correlated with various Sturtian (750–720 Ma) glaciations around the world (Hoffmann *et al.*, 2004). The aluminous metapelitic schists and gneisses of the lower part of the Kuiseb Formation that occur in the Central Zone are described as deeper water facies (Miller, 1983), and are much less extensive than the metapelite and metagreywacke turbiditic upper Kuiseb rocks in the Southern Zone, where they are interpreted as an accretionary prism sequence (Kukla *et al.*, 1991; Basson & Greenway, 2004).

2.1.2 Tectonics, metamorphism and magmatism

Deformation in the Central Zone has been divided into anywhere between two and four phases (Miller, 1983; Nex *et al.*, 2001; Basson & Greenway, 2004; Kisters *et al.*, 2004). D_1 and D_2 are associated with recumbent and isoclinal folds, bedding-parallel foliation and migmatitic banding (Miller, 1983; Basson & Greenway, 2004), and low-angle thrusts, the vergence of which is unclear (Kisters *et al.*, 2004). D_3 is a later event characterised by NE–SW oriented kilometer-scale domes and synclines, which define the main structural trend

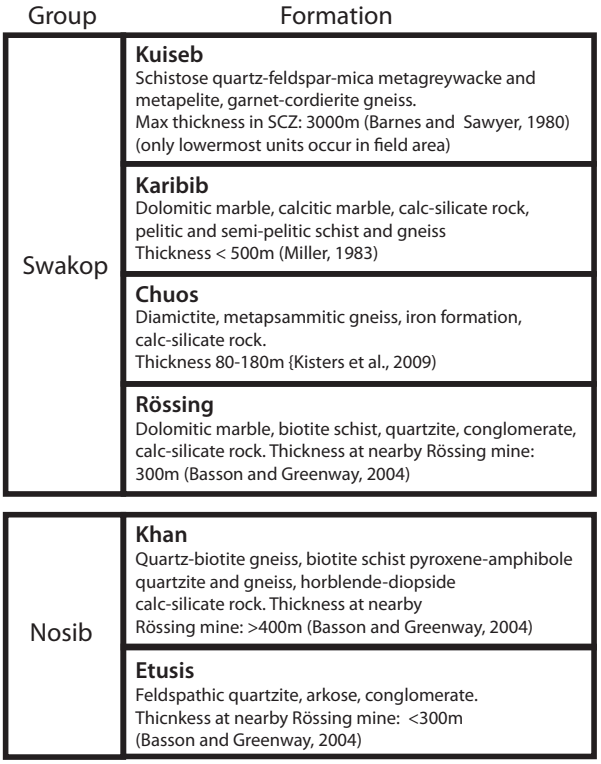

Figure 2.2: Stratigraphic column showing the simplified Damara Sequence stratigraphy of the southern Central Zone. Approximate thickness estimates are given for nearby areas, however large amounts of tectonic duplication and attenuation makes estimates rough and highly variable.

in the southern Central Zone. D_1 and D_2 are interpreted to be related to peak Damaran transpressional deformation, whereas D_3 shows evidence of constrictional tectonics, caused by post-collisional, collapse-related oblique extrusion of the central zone towards the WSW (Poli & Oliver, 2001; Kisters *et al.*, 2004). Later deformation (D_4) led to strike-slip movement on the Omaruru and Okahandja lineaments, as well as thrusting in the northern Central Zone (Miller, 1983), and is also responsible for the current NNE-trending Rössing Dome axis, and various NNE-trending shears in the surrounding area (Basson & Greenway, 2004).

The metamorphic grade of the exposed rocks of the Damara orogen increases progressively from greenschist facies in the east, through rocks near Karibib, where P–T estimates are around 550 °C and 2–3 kbar (Puhan, 1983; Miller, 1983), to high-temperature, medium-pressure amphibolite to granulite facies metamorphism at the Atlantic coast. At the coast metamorphic conditions of 7 kbar and 760 °C are estimated for migmatitc gneisses (Masberg, 2000). Peak metamorphic conditions for areas slightly inland are estimated at lower pressure

of around 5 kbar and 750 °C (Jung & Mezger, 2003; Ward *et al.*, 2008). Dating of monazite and garnet constrain peak metamorphism to have occurred at 550–540 Ma (Jung & Mezger, 2003). However, the southern Central Zone is thought to have undergone multiple later metamorphic events from 525–470 Ma which coincide with emplacement of syn- to post-tectonic granites at structurally higher levels to the east (Nex *et al.*, 2001; Jung *et al.*, 2001; Jung & Mezger, 2003). These granites have a wide range of crystallisation ages (which are not well constrained) roughly between 840 and 460 Ma. This range is constrained from a number of ages determined for different Damaran granitoids using: U-Pb whole zircon (errors +/- 1-2 Ma) (Briqueu *et al.*, 1980), whole rock Sr-Nd (no errors provided) (Miller, 1983), U-Pb monazite (errors +/- 7 Ma) (Nex *et al.*, 2001), and U-Pb monazite (errors +/- 2-4 Ma) (Jung & Mezger, 2003). The composition of these granitoids vary from syenitic, dioritic, granodioritic to leucogranitic in composition (Jung *et al.*, 2001).

2.2 Geology of the study area

The study area comprises spectacularly exposed outcrops along the banks of the Swakop and Khan Rivers and consists of rocks that are typical of the south Central Zone of the Damara Belt. The area is 30 km southwest of Rössing mine, where pegmatites and leucogranites are mined for uranium, and the field area includes similar uraniferous leucogranites (Nex *et al.*, 2001). The Swakop River trends roughly perpendicular to the NE-SW structural grain of the belt, providing a natural cross section (Fig. 2.3). The eastern part of the area is dominated by outcrops of the Abbabis Complex that are exposed in a regional-scale domal structure, the Palmenhorst dome (Fig. 2.3).

The basement rocks are unconformably overlain on all sides of the Palmenhorst dome by the basal Damara sequence rocks of the Etusis and Khan Formations. The Palmenhorst dome also includes several inlying Damara Group metasedimentary packages (Jacob, 1974). The stratigraphy youngs towards the west, and the Rössing and Chuos Formations that overlie the Khan Formation are the dominant lithologies in the central parts of the study area. This area consists of a number of shallowly NE-plunging folds that thicken and repeat the Chuos and Rössing metasediments. The western part of the study area exposes the stratigraphically highest metasediments of the Karibib and Kuiseb Formations. These formations occur around the outer parts of the NE-SW trending Birkenfels Dome, the core of which contains Chuos Formation metasediments (Fig. 2.3).

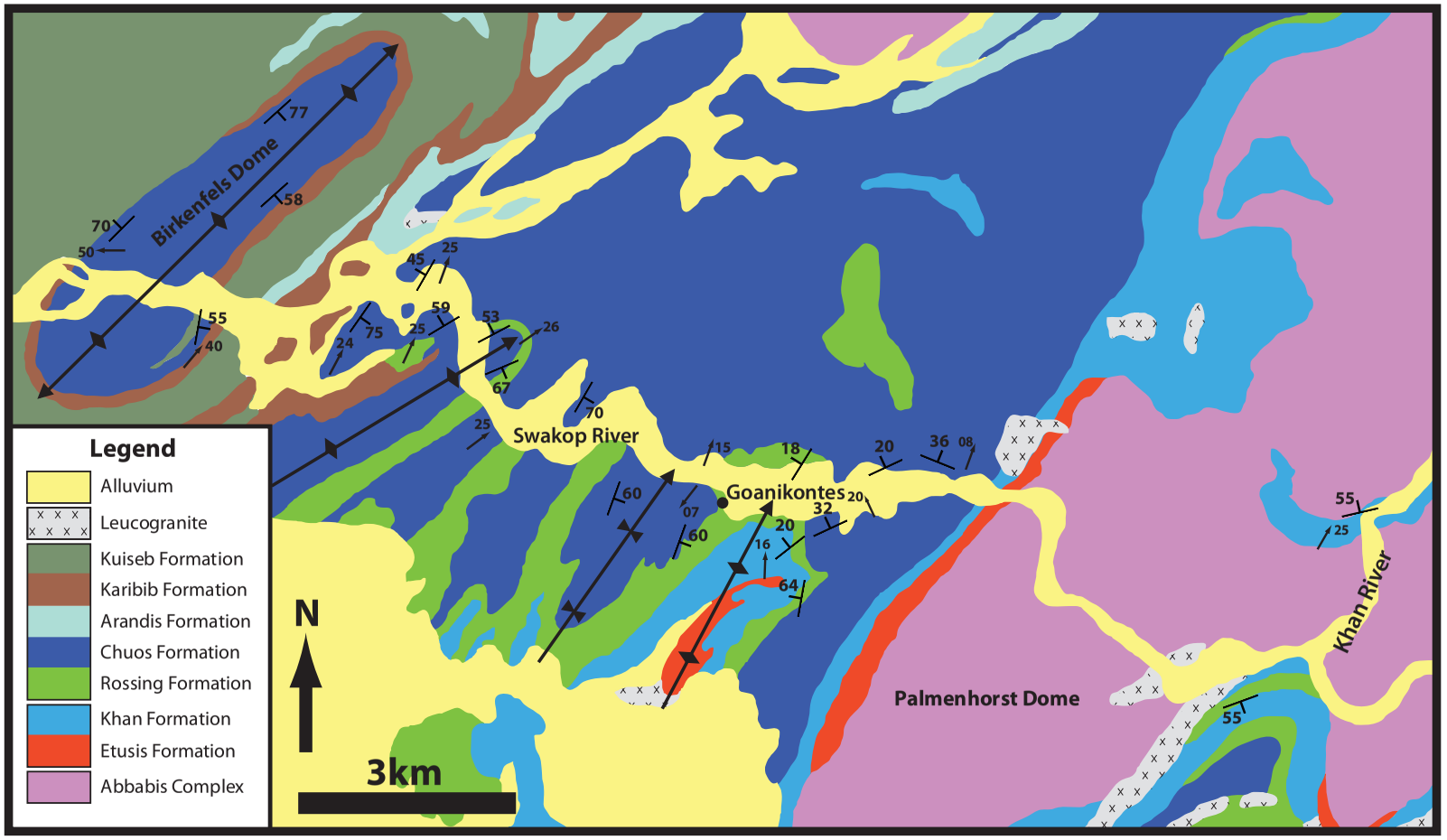

Figure 2.3: Lithological map of rocks along the Swakop and Khan Rivers (after Wells *et al.* (1988) and Bannerman Mining Resources Namibia Pty Ltd, Map Code: AS MAP 1, 21 November 2007) overlain with structural data from this study.

2.2.1 Lithology

The angular unconformity between the basement and overlying metasediments is undisputed as evidence of pebble deposits at their base is widespread (Kisters *et al.*, 2004). The stratigraphically lowest unit in the field area, the Etusis Formation, occurs predominantly as a medium- to coarse-grained pinkish-red feldspathic quartzite with minor conglomerate. It occasionally shows preserved cross-bedding, and mineral laminations are common (Miller, 1983). It is conformable with the Khan Formation above it, which occurs predominantly as diopside- and hornblende-bearing calcic metapsammitic gneisses. The lower units of this formation are usually more calcareous, often containing thick layers (0.5–3 m thick) and boudins of green clinopyroxene-amphibole calc-silicate rock. An unconformity separating the Nosib and Swakop Groups is thought to exist between the Khan and Rössing Formations, and is evidenced by discontinuous pebble horizons at the top of the Khan Formation (Nash, 1971; Miller, 1983) near Rössing. However, Nex *et al.* (2001) documented a gradational contact between the two formations in the Goanikontes area, and suggested that the unconformity does not exist there.

Outcrops of the Rössing Formation in the field area typically consist of serpentinitic and diopside-quartz bearing marbles, with thin layers of cordierite-biotite-sillimanite metapelitic gneiss (Basson & Greenway, 2004). The Chuos Formation, the most extensive rock unit in the field area, is generally conformable with the rocks below it (Miller, 1983); however, a local unconformity has been described between the Rössing and Chuos Formations (Henry, 1992; Nex *et al.*, 2001). The Chuos Formation is comprised of dark-grey massive and clast-bearing quartz-biotite metapsammitic gneiss. It is described as diamictite and suggested to be of glacial origin due to the mixed source of the clasts in some locations, but outcrops of proper diamictite are rare in the study area. This formation also contains some iron formation rocks, as well as cap carbonates that are mainly associated with the Chuos Formation in the Northern Zone of the orogen (Hoffmann *et al.*, 2004). The Karibib Formation conformably overlies the Chuos Formation and is comprised of carbonaceous rocks, which locally occur as massive marbles with minor calc-silicate layers. The conformable Arandis Formation occurs locally in the north of the field area and is comprised of biotite-cordierite schists, marbles and calc-silicate rocks. The Kuiseb Formation, only the lower-most parts of which are exposed in the field area, conformably overlies the Arandis Formation, and occurs locally as biotite and quartzofelspathic schists.

2.2.2 Structure and metamorphism

Regional D_1 deformation in the study area is only preserved as an early S_0-parallel foliation (S_1), as described by Basson & Greenway (2004) and Kisters *et al.* (2004). This S_0/S_1 planar fabric is folded to form the NE-SW trending fold structures, equivalent to D_2 of Kisters *et al.* (2004) and D_3 of Basson & Greenway (2004). These folds have an approximate wavelength of 3 km in the centre of the area (Fig. 2.3). There is no evidence of D_4 in the field area. Deformation is heterogeneously distributed across the area so that NE–SW-trending high- and low-strain zones exist on a kilometre scale. A particularly high-strain zone is localised along the basement–metasediment contact on the western edge of the Palmenhorst dome (Fig. 2.3; Oliver, 1994). This zone is characterised by constrictional deformation (Oliver, 1994) and the occurrence of voluminous sheeted granite intrusions (Nex *et al.*, 2001).

Peak metamorphic conditions in these rocks are similar to those of 5 kbar and 750 °C estimated by Ward *et al.* (2008) for aluminous metapelites ∼15 km to the northeast. Importantly, the peak metamorphic conditions are very close to the onset of partial melting for these rocks. Ward *et al.* (2008) reported that aluminous metapelitic rocks of the Kuiseb Formation have experienced partial melting, likely through a fluid-present melting reaction. However, significant melting is restricted to these fertile lithologies, and the more refractory rocks such as metapsammitic gneisses, hornblende-biotite schists, diamictites and calc-silicates that constitute most of the study area have not experienced any, or only very limited, partial melting.

2.2.3 Magmatic activity

The rocks of the study area are intruded by a number of different igneous phases. Early, deformed phases include a range of equigranular syenogranites, monzogranites and syenomonzogranites (Nex *et al.*, 2001; Basson & Greenway, 2004). A group of later sheeted leucogranites, most of which exhibit little to no deformation, occur as the predominant phases in the field area, particularly within high strain zones, and represent multiple phases of syn- to post-deformation intrusion (Nex *et al.*, 2001; Basson & Greenway, 2004). When all the granites are considered, there is an overall compositional trend defined by an increase in alkali feldspar content over time (Basson & Greenway, 2004), which is confirmed by the observations of this study. Using field evidence (the presence of the leucogranites within basement rocks, and the lack of partial melting in the metasediments), isotopic evidence from McDermott *et al.* (1996), and major element geochemistry, Nex *et al.* (2001) showed that the granites

are not sourced from the metasediments themselves, but appear to have multiple sources. The most likely source of the granites in the field area are the Abbabis Complex basement rocks, which are heterogeneous, show evidence of anatexis, and contain multiple leucogranite phases similar to those that intrude the overlying Damara sequence (Jacob *et al.*, 1986; Nex *et al.*, 2001).

When one considers the presence of the likely source region of melt at, and structurally below, the current exposure level in the study area, coupled to the presence of syn-tectonic granite plutons at structurally higher levels of the orogen to the east, the relationship indicates that the current study area intersects part of the melt migration pathway between the lower-crustal source and upper-crustal sink. Since the rocks of this study are situated close to, but below their solidus, they provide the opportunity to investigate the first stages of melt migration through mid-crustal subsolidus rocks.

2.3 Study localities

Specific study sites were chosen because they exhibit good examples of melt migration in different structural and lithological contexts. This allows for the comparison of melt migration style with change in variables such as lithology, fabric orientation, strain intensity, strain type, melt volume and number of melt phases. The locations of all outcrops are shown on Figure 2.4.

The Birkenfels Outcrop (Chapter 3), is on the western limb of the Birkenfels Dome and offers a comparison of low volume melt migration through steeply dipping metasediments exhibiting variable strain intensity and styles, and across two rock types. The Swakop Pavement Outcrop (Chapter 3) is an example of low volume melt migration in rocks that have experienced strongly prolate strain. The Calc-silicate Outcrop (Chapter 4), offers a spectacular example of high-volume melt migration through, and emplacement within, highly anisotropic metasediments via the use of boudin necks and the pre-existing anisotropy.

The High Strain Cliff, and the Etusis Pavement (Chapter 5), occur in the high strain zone along the western edge of the Palmenhorst dome. Both exhibit examples of medium to high volume melt migration through high strain rocks in a plane strain environment, however they are examined at different scales and show different migration mechanisms. The Fold Hinge (Chapter 6), was chosen to investigate the occurrence of axial-planar leucosome in a large (500 m $\times$ 650 m) fold hinge. The metasediment package outcrop (Chapter 7)

examines the movement of melt though an 80 metre-thick, shallowly-dipping heterogeneous metasedimentary package sandwiched within basement rocks. This situation provides an opportunity to study the vertical migration of melt from its source within the basement rocks, across the anisotropic rock package (a good analogy for the crust), to where it is emplaced near the top of the metasediments. The data and results from each of these outcrops are presented in the following chapters.

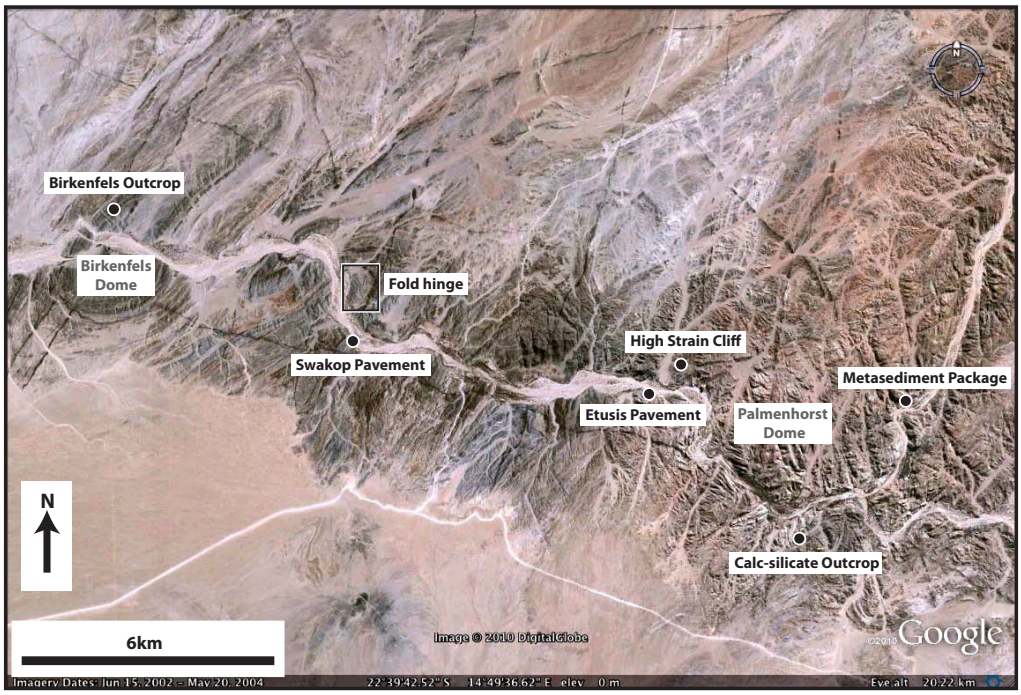

Figure 2.4: Google Earth^{TM} image showing the location of the seven outcrops used for this study.

Chapter 3

The Birkenfels and Swakop Outcrops

3.1 Outcrop Geology

This chapter describes two examples of low-volume melt movement within fairly homogenous rocks, but which exhibit contrasting strain styles. The first locality, the Birkenfels outcrop, is located north of the Swakop River at 22°38'03"S 014°44'04"E (Fig. 3.1). This study site is a southwest-facing outcrop approximately 70 m long, and 5–15 m high. It is comprised of steeply-dipping metasediments of the Chuos Formation, which exhibit local lithological variation, and provides a cross-section through the western limb of the NE–SW-trending Birkenfels dome (Fig. 3.1). The outcrop is close to the contact between the Chuos Formation and the marbles of the Rössing Formation that define the outline of the dome (Fig. 3.1). The dome is surrounded by metapelitic schists of the Kuiseb Formation. The second locality is a pavement along the southern edge of the Swakop River at 22°39'34"S 14°47'30"E. It is an approximately N–S trending flat pavement 50m long and 30m wide and is comprised of homogenous Chuos Formation rocks. The two outcrops are examined together in this chapter because they show comparably similar melt segregation structures within similar rock types and allow for the comparison of melt network styles within contrasting strain regimes.

3.1.1 Lithologies

The Birkenfels outcrop is comprised of two metapsammitic gneisses, which differ mainly in their quartz and biotite content, and the presence of magnetite and calc-silicate minerals.

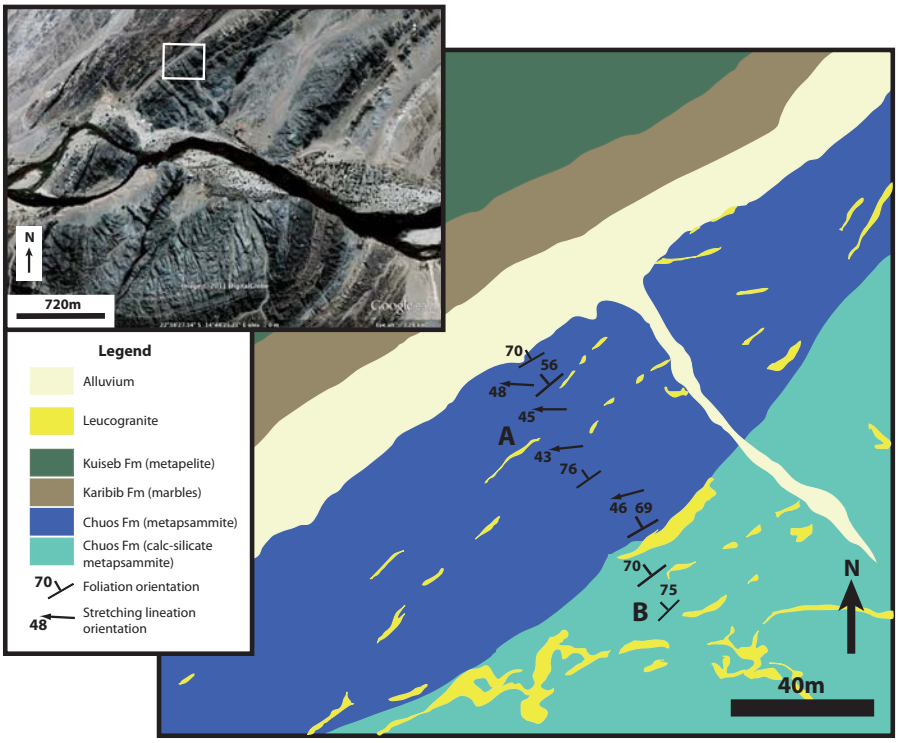

Figure 3.1: Lithological map of the area surrounding the Birkenfels outcrop found along the northwestern side of the Birkenfels Dome. This map was created on a Google Earth/^{TM} image. Features greater than 1m in size are shown. The position of the outcrop is shown by a NW-SE trending structural transect, shown by the line of dip and strike and lineation symbols, through the lithologies. Inset: Google Earth^{TM} image of the southern portion of the Birkenfels dome, showing the location of the lithological map (white box).

The northwestern side of the outcrop is comprised of fine- to medium-grained (1–5 mm grain size), grey metapsammitic gneiss (Fig. 3.2A). This unit comprises 50 m of the outcrop and at A in Figure 3.1, is comprised of approximately 90% quartz and 10% biotite. All modal mineralogy described in this work was estimated visually in the field. This lithology is very homogenous and any layering present is created by stromatic leucosomes and pods of early dismembered feldspar-rich leucosome that constitutes less than 2% of the rock. The proportion of calc-silicate minerals, which occur in oval-shaped pods (Fig. 3.2B), increases towards a sharp contact on the southeastern half of the outcrop, when the lithology becomes a fine- to medium-grained (1–3 mm grain size), brown-grey calc-silicate–magnetite metapsammitic gneiss (Fig. 3.2C). This unit comprises the southeastern 30 m of the outcrop (labeled B in Fig. 3.1). It contains a higher proportion of biotite (20–25% of the rock), and less quartz

(70% modal abundance).

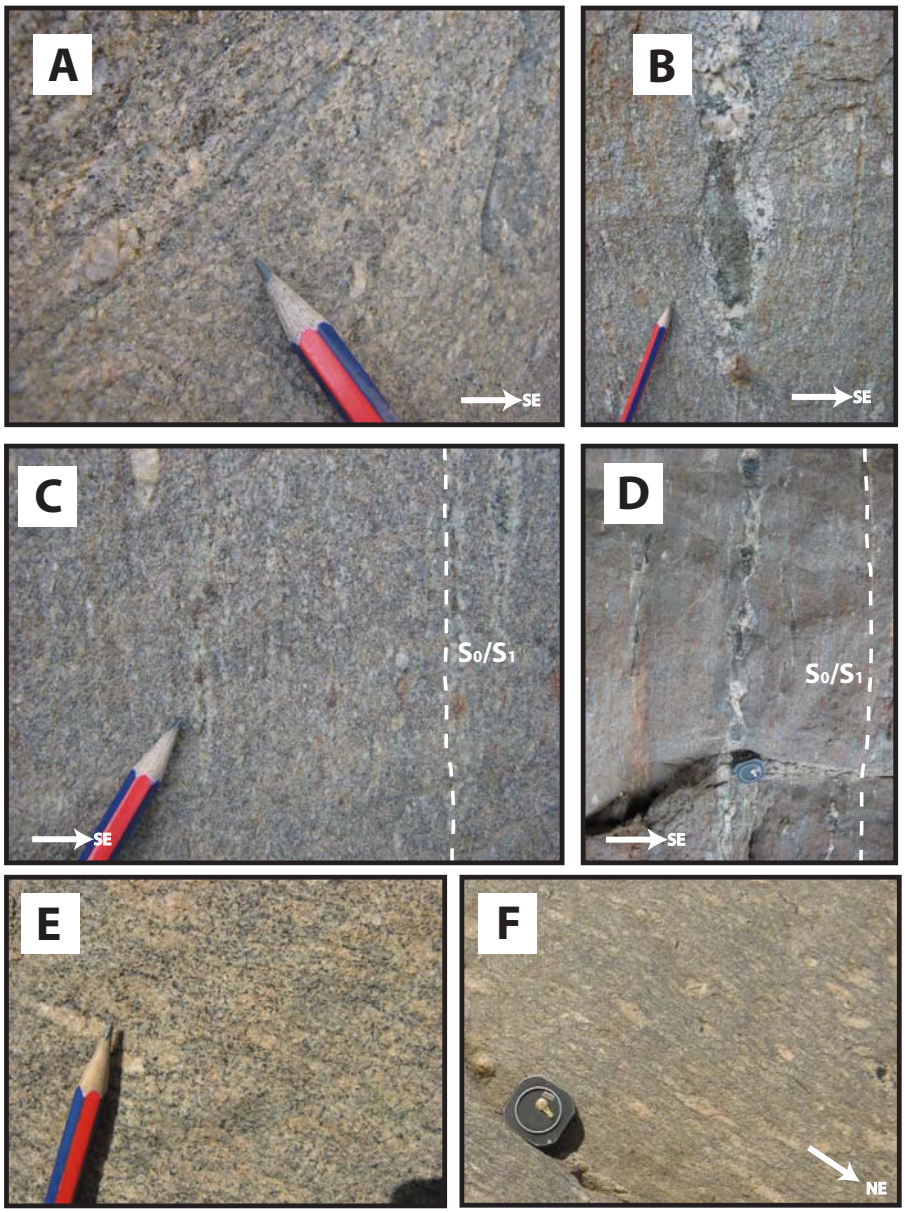

Figure 3.2: Rock type variation in the Birkenfels and Swakop outcrops. (A) The metapsammitic gneiss which comprises the northwestern half of the outcrop. (B) A calc-silicate pod comprised of diopside, hornblende, quartz and biotite. (C) The calc-silicate magnetite metapsammitic gneiss which comprises the southeastern half of the outcrop. (D) A calc-silicate boudin train. (E) Typical metapsammitic gneiss that comprises the Swakop River outcrop. (F) Dismembered leucosome within the metapsammitic gneiss of the Swakop River outcrop.

The main difference is the presence of magnetite (<5% modal abundance) and calc-

silicate pods (<5% modal abundance), which occur as 0.5–30 cm-sized isolated lenses and as layers of boudin trains (Fig. 3.2D). The mineralogy of the calc-silicate layers and pods includes diopside (60–90% modal abundance), hornblende (5–20% modal abundance), biotite (<5% modal abundance), and quartz (2–10% modal abundance). The Swakop River outcrop is comprised of a very homogenous, fine-medium grained (1–3 mm grain size), light grey metapsammitic gneiss (Fig. 3.2E). Its mineralogy includes 10–15% biotite, 80% quartz, and cream-coloured, oval-shaped lenses of feldspar with minor quartz. The lenses have sharp contacts with the surrounding rock, and are occasionally surrounded by a rim of biotite. They are interpreted as early dismembered melt phases, and comprise approximately 5–10% of the rock (Fig. 3.2F).

3.1.2 Intrusive Phases

Both outcrops contain a very low volume (approx.<5% volume) of intrusive phases, the majority of which occurs as folded layers exhibiting pinch-and-swell structures, or dismembered rods of the early intrusive phase. These early phases are crosscut and displaced by leucogranite-bearing shears which often exhibit diffuse edges. In addition, the Birkenfels outcrop also contains isolated, late, sharp-edged garnet-bearing leucogranite dykes.

The early dismembered and deformed leucosome in the Birkenfels outcrop is a fine- to medium-grained (1–3 mm grain size) grey quartz-rich granitoid. It is comprised of 80–85% quartz, 10–15% feldspar, and 5% biotite and occurs exclusively as rodded boudins and layers that are parallel to S_0/S_1 . Within biotite-rich leucosomes, the biotite is aligned parallel to S_1. Dismembered boudins of this quartz-rich granitoid tend to be the most quartz-rich, with younger pinch-and-swell layers containing a slightly higher proportion (10–15% more) of feldspar.

A later white leucogranite (Fig. 3.3A), crosscuts the older grey quartz-rich granitoid (Fig. 3.3B) and occurs within shears. It contains a greater proportion of feldspar and exhibits diffuse contacts with the surrounding rock. It is whiter in colour than the early phase, and slightly coarser grained (2–5 mm grain size). Its mineralogy includes 50% quartz, 45% feldspar, and 5% biotite. The youngest leucogranite phase in the Birkenfels outcrop occurs as sub-vertical sheets in the calc-silicate metapsammitic gneiss on the southeastern side of the outcrop (Fig. 3.3C). It is coarse-grained (0.2–2 cm grain size), cream-orange in colour, and contains 70% feldspar, 20% quartz, 5–8% garnet, and <5% biotite, and is in sharp contact

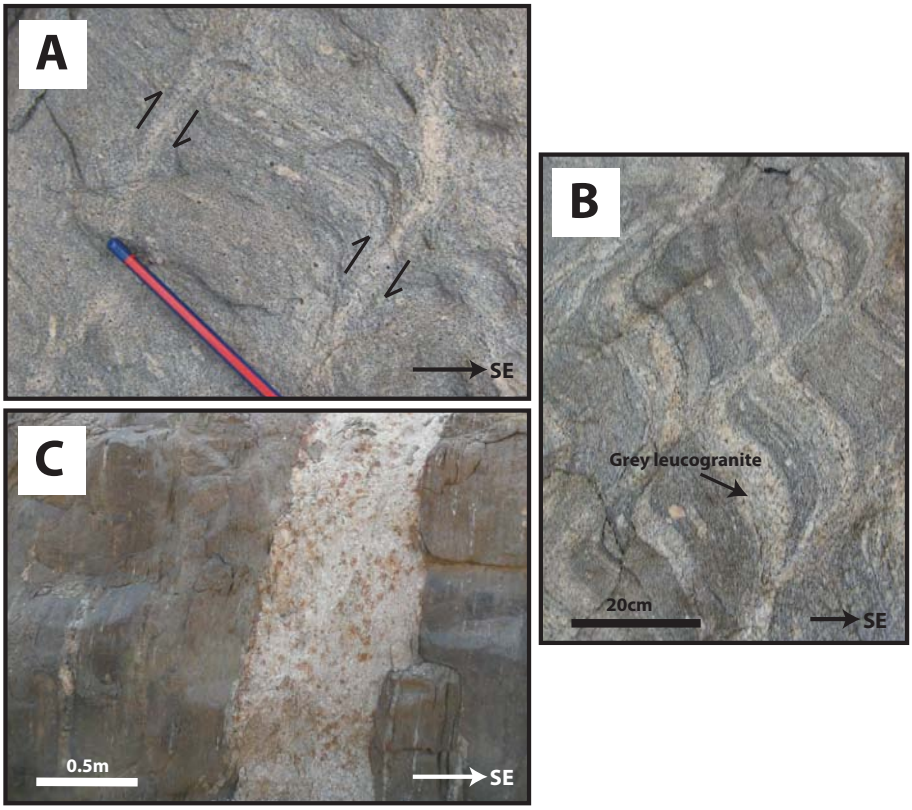

Figure 3.3: Intrusive phases in the Birkenfels outcrop. (A) Diffuse white leucogranite-filled shears showing reverse offset. (B) Early layers of grey quartz-rich granitoid crosscut by multiple later shears. (C) Late, thick, garnet-bearing leucogranite sheet.

with the surrounding metasediments.

At the Swakop River outcrop the predominant early intrusive phase is a pink, fine- to medium-grained quartz-rich granitoid that occurs as L_1-parallel cylindrical rods (Fig. 3.4A) and as folded layers (Fig. 3.4B) within the outcrop. It is comprised of 60–70% quartz (2–7 mm grain size), 25–35% potassium feldspar (1–5 mm grain size), and 5% biotite (2–5 mm grain size), and is crosscut by ductile shears which are often filled with younger white leucogranite (Fig. 3.4C). The younger white leucogranite is medium- to coarse-grained and grey-white in colour. It is also found as occasional L_1-parallel layers, and within irregular-shaped coarser-grained patches with sharp boundaries (Fig. 3.4D). The mineralogy of the white leucogranite includes 45–50% quartz (1–4 mm grain size), 45% feldspar (1–3 mm grain size), and 5% biotite (1–2 mm grain size); however, in the coarse-grained patches the quartz and feldspar reach between 0.5–1 cm grain size.

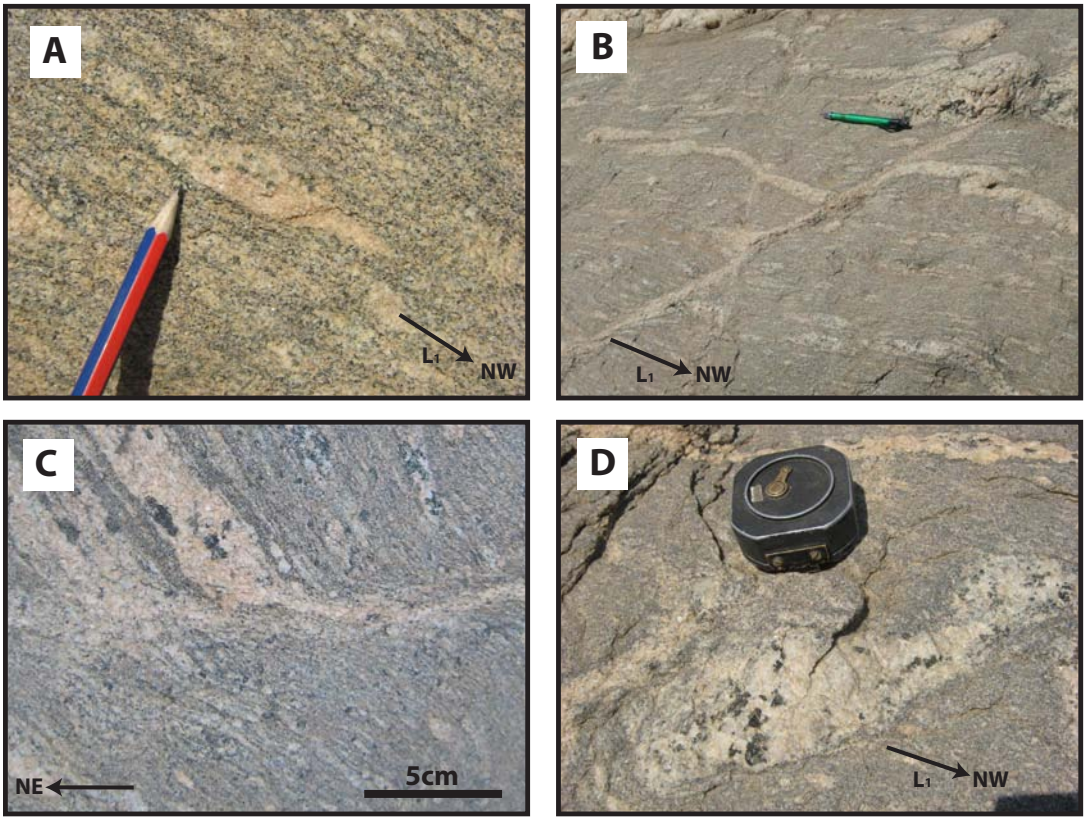

Figure 3.4: The leucogranite phases in the Swakop River outcrop. (A) Metapsammitic gneiss with and L_1-parallel rod of early pink quartz-rich granitoid. (B) Folded early pink quartz-rich granitoid crosscut by a later white-leucogranite filled shear. (C) Diffuse white leucogranite in a shear which offsets earlier pink quartz-rich granitoid. (D) A patch of coarser grained white leucogranite.

3.1.3 Fabrics and Structures

The predominant difference between the Birkenfels and Swakop River outcrops is their fabrics. The two lithologies of the Birkenfels outcrop exhibit variable flattening fabrics, whereas the Swakop River outcrop exhibits a constrictional fabric.

Birkenfels Outcrop

The main fabric in the Birkenfels outcrop is a steeply northwest-dipping, well-developed, penetrative foliation which is parallel to the bedding and therefore termed S_0/S_1. This foliation is oriented around 045–60°/70–90°NW (Fig. 3.5A). In both the quartz metapsammite and the calc-silicate metapsammite the foliation is defined by biotite, with the fabric being

better-developed in the more biotite-rich calc-silicate metapsammite. Both units also show a well-developed, moderately west-plunging (around 270°/50; Fig. 3.5A) stretching lineation which is defined by the the rodding of quartz, elongation of calc-silicate lenses and the alignment of early dismembered leucosome (Fig. 3.2 A–D).

Centimetre-scale shears crosscut the S_0/S_1 fabric within the quartz metapsammite. The shears are between 0.5–2 cm wide and 5–30 cm long. Dragged foliation and older leucosome layers show evidence of offset between 1–5 cm. The shears occur in two predominant orientations that are approximately 90° from one another. The first is a moderately to shallowly NW-dipping set (around 230°/40°NW; Fig. 3.5B) with reverse, top-to-the-SE displacement. This set is oriented 40° from the average S_0/S_1 (Fig. 3.6). The second set is less common and is moderately SE-dipping (around 040°/50°SE; Fig. 3.5B) with reverse, top-to-the-NW displacement. This set is oriented 50° from average S_0/S_1 (Fig. 3.6).

The distribution of shears across the outcrop is heterogenous, with a predominance of shears, particularly NW-dipping shears, occurring on the NW side of the outcrop, and slowly decreasing in abundance towards the contact between the two metapsammites. This leads to the shears being able to form a network on the northwestern side of the outcrop, but to occur as isolated structures towards the southeastern side.

Swakop River Outcrop

The predominant fabric in the Swakop River outcrop is a strong, moderately NE-plunging stretching lineation (L_1) centred around 055°/25° (Fig. 3.5D). It is defined by the rodding and alignment of quartz, and the alignment of oval- to rod-shaped dismembered early leucosome. The outcrop is pervaded by small 5–50 cm long, 0.5–4 cm wide shears that exhibit foliation drag along their edges and offset older leucosomes by 0.5–5 cm. The shears occur in two main orientations, as shown by the clustering of measurements on Figure 3.5D. A moderately-dipping set around 330°/40°NE, exhibits normal, top-to-the NE displacement, and a steeply-dipping set around 305°/75°NE shows reverse, top-to-the SW displacement. The acute angle between the two orientations, which contains the downthrown block, is 40°. This geometric relationship is shown in Figure 3.7.

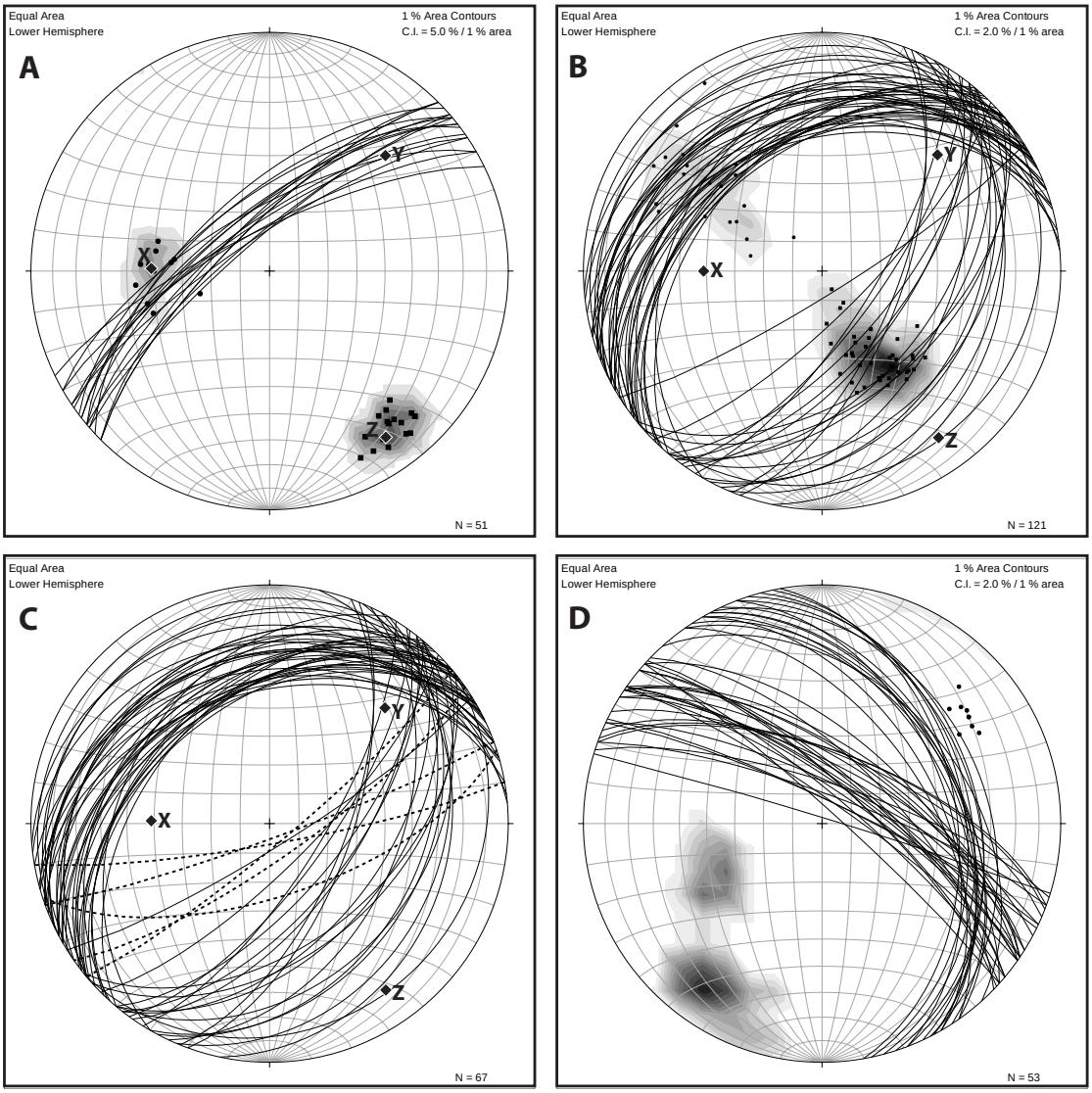

Figure 3.5: Stereonets showing fabric and planar intrusive feature orientations. (A) Stereonet showing the orientation of the foliation (S_1), poles to S_1 (black squares) and lineation (L_1) at the Birkenfels outcrop. XYZ are strain axes calculated using L_1 and S_0/S_1 orientations. (B) Stereonet showing the orientation of all crosscutting planar intrusive features in the Birkenfels outcrop. Poles to the structures have been plotted and contoured using 1% area contours. (C) Stereonet showing the steeply-oriented younger dykes (dashed lines) relative to earlier leucogranite-filled shears (solid lines) (D) Stereonet showing the orientation of the lineation (L_1), shown as black squares, and all leucogranite-filled shears in the Swakop River outcrop. Poles to shears are also plotted (black dots) and contoured using 1% area contours.

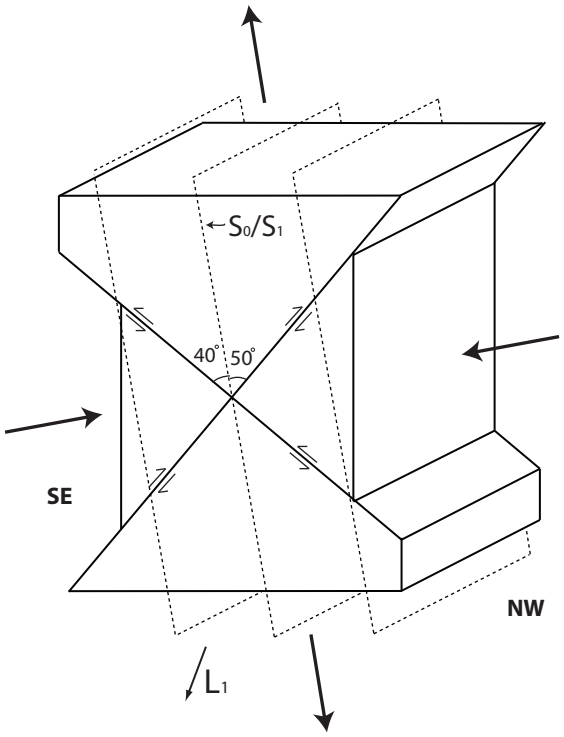

Figure 3.6: Block diagram of the current geometrical relationship between the shears, the foliation, and the lineation in the Birkenfels outcrop. The conjugate shears are 90° apart. S_0/S_1 dips steeply NW, and the NW-dipping and SE-dipping reverse shears are shown 40° and 50° from S_0/S_1, respectively.

3.2 Former melt-bearing structures

The leucosome-bearing structures in both outcrops are mostly small-scale (several cm's) with the exception of the thick late dykes in the Birkenfels outcrop, with individual structures typically between 0.2–5 cm wide and up to 1.5 m long. In the Birkenfels outcrop, stromatic leucosome is more common than shear-hosted leucosome, whereas leucosome in the Swakop River outcrop is predominantly hosted in shears.

3.2.1 Stromatic / Concordant Leucosome

Both outcrops contain a significant proportion of early stromatic leucosome that is deformed, either folded or as pinch-and-swell layers. Within the Birkenfels outcrop they form 0.5–5 cm thick layers parallel to S_0/S_1 (Fig. 3.8A). Within the Swakop River outcrop these layers are oriented subvertically and parallel to L_1, and are 0.2–10 cm thick (Fig. 3.8B). They do not strictly fall within the "concordant" category, but do form parallel remnants of stromatic-

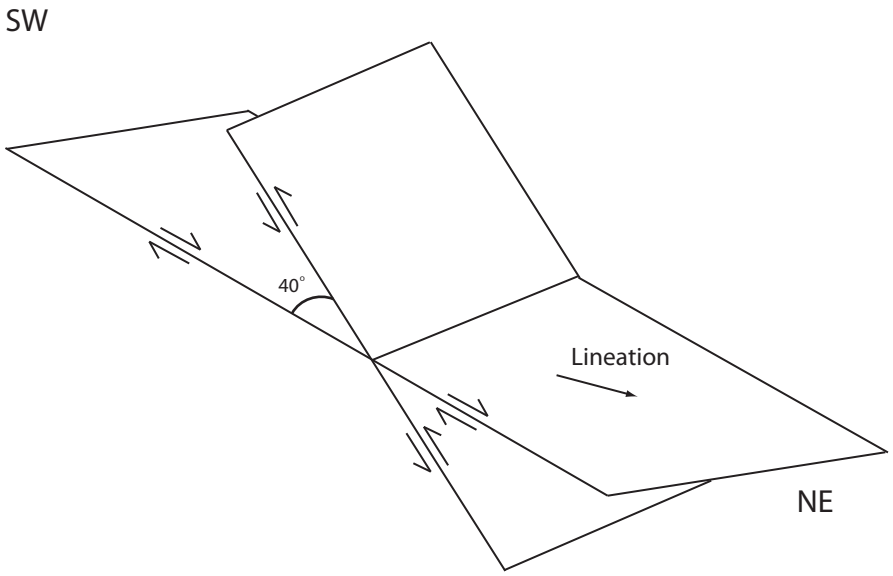

Figure 3.7: Sketch illustrating the current geometrical relationship between the shears and the lineation in the Swakop River outcrop.

looking leucosome. Both intrusive phases in the Swakop River outcrop occur as these L_1 parallel layers, and the ones containing younger white leucogranite are often connected to, and continuous with, leucogranite-bearing shears.

3.2.2 Melt-filled Shears

The ductile shears described above in both outcrops often contain leucogranites which form sheets within the conjugate shear planes (Fig. 3.8). The leucogranites within shears tend to have diffuse boundaries with the surrounding metasediments, suggesting that the leucogranites formed in situ, through segregation of very low volumes of melt from the surrounding metasediments. In both outcrops these leucogranite-filled shears truncate and offset earlier stromatic leucosome (Fig. 3.8A–C). The leucogranite-filled shears in the Birkenfels outcrop are smaller (on average 10–20 cm shorter) and contain less leucogranite than those in the Swakop River outcrop, so that most shears in the Birkenfels outcrop contain leucogranite sheets between 0.5–3 cm in width, whereas the leucogranite sheets within shears in the Swakop River outcrop often exceed 5 cm in width. In both outcrops the shears only contain a single melt phase, the white leucogranite. In the Swakop River outcrop the coarse-grained leucogranite patches are often connected to the end of leucogranite-filled shears, and the

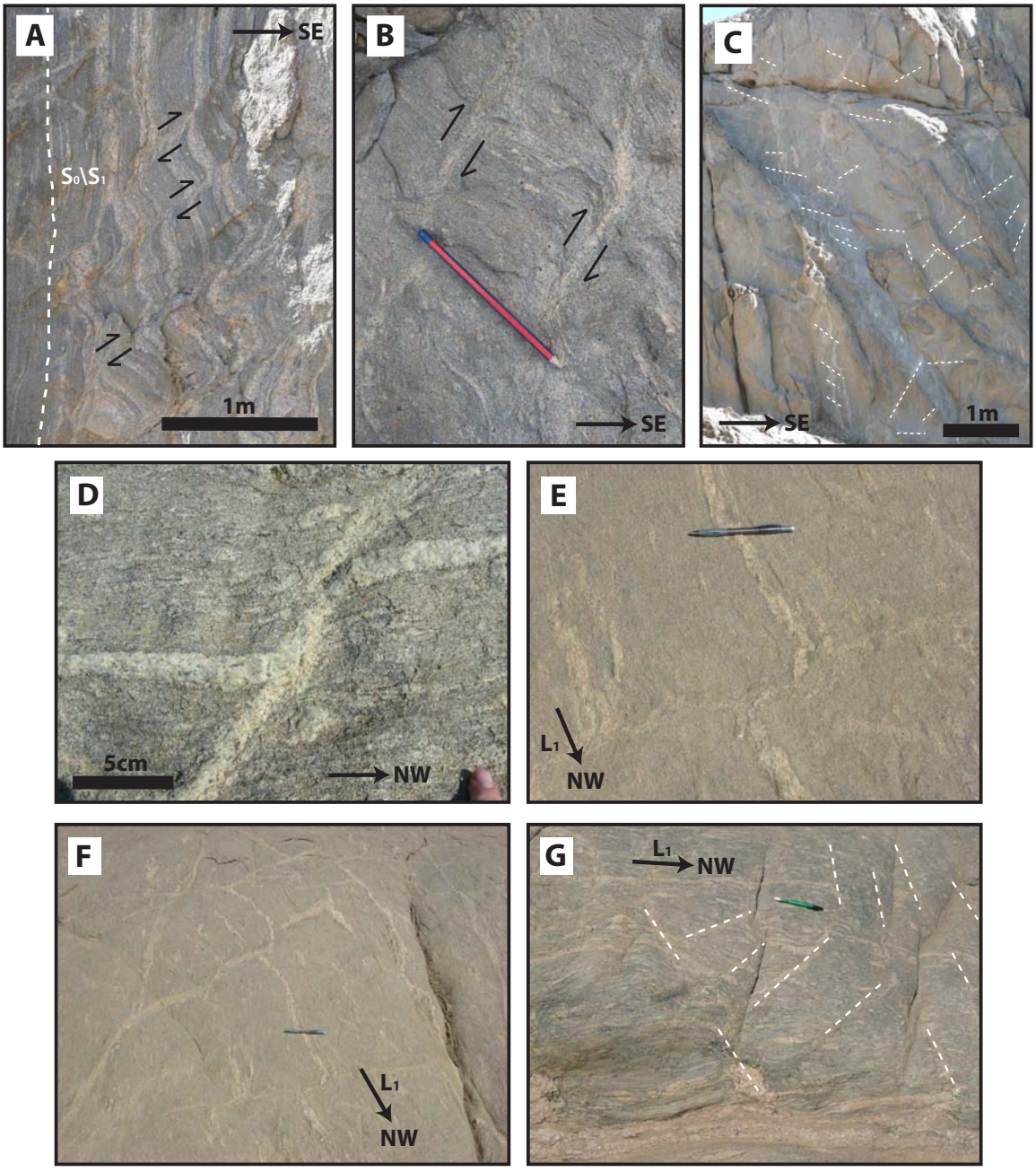

Figure 3.8: Leucogranite-filled structures in the Birkenfels (A–C) and Swakop River (D–G) outcrops. (A) Several parallel leucogranite-filled shears with reverse sense of displacement shown by displaced early stromatic leucosomes. (B) Photograph of two leucogranite-filled shears both exhibiting a reverse sense of displacement. (C) An interconnected network of diffuse leucogranite-filled shears within the Birkenfels outcrop. (D) Leucogranite-filled shear with sinistral displacement shown by offset early intrusive phase. (E) Diffuse shear zone with dextral displacement shown by offset early stromatic leucosome. (F) Interconnected diffuse leucogranite-filled shears that are connected with sheets parallel to L_1. (G) Several diffuse leucogranite-filled shears (shown by dashed white lines) within the Swakop River outcrop. This oblique section exposes shears in two orientations which form a conjugate set.

leucogranites are petrographically continuous with one another suggesting that the patches are accumulation sites for the leucogranite in the shears (Fig. 3.4D).

3.2.3 Subvertical dykes

Leucosome-bearing subvertical dyke structures are only found on the southeastern side of the Birkenfels outcrop. They contain the late garnet-leucogranite, and are oriented around 061°/77°SE (Fig. 3.5C). They are oriented between S_0/S_1–parallel and 30° from average S_0/S_1, and are typically 0.3–1 m wide and 5–8 m long (Fig. 3.3D).

3.3 Structural analysis

3.3.1 The Birkenfels Outcrop

The orientation of S_0/S_1 at the Birkenfels outcrop is consistent with its location along the northwestern side of the Birkenfels dome. On the SE side of the outcrop, the strength and orientation of S_0/S_1, and the boudinage of calc-silicate layers, together with the lack of a strong lineation, suggests that the overall strain is coaxial. However, the presence of a visible stretching lineation within the S_0/S_1 plane on the NW side of the outcrop suggests that there, some component of non-coaxial strain exists. The west-plunging orientation of this lineation is also not consistent with the typical NE-SW regional stretch observed in the rest of the field area.

The presence and anomalous orientation of L_1 is attributed to the existence of marbles along the outer edge of the Birkenfels dome, ∼35 m northwest of the outcrop. These marbles are highly attenuated and represent sites of localized high strain and shearing. Within rocks undergoing ductile deformation, strain is distributed, so that high strain localizes in zones, but also diffuses into rocks around these zones, so that strain gets incrementally lower away from the shear zone. The metapsammites in the NW part of the outcrop are closest to the high strain marbles, and thus have accommodated some of the strain which is shown by the strong L_1 and its anomalous orientation in comparison with the typical L_1 elsewhere. Using L_1 and S_1 the orientation of the strain axes (XYZ) were resolved, where X represents maximum elongation and Z represents maximum shortening, so that $X \geq Y \geq Z$ (Fig. 3.5A, B).

Most secondary melt movement in this outcrop occurs along two conjugate sets of shears that intersect each other to form an interconnected, permeable network (Fig. 3.8C). The ori-

entation and relative displacement along the conjugate shear set is approximately consistent with the direction of maximum apparent shortening, normal to S_0/S_1 (Fig. 3.5A, B) and the intersection of the shear planes is approximately parallel to Y. According to the Von Mises criterion conjugate shears should form 90° from one another and at 45° from the plane of maximum compressive stress in ductile rocks (Twiss & Moores, 1992, p. 175).

Therefore, in an apparent flattening strain regime, conjugate ductile shears should form $\leq 45°$ on either side of S_1, and the orientation of the NW-dipping shear set 30–50° from S_0/S_1 is mostly consistent with this. The SE-dipping shear set, which is 60–90° from S_0/S_1 is less consistent; however, the 90° angle between the shears is consistent with Von Mises criterion for ductile conjugate shear sets forming at 90° to one another (Twiss & Moores, 1992, p. 175). The most likely explanation for the difference in orientation relative to S_0/S_1 is that the shears were re-orientated during shearing along the marbles. The SE-dipping shear set is more favorably oriented to show rotation with respect to apparent stretching (X) created by this shearing. It is therefore plausible that both sets originally formed at 45° to S_0/S_1 and were passively rotated during continued flattening and dome formation.

The presence of the more prominent NW-dipping shears on the NW side of the outcrop relative to the SE side is attributed to the higher strain caused by a closer proximity to the sheared marbles. The networks that result have a higher connectivity and more established structure due to the greater abundance of shears, and because they are oriented such that they intersect the predominant SE-dipping shear orientation.

3.3.2 The Swakop River Outcrop

The intensity of the stretching lineation and the lack of a foliation in the Swakop River outcrop suggests that the rocks were subjected to strong apparent constriction and thus non-coaxial strain. The NE orientation and shallow plunge of L_1 is consistent with regional D_2 extrusion in the Damara Belt. The development of conjugate shears in flattening regimes is commonly observed, but their development during constriction is less well-documented. The two sets of melt-bearing shears in this outcrop do form an interconnected network, and have a relative sense of movement that suggests that they are conjugate. However, their relative orientations are only 40° apart, and their orientation is not consistent with the apparent extension shown by L_1 (Fig. 3.7). This was likely caused by rotation and re-orientation of the shears caused by the strong constriction associated with L_1.

3.4 Melt Migration

These two outcrops are examples of the initial steps in the melt segregation and migration process. Typical field evidence for *in situ* melting in migmatite terrains is shown by diffuse-edged leucosome, which has been evidenced by the chemistry of diffuse versus sharp-edged leucosome relative to host rocks (Jung *et al.*, 1999; Sawyer, 2001; Ward *et al.*, 2008). The diffuse nature of the leucogranite within the shears in the outcrops is interpreted as *in situ* melt formation, suggesting that the leucogranite-filled shear networks represent the segregation step in the melt movement process. The two outcrops show that leucogranite preferentially localizes within pre-exisiting ductile shears that are formed within the dominant strain regime. Evidence for melt movement, and not just melt localization, along the shears in the Swakop River outcrop is the presence of the attached coarser grained patches, which indicate melt localization along shears zone, followed by movement into accumulation sites.

The lower relative leucogranite volume within the SE side of the Birkenfels outcrop, and the presence of occasional steep dykes, shows that melt migration along a steep pre-existing foliation is very effective at vertical melt migration.

Chapter 4

Calc-silicate Outcrop

This chapter describes an outcrop that contains bouding necks that are utilised as long-lived dilational sites by different melt batches to become settings for medium-volume (10^2–10^5 m^3) melt accumulation, with melt migrating to these sites over distances of 10's to 100's of metres through the surrounding rocks. The outcrop is comprised of interlayered clastic metasediments and calc-silicate rocks of very different relative competency. This heterogeneous package experienced flattening strain, leading to extensive boudinage of the competent lithologies on a range of scales, depending on the thickness of individual layers. Leucogranite occurs in boudin necks that vary in size from a few centimetres to in excess of 30 m. To investigate the mechanisms involved in the migration and accumulation of melt in these structures, one very well-exposed, 30 m-wide leucogranite-filled boudin neck was described, along with its associated feeder dykes. This boudin neck is one of a series of large-scale boudins developed over a few 100 m along strike (Fig. 4.1).

4.1 Outcrop Geology

This outcrop is found south of the confluence between the Swakop and Khan Rivers at 22°42'10"S 14°53'28"E. It is located on the SE side of a narrow gully and comprises a steep NW-facing slope about 85m long and 50 m high. It consists of metapsammites interlayered with calc silicates and calc-silicate bearing metapsammites, rocks that are typical of the lower part of the Khan Formation. On a regional scale, this outcrop occurs on the SE side of the Palmenhorst Dome, quite close to its SW termination, and is about 120 m SE of the contact between the Damara Group and the Abbabis Complex basement (Fig. 4.1).

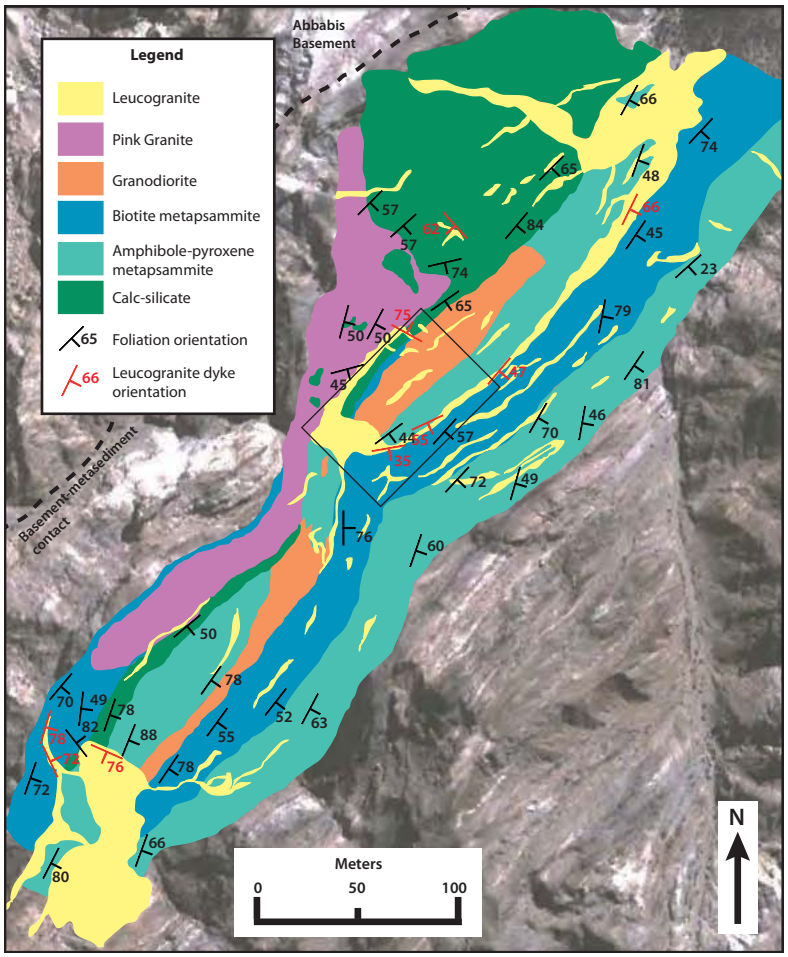

Figure 4.1: Geological map of the outcrop (black box) and surrounding area overlain on a Google Earth^{TM} image. All leucogranite bodies greater than 3m wide are shown. Note that different phases of leucogranite are not distinguished.

4.1.1 Lithologies

Several different metasediments occur at this study site, and are illustrated in Figure 4.2. The lower part of the outcrop is comprised of a 20 metre-thick clinopyroxene-amphibole-bearing metapsammitic gneiss, overlain by a 1–4 m thick layer of calc-silicate rock (Fig. 4.3). Both lithologies also occur as 10 cm–4 m-wide xenolithic blocks within the intrusive leucogranites. A 20 m-thick metapsammitic biotite schist comprises the upper parts of the outcrop (Figs. 4.1 and 4.3).

The clinopyroxene-amphibole-bearing metapsammitic gneiss (Fig. 4.2A) contains pods of black amphibole (hornblende), green clinopyroxene (diopside), quartz and biotite within an equigranular grey matrix of quartz (50% modal abundance), biotite (45% modal abundance),

and minor hornblende (<5% modal abundance). The pods have a variable ratio of coarse-grained minerals (0.2–3 cm grain size), with the biotite being mostly minor, and hornblende as the most predominant mineral. The biotite in the matrix is aligned and defines a penetrative foliation.

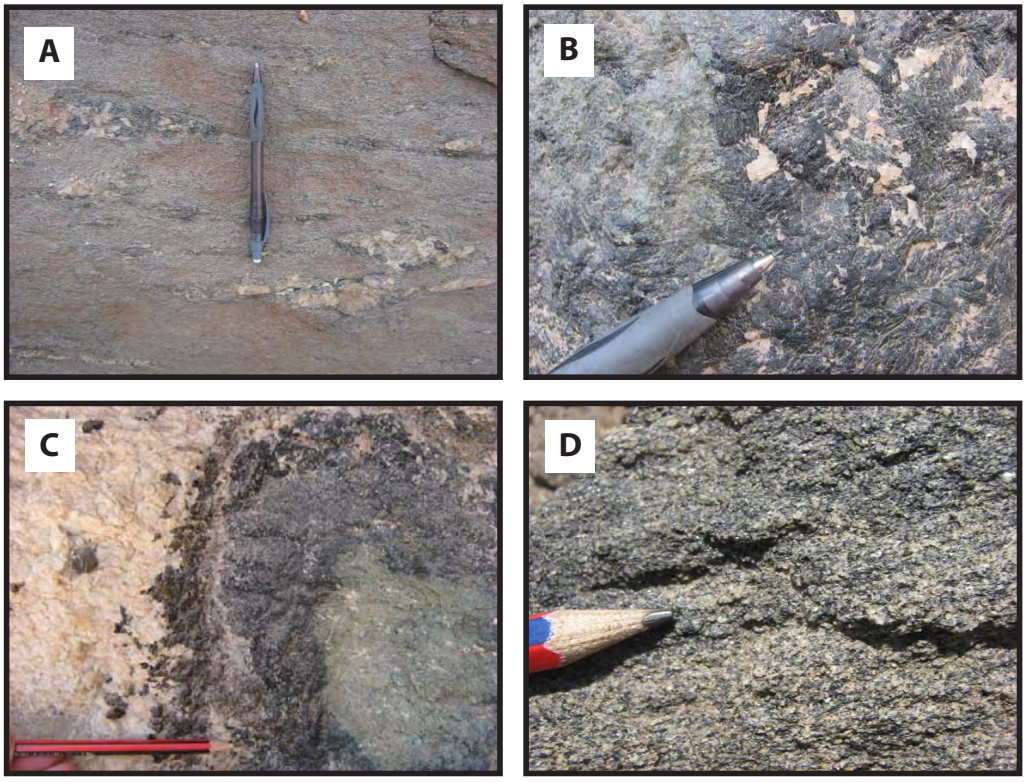

Figure 4.2: Field photographs of the metasediments. (A) Pyroxene-amphibole metapsammitic gneiss with pods of quartz, diopside and hornblende, surrounded by quartz-biotite gneiss. Pen = 15 cm. (B) Coarse-grained diopside-hornblende calc-silicate. Pen head = 1.5 cm. (C) Calc-silicate block in contact with pegmatitic leucogranite showing a thick, layered biotite–quartz–hornblende reaction rim. Pencil = 15 cm. (D) Quartz-biotite metapsammitic gneiss. Pencil head = 2 cm.

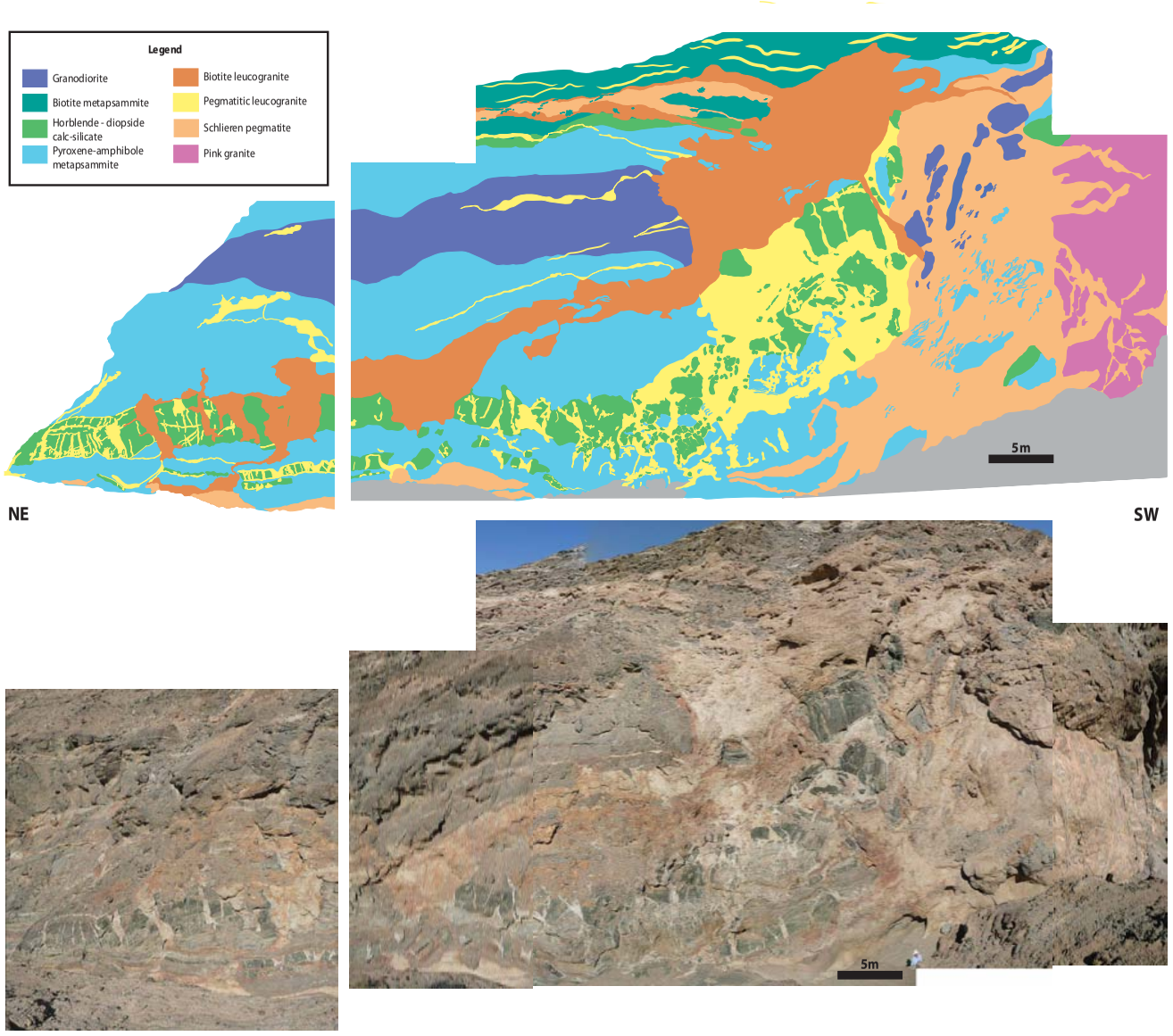

Figure 4.3: Top: A map of the outcrop showing all rock types and leucogranite phases. The map was overlain on the photograph (bottom), and features greater than 20 cm in size are shown. Bottom: Outcrop photograph on the same scale and orientation as the map.

The calc-silicate rock (Fig. 4.2B) is green and black in colour, and is comprised predominantly of diopside (at least 60%), and patches of hornblende (30%), quartz (less than 10%), and biotite (less than 5%). The grain size is highly variable, with grain size variation between 0.1–5 cm. The grain size is finer in patches with intergrown diopside and quartz. When hornblende and biotite occur intergrown with the diopside and quartz the grain size is typically larger (around 0.5–1 cm grain size). Both the diopside and hornblende show distinct crystal faces, whereas the biotite occurs as books. Hornblende and biotite occur predominantly when the calc-silicate is in close proximity (within 20–50 cm) of leucogranite. Xenoliths of calc-silicate which occur within leucogranite exhibit thick, concentrically zoned rims of biotite, biotite intergrown with quartz and hornblende intergrown with minor quartz (Fig. 4.2C). These rims are caused by the reaction of the calc-silicate rock and leucogranite melt.

The metapsammitic biotite schist (Fig. 4.2D) is dark brown-grey, and fine- to medium-grained with 1–3 mm grain size. It contains 40–50% quartz, and 50–60% biotite, with minor hornblende. The alignment of biotite and hornblende forms a strong penetrative foliation.

4.1.2 Intrusive Phases

There are several different intrusive phases present in this outcrop that can be distinguished by their mineralogy, grain size, crosscutting relationships, and the presence or absence of a planar or linear fabric. Two early phases that are deformed with the metasediments exhibit minerals that are aligned parallel to the foliation in the surrounding rock. These early phases include the sheeted granodiorite and a pink granite. The granodiorite is interlayered with the pyroxene–amphibole-bearing metapsammitic gneiss, whereas the pink granite occurs as a semi-concordant sheet to the northwest of the outcrop (Fig. 4.1). Both of these intrusive phases also occur as xenoliths within the younger leucogranites.

The granodiorite is medium- to coarse-grained (1–3 mm grain size), equigranular, and dark-grey in colour (Fig. 4.4A). It contains 35–40% plagioclase feldspar, 30% biotite, 10% hornblende, and 10% quartz, and the biotite is aligned, defining a solid-state foliation. The pink granite is fine- to medium-grained with grain size <1 mm. It contains 40–45% quartz, 40% orthoclase feldspar, and 15–20% biotite, with a strong planar fabric parallel to the overall foliation defined by aligned biotite (Fig. 4.4B).

In addition to these two early phases, three younger, planar/linear fabric-free leucogran-

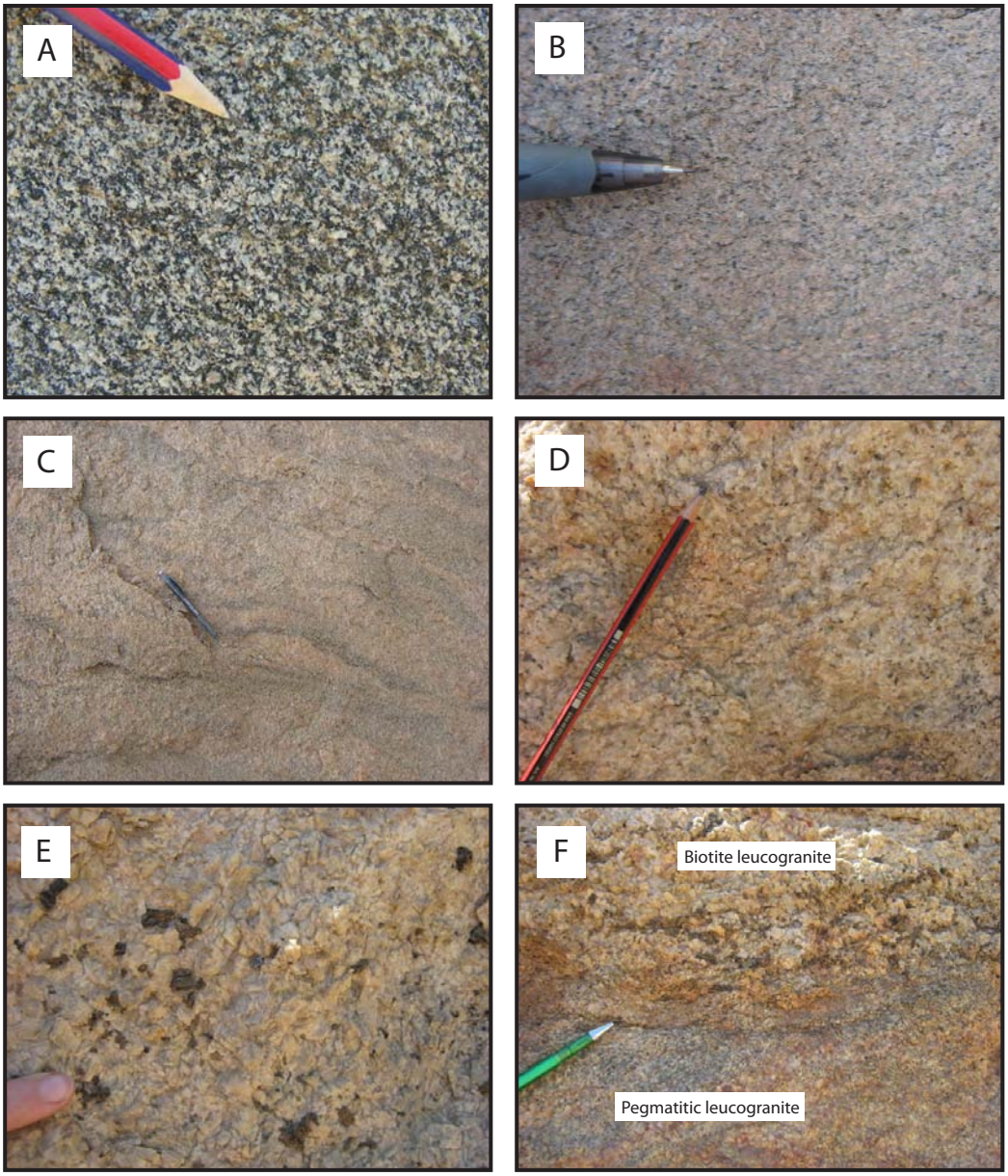

Figure 4.4: The intrusive phases. (A) Medium-grained granodiorite with pencil head (2 cm) for scale. (B) Fine-grained pink granite showing aligned biotite grains. Pen head = 1.5 cm. (C) Medium-grained schlieren granite showing layered appearance created by biotite schlieren. Pen = 15 cm. (D) Medium-coarse-grained leucogranite showing intergrown quartz and feldspar, with fine biotite grains. Pencil = 17 cm. (E) Pegmatitic biotite leucogranite with coarse feldspar crystals and biotite books. Fingernail = 1 cm. (F) A contact between the biotite leucogranite and the pegmatitc leucogranite showing a biotite rim between them. Pen head = 1.5 cm.

ite phases are also found. They tend to have mutually crosscutting relationships with one another, suggesting that they are of similar age. The most crosscut, likely oldest of the three phases is a fairly equigranular, fine- to medium-grained leucogranite that preserves evidence of magmatic layering. The layering is defined by trains of biotite schlieren that could possibly be dismembered remnants of the calc-silicate reaction rims. This schlieren granite is cream-pink in colour and is comprised of 55–60% feldspar (predominantly potassium feldspar), 30–35% quartz and 5–15% primary biotite (Fig. 4.4C). Schlieren-rich areas have a much higher proportion of fine biotite grains (up to 60%), the majority of which are aligned. Biotite in these zones is not as coarse-grained as primary biotite, which is typically randomly oriented. The schlieren granite also shows patches with magmatically-aligned feldspar crystals.

A phase of pegmatitic leucogranite has a more variable grain size, and is lighter in colour than the other two phases. It is typically a creamy white colour with red-staining on some quartz grains. Its mineralogy is comprised of 60–75% feldspar (predominantly plagioclase), 20–30% quartz, with quartz and feldspar intergrown and fairly equigranular, and less than 5% biotite (Fig. 4.4D). Grain size of the quartz and feldspar varies between 0.1–1 cm, but biotite grains are typically less than 3 mm.

The youngest of the three phases is a biotite leucogranite that is cream-pink in colour and very coarse-grained. Grain size varies between 1 and 3 cm, but some biotite books can exceed 5 cm in size (Fig. 4.4E). This phase is mostly equigranular, and is the most feldspar-rich leucogranite, with 70% feldspar (mostly plagioclase), 10–15% biotite, and less than 15% quartz. This youngest phase often exhibits a thin rim of biotite when in contact with earlier phases (Fig. 4.4F).

4.1.3 Fabrics and Structures

The predominant fabric in the outcrop is a well-developed steeply SE- to east-dipping penetrative foliation that is parallel to lithological layering and therefore designated S_0/S_1 (Fig. 4.5A). The orientation of this fabric varies locally around the edges of the large leucogranite bodies (Figs. 4.1 and 4.5A). The orientation of S_0/S_1 shows a predominant cluster around 030–040°/50–65°SE, and varies between 070°/40°SE and 355°/45°E around the edges of the large-scale leucogranite bodies (Fig. 4.5A). The foliation is associated with a very weak mineral elongation lineation (L_1) that is only occasionally developed. It is defined by elongated quartz grains in the metapsammite, and plunges shallowly to moderately NE (Fig. 4.5A).

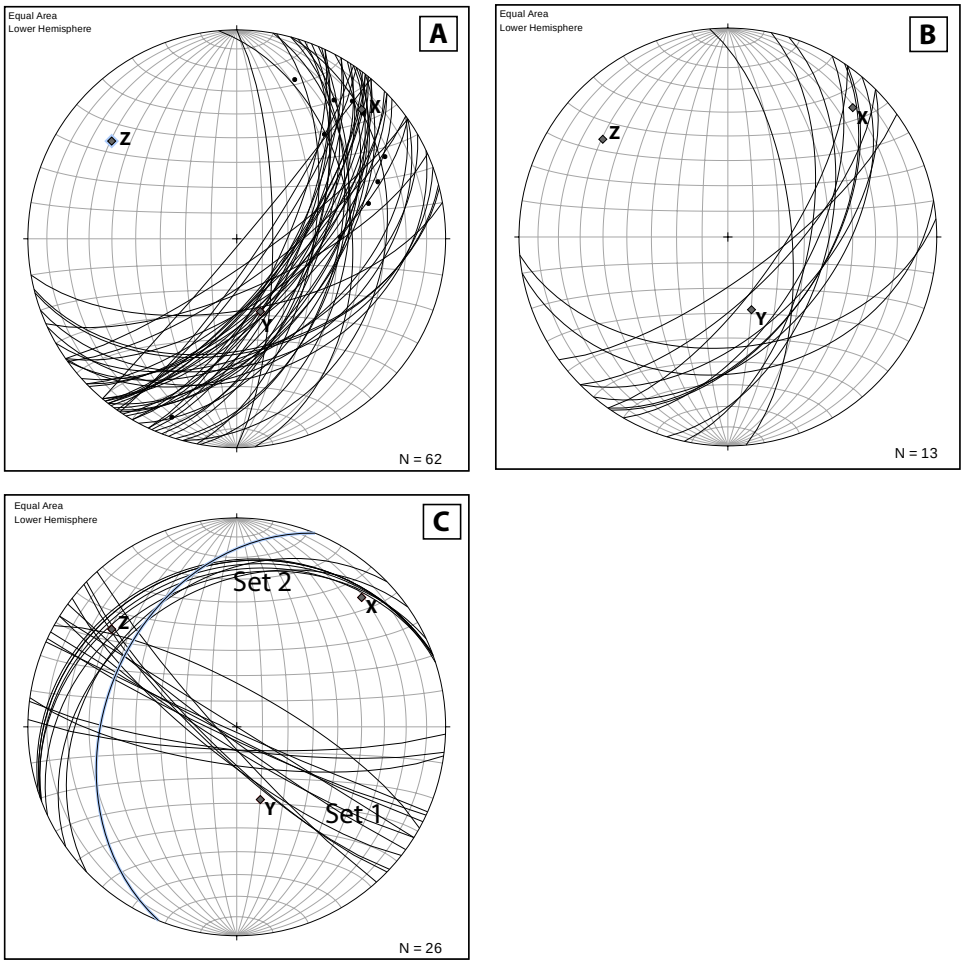

Figure 4.5: Stereonets showing the fabrics and structures in the outcrop. (A) Stereonet showing foliation (S_1; black lines) and lineation (L_1; black dots) measurements. XYZ represent strain axes resolved from S_1 and L_1. (B) Stereonet showing S_0/S_1 concordant leucosomes. C) Orientations of discordant leucogranite sheets represented as planes showing two distinct populations. XYZ represent strain axes.

The penetrative foliation is most strongly developed within the metapsammitic biotite schist, and is not present within the calc-silicate units. It is moderately strong within the pyroxene–amphibole-bearing metapsammitic gneiss, where calc-silicate nodules are elongated and aligned in the same orientation. Layers of calc-silicate, as well as a bedding-parallel early intrusive sheeted granodiorite (Fig. 4.1), are boudinaged so that they typically occur as angular, rectangular blocks (Fig. 4.6A–F). The boudins are often rotated and the surrounding gneissosity locally wraps around them (Fig. 4.6B).

4.2 Former melt-bearing structures

The various leucogranite phases are found in two main types of structures, namely either as stromatic and concordant sheets oriented parallel to S_0/S_1 or as irregularly-shaped bodies in interboudin spaces. The sheets are between 1 cm and 4 m wide, whereas the irregular bodies vary from a few centimetres to leucogranite bodies that are several 10's of metres in size. Where the same leucogranite phase is found in more than one setting, there is often petrographic continuity between the two, indicating that the structures formed a connected leucogranite network. Conversely, the same structure often contains more than one phase of leucogranite, with older phases occurring as xenoliths or layers enveloped by younger leucogranite.

4.2.1 Stromatic / concordant leucosome

Stromatic or concordant leucosomes are oriented parallel to S_0/S_1 (Fig. 4.5B). All leucogranite phases in the outcrop can be found as concordant leucosome on varying scales. Thin, <1 cm-wide veins occur within the pyroxene-amphibole-bearing metapsammitic gneiss and along the edges of the calc-silicate rock layers. Within the main outcrop, larger-scale (several centimetres to metres thick) concordant leucosome occurs along lithological contacts, particularly within the strongly foliated biotite metapsammite that occurs at the top of the outcrop, where concordant sills are at least 20 cm–3 m in width (Fig. 4.3).

4.2.2 Discordant leucosome in boudin necks

Discordant leucosomes are oriented nearly orthogonal to S_0/S_1 and are mostly found within boudin necks in the competent calc-silicate rocks (Fig. 4.6). They are 1–3 m wide, and two sets of discordant leucogranite orientations can be distinguished. The most prominent ones are NW–SE striking and steeply dipping (100–130°/75–85°SW; Figs. 4.5C and 4.6C, E). They are thicker and contain more leucosome than the less prominent set, which has a shallowly NW-dipping orientation (030–065°/25–35°NW; Figs. 4.5C and 4.6C). The orientations of these two discordant dyke sets are 80–100° from one another, and both are between 85 and 95° from average S_0/S_1 (Fig. 4.5C). All three of the late leucogranite phases occur in these structures, and where the two sets intersect each other there is petrographic continuity between the leucogranite in the structures (Fig. 4.6C).

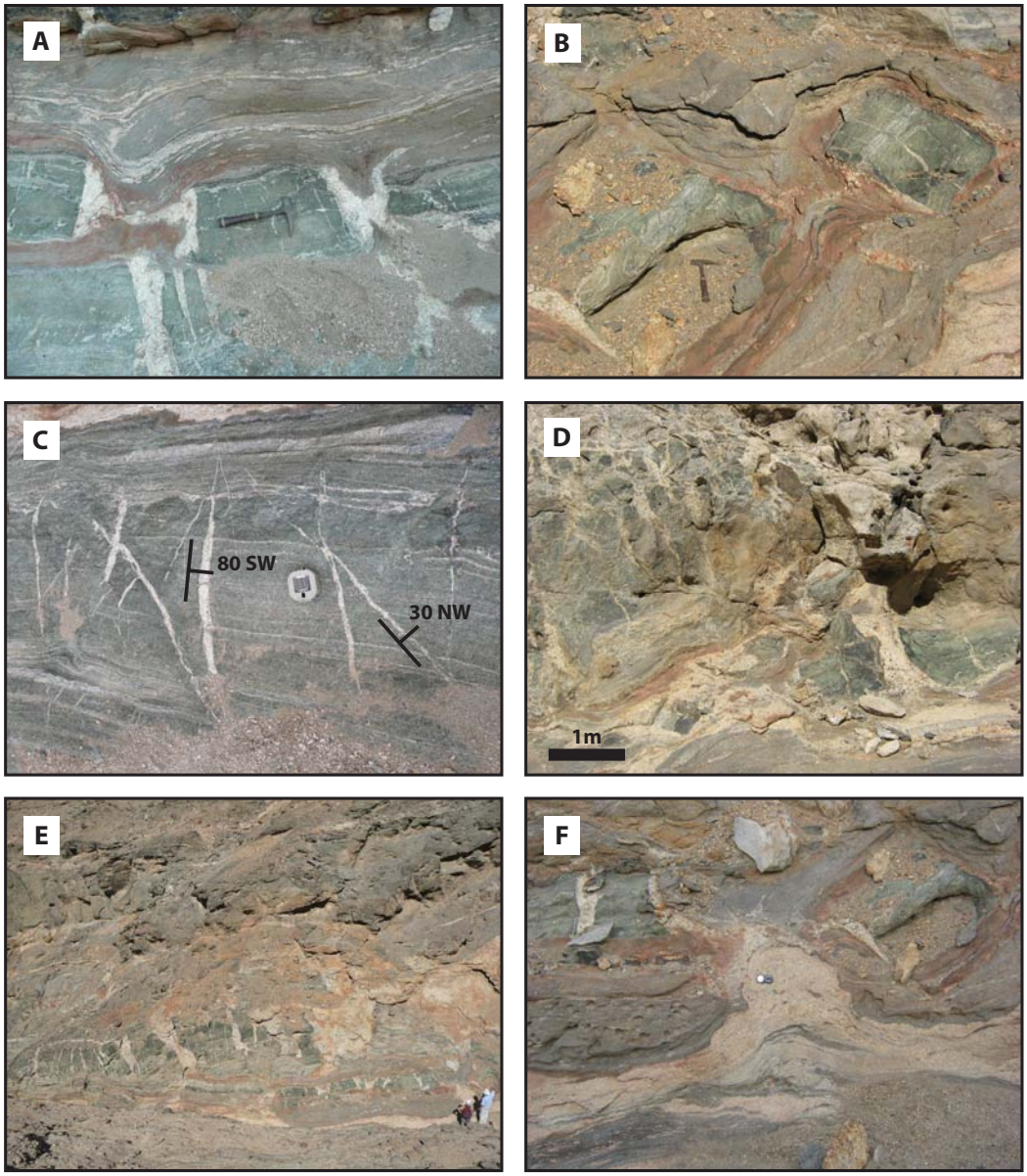

Figure 4.6: Leucogranite-filled structures in the outcrop. (A) Calc-silicate boudins, with pegmatitic leucogranite-filled boudin necks. The pyroxene-amphibole metapsammite in the top of the photograph shows foliation and concordant leucosome bent in towards the boudin necks. Hammer = 32 cm. (B) Rotated rectangular boudins surrounded by folded pyroxene-amphibole metapsammite. Hammer = 32 cm (C) Calc-silicate rock with discordant leucogranite-filled veins, showing their two predominant orientations. Compass = 8 cm. (D) Photograph of the edge of the main leucogranite body, showing blocks of calc-silicate rock surrounded by pegmatitic leucogranite. (E) Photograph of the calc-silicate layers with leucogranite-filled boudin necks. (F) An example of the early stages of leucogranite moving into a boudin neck, and rotated calc-silicate blocks. Open compass = 16 cm across.

4.2.3 Large Leucogranite Bodies

Within the field area, three leucogranite bodies of approximately the same size are observed along strike from one another (Fig. 4.1). The three bodies are in roughly the same orientation as smaller leucogranites in the NW–SE striking, steeply dipping boudin necks (Fig. 4.3). The central leucogranite body dips perpendicular to the foliation so that its walls crosscut the pyroxene-amphibole-bearing metapsammitic gneiss, the interlayered calc-silicate rock, and granodiorite. It is composite and contains all three leucogranite phases as well as xenoliths of all three metasedimentary lithologies (Fig. 4.7). Several of the larger concordant, composite leucogranite dykes connect with the intrusion, and the leucogranite phases are petrographically continuous between the two structures (Fig. 4.7).

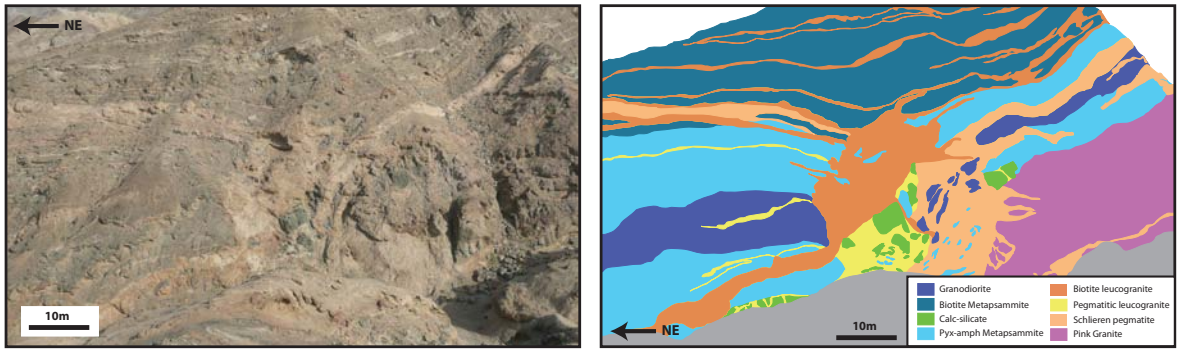

Figure 4.7: Left: Photograph of the calc-silicate leucogranite body showing its boudin-neck orientation, and right: a sketch map of the leucogranite-filled boudin neck and boudinaged lithologies, which include pyroxene-amphibole metapsammitic gneiss, interlayered with granodiorite and calc-silicate, and pink granite.

4.3 Structural analysis

The strength and orientation of the penetrative foliation within the metasediments of the outcrop, coupled to the chocolate-tablet boudinage developed in the calc-silicate, suggest an overall coaxial (flattening) strain, close to pure shear. The weak NE-plunging lineation is consistent with the typical Damara NE-SW stretch observed elsewhere in the area. The boudinage of the calc-silicate rocks, and the brittle fractures within them, in comparison with the folding and flow-structures in the metapsammites that bound them, suggests a large competency contrast between the two lithologies, with the calc-silicate rocks being considerably

more competent. The sharp fracture-like nature of the boudin necks is also consistent with this competency contrast, suggesting that the calc-silicates deform in a predominantly brittle manner.

The approximately 90° angle between the two discordant leucosome sets, and their 90° angle to S_0/S_1 suggests that they are the boudin necks that form two of the bounding surfaces of the boudins (Fig. 4.5C). The strain axes were resolved from S_1 and L_1 and are shown on Figure 4.5. X is shown to be approximately perpendicular to the prominent discordant leucosome, whereas Y is approximately perpendicular to the subordinate discordant leucosome. Since the structures perpendicular to X and Y are both dilational, X and Y both represent extension directions, which is consistent with flattening strain. The greater proportion of leucogranite within the prominent boudin necks relative to the subordinate boudin necks is consistent with them being perpendicular to the direction of greatest extension and, therefore, dilation. The consistency of the strain axes resolved from the planar and linear fabrics in the competent and incompetent rocks suggests that fabric formation and boudinage occurred concurrently, as part of the same deformation event.

4.4 Melt migration and accumulation

This outcrop represents a snapshot of lateral and/or vertical melt migration along foliation surfaces over 100's of metres to accumulation sites in dilatant boudin necks. It illustrates the interplay between deformation to create the dilatancy, and pulsed melt movement to fill the dilatancy as it becomes available.

The mutually crosscutting relationship between the three leucogranite phases suggests that they are of similar age, and the degree of deformation of the granodiorite and pink granite shows that the overeall intrusion of magma into the metasediments was protracted. The parallel alignment to S_0/S_1 of minerals within these two early phases is consistent with the overall coaxial strain experienced by the metasediment package, and the lack of planar or linear fabrics and lack of deformation of the younger leucogranite phases suggests that they intruded relatively late during Damaran deformation.

The composite nature of the top two S_0/S_1 concordant leucogranites, and their connection to the large leucogranite body, suggests that they accommodated a large volume, and multiple phases of magma through them to feed the large leucogranite body. The large central intrusion now represents a site of melt emplacement, but many of the smaller-scale leucogranite-filled

boudin necks on the northeastern side of the outcrop are connected to concordant leucosome (Fig. 4.6E). This, along with the presence of rotated boudin blocks that have only minor leucogranite preserved along their edges (Fig. 4.6B) suggests the former presence of a higher volume of melt. These boudin necks therefore were transient sites of melt accumulation, but ultimately became sites of melt loss.

It is likely that melt migration on the scale of the outcrop occurred in a pulsed manner, with at least three pulses of magma, represented by the different leucogranite phases. These different pulses utilised the same migration pathways and accumulation sites in the rocks. The force required for this protracted migration is provided by the opening of boudin necks (dilation) which, through the creation of hydraulic and pressure gradients, draw melt towards them (Vanderhaeghe, 1999). Once in a boudin neck, the melt has access to a structurally higher S_0/S_1 surface, and can move along it when a hydraulic or pressure gradient allows for it. In this way melt migration occurs in a process of alternating vertical and horizontal migration. It also means that migration would occur as a pulsed process whereby melt resides in boudin necks and along foliation surfaces until progressive tectonic deformation causes space to open elsewhere in the rock.

In the example of this outcrop, the steep orientation of S_0/S_1 is favourable for buoyancy-driven vertical melt migration and thus the boudin necks are not necessary to facilitate melt ascent. The presence of accumulated leucogranite within the large-scale boudin necks shows that local dilation forces can be stronger than buoyancy, such that melt accumulation in interboudin spaces is preferred to upwards migration. In this example and strain orientation, the presence of boudin necks actually hinders upwards melt movement when dilation sucks melt out of the S_0/S_1 surfaces. Nevertheless, the outcrop shows that boudin necks create effective connectivity between S_0/S_1 surfaces, which is necessary for vertical melt migration in outcrops with a relatively shallow S_0/S_1, discussed later in chapter 7.

Chapter 5

Melt Migration within a High Strain Zone

This chapter describes two outcrops in a high strain zone located along the WNW side of the Palmenhorst Dome (Fig. 5.1). The zone is 500m to 1km in width, and is characterised by concentrated, multiple phases of intrusion (Fig. 5.1). The geochemistry and age relationships of these granites has been previously described by Nex *et al.* (2001). The first outcrop, the Etusis Pavement, provides an example of relatively low-volume, small-scale melt movement, whereas the second outcrop, the High Strain Cliff contains higher volumes of melt migrating on a larger scale.

5.1 Outcrop Geology

Both outcrops are inclined, ESE-facing exposures that are oriented parallel to the strike of the high strain zone, but roughly perpendicular to the WSW-dipping foliation such that they are oriented in the X–Z plane of the strain ellipse (see below). The Etusis Pavement (Fig. 5.2A) occurs on the southern bank of the Swakop River at 22°40'16"S 14°51'30"E, and is approximately 30m long and 15m high. A section of this pavement was mapped in detail on a 18×8m, square-metre grid. The High Strain Cliff (Fig. 5.2B) is found 500m north of the Swakop River at 22°39'54"S 14°51'57"E and is approximately 30m long and 15m high. Both outcrops consist of metasediments belonging to the Etusis and lower Khan Formations, with the contact between the two formations cutting through the middle of the Etusis Pavement, but occurring at the base of the High Strain Cliff.

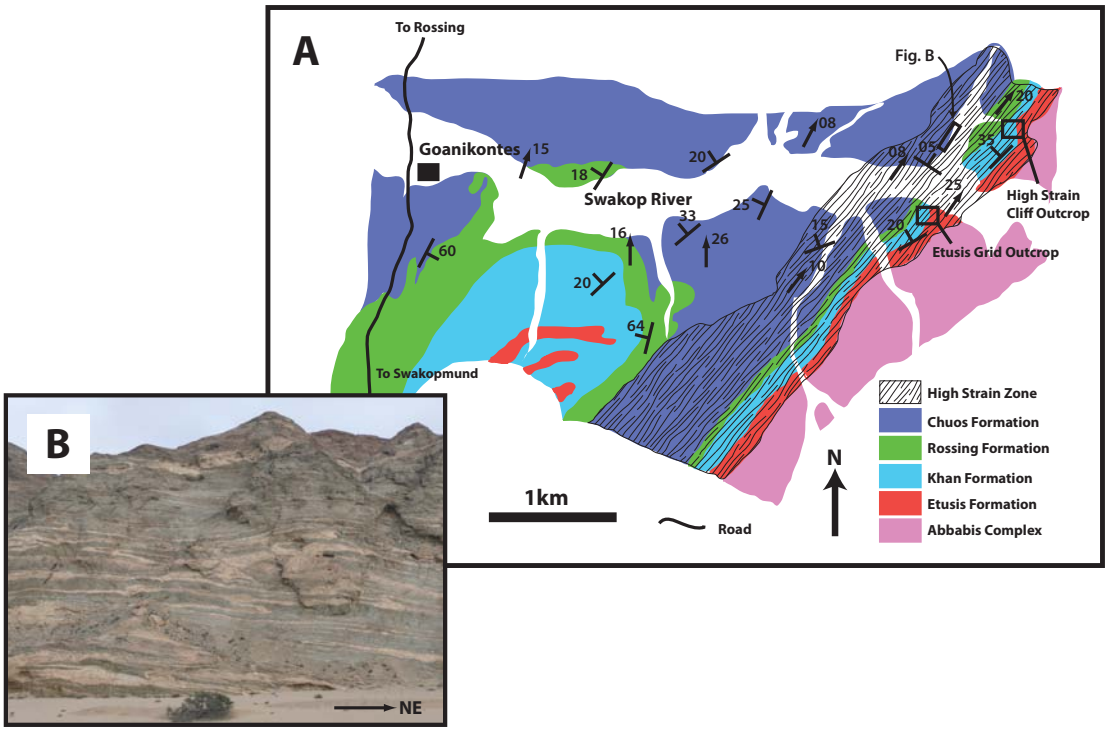

Figure 5.1: (A) Map illustrating the geology (after Nex *et al.* (2001)) and structure (from this study) of the area toward the west of the Palmenhorst Dome showing a high strain zone that affects rocks of the Etusis, Khan, Rössing, and Chuos Formations. (B) Photograph of a typical view in the high strain zone with the cliff oriented parallel to the lineation. Leucogranite sheets intruded into the Chuos Formation metapsammitic gneiss are folded and boudinaged. The cliff is about 100 m high.

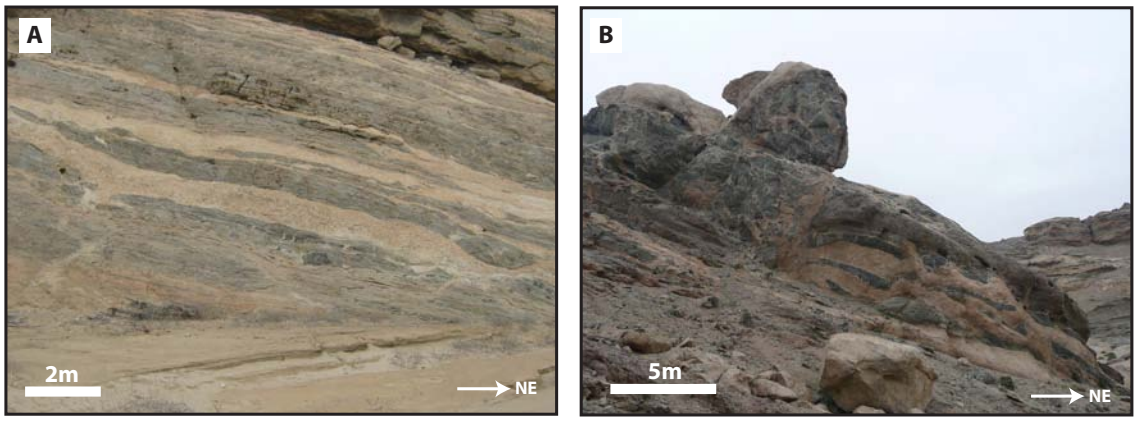

Figure 5.2: Outcrop photographs of (A) the Etusis Pavement and (B) the High Strain Cliff. Both strike approximately NE–SW.

5.1.1 Lithologies

Figure 5.3 shows the rock types found within the high strain zone at both outcrops. Figure 5.4 is a geological map of the gridded section of the Etusis Pavement. The Etusis Formation is present in the lower half of the outcrop and consists of interlayered feldspathic red quartzite and blue quartzite. The lower Khan Formation occurs in the top half of the outcrop and is comprised of calc-silicate-bearing metapsammitic gneiss. All lithologies also contain dismembered pods and lenses of calc-silicate rock (Fig. 5.4). A geological map of the High Strain Cliff is shown in Figure 5.5, and shows that this outcrop consists exclusively of the same calc-silicate-bearing metapsammitic gneiss that is observed in the Etusis Pavement outcrop. Here the calc-silicate rock is less abundant and lenses are smaller. The red quartzite (Fig. 5.3A) is orange-red in colour, and is medium to coarse-grained (0.5–5 mm grain size). It is comprised of 60–65% quartz, which has a red-stained appearance, but also occurs as smoky and white quartz, 20–30% feldspar, and 10–15% magnetite. The presence of thin (<1–2 mm) bands of magnetite grains gives this rock a laminated appearance (Fig. 5.3A).

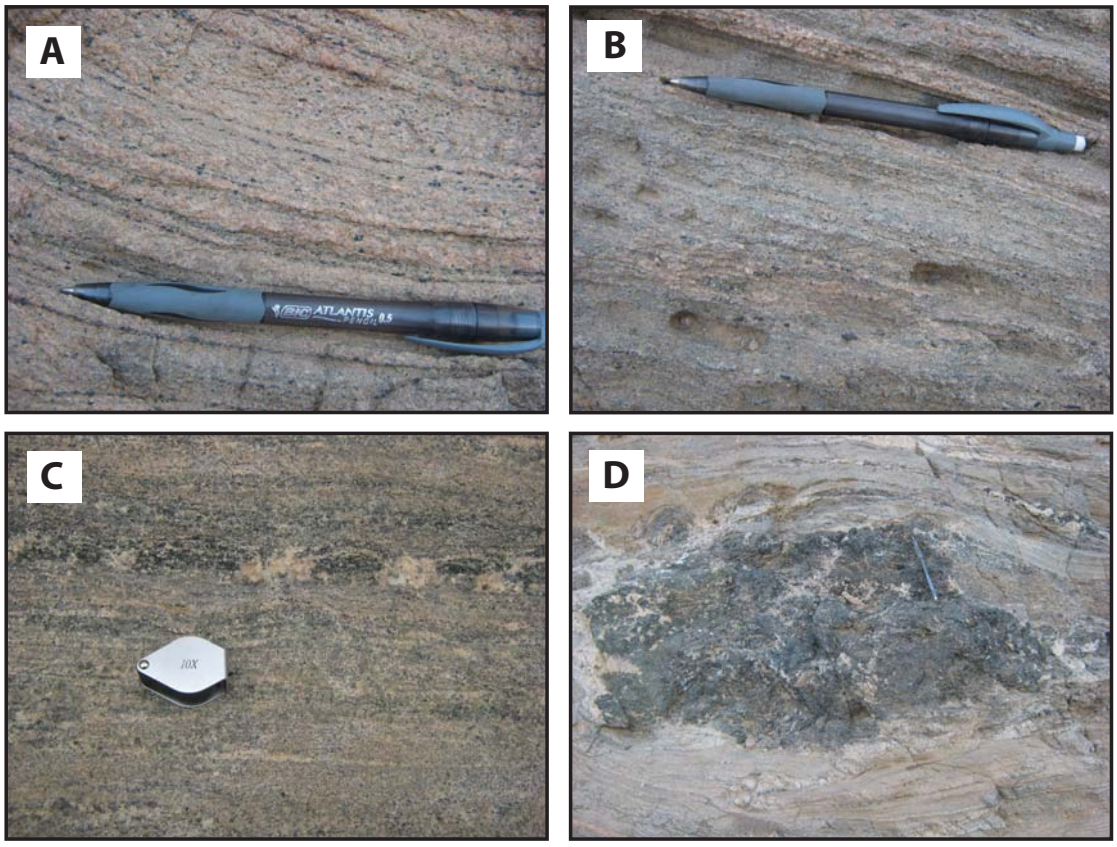

Figure 5.3: Lithologies found within the high strain zone at both outcrops. (A) Red quarzite of the Etusis Formation showing fine laminations defined by thin magnetite bands. (B) Blue quartzite of the Etusis Formation. (C) Calc-silicate-bearing metapsammitic gneiss of the lower Khan Formation. (D) Pod of calc-silicate rock found as boudins and lenses within the blue quartzite and metapsammitic gneiss.

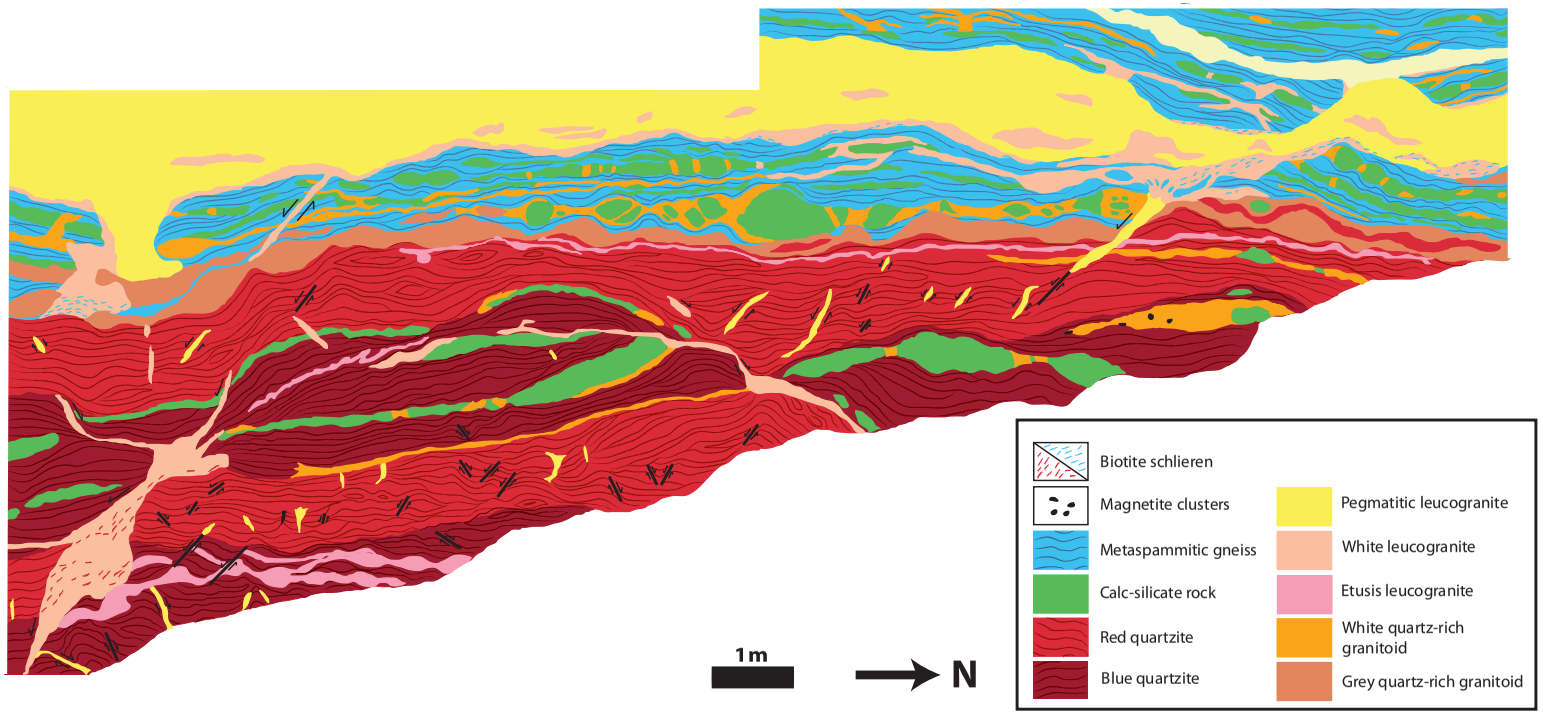

Figure 5.4: Geological map of the Etusis Pavement showing the distribution of rock types, intrusive phases, structures and linear/planar fabric trends within the outcrop. This map was created on an empty 18 m x 8 m-sized, square-metre grid. All features greater than 4 cm in size are represented. The lines in the metapsammitic gneiss and the quartzites represent foliation planes intersected by the outcrop surface.

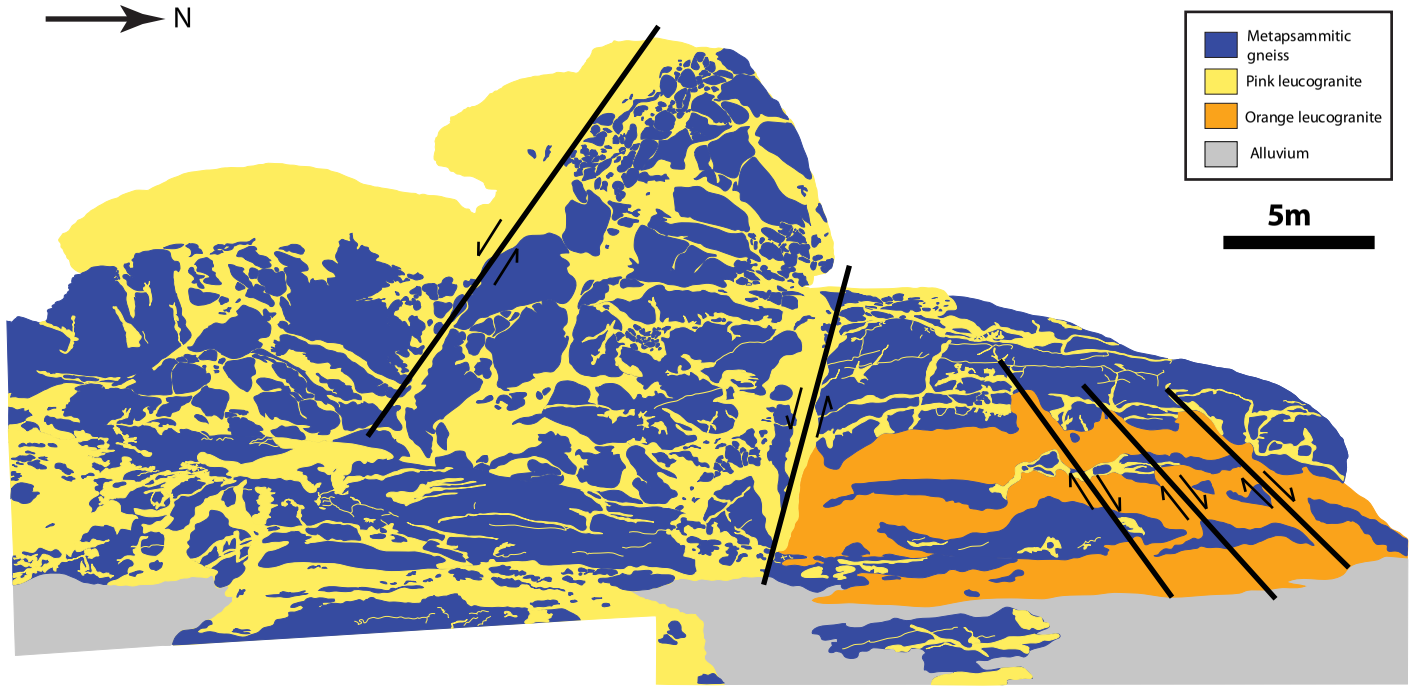

Figure 5.5: Geological map of the High Strain Cliff showing the distribution of the intrusive networks and structures in this outcrop. This map was overlain on an outcrop photograph. All features greater than 20 cm in size are represented.

The blue quartzite (Fig. 5.3B) is blue-grey in colour, and is slightly finer-grained than the red quartzite, with grain size varying between 0.2 and 3 mm. It contains nodules of calc-silicate rock, and the quartz has less red staining than the red quartzite. It also contains significantly less feldspar and magnetite. The mineralogy includes 70–80% quartz, 5–10% feldspar, 5–10% biotite, 5% magnetite and 5% calc-silicate minerals (diopside and hornblende). It has a banded appearance caused by thin layers (0.5–2 mm thick) of calc-silicate pods, biotite and magnetite occurring within the rock.

The calc-silicate-bearing metapsammitic gneiss (Fig. 5.3C) that is found at both outcrops, is fine- to medium-grained (<0.2 mm–3 mm grain size). It is comprised of dark-grey layers of quartz-rich (55–70% modal abundance) and biotite-rich (30–45% modal abundance) metapsammitic gneiss, with layers defined by variation in biotite content. These are interlayered with 2 cm–1 m thick boudinaged green-black bands of calc-silicate rock (Fig. 5.3D). The calc-silicate rock has a variable grain size (between 1 mm and 5 cm grain size), and is comprised of variable amounts of hornblende (50–90%), diopside (5–40%), biotite (<5%), calcite (<5%) and quartz (<5%).

5.1.2 Intrusive Phases

Nex *et al.* (2001) describe the petrology, geochemistry and timing of the leucogranite phases in the vicinity of Goanikontes, and specifically within the high strain zone investigated in this chapter. Several of the phases documented by Nex *et al.* (2001) have been recognized in both outcrops, and the observations here agree with Nex *et al.* (2001)'s descriptions and relative timing relations (Table 5.1). Seven different intrusive phases were distinguished in the two outcrops, and five of these can be correlated with leucogranite phases documented by Nex *et al.* (2001).

Both outcrops have a relatively high ratio of intrusive phase to metasediment compared to other outcrops studied, which is consistent with observations of a higher volume of intrusive phases within the high strain zone relative to areas around it. Intrusive phases constitute 39% of the total surface area of the Etusis Pavement, and 26.5% of total surface area of the High Strain Cliff. All intrusive phase percentages are estimated from outcrop image analysis using Adobe Photoshop CS4.

Phase (this study)	Phase (Nex *et al.*, 2001)	Relative timing
Etusis Pavement		
Grey quartz-rich granitoid	None	1
White quartz-rich granitoid	None	2
Etusis leucogranite	Type A	4
White leucogranite	Type D	6
Pegmatitic leucogranite	Type E	7
High Strain Cliff		
Pink leucogranite	Red	3
Orange leucogranite	Type C	5

Table 5.1: Summary of the relative timing of the granites in the high strain zone, compared with those documented by Nex *et al.* (2001).

Etusis Pavement Leucogranites

Five different inrtusive phases can be distinguised in the Etusis Pavement (Fig. 5.4). The oldest two phases, the grey and white quartz-rich granitoids, have planar fabrics and exhibit the most deformation of the intrusive phases. The oldest quartz-rich granitoid, the grey granitoid (Fig. 5.6A) is fine- to medium- grained (<1–5 mm grain size), equigranular, white-grey in colour and comprises 10% of the outcrop. It occurs as one concordant sheet within the outcrop, and as boudins within the younger white quartz-rich granitoid. It consists of 80–90% quartz (occasionally smoky), and 10–20% magnetite, and it exhibits a plano-linear fabric defined by aligned, stretched quartz grains. The second intrusive phase, the white quartz-rich granitoid (Fig. 5.6B), is a predominantly white, coarse-grained phase that is associated with the calc-silicate rock layers. It occurs in the interboudin spaces and as concordant leucosome along contacts with other lithologies. It makes up 9% of the outcrop, and is composed of 80–95% quartz (1–5 cm grain size), 5–20% magnetite found in patches of 1–4 cm crystals, trace amounts of fine-grained hornblende, and occasional minor feldspar. Neither of these two early phases correspond to any of the leucogranites described by Nex *et al.* (2001) because they are not leucogranites, and their high proportion of magnetite is unusual. Both the grey and white quartz-rich granitoids have solid-state plano-linear fabrics, suggesting that they intruded the metasediments prior to the majority of the deformation.

The Etusis leucogranite (Fig. 5.6C) (4% of the outcrop surface) does not appear to cross-

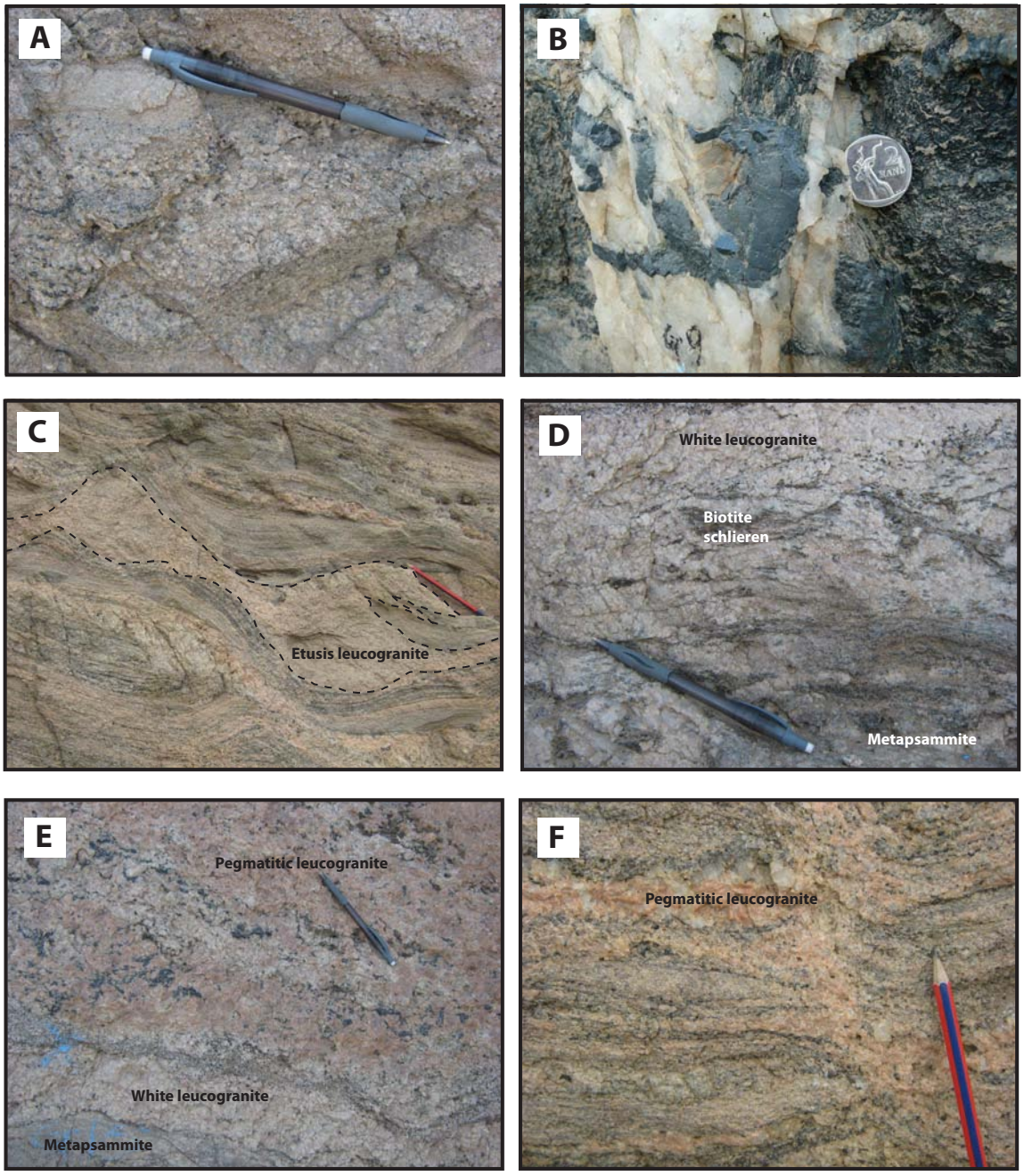

Figure 5.6: Intrusive phases in the Etusis Pavement outcrop. (A) Grey quartz-rich granitoid (B) Coarse-grained white quartz-rich granitoid with a large cluster of magnetite. (C) Etusis leucogranite boudins within red quartzite. (D) White leucogranite along the top contact of the metapsammitic gneiss, with biotite schlieren of the gneiss within the leucogranite. (E) Pegmatitic leucogranite from the upper leucogranite sheet containing clusters of magnetite. It is shown in contact with white leucogranite below, which is in turn in contact with metapsammitic gneiss. (F) A shear in the red quartzite containing pegmatitic leucogranite.

cut the two earlier phases; however, the lesser degree to which is is deformed suggests that it is younger. It likely corresponds to the type A sheeted leucogranite described by Nex *et al.* (2001), is pale-pink in colour, fine- to medium grained, equigranular, and has a saccharoidal texture. It only occurs as pinch-and-swell concordant leucosome layers within the red quartzite, and is often crosscut by shears that contain younger leucogranites (Fig. 5.6C). It is comprised of 60% feldspar (predominanty potassium feldspar), 35% quartz, <3% biotite, and <2% magnetite. This leucogranite also exhibits a weak planar fabric defined by aligned biotite grains.

The two youngest phases are the white and pegmatitic leucogranites, which comprise 4% and 11% of the outcrop, respectively, and which are observed to crosscut all earlier phases. They correspond to the type D and type E leucogranites of Nex *et al.* (2001). The white leucogranite (Fig. 5.6D) is cream-white in colour, medium- to coarse-grained, and fairly equigranular. It occurs predominantly within shears, but also as concordant sheets and as xenoliths within the pegmatitic leucogranite. It is comprised of 50% quartz that is predominantly smoky and 1–3 mm in size, 40% feldspar (1–5 mm grain size), 5% biotite (<1 mm grain size), and 5% magnetite (1–2 mm grain size).

The youngest leucogranite in the outcrop, the pegmatitic leucogranite (Fig. 5.6E) is very coarse grained, and pink–orange in colour. It is typically found in shears (Fig. 5.6F) and as large, 1–3 m thick, occasionally bifurcating sheets oriented parallel to S_0/S_1. It is comprised of 70% potassium feldspar (1–5 cm grain size), 20% clear quartz (1–5 cm grain size), 5% magnetite (0.3–0.8 cm grain size) and 5% biotite. Magnetite tends to occur in clusters (Fig. 5.6 F). Biotite occurs as two textural types, with primary biotite being finer-grained (0.5–1 cm grain size) than biotite clusters (0.5–3 cm grain size) that are likely partially assimilated xenoliths of country rock.

High Strain Cliff Leucogranites

Two leucogranite phases intrude the metasediments in the High Strain Cliff outcrop (Fig. 5.5). Figure 5.7A shows them in contact with one another. The older phase, a red-pink coloured leucogranite (Fig. 5.7B), is medium-grained, fairly equigranular, comprises 20% of the outcrop surface, and likely corresponds with the early red leucogranite described by Nex *et al.* (2001). It occurs throughout the outcrop, but is more abundant on the southern side. It occurs in melt-cemented breccias surrounding blocks of rotated metapsammite and within shears which

crosscut the metasediments. Its mineralogy includes 60% potassium feldspar (<1 mm–3 mm grain size), 30–35% quartz (<1–2 mm grain size), which occasionally exhibits red staining, approximately 3% magnetite that usually occurs in clusters of 1–4 mm-sized grains, and occasional fine-grained biotite (<1%).

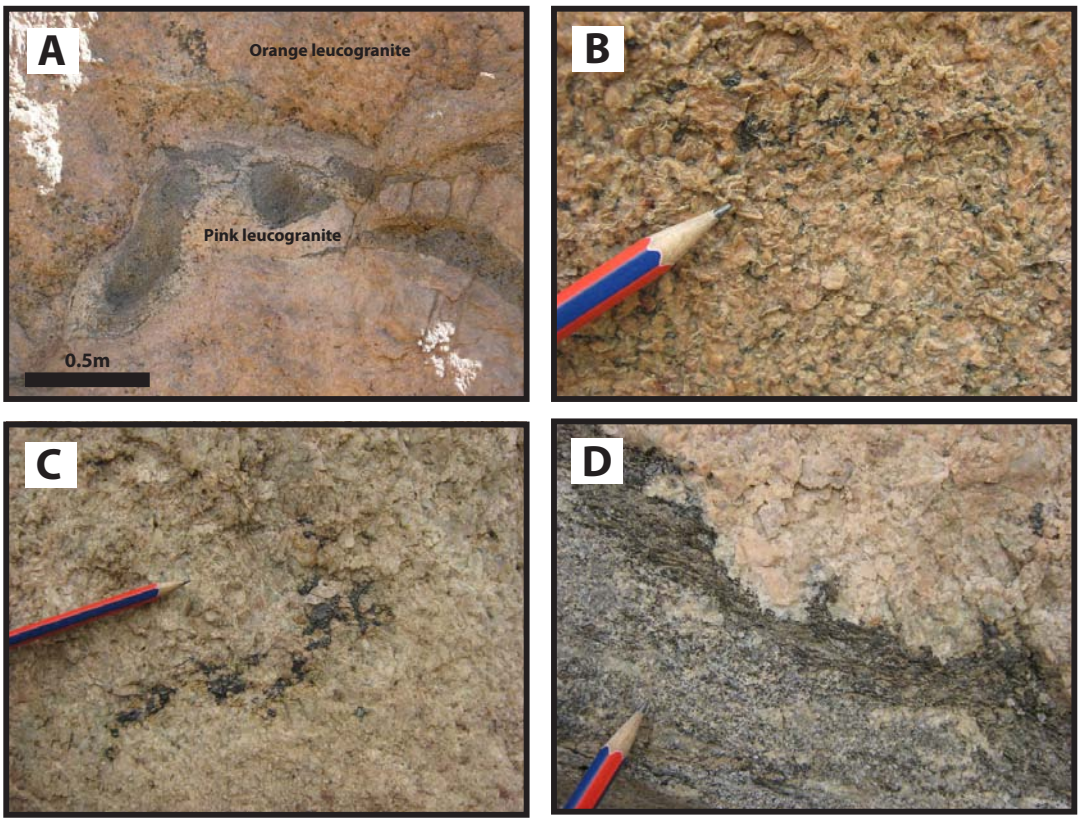

Figure 5.7: Leucogranites in the High Strain Cliff outcrop. (A) Pink leucogranite around xenoliths of metapsammitic gneiss, which together form a boudinaged layer within orange leucogranite. (B) Pink leucogranite with quartz, K-feldspar and magnetite. (C) Orange leucogranite showing clustered magnetite within coarse-grained quartz, feldspar and biotite. (D) Biotite reaction rim developed along the contact between orange leucogranite and metapsammitic gneiss.

The younger orange leucogranite (Fig. 5.7C) crosscuts the pink leucogranite, and when in contact with each other, often develops a 0.5–2 cm thick rind of biotite along the contact edge. The metapsammitic gneiss also develops 1–4 cm thick biotite reaction rims when in contact with the orange leucogranite (Fig. 5.7D). This phase corresponds to the type C leucogranite described by Nex *et al.* (2001), and comprises 6.5% of the outcrop. It occurs as thick concordant sheets and as thick, blunt-ended dykes within shears. The orange leucogranite is

equigranular and considerably coarser-grained than the pink leucogranite, with a grain size between 0.5 and 4 cm. It is composed of 70% feldspar (potassium feldspar and plagioclase in variable amounts), 15–20% interstitial clear quartz, 5–10% very coarse-grained (3–5 cm sized grains) biotite, and approximately 5% magnetite, which occurs as coarse-grained (1–3 cm grain size) clusters (Fig. 5.7C).

5.1.3 Fabrics and Structures

The high strain zone is distinguished from the surrounding areas, and most of the other studied localities, by the presence of a strongly developed, penetrative mineral stretching lineation (L_1) that occurs in all rock types. This lineation plunges shallowly to the NNE, at around 015°/20–30° (Fig. 5.8 A,C). It is defined by elongated and stretched quartz grains in the quartzites and metapsammitic gneisses, as well as the orientation of stretched and elongated pods of calc-silicate rock. A weakly-developed foliation that is oriented parallel to bedding (S_0/S_1) is also developed in the high strain zone. The foliation dips shallowly to the NW and is best-developed in the metapsammitic gneiss where it is defined by aligned biotite grains. In the Etusis Pavement it is oriented around 060°/20°NW (Fig. 5.8A), whereas at the High Strain Cliff it is more variable, oriented around 020–065°/30–45°NW (Fig. 5.8C).

The most prominent structural features found in both outcrops are 5 cm to 3 m-long, 0.5 to 5 cm-wide shear zones that crosscut the S_0/S_1 fabric (Figs. 5.4, 5.5 and 5.8B,D). The shears are found in two different orientations in the Etusis Pavement outcrop. Both sets show a normal sense of displacement and are oriented 105° (the angle which contains the downthrown block; Fig. 5.9) from one another, indicating that they form a conjugate set (Fig. 5.8B). One set is oriented at 130°/35°SW, shows top-to-the SW displacement, and is around 50° from S_0/S_1 whereas the other is at 080°/40°NE, with top-to-the NE displacement, and is around 25° from S_0/S_1 (Figs. 5.8B and 5.9). Foliation drag, and the offset of lithological layers and early leucosome suggest that their apparent offset is typically between 1 and 50 cm.

A second structural feature found in the Etusis Pavement are near-vertical fractures oriented at a high angle to L_1. These fractures are typically 1–5 cm wide and around 0.5 metres long and the foliation at their edges is usually symmetrically bent into the centre of these structures. The absence of a foliation drag suggests that they are not shears, which, coupled to their high angle relative to L_1, identifies them as tensile fractures. These fractures are often connected to less steeply-dipping shears and occur in two predominant steeply-

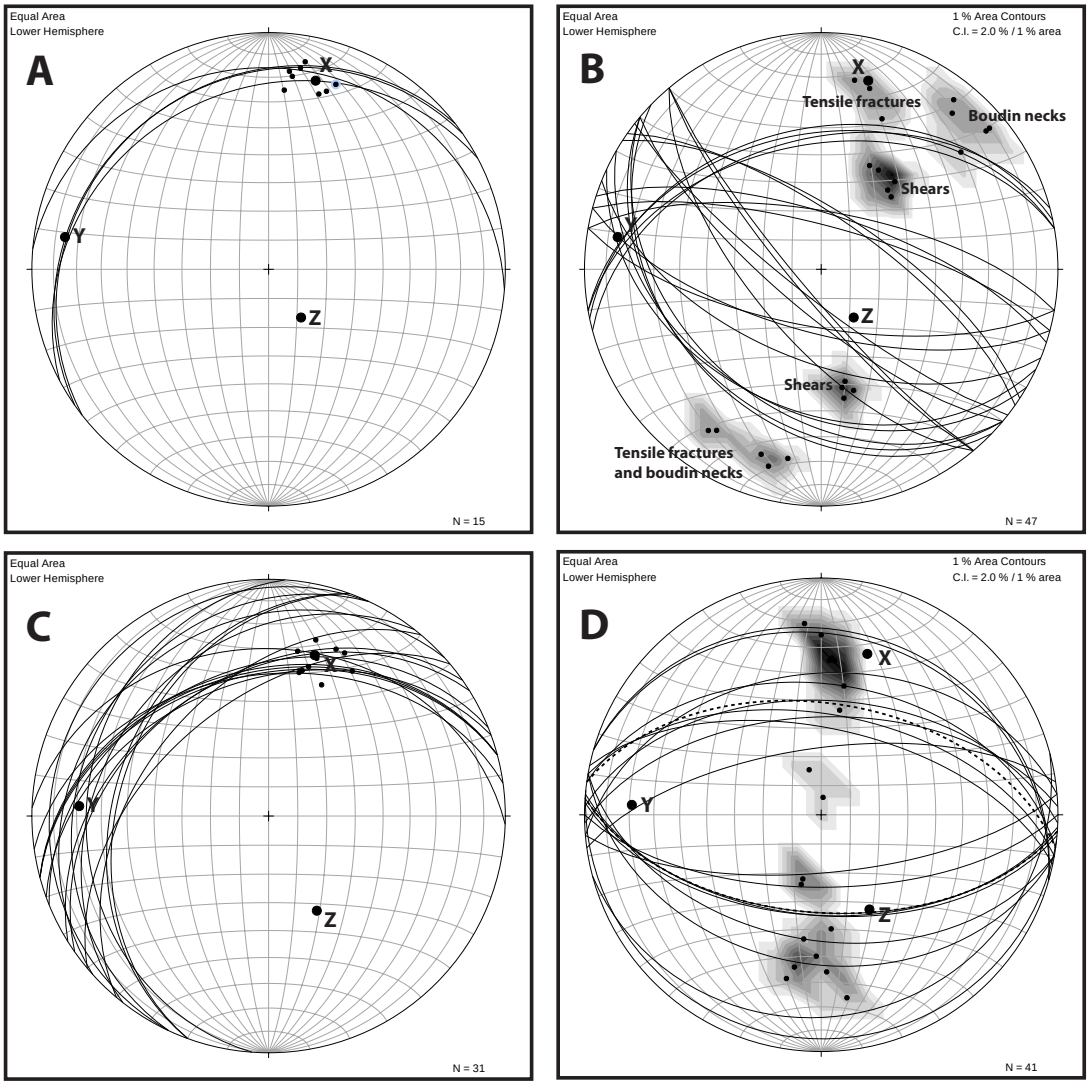

Figure 5.8: (A) Stereonet showing the orientation of the L_1 lineation (dots) and S_0/S_1 foliation (great circles) in the Etusis Pavement outcrop. XYZ are the strain axes calculated using L_1 and S_0/S_1 orientations. (B) The orientation of all crosscutting melt-filled structures (represented as planes) in the Etusis Pavement outcrop. Their poles are also plotted, and contoured using 1% area contours. (C) Stereonet showing the orientation of the L_1 lineation (dots) and S_0/S_1 foliation (great circles) in the High Strain Cliff outcrop. XYZ are strain axes calculated using L_1 and S_0/S_1 orientations. (D) Stereonet showing the orientations of crosscutting melt-filled shear structures (represented as planes) at the High Strain Cliff outcrop. Their poles are also shown, and contoured using 1% area contours. The dashed lines show the two most typical melt-filled shear orientations.

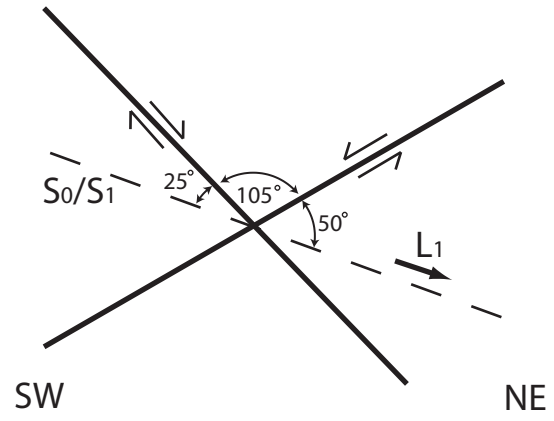

Figure 5.9: A simplified 2D sketch of the geometrical relationship between the conjugate shears, L_1 and S_0/S_1 in the Etusis Pavement.

dipping orientations, one around 100–120°/70°NE, and the other around 100–110°/65–70°SW (Fig. 5.8B). Leucogranite-filled interboudin spaces also occur and show a similar orientation at 120–140°/75–80°SW (Fig. 5.8B).

The High Strain Cliff outcrop contains fewer shears than the Etusis Pavement, but also has two sets with oppositely-dipping orientations and normal displacement (Fig. 5.5). The strike orientation of each set is relatively constant, but there is a large variation in the dip angle of each. The orientation of the north-dipping set, with top-to-the-north displacement, varies around 090–110°/23–65°N, with an average orientation of 100°/50°N (Fig. 5.8D). It is 22–30° from S_0/S_1 (Fig. 5.10). The south-dipping set, with top-to-the-south displacement, varies around 080–100°/06–70°S, with an avarage orientation of 095°/ 55°S (Fig. 5.8D). It is 85–90° from S_0/S_1. The angle between the shear planes which contains the downthrown block is 73–100° (Fig. 5.10).

5.2 Former Melt-bearing Structures

Both outcrops exhibit a variety of previously melt-bearing structures. Crosscutting intrusive structures vary between several centimetres and 2 metres thick, and 0.1 to 4 m in length, whereas concordant structures are often wider, and much longer, reaching at least 3–4 metres thickness, and >10 metres length. These structures are often connected to one another, with structures containing the same intrusive phase exhibiting petrographic continuity between

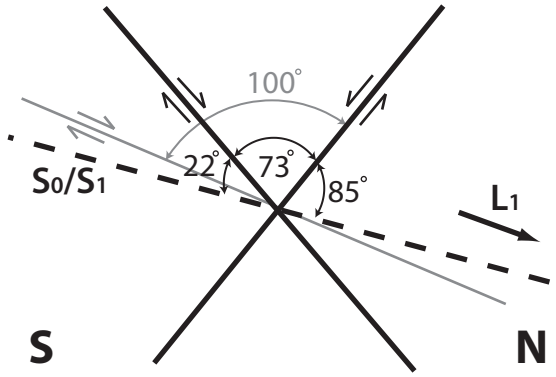

Figure 5.10: A simplified 2D sketch of the current geometrical relationship between the conjugate shears, L_1 and S_0/S_1 in the High Strain Cliff. The solid black lines represent the predominant conjugate shear orientations, while the grey line shows a subordinate, flatter shear orientation that likely progressive flattening of leucogranite-filled shears.

them, so that they form interconnected networks. Structures can contain single or multiple intrusive phases, with older phases occurring as xenoliths or along the edges of younger phases (e.g. Fig. 5.6E).

5.2.1 Stromatic / Concordant Leucosome

Stromatic or concordant leucosomes are oriented parallel to S_0/S_1, and are the most common melt-bearing structures within the metasediments. All the intrusive phases observed in both outcrops occur as concordant leucosome on varying scales. Both the early grey and white quartz-rich granitoids at the Etusis Pavement occur as 10–30 cm wide concordant leucosome, and exhibit considerable pinching and swelling along their length. The Etusis leucogranite occurs exclusively as stromatic leucosome within the red quartzite, forming 1–20 cm wide pinch-and-swell layers.

The white leucogranite is found less predominantly as concordant layers, but does form several 10–20 cm thick S_0/S_1-parallel sheets within the Etusis Pavement outcrop. The pegmatitic leucogranite forms thick, 1–2 m wide concordant sheets, which anastomose in and out of parallelism with S_0/S_1. These thicker concordant sheets often have at least two leucogranite phases giving the sheets a composite and layered appearance. The pink leucogranite in the High Strain Cliff occurs occasionally as 10–30 cm wide concordant leucosome, whereas the orange leucogranite occurs predominantly as 1–3 m thick concordant sheets on the northern

side of the outcrop.

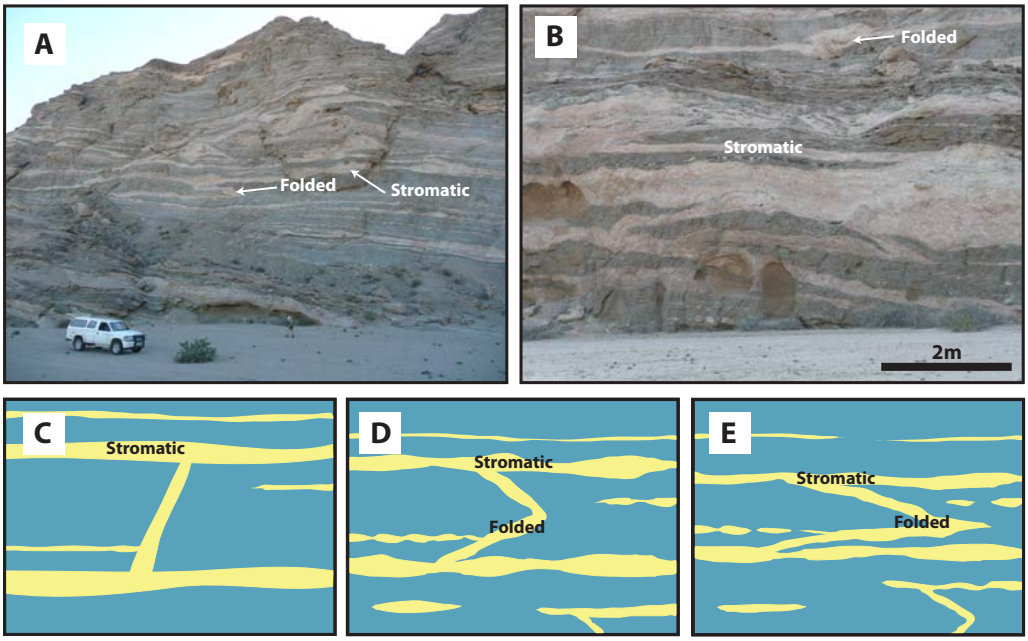

Figure 5.11: Transposed leucosome in the high strain zone. (A) A 100 m high cliff face with transposed and stromatic leucosome. (B) An outcrop showing the difference between folded and transposed discordant leucosome and concordant/stromatic leucosome. (C), (D), (E) are idealised sketches showing progressive folding and transposition of leucosome during progressive flattening.

Many 1–5 m wide leucosomes in the high strain zone that appear macroscopically stromatic are, on closer inspection, slightly discordant and exhibit evidence of folding, stretching and transposition (e.g. Fig. 5.11A, B). The variation in the degree of deformation shown by the leucosomes, with earlier phases transposed and boudinaged, and younger phases showing pinch-and-swell structures and folds, suggests that the leucosomes that form in a highly discordant position (e.g. conjugate shears and tensile fractures) have been folded, rotated and stretched into near-parallelism with the planar fabric during progressive deformation (Fig. 5.11).

5.2.2 Melt-filled Shears

The ductile shears described above mostly contain sheets of leucogranite along the shear plane (Figs. 5.12B, F, G, H and 5.13A, B, D). These sheets are typically in sharp contact with the metasediments around them, and are usually comprised of only one leucogranite phase. They are 1 cm–1 m thick, and vary in length between 0.2 and 5 m. Both the white

and pegmatitic leucogranites of the Etusis Pavement are found within shears. The white leucogranite occurs predominantly within shears that crosscut the quartzites and which are often continuous with concordant leucosomes. Shear-hosted pegmatitic leucogranite tends to form discontinuous, tabular intrusions that are 0.1–2 m long and 2–20 cm thick and exhibit pointed ends (Fig. 5.12B). These bodies often steepen towards the top of the shear to connect with leucogranite-filled tensile fractures (Fig. 5.12D,E,F).

Both leucogranites in the High Strain Cliff are found within crosscutting shears. The pink leucogranite occurs within two well-defined 10 m-long shears which crosscut the cliff face, as well as smaller <1m-long shears throughout the outcrop (Fig. 5.13B, C). Most leucogranite-filled shears connect with one another to form an interconnected network across the outcrop. The orange leucogranite occurs within three 5–10 m long shears on the northern side of the outcrop, forming 5–8 m long, 0.5–1 m wide tabular sheets which are connected to concordant leucosome containing the same leucogranite phase. The tabular sheets all end abruptly, at about the same height in the cliff face, with blunt terminations (Fig. 5.13D).

5.2.3 Tensile Fractures and Boudin Necks

Two types of melt-bearing structures that are oriented approximately normal to L_1 are observed in the Etusis Pavement. The first of these are leucogranite-filled interboudin spaces that occur within layers of boudinaged calc-silicate rock (Fig. 5.12A). The width of the boudin necks varies between <1 cm and 30 cm, they are predominantly filled with white quartz-rich granitoid, and they are often connected to stromatic leucosome.

The second are tensile fractures that occur exclusively within the red quartzite, and are filled with pegmatitic leucogranite (Fig. 5.12D,E). These structures are usually isolated from other structures, with the exception of some leucogranite-filled shears which contain the same phase, and with which they exhibit petrographic continuity.

5.2.4 Leucogranite-Cemented Breccias

The southern half of the High Strain Cliff contains leucogranite-cemented breccia consisting of subangular, sharp-edged blocks of metapsammitic gneiss cemented together by a single phase of pink leucogranite (Fig. 5.13C, E). The orientation of foliation and lineation within many of the blocks is not consistent with the planar and linear fabrics in the surrounding metapsammitic gneisses, indicating that individual blocks have been rotated.

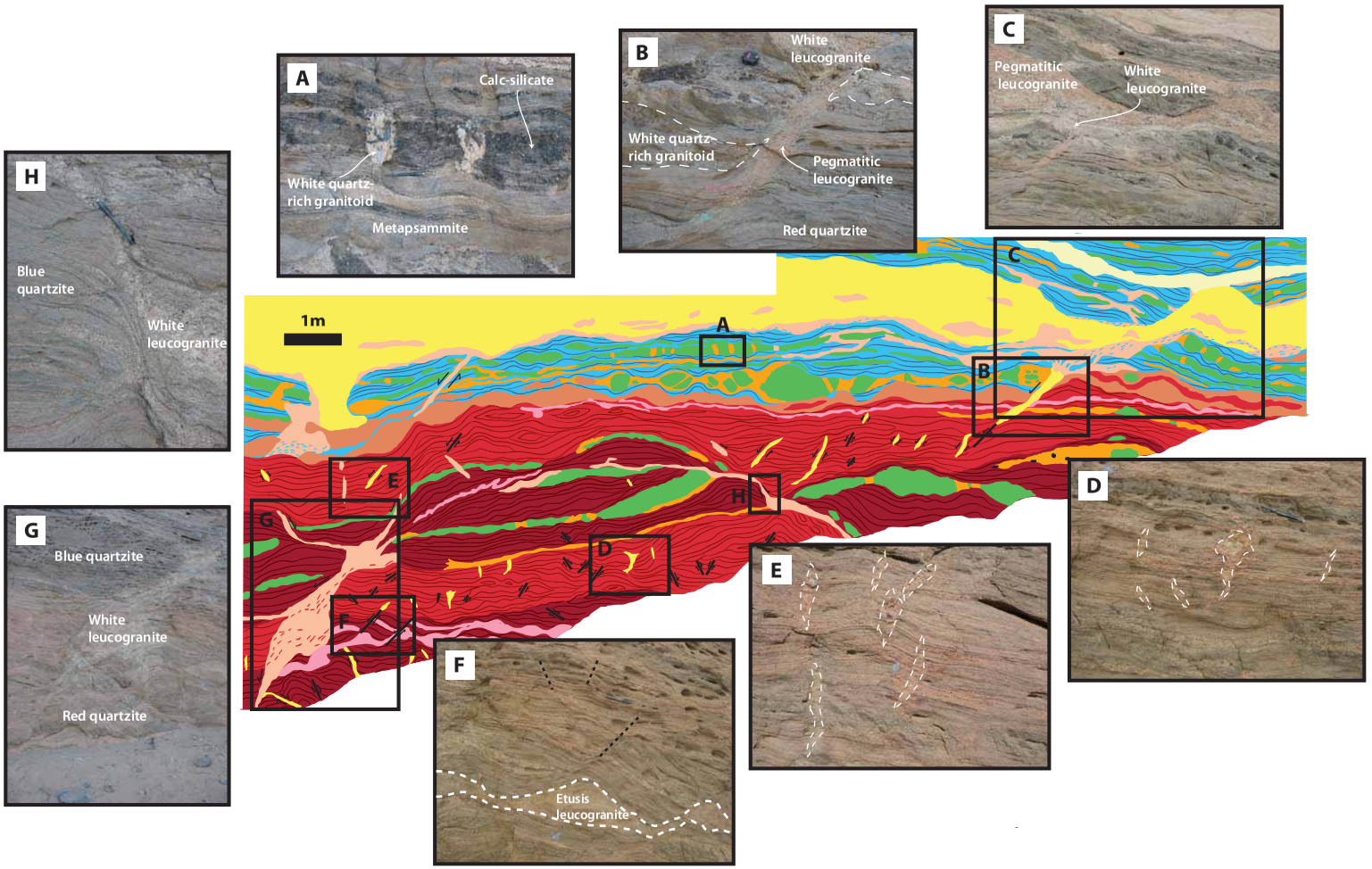

Figure 5.12: Figure illustrating the various crosscutting melt-filled structures in the Etusis Pavement outcrop. (A) Boudin necks in calc-silicate rock. (B) Melt-filled shear offsetting the red quarzite–metapsammitic gneiss contact. (C) Early leucogranites in metapsammitic gneiss with interlayered calc-silicate rock. (D) Shears and vertical structures in red quartzite. (E) Vertical structure in red quartzite. (F) Shears and early leucogranite boudins in red quartzite. (G) Large inflated melt-filled shear offsetting contact between blue and red quartzites. (H) Partially melt-filled shear offsetting contact between blue and red quartzite.

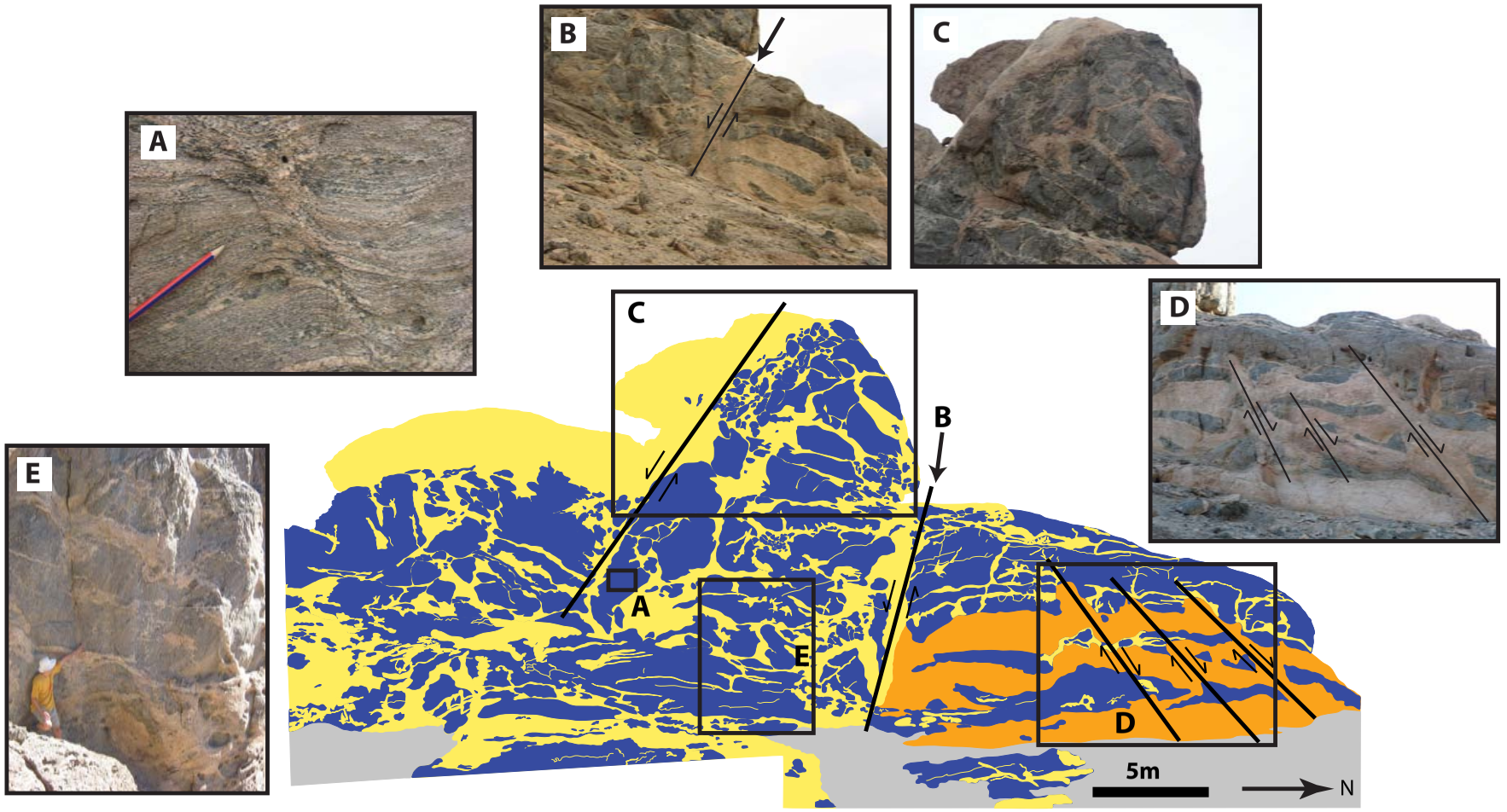

Figure 5.13: Leucogranite structures in the High Strain Cliff outcrop. (A) A typical ductile shear with dextral offset crosscutting calc-silicate metapsammitic gneiss. (B) A larger scale (5 m length), south-dipping red-leucogranite filled shear with dextral offset. (C) Leucogranite-cemented breccia at the top of the outcrop. (D) Large-scale north-dipping orange leucogranite-filled shears. (E) Leucogranite-cemented breccia at the bottom of the outcrop.

The foliation within blocks also deflects along their edges, similar to the foliation deflection along shear zone edges. Individual metapsammite blocks have variable shapes, but most have roughly diamond or rectangular shapes (Fig. 5.13). The size of blocks varies from 10 cm to 4 m in diameter. The proportion of clasts (blocks) to matrix (leucogranite) varies between 75:25 and 65:35, as estimated from image analysis in Adobe Photoshop CS4. The high proportion of clasts suggests that the breccia is currently clast-supported; however, individual blocks are not often in direct contact with each other and are almost always separated by films of leucogranite.

5.3 Structural analysis

The intensity of the penetrative lineation fabric and the variation in strength of the S_0/S_1 fabric indicates that the overall strain within the high strain zone is close to plane strain, with some areas more strongly constrictional. This is consistent with descriptions of L-tectonites in the high strain zone by Nex *et al.* (2001), and suggests that strain was non-coaxial. The strain axes XYZ were resolved from the orientation of L_1 and S_0/S_1 in both outcrops and have very similar orientations, confirming that they have experienced similar strain (Fig. 5.8A,C).

The orientation of the conjugate shear sets in the Etusis Pavement outcrop is consistent with the orientation of XYZ strain axes. The shears suggest NE-SW extension, which is approximately parallel to the NE-plunging X-axis of the strain ellipse; approximately vertical contraction that is consistent with the steeply SE-plunging Z-axis, and the intersection of the two shear planes parallel to the Y-axis. This indicates that the penetrative fabric and conjugate shears formed concurrently. Since ductile shears are predicted to form $\leq 90°$ from one another, and 45° from the plane of maximum compression (Twiss & Moores, 1992) (here interpreted as the S_0/S_1 plane), the 105° angle between the shears together with their 50° and 25° angles from S_0/S_1 (Fig. 5.9) suggests that they have experienced flattening and rotation.

The 25° angle between the north-dipping shear set and S_0/S_1 suggests that it has accommodated more rotation than the south-dipping shear set, which is consistent with the current position of XYZ and prolate to plane strain. The presence of a conjugate set of shears within this strain environment suggests that there was some component of flattening, consistent with the component of plane strain, where X>1>Z, and is also a function of the anisotropy of the rocks, which exhibit stronger layering than, for example, the Swakop Pavement outcrop (Chapter 3), which displays strongly prolate strain, and which does not show

perfectly-oriented conjugate shears.

The orientations of tensile fractures and boudin necks in the Etusis Pavement are more variable than that of the shears, with these structures occuring as three clusters on Figure 5.8B. One cluster of sub-vertical structures is exactly perpendicular to X so that their poles cluster exactly around X (Fig. 5.8B), the direction of apparent extension. In contrast, the poles of the boudin necks and other sub-vertical structures are 30—40° away from X, suggesting that they formed early, and have been rotated towards S_0/S_1. This is supported by the presence of older leucogranite in the boudin necks compared with most other sub-vertical structures.

The petrographic continuity of leucogranite in shears which steepen upwards and connect with tensile fractures above them in the Etusis Pavement (e.g. Fig. 5.12D,E) suggests that the tensile fractures required the presence of the shears to form. The presence of abundant shears that are not connected with tensile fractures, compared with the high number of tensile fractures that are connected with shears, and the two different clusters of tensile fracture orientations which appear related to the two shear orientations, suggests that tensile fractures propagated from already present shears during favourable conditions for their formation. Such conditions might include a favourable strain orientation, and the presence of a high enough melt volume to allow embrittlement.

The orientation and sense of shear of the shear sets in the High Strain Cliff are mostly consistent with the orientation of XYZ strain axes calculated from L_1 and S_1 (Fig. 5.8D). However, the variation in dip angle of both shear sets could suggest that these shears have undergone significant re-orientation after their formation, during progressive deformation. This is supported by the current 105° angle between the shears being greater than the $\leq$90° angle expected at formation.

5.4 Melt Migration

The presence of a high volume of injected leucogranite in the high strain zone provides an opportunity to examine the degree to which ongoing, widespread and intense deformation influences melt migration through the rocks relative to the less strongly deformed outcrops outside of the high strain zone (e.g. Chapters 3 and 6). The sharp contacts between all the leucogranite phases and the metasediments in both outcrops of this chapter shows that all observed leucogranite represents injected melt, and none is interpreted to have formed in situ.

The lack of grain size variation between the edge and centre of all intrusive phase sheets also suggests there was no significant temperature difference between the metasediments and the leucogranite melt when it intruded, and the presence of biotite rinds between the younger leucogranite and the metasediments suggests that the leucogranite remained liquid long enough for diffusion of elements across contacts to take place. The folding and transposition, as well as the pinch-and-swell of stromatic layers of early leucogranite-filled structures, together with progressively younger phases showing less deformation with age, and young crosscutting undeformed leucogranite dykes which include petrographically similar leucogranites shows the continuity of the high-volume syn-deformational intrusion of leucogranites in the high strain zone.

The composite nature of the sheets, and their progressive deformation shows that the melt-bearing history of the high strain zone lasted through most of the deformation that produced the planar and linear fabrics in the area. The strong deformation of the early phases, relative to the level of deformation exhibited by early phases outside of the high strain zone allows for the possibility that the high volume of early melt promoted weakening of the metasediments and contributed to the high strain intensity. The very high relative volume of young leucogranite phases appears to be as a result of an increased number of dilational sites that formed to accommodate the high strain.

The main macroscopic differences between the high strain zone and the rocks in the rest of the field area are the more abundant, higher volume, predominantly stromatic intrusive bodies (Fig. 5.11A,B). However, the presence of weakly discordant, folded and transposed leucogranites suggests that the stromatic appearance of the rocks in the high strain zone is purely a function of the stronger relative deformation which has caused folding and rotation of discordant leucosomes towards the foliation, and suggests that these leucogranites did not exclusively intrude in a fabric-parallel orientation.

The rotation and flattening of the young leucogranite-bearing conjugate shear sets towards the fabric at both high strain outcrops is consistent with re-orientation of the of discordant leucosomes. The current position of folded leucosomes suggests that they formed at a high angle to the plane of maximum shortening (approximated here by S_0/S_1), suggesting that many leucogranites that are now only slightly discordant were originally emplaced into shears and tensile fractures. If this is the case, then the leucosomes would have formed a network with an internal structure created by interconnected concordant sills and discordant structures, similar to networks observed in lower strain areas. However, here the network has

subsequently been flattened and rotated into parallelism with the foliation during progressive intrusion and deformation, obliterating many of the details of its internal structure.

The networks observed in both outcrops of this chapter still have relatively unrotated discordant structures, and so their internal structure is considered to be mostly intact. The strong layering in the Etusis Pavement outcrop, combined with the shallow dip of those layers makes the primary stromatic leucosome an inefficient mechanism for melt to migrate upwards. The presence of leucogranite within the discordant shears, sub-vertical structures, and boudin necks shows that melt can exploit these structures to cross the strong bedding anisotropy and migrate upwards.

Within the High Strain Cliff, the predominance of leucogranite within brittle-looking leucogranite-cemented breccia suggests a different migration mechanism. Since most of the leucogranite surrounding the metapsammite blocks is not in a planar orientation, it was difficult to measure the structure of the interconnected network it formed. The blocks are typically surrounded by a volume of leucogranite that appears insufficient to account for the amount of rotation that the blocks exhibit. This suggests that the leucogranite-cemented breccia has lost melt, and therefore preserves evidence of melt migration through this structure.

Similar breccias were described by Kisters *et al.* (1998) from Namaqualand in South Africa. They described breccias from anatectic rocks which function as segregation structures that slowly fill with melt and which function as melt conduits away from the source rocks. The breccias described here are different because they accommodate pure migration through subsolidus rocks, and require the presence of pre-existing anisotropies coupled with fracturing to create permeability.

A model for the formation of leucogranite-cemented breccias is shown in Figure 5.14. The foliation drag present along block edges suggests that they have undergone some shearing during their formation, indicating that the network of leucogranite surrounding them likely started as a network of interconnected shear zones (Fig. 5.14A,B). This is supported by the presence of shears within the wallrocks to the breccia zone (Fig. 5.13A).

If there is an oversupply of melt, such as intimated by the high leucogranite volume in the high strain zone, and the rock is not permeable enough to accommodate migration of that large volume through it, then melt pressure increases, leading to extensive melt embrittlement This embrittlement allows for the development of new brittle structures such as tensile fractures that increase the permeability of the melt network. This new network is

infiltrated by the melt, leading to inflation of pre-existing and new melt-bearing structures (Fig. 5.14C).

Once the interconnected network is fully inflated, the metasedimentary blocks lose cohesion and become melt-supported (Fig. 5.14D). Ongoing deformation causes melt to move upwards and out of the conduit along this newly formed highly permeable structure. As long as the melt supply from beneath equals the removal of melt from the conduit, the melt pressure is retained, and the conduit remains open. During this stage, the blocks remain melt-supported, although they might rotate and sink due to gravity (Fig. 5.14E). Once the melt supply begins to dwindle, melt is expelled from the breccia and structures begin to deflate. A further drop in melt pressure leads to the collapse of the structure and the formation of a leucogranite-cemented implosion breccia (Figs. 5.14F and 5.13C, E).

The tablet-shaped leucogranites on the north side of the High Strain Cliff likely represent the failed propagation of fully inflated shear zones. The bulbous top ends of these three structures (Fig. 5.13D) suggests that melt tried to force its way upwards but was unsuccessful at propagating these structures. The continuity of leucogranite within these shears with the fully-inflated stromatic leucosome containing the same leucogranite suggests that concordant melt tried to exploit discordant shears, however the melt pressure was not high enough to propagate the shears sufficiently so that they could connect with a draining network, leading to migration failure.

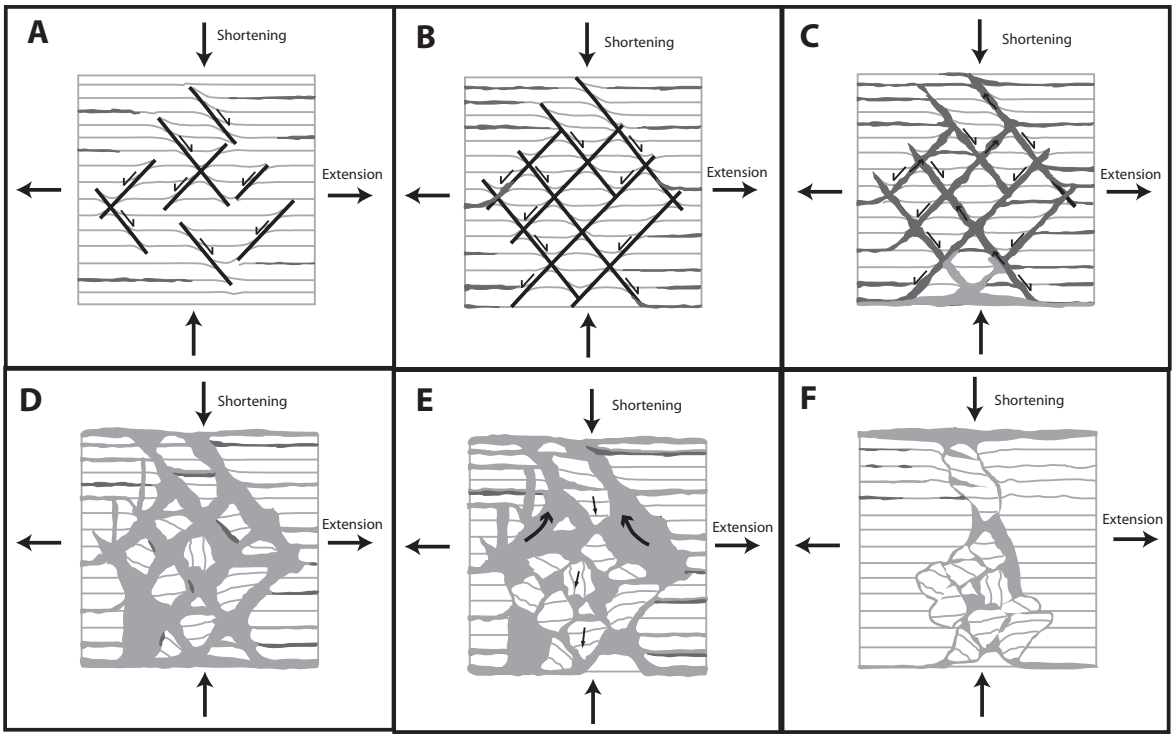

Figure 5.14: A model for the formation of leucogranite-cemented breccia within subsolidus rocks. (A) During progressive deformation fabrics and discordant structures (e.g. conjugate shears (shown)) form to accommodate the strain. Low melt volumes exploit the planar S_0/S_1 fabric. Some shears may contain small volumes of melt. (B) With increasing deformation and increasing melt volumes (i.e. melt pressure) the melt-bearing structures become interconnected. The discordant structures may also rotate towards the plane of flattening (not represented). (C) The interconnected discordant and concordant melt-filled structures form a network that increases the permeability of the rocks and if melt solidifies, provides an increased number of planes of weakness for intruding melt to exploit. (D) A second, voluminous melt batch intrudes along pre-existing structures, and because of high melt pressure creates additional structures such as tensile fractures. The high melt volume forces these structures and pre-existing structures to inflate and the metasedimentary blocks lose cohesion. (E) Compaction squeezes the melt upwards and out of the structure, while the blocks sink and rotate due to their density contrast with the melt. (F) The structure collapses as melt drains upward and melt pressure decreases to create a leucogranite-cemented breccia.

Chapter 6

Melt Migration through a Fold Hinge

This chapter investigates the movement and accumulation of low- to medium melt volumes in a kilometre-scale fold structure. Much of the migration occurs along dykes intruded in an axial-planar orientation, the common occurrence of which is not well understood (e.g. Vernon & Paterson, 2001; Kisters *et al.*, 2009). Conventional stress models for the formation of folds indicate that the axial plane is a direction of shortening and should therefore not be a favourable orientation for melt-bearing structures which require dilation. The presence of numerous leucogranite dykes and almost perfect exposure of the structure allows for a large-scale analysis of the structures and mechanisms that facilitated melt movement, particularly within an apparent plane of shortening.

6.1 Outcrop Geology

The studied area is approximately 500×650m in size and centred around 22°38'56"S 14°47'29"E along the northern bank of the Swakop river (Fig. 6.1). The antiformal structure has a core previously mapped as Chuos Formation metasediments (Wells *et al.*, 1988), and is comprised of metapsammites that occasionally contain clasts of other lithologies, supporting its suggested origin as a diamictite. Here it is referred to as metapsammitic gneiss (Fig. 6.1). The Chuos Formation core is surrounded by stratigraphically higher metapelites and quartzites that have been previously mapped as Rössing Formation rocks (Wells *et al.*, 1988).

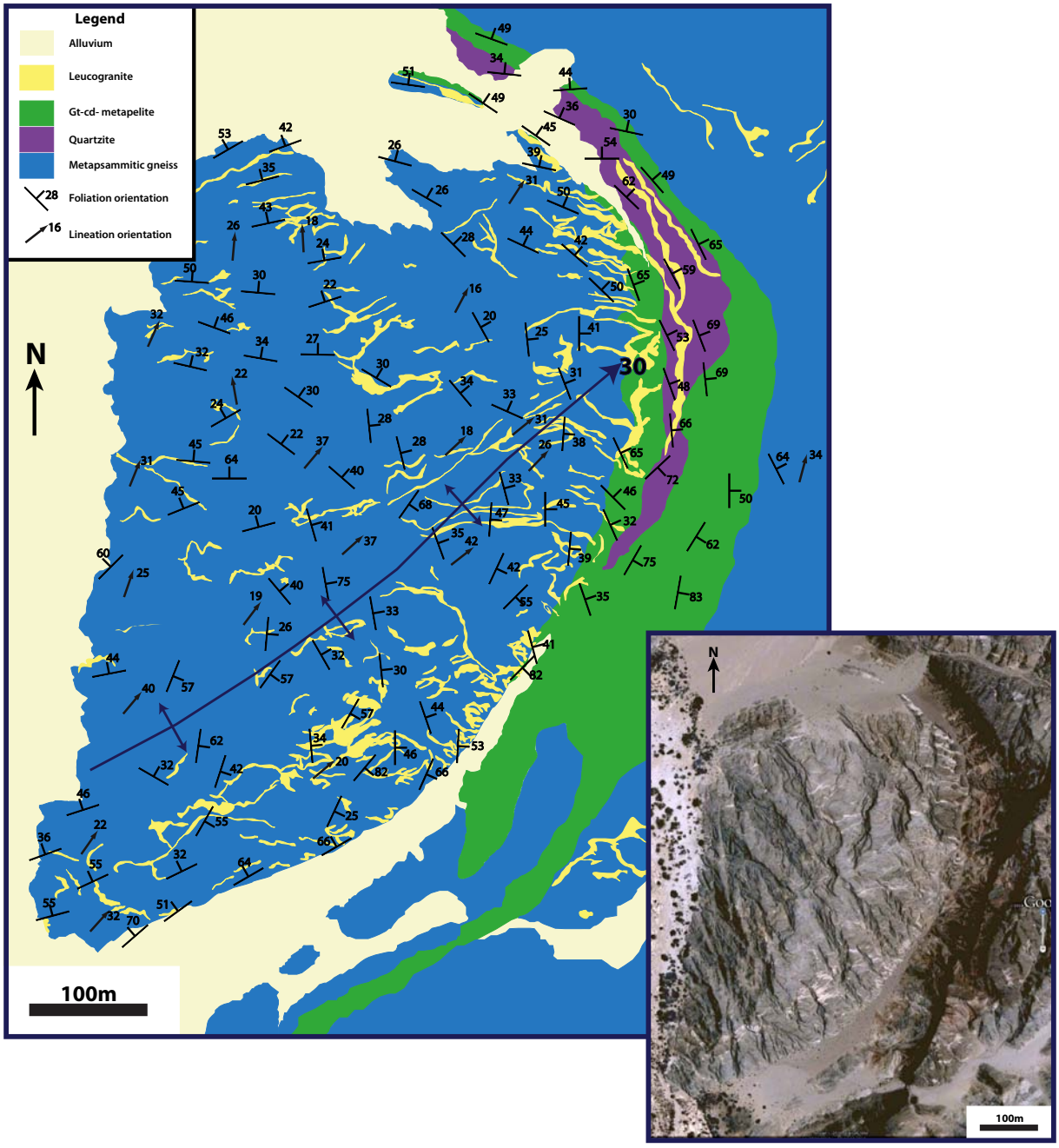

Figure 6.1: Lithological and structural map showing the orientation of foliation and lineation across the fold structure. This map was overlain on the inset Google Earth^{TM} image of the study area. All leucogranite bodies greater than 3 m wide are shown.

6.1.1 Lithology

The main lithology in the study area is grey metapsammitic gneiss (Fig. 6.2A). The mineralogy varies from 70–80% quartz, and 20–30% biotite, and occasionally contains trace amounts of garnet (<1%). This metapsammite is medium-grained with grain size between 0.1 and 2 mm, and often contains 1–20 cm sized pods of crystalline quartz or calc-silicate (Fig. 6.2B, C). The metapsammite also contains rare beds of polymict conglomerate containing clasts of granitic gneiss, quartzite and calc-silicate (Fig. 6.2D).

The outer parts of the fold are defined by a 40 m-thick unit of metapelitic gneiss (Fig. 6.2E). The metapelite has a dark grey-brown colour and contains 40% quartz, 30% cordierite, 15–20% garnet and 10–20% biotite. It is medium-grained and fairly equigranular, with grain size ranging from 0.5–4 mm. A discontinuous, red-brown bedded quartzite unit occurs interlayered with the metapelitic gneiss (Fig. 6.2F). It contains 95% quartz and 5% biotite and is very equigranular, with most grains around 1mm in size. The quartzite is concentrated in the nose of the fold where it can reach a thickness up to 100 m (Fig. 6.1).

6.1.2 Intrusive Phases

Two leucogranite phases are intrusive into these rocks, and both occur in concordant and discordant dykes. The older phase is a quartz-rich, garnet-bearing leucogranite that is often folded or stretched (Fig. 6.3A). The garnet-bearing leucogranite is not as voluminous as the younger feldspar-rich pegmatitic leucogranite, which always crosscuts the earlier phase. The quartz leucogranite (Fig. 6.3A) is grey-white in colour, and tends to contain large 0.5–3 cm-sized garnets. It typically contains 60–70% quartz, 20% feldspar, 5–10% biotite and 0–3% garnet, and is medium- to coarse-grained, with a grain size of 0.2–3 cm. The pegmatitic leucogranite is pinker in colour, and contains a much higher proportion of feldspar. Its mineralogy consists of 50–60% feldspar (mostly potassium-feldspar), 25–40% quartz, 5–10% biotite, and it often contains tourmaline (usually intergrown with smoky quartz) and beryl as accessory phases (Figs. 6.3C, D). It is very coarse grained, with a grain size between 0.5 and 10 cm.

6.1.3 Fabrics and Structures

The fold axis of the antiform plunges at 036°/28° and the fold verges to the SE, with the axial plane dipping to the NW at 055°/60–65° (Fig. 6.4A). The fold is asymmetrical and has

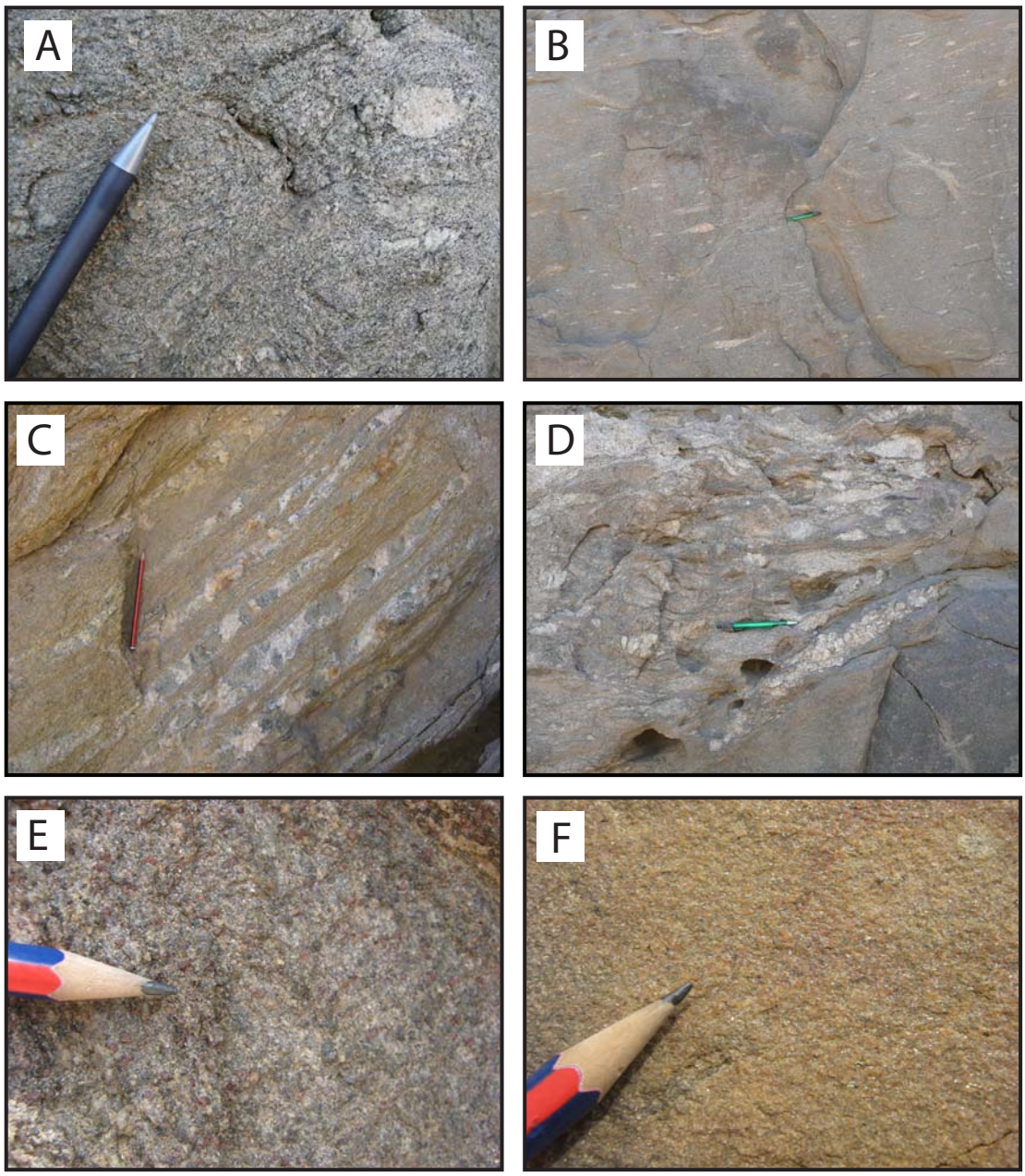

Figure 6.2: The lithologies that comprise the large-scale antiform. (A) Typical metapsammite. Pen head = 20 mm. (B) Metapsammite with dismembered early quartz vein material, and diffuse melt-filled shears. Pen = 150 mm. (C) Layers of boudinaged diopside-hornblende calc-silicate within metapsammite. Pencil = 150 mm. (D) Pebble bed within the metapsammite with clasts of gneiss and quartzite. (E) Garnet-cordierite metapelite. Pencil head = 20 mm. (F) Red-brown quartzite. Pencil head = 20 mm

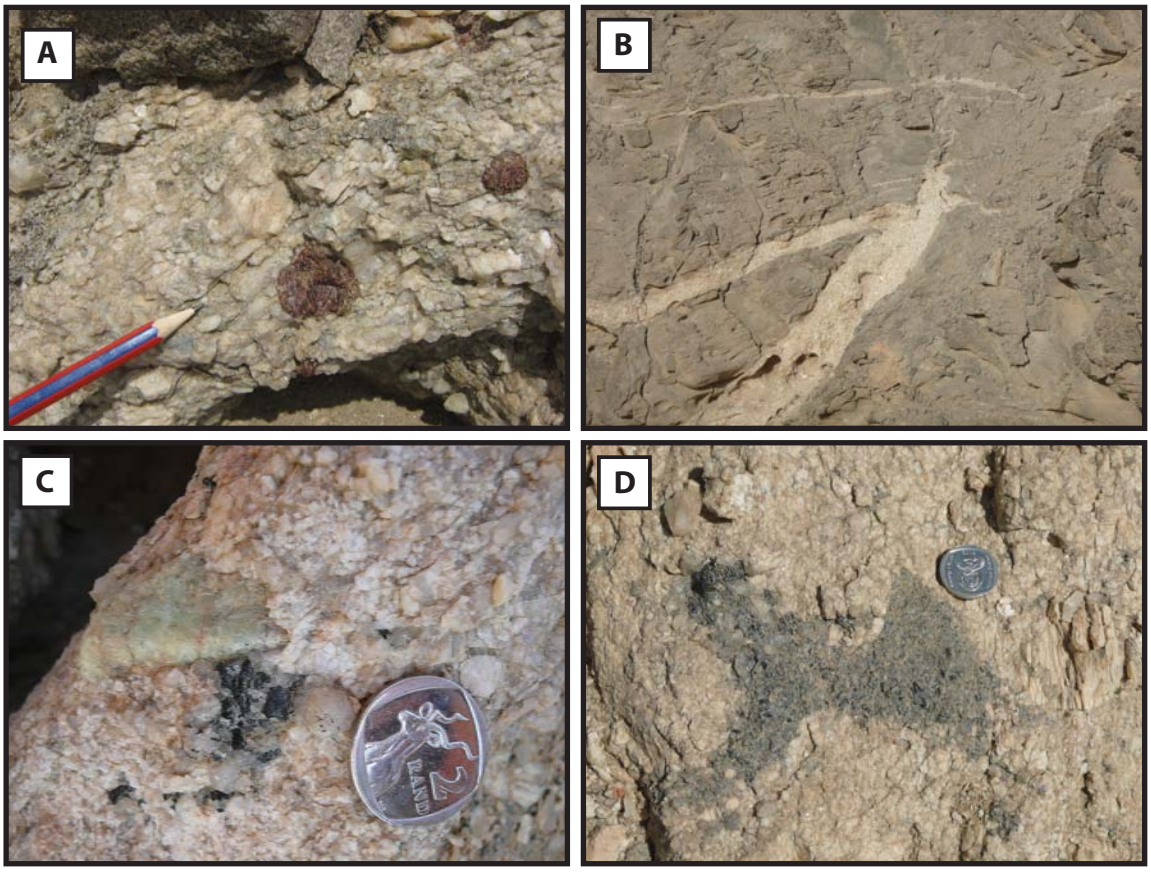

Figure 6.3: Intrusive phases within the antiform. (A) Garnet-bearing quartz rich leucogranite. (B) Typical dykes and sills containing pegmatitic leucogranite. (C) Accessory phases beryl and tourmaline in the pegmatitic leucogranite. (D) Smoky quartz intergrown with tourmaline in pegmatitic leucogranite.

a half-wavelength of 450 m. Its near-parallel north-dipping limbs also suggests that it is very tight to isoclinal. All rocks display penetrative tectonic planar and/or linear fabrics. The first is a foliation (S_0/S_1) defined by aligned biotite as well as the preferred orientation of elongated clasts and pods, and oriented parallel to the map-scale lithological boundaries that define the fold (Figs. 6.1, 6.4A). The S_0/S_1 foliation is variably developed, and is strongest on the limbs of the fold and weakest within its core. Associated with this foliation is a moderately to steeply NE-plunging stretching lineation (L_2; 020–060°/15-50°; Fig. 6.4B), defined by rodded quartz clasts in metapsammitic gneiss. This lineation is most strongly developed in the fold core, and is absent, or only weakly developed along the limbs of the fold (Figs. 6.1, 6.4B). There is no secondary penetrative foliation associated with the axial

plane, despite the presence of leucogranite dykes in axial planar orientation.

Centimetre- to metre-scale shear zones crosscut the bedding and S_1/L_2 fabric (Fig. 6.5A, B). These shears are most common in and occur close to the axial trace of the antiform, and are between 2 cm and 5 m in length and 0.2 cm to 0.5 m in width. Small centimetre-scale shears are more common than larger scale ones, and they sometimes contain leucosome (Fig. 6.5C). The shears exhibit a range of orientations which form three main clusters. The main orientation is at 130°/30°NE, and shows top-to-the-SW (reverse) sense of shear. Two less predominant shear orientations are at 070–080°/40–60°NW, with predominant top-to-the-NW (normal) shear, and 120°/70°NE, with top-to-the-NE (normal) displacement (Fig. 6.4C). The sense of shear is identified by foliation drag and offset markers such as sheared quartz clasts and older dismembered leucosome (Fig. 6.5B). Offset on these shears is on the order of a few centimetres (1-10 cm).

Small, centimetre to a few metres-scale, shallow-dipping planar structures that exhibit no shear along their edges are oriented around 130°/20°NE. They are most abundant in the fold limbs, where they occur at high angles to S_0/S_1, and are interpreted as tensile fractures (Fig. 6.5D).

6.2 Leucogranite-bearing Structures

The leucogranites are found in a variety of orientations and structures that range from a few centimetres to 1–3 m in width. The pegmatitic leucogranite exhibits crosscutting relationships with the older garnet-bearing phase and composite dykes are rare. However, there is petrographic continuity between different structures that are filled with the pegmatitic leucogranite, showing that this phase forms a connected network across the antiform (e.g. Fig. 6.3B). Dykes occur in three major orientations: as S_1 concordant leucosome, as steeply NW-dipping dykes, and as shallowly NE-dipping sheets. The predominance of these dyke orientations varies with location around the antiform (Fig. 6.6).

6.2.1 Distribution of Leucogranite

The distribution of leucogranite across the fold and within the different metasediments is variable. The core of the fold contains the most leucogranite relative to the rest of the fold, particularly within the metapelite and quartzites on the outer part of the fold. Quartzite is the most leucogranite-rich, whereas metapelite is almost leucogranite-free, with the exception

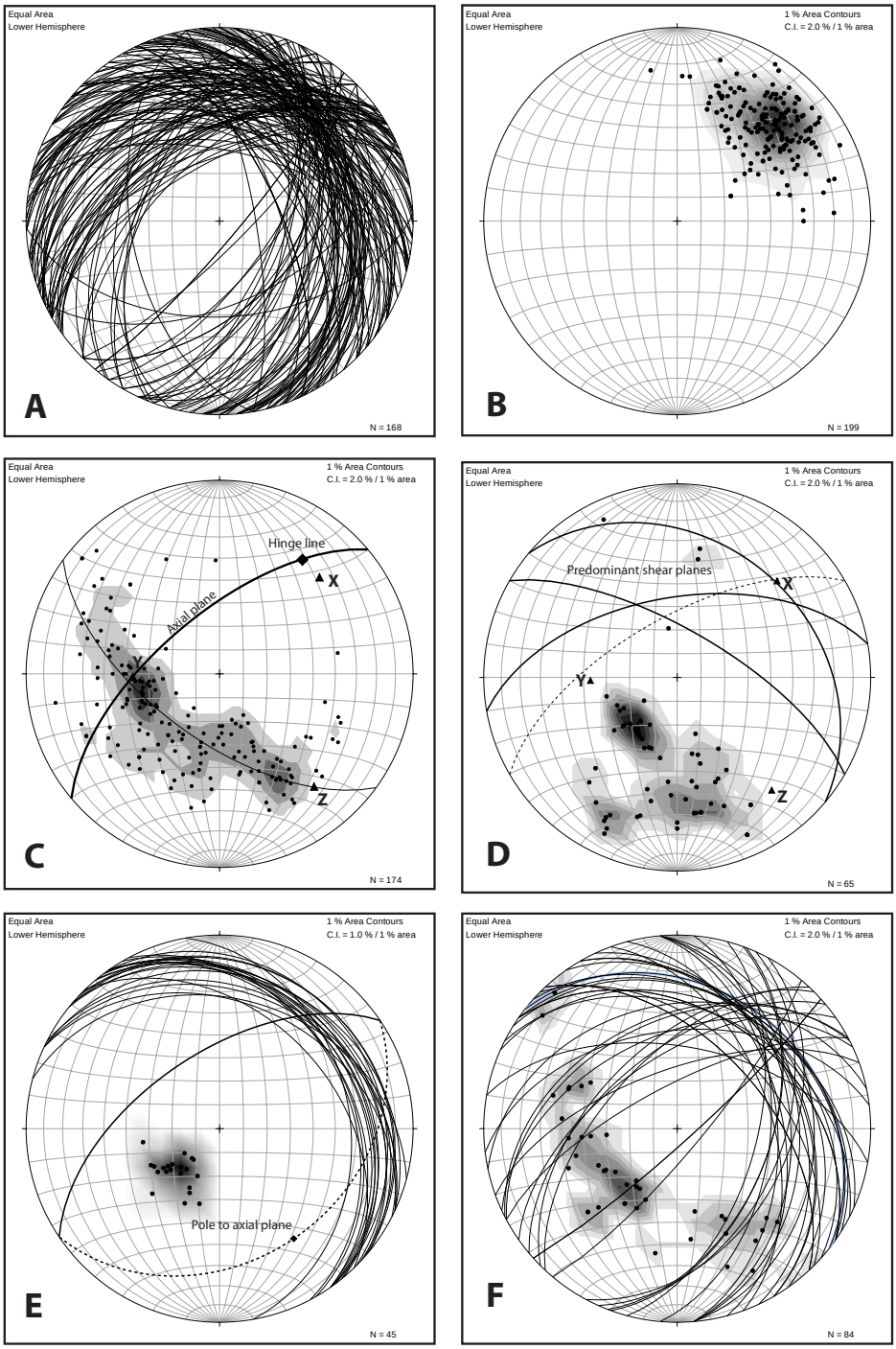

Figure 6.4: Equal area stereonets showing foliation and dyke orientations. All contours are 1% area contours with a confidence interval of 2% (A) Foliation (S_1) orientations for the entire field area. (B) Contoured (1% area contours with a 2% confidence interval) lineation (L_2) orientations. (C) Pi-diagram showing contoured poles to S_1, hinge line and axial plane of the folds. (D) Contoured poles to orientations of small shears, and diffuse melt-filled shears. The three predominant shear plane orientations are also shown, along with the orientation of the axial plane (dashed line). (E) Orientations of leucogranite-filled tensile fractures with contoured poles. (F) All S_0/S_1 concordant leucogranite dyke orientations.

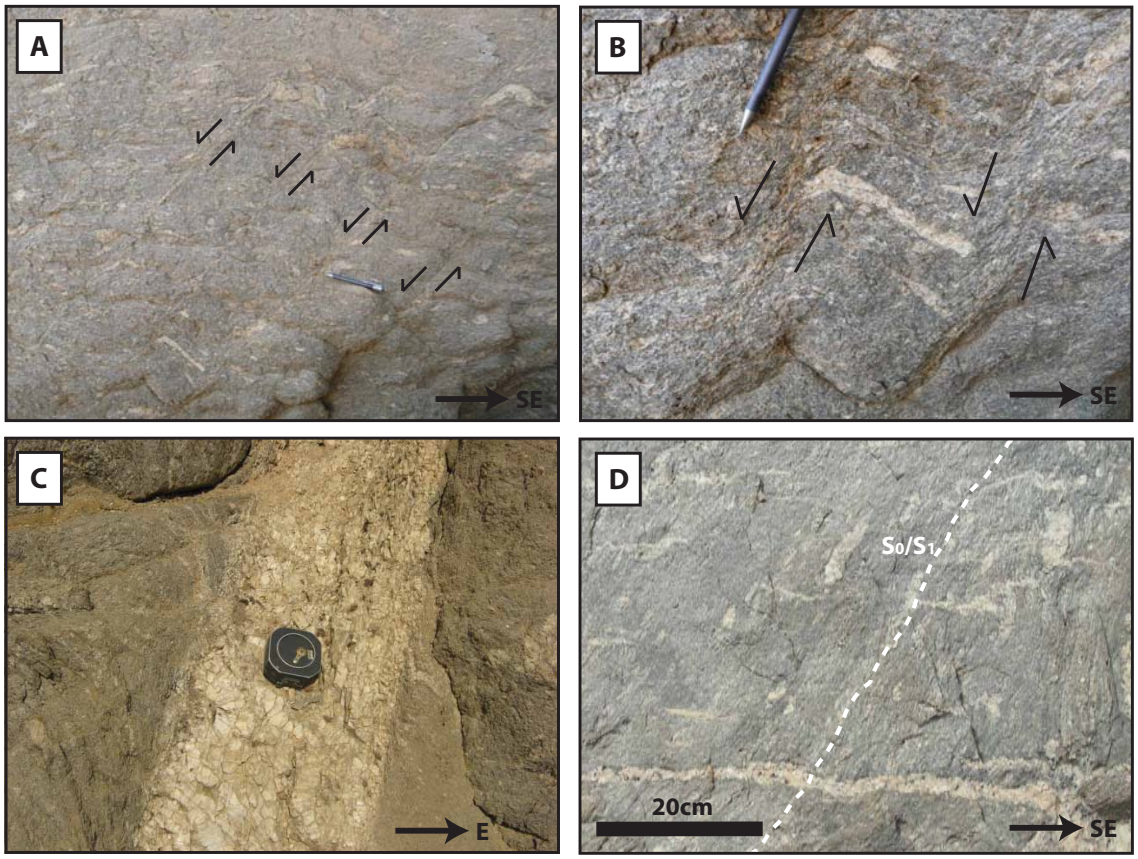

Figure 6.5: Small to meso-scale shears in the metapsammitic gneiss. (A) Subparallel shear set with normal offset in metapsammite. (B) Photograph of older sheared leucosome acting as a marker to indicate normal offset on a shear. (C) Thick shear-hosted dyke showing foliation drag along both edges indicating dextral shear. (D) Flat-dipping diffuse leucogranite-filled tensile fractures at a high angle to S_0/S_1.

of the fold hinge. The map in Figure 6.6 suggests that there is a high volume of leucogranite on the southern limb of the antiform but this is a misrepresentation due to the dyke orientation being parallel to local topography.

6.2.2 Concordant / Stromatic Leucosome

Stromatic or concordant leucosomes are oriented parallel to S_1. Both leucogranite phases occur as concordant leucosome, with the garnet-bearing leucogranite occurring more commonly in this orientation than the pegmatitic leucogranite. The concordant sills are 0.2–2 m wide and their orientation changes with that of the S_1 foliation over the large-scale antiform (Fig. 6.4F). The garnet-bearing leucogranite, when found as concordant leucosome, often

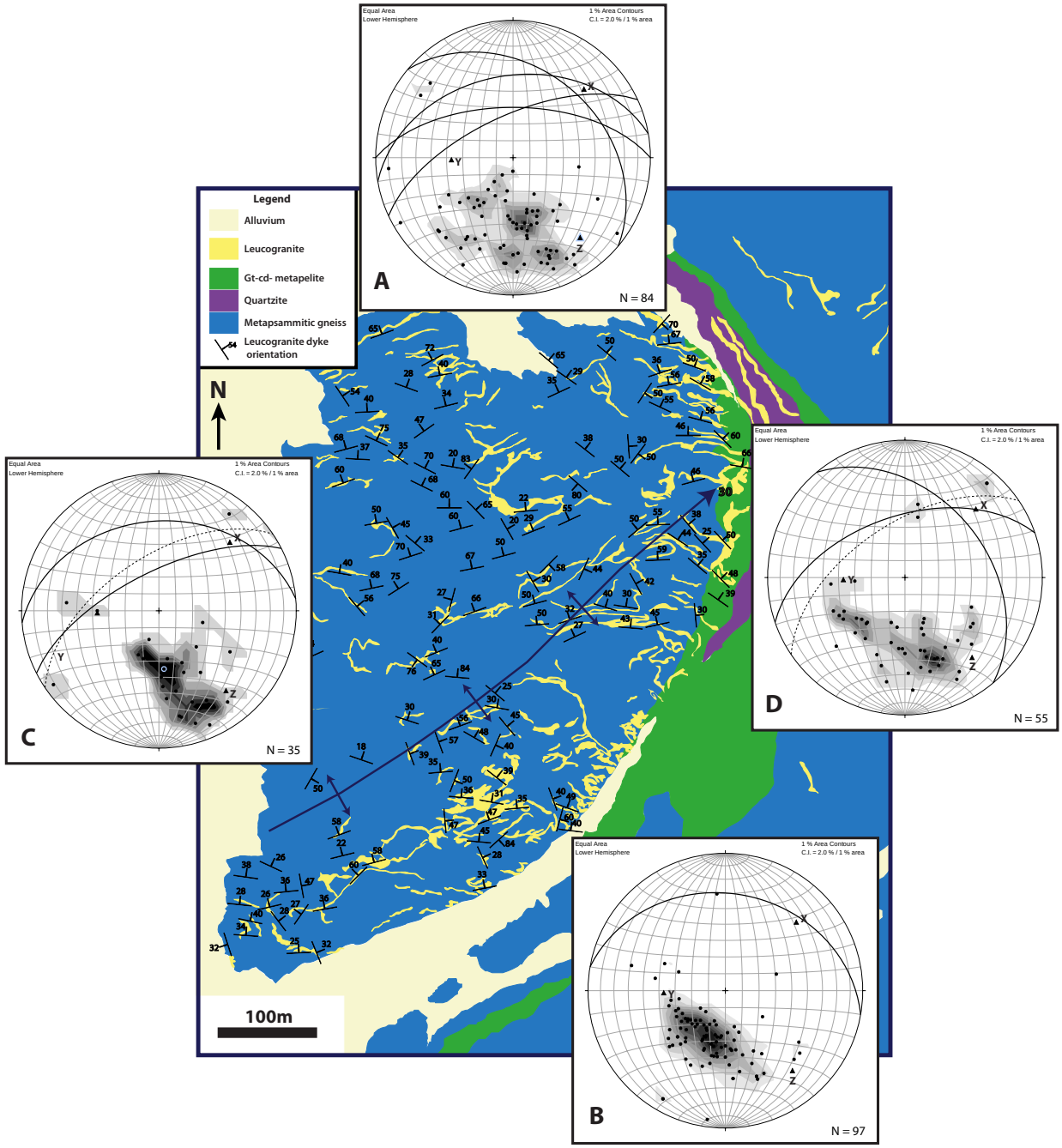

Figure 6.6: Map showing the variation in leucogranite distribution and dyke orientations (black dip symbols) across the fold. The stereonets compare the predominant dyke orientations (shown by the black great circles, and calculated from contours of all discordant leucosome poles) in the northern and southern limbs (A and B, respectively), and the dyke orientations in the SW and NE parts of the core of the fold (C and D, respectively). The dashed line in C and D represents the approximate axial plane of the large-scale antiform.

exhibits evidence of stretching in the form of pinch-and-swell structures. The sheets, when found within the fold core, are often folded and shortened with the small-scale fold hinges plunging parallel to the axis of the large-scale antiform. This is more predominant in the garnet-bearing leucogranite phase, but both do exhibit folding.

6.2.3 Shear-Hosted Dykes

Discordant leucosomes are distinguished from concordant leucosomes by their crosscutting relationship with S_0/S_1. Both leucogranite phases occur as discordant leucosome, but the pegmatitic leucogranite is more common in this orientation than the garnet-bearing leucogranite. The main type of discordant dyke are shear-hosted dykes. They occur in a variety of orientations, and vary between 5 cm to 3 m thick with larger ones continuous for 10's of metres. They only occur within the metapsammite, and exhibit dragged foliation along their edges, showing that these dykes lie within shear planes (Fig. 6.7A,B and C), which is confirmed by older dykes and veins that are offset by these structures.

The dyke edges are sharp and often have a rind of biotite separating the leucogranite from the surrounding rock (Fig. 6.7B) showing that dykes are injected. The shear-hosted dykes occur in at least three predominant orientations shown by the stereonets at 110–140°/35–70°NE , with the steeper dipping ones showing top-to-the NE (normal displacement) and the shallower ones showing top-to-the SW (reverse) displacement, 080–090°/35–60°N, with top-to-north (normal) displacement, and 060–070°/60–70°NW, with predominant top-to-NW (normal) displacement, but that also show occasional top-to-SE (reverse) displacement. The similarity of these orientations with that of leucogranite-free shears and diffuse leucogranite-filled shears provides further evidence that the larger leucogranites are shear-hosted dykes.

Shear-hosted dykes occur throughout the fold, but are more predominant within the core of the fold, with the 065°/65°NW orientation predominant there (Fig. 6.6C,D). This orientation is approximately parallel to the axial plane of the antiform (Fig. 6.4C), and these dykes shall therefore be referred to here as axial planar dykes. The 110–140°/35–70°NE reverse/normal offset and 080–090°/35–60°N normal offset shear-hosted dykes are respectively oriented approximately 50–80° and 25–35° from the axial plane (Fig. 6.6C,D).

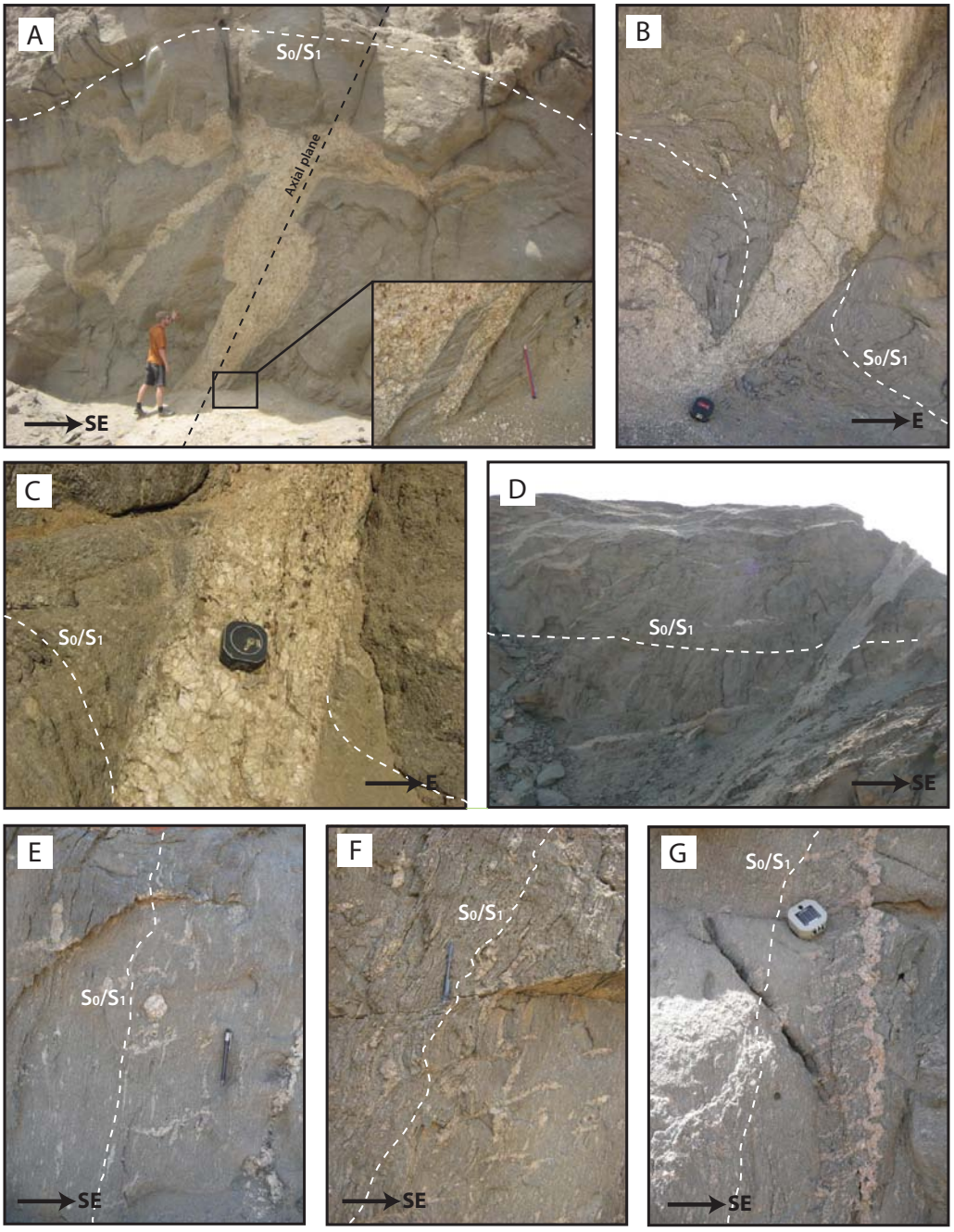

Figure 6.7: Examples of discordant leucogranite structures. S_0/S_1 is shown by the white dashed lines: (A) Photograph looking down plunge along the antiform fold trace from within the fold hinge. It shows a T-shaped leucogranite intrusion. The steep leucosome is an example of a shear-hosted dyke which is in an orientation parallel to the axial plane of the antiform (inset: see sheared edges). It is petrographically continuous with the sill above it. Both have been horizontally shortened. (B) A shear-hosted dyke with biotite rind. The dyke is petrographically continuous with the concordant sheet in the bottom left of the picture. (C) A shear-hosted dyke with dextral offset. (D) A typical shear-hosted dyke in axial planar orientation. The dyke is approximately 2 m wide. (E) Small flat dipping, diffuse, leucogranite-filled, folded tensile fractures. (F) Leucogranite-filled tensile fractures petrographically continuous with S_0/S_1 parallel leucosome. The bending of foliation into the structures can also be seen. G) Small flat-dipping diffuse leucosomes in tensile fracture orientation connected to a sub-vertical shortened sharp-edged dyke.

6.2.4 Tensile Fractures

A second type of discordant leucosome occurs parallel to the tensile fractures described above and are interpreted as such. They sometimes exhibit a radial deflection of the foliation symmetrically into the structure, which is different to the dragged foliation observed along shear boundaries. They have a relatively constant shallow NE-dipping orientation around 110–140°/20°NE, occur as highly elongate lenses parallel to the L_2 lineation, and are not as continuous as the shear-hosted dykes (Fig. 6.7E,F,G). Individual leucogranite lenses are around 0.1–2 m in length, 5–20 cm in width and 1–10 cm thick, but a few larger metre-thick lenses are found. The smaller lenses have diffuse edges suggesting that they might represent melt segregation structures containing in situ leucosome. Most lenses occur in isolation and often exhibit evidence of shortening, specifically slight folding and buckling (Fig. 6.7E), while some lenses connect to shear-hosted or concordant dykes with petrographic continuity (Fig. 6.7F,G).

6.3 Structural Analysis

The variation in orientation of S_0/S_1 (Fig. 6.4A) shows that it has been folded into a large-scale NE-plunging antiform. Analysis with a pi-diagram suggests that the hinge line plunges approximately 036°/28° (Fig. 6.4A,C). From the position of the hinge line and the axial trace of the fold, the orientation of the axial plane of the antiform is resolved at approximately 050–60°/60–65°NW (given the variation in the axial trace). The current vergence of the antiform suggests that it formed in response to large-scale top-to-the-SE shear. The current orientation of the L_2 lineation around 046°/28°, is consistent with the general D_2 NE-SW stretching (Fig. 6.4C). The parallel relationship between L_2 and the fold hinge suggests either a component of fold hinge extension concurrent with folding (Poli & Oliver, 2001), or rotation of the fold hinge into the parallelism with the apparent stretching direction after the formation of the fold (e.g. Escher & Watterson, 1974).

The spatial variation in the development and intensity of the foliation and lineation within the antiform suggests that there is a variation in the strain style between the limbs and core of the fold. The strong lineation in the core shows concentrated local constriction, whereas the strong foliation in the limbs suggests predominant flattening suggestive of coaxial strain in these areas. Assuming that the stretching lineation represents the direction of maximum apparent extension (X), and that the axial plane is perpendicular to the maximum apparent

constriction (Z), then the the principal strain direction axes XYZ can be calculated on the scale of the fold. These are plotted on Figure 6.4C and the stereonets in Figure 6.6.

The expected orientation for formation of tensile fractures within a fold is perpendicular to σ_3, which at the time of formation should be perpendicular to the axial plane (Fig. 6.8), so for a fold with a steep axial plane, tensile fractures should be relatively shallow-dipping. The tensile fractures in the antiform are orientated approximately 60° from the calculated axial plane (Fig. 6.4E), suggesting that they formed when the axial plane was not in its current orientation and that the tensile fractures are older relative to the shears and shear-hosted dykes. This is supported by the fact that they are shortened. The continuity between these shortened tensile fractures and some sub-vertical S_0/S_1 parallel dykes in the fold limbs shows that they are the same age, and that the some of the earlier S_0/S_1 parallel dykes have experienced the same strain.

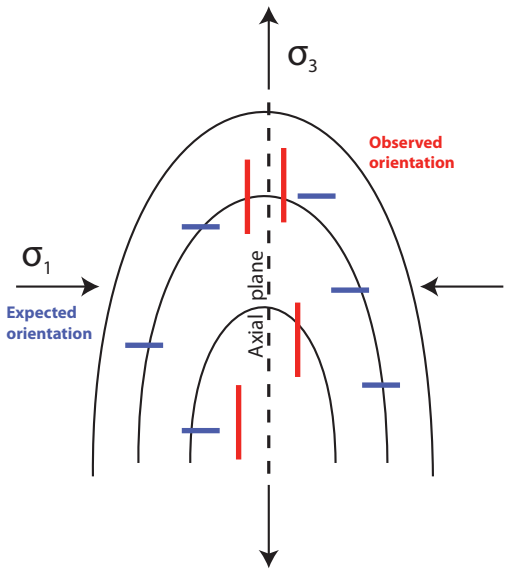

Figure 6.8: An idealized sketch the directions of σ_1 and σ_3 typically required to form a fold. The blue lines represent the orientation of dykes expected to form in the stress regime, and the red lines represent the orientation of axial planar sheets that are observed to form.

The orientations of shear-hosted dykes not in the axial plane is similar to that of the small-scale melt-free shears, although with more scatter (Fig. 6.4D and 6.6), suggesting that the dykes have been subjected to more deformation and rotation than the melt-free shears. The folding and shortening of dykes (e.g. Fig. 6.7A) indicates that deformation outlasted melt emplacement in these rocks. Therefore, the dykes likely formed during deformation while the

system was melt-bearing, and the melt-free shears formed later, during melt-absent deformation. This implies that the orientation of the shears is more representative of the apparent strain towards the end of deformation, as they would be less affected by re-orientation during subsequent deformation.

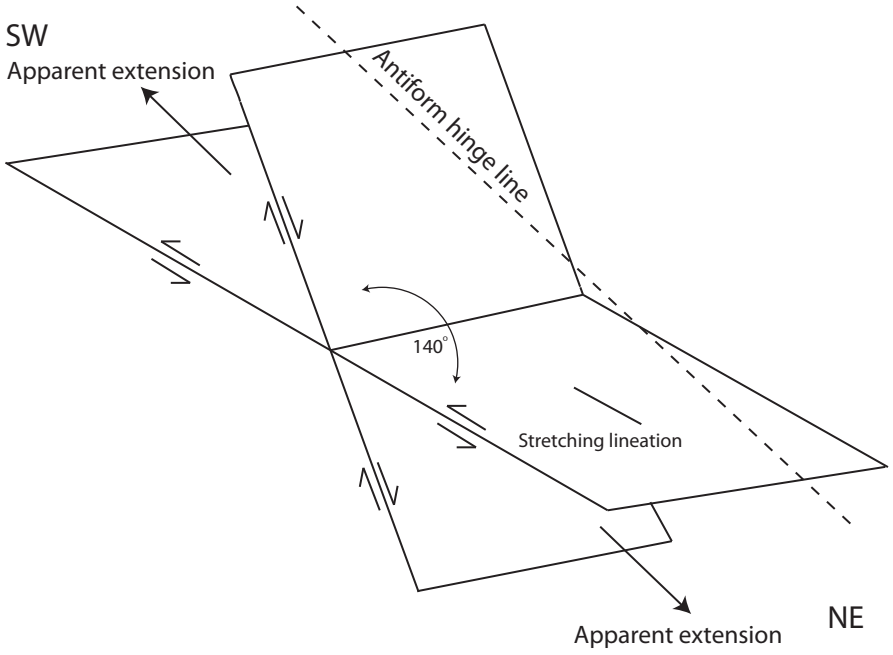

Figure 6.9: An idealized sketch showing the relationship between the two shallow and steep NE-dipping shear orientations in the fold core. The shears show opposite sense of shear, and the stretching lineation is shown as a line within the shallowly dipping shear plane. The hinge hinge line of the antiform is shown parallel to the apparent extension.

The two NE-dipping shear planes (Fig. 6.4D) which exhibit opposite shear sense for shallow and steep dipping shears (Fig. 6.9, for both the shears and shear-hosted dykes, form a conjugate set and are different to the axial-planar shears and dykes. This conjugate set indicates apparent extension consistent with the orientation of the L_2 stretching lineation (Fig. 6.9) and appear to have accommodated extension parallel to the hinge line of the antiform. The orientation of the shears also agrees with the current orientation of the strain axes provided that Y and Z have approximately equal magnitude, as would be the case for local prolate strain. Ductile shears are predicted to form with an approximate 90° between them, therefore the 140° angle which contains the downthrown block between the shear sets (Fig. 6.9), and the even larger 140–160° angle between the shear-hosted dyke orientations suggests progressive stretching of the shear sets after their formation, resulting in their rotation

towards one another

The axial planar-parallel shears and dykes show very similar orientations to one another (Figs. 6.4D and 6.6). The presence of rotated and dragged foliation along dyke edges, and the similarity of the dyke orientations to the shears, together with the sharpness of the intrusive contacts of the leucogranites, shows that the dykes occur within shear planes. The predominant normal offset on both the axial planar dykes and shears suggests local NW-SE extension, which contradicts the overall NE-SW extension shown by L_2 and the NE-dipping shears. The origin of these axial planar structures is discussed further in the next section.

6.4 Melt Migration and Axial Planes

The relatively low volume of leucogranite within the core and limbs of the antiform compared to the hinge suggests that the structures within the fold accommodated melt movement through the fold. Much of this melt seems to have accumulated in the thickened quartzite lens in the hinge, where it was trapped by the impermeable metapelite layer that surrounds the quartzite. The structures that were utilised as part of the melt network include S_0/S_1 planes and shear planes, with the predominance of concordant leucosome along the limbs suggesting that the S_0/S_1 plane is the most common migration structure along the limbs. This makes intuitive sense since S_0/S_1 along the limbs is in a favourable sub-vertical orientation for upwards melt movement along it. S_0/S_1 within the fold core is shallowly-oriented, and therefore unfavourable for upward melt movement. The predominance of shear-hosted and axial planar dykes within the fold core suggests that melt is forced to utilise these pre-existing discordant structures in order to migrate through the hinge zone.

Since many of the older dykes and sills show evidence of shortening subsequent to their crystallization, it is reasonable to expect that the current orientation of these structures might not be the same as when they originally formed. It is likely that structures, particularly those oriented at an angle to the axial plane, would have been rotated towards the axial plane during progressive tightening of the fold (Vernon & Paterson, 2001). This is consistent with the scatter in the dyke orientation compared with the lack of scatter in the orientation of melt-free shears.

However, the presence of some planar, undeformed, near axial plane-parallel shear-hosted dykes which contain the young pegmatitic melt, suggests that at least some of the dykes represent emplacement into a plane of approximate shortening. The normal displacement

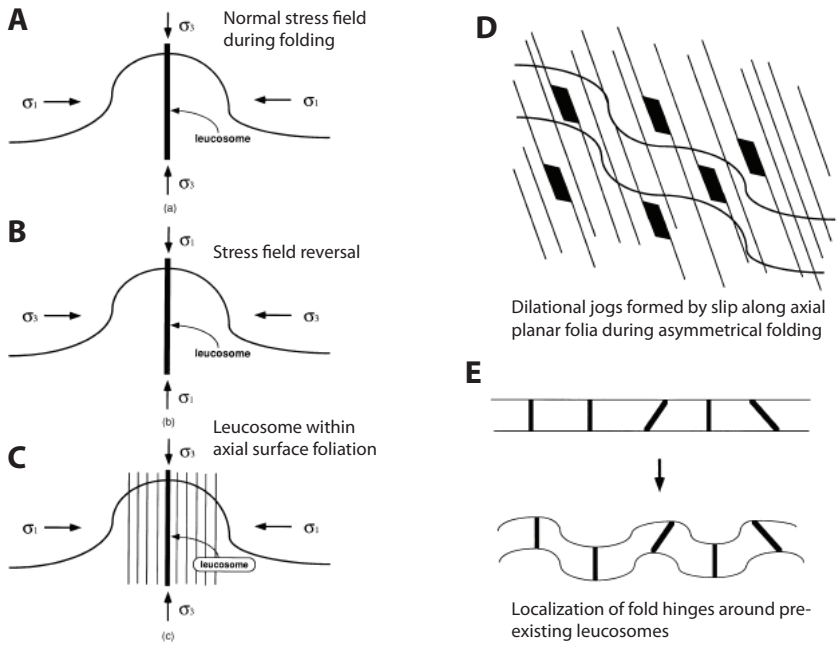

Figure 6.10: Models explaining the presence of leucogranite within the axial plane of a fold (from Vernon & Paterson, 2001). (A) The normal stress field during folding. (B) A stress field reversal allowing for axial- planar intrusion. (C) Leucosome within axial planar foliation. (D) Dilational jogs formed by secondary asymmetrical folding on fold limbs. (E) Localization of fold hinges around pre-existing solidified dykes.

along their edges suggest that the shear structures were extensional, at least at the time of dyke emplacement. This conflicts with the general understanding of stress directions in a fold that assumes that the axial plane is a plane of maximum shortening (Fig. 6.8; Vernon & Paterson, 2001).

Several models have been proposed to explain the presence of leucogranite dykes with axial planar orientation. The first requires temporary relaxation of folding so that either large-scale or small-scale stress fields change and allow for dilation along the axial plane (Fig. 6.10A, B; Means, 1987; Vernon & Paterson, 2001). The second requires that the fluid pressure overcomes σ_1 plus the tensile strength of the rock parallel to σ_1 (Wickham, 1987; Simpson, 1998), an unlikely occurrence unless a pre-existing axial planar foliation is present to provide rheological weakness (Fig. 6.10C). A third model explains the presence of axial plane-parallel leucosomes in strongly asymmetrical folds that develop macrocrenulations on their limbs.

It suggests that transient dilation jogs and shears are created during relative movement along axial planar foliation surfaces (Fig. 6.10D; Kerrich & Allison, 1978; Sawyer & Robin, 1986; Allibone & Norris, 1992; Vernon & Paterson, 2001). However, this mechanism only explains the presence of axial planar leucosome in the limbs of folds where such slip can be expected to occur. A final mechanism for the presence of axial planar leucosome requires that the leucosome intrudes early and solidify, so that, due to rheology contrasts, folds localise around the leucosome, or leucosomes rotate into the axial plane (Fig. 6.10E; Vernon & Paterson, 2001). None of these models account for the apparent dilation in the axial planar orientation described here, and most require the presence of a pre-existing axial planar foliation that is not present in these rocks.

It has been demonstrated by e.g. Escher & Watterson (1974) that it is possible for extensional regimes to locally form under larger-scale simple shear conditions, and that even compressional shear zones can experience periods of extension, so that they can be locally extending at times, but not extensional overall. If we assume that the vergence of the antiform indicates that it formed due to large-scale simple shear, then it is possible to explain the axial planar dykes with this model. Figure 6.11 is a series of idealized sketches that show how the strain ellipse changes during progressive simple shear. As strain increases, the X-axis progressively stretches and rotates and a local extending environment is created, concurrent with Z-axis rotation and constriction. Importantly, the orientation of the X axis is parallel to the axial plane of the developing fold. This implies that the fold hinge and axial plane do not exclusively experience shortening throughout their history, but rather would undergo transient extension, allowing for the formation of dilation accommodated by dilational shears within the hinge zone. The orientations of these are difficult to predict because during progressive simple shear the X-axis would rotate constantly and so the extending direction would be transient. This is illustrated in Figure 6.12, which shows idealized sketches of strain axes during progressive simple shear and the rotation of shears formed in response to extension along X and shortening along Z.

After their formation the shears would remain planar and rotate towards one another and the axial plane so that two approximately similar near axial-planar parallel shear orientations with opposite shear directions eventually occur. The timing of melt intrusion along the shears is dependent on melt supply, and if melt intruded along the shears when they are in the orientation shown in A on fig. 6.12 and subsequently crystallised, their rheological contrast with the surrounding rock would allow for passive rotation into axial planar orientation and

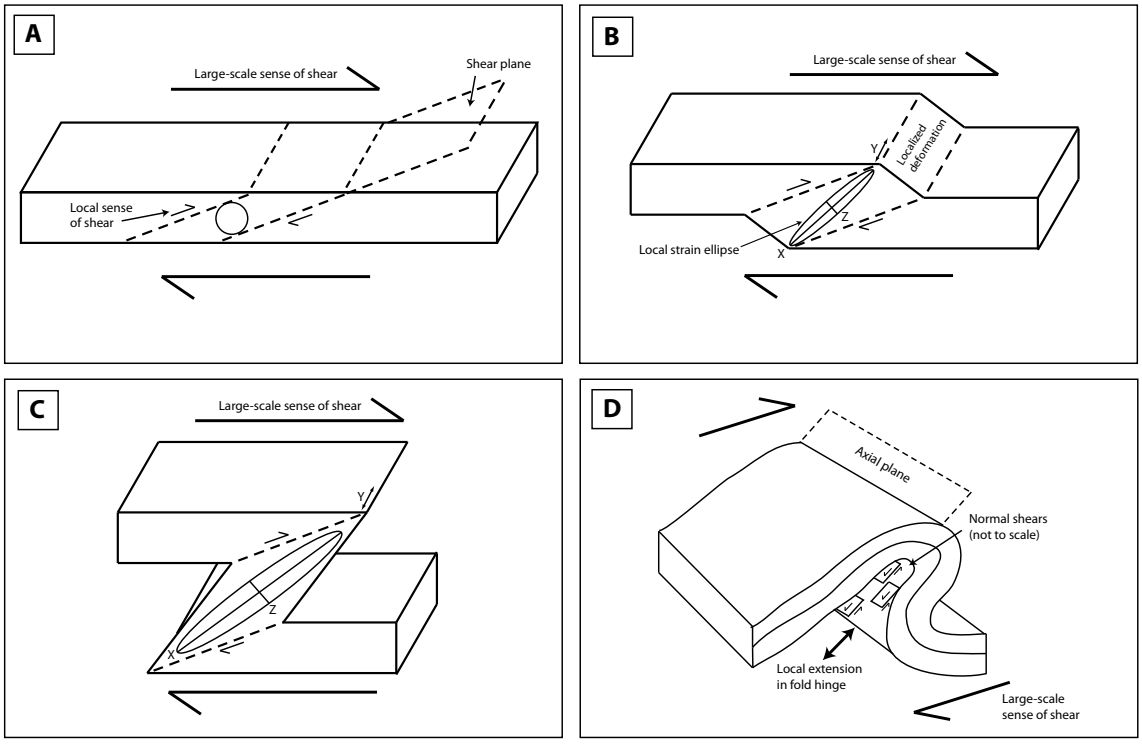

Figure 6.11: Idealized model for the formation of extension within a simple shear environment (A, B and C are after Escher & Watterson, 1974). (A) Shows an undeformed layer containing an undeformed circle. The shear zone that accommodates the large-scale right-lateral displacement is demarcated by dashed lines. (B) As deformation begins the shear is localized within the demarcated zone, and the circle is deformed so that it experiences extension along its X axis and compression along its Y axis. (C) Shows further deformation and more extension along the X-axis. (D) Shows an idealized sketch of how this model applies to a fold structure, where normal shears form to accommodate the local extension within the hinge of the fold.

we would expect the axial planar dykes to show significant evidence of extension. Many do show this evidence with pinch and swell structures, however there are plenty currently in axial planar orientation and that are almost perfectly planar and showing very little to no evidence of extension.

In order to accommodate accumulating extensional strain parallel to X, it is expected that either new shears will keep forming, or the already-formed shears will remain active as they rotate towards the axial plane. Observations of slip along structures at unusually high angles ($> 45°$) to σ_1, such as actively slipping low-angle normal faults (Chiaraluce *et al.*, 2007; Hreinsdóttir & Bennett, 2009), show that the latter is possible, and likely occurs because

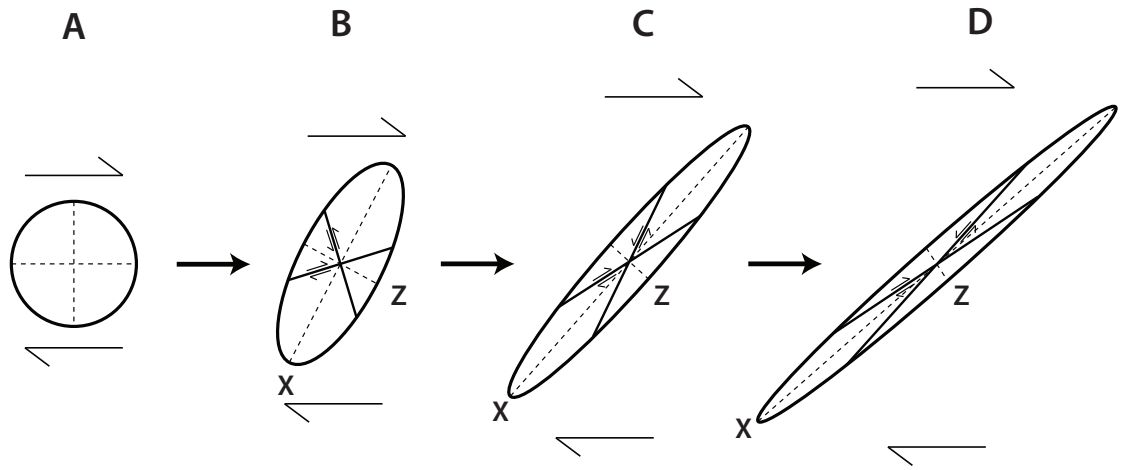

Figure 6.12: Two dimensional strain axes showing the progressive extension of X and shortening of Z during broadening general shear. A set of conjugate shears are shown to form 45° to X in (B) in response to the extension parallel to X and flattening parallel to Z. These shears then rotate towards one another and extend as their angle to X decreases (C–D), thereby accommodating strain as X progressively extends and Z progressively shortens.

pre-existing structures (particularly ones that are already experiencing slip) are much weaker than the surrounding rock (White *et al.*, 1986; Holdsworth *et al.*, 1997).

Provided there is low to no melt supply, progressive rotation of empty shears would occur, and despite their increasingly less favourable orientation and progressively higher angle to the overall direction of compression, shearing will still accommodate most of the strain, providing a continued extending environment such as in C on fig. 6.12. During periods of higher melt supply, the extending shears are perfect sites for melt intrusion, despite their high angle to larger-scale compression, and melt intrudes into planes near parallel to the axial plane of the large-scale fold (i.e. when the shears are in orientation C on fig. 6.12) and crystallises. This explains the presence of undeformed axial planar leucogranite dykes. Evidence for shearing along the shear planes once intruded by granite (such as mineral alignment) is lacking, suggesting that the melt-bearing shears do not accommodate much shearing once melt is within the shear planes, and thus the melt likely crystallises rapidly.

The presence of leucogranite predominantly within the axial planar shears that show normal offset suggests that these were more favourable sites for melt to exploit than the less frequent axial-planar reverse offset shears. This is consistent with the normal shears being

more dilational than the reverse shears, and therefore more favourable melt sites. Importantly, the lack of composite dykes within the antiform indicates that these structures are relatively short-lived, compared to the more long-lived dyke structures that are exploited by multiple leucogranite phases (e.g. Chapters 4, 5 and 7). This provides further support for the origin of these structures in a variable and evolving strain regime.

Chapter 7

Migration through an Idealised Crustal Section

This chapter investigates the movement of melt through an ∼80 m-thick section of interlayered supracrustal rocks that is bounded at the top and bottom by basement orthogneisses. The section contains several phases of injected leucosome that occur in a variety of structures and represent different melt pulses of varying volume. These leucogranite-bearing structures are connected and continuous and can be traced from their local accumulated source at the base of the section, through the various melt pathways, to their local emplacement level at the top of the section. This outcrop therefore offers a snapshot of multiple episodes of melt migration from the source to the sink, across subsolidus rocks, analogous to what likely occurs on large scale in the mid-crust, and provides the opportunity to examine all aspects of the melt migration process in a single, contained outcrop.

7.1 Outcrop Geology

The studied outcrop occurs in the Palmenhorst Dome and is located on the western bank of the Khan River at 22°40'34"S 14°54'45"E. It consists of two near-orthogonal, ∼80 m-high cliff sections, an ESE-facing section about 150 m long (Figs. 7.1A and 7.2) and a south-facing section about 110 m long (Figs. 7.1B and 7.3).

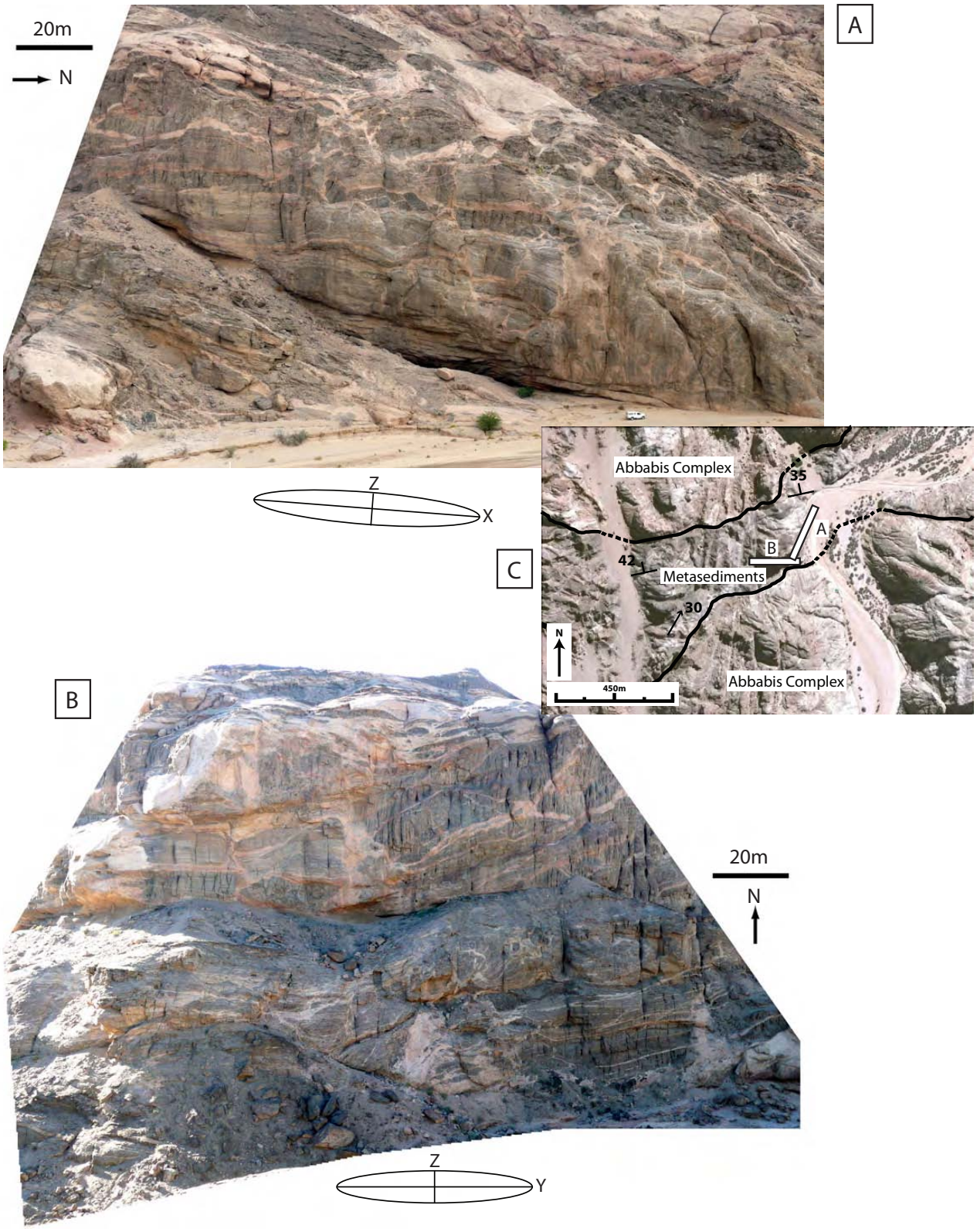

Figure 7.1: Photographs of the two cliff faces studied. They are oriented roughly orthogonal to each other (C), with the ESE-oriented side face (A) containing the X–Z plane of the strain ellipse and the south-facing cliff (B) containing the Y–Z plane, as indicated.

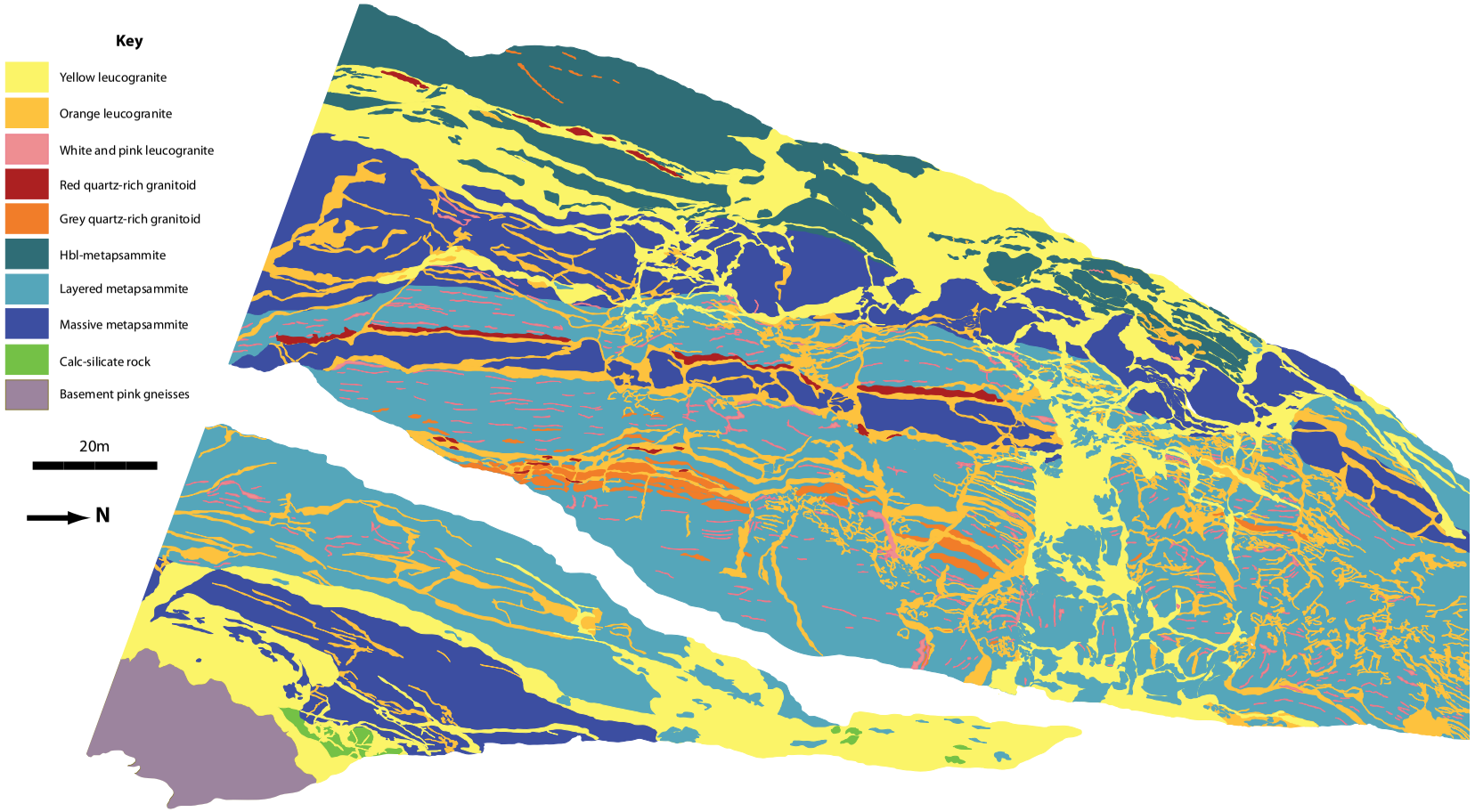

Figure 7.2: Map of ESE-facing cliff face showing all lithologies and intrusive phases. The map was overlain on an outcrop photograph, and all features greater than 30 cm in size are represented.

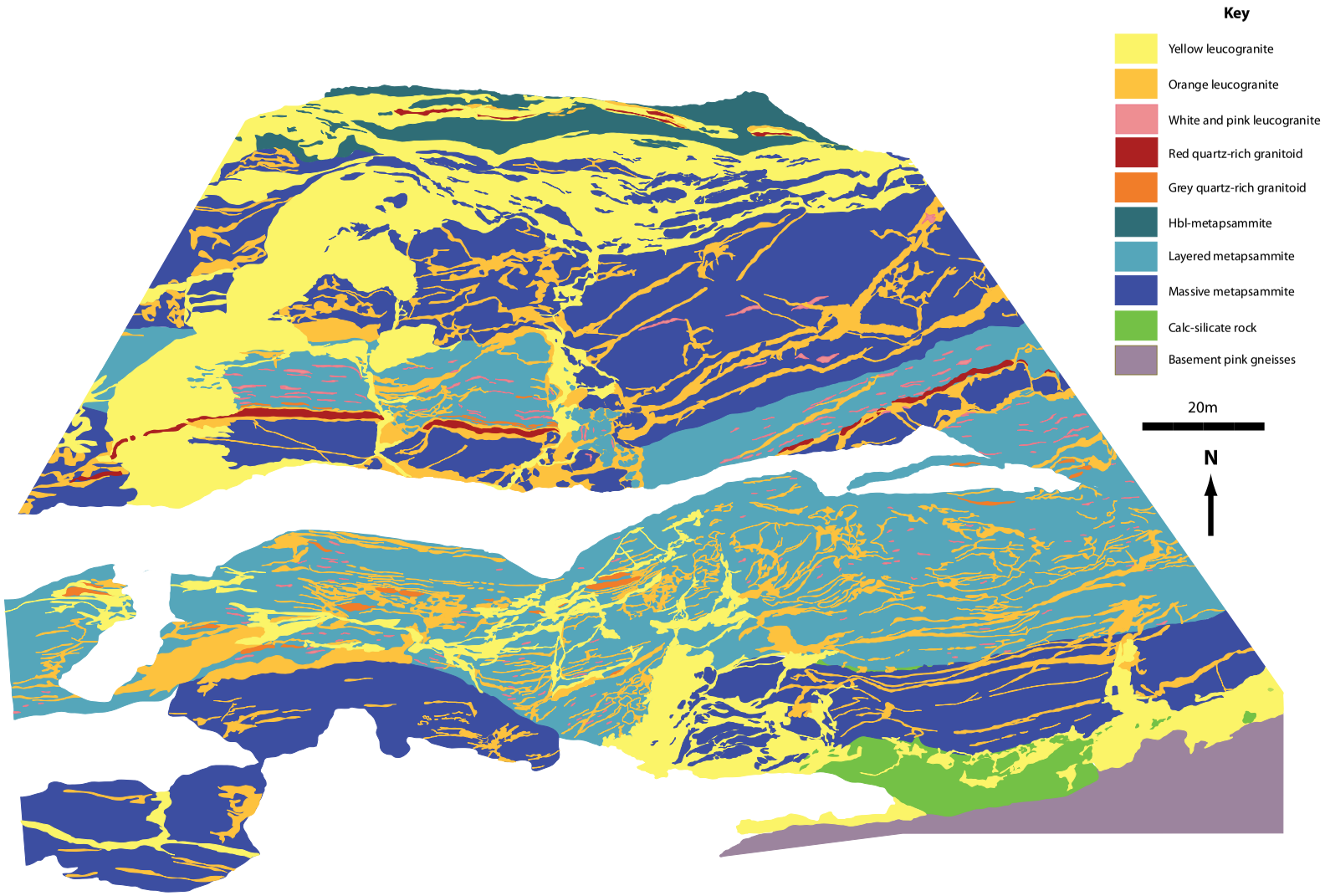

Figure 7.3: Map of south-facing cliff showing all lithologies and intrusive phases. This map was overlain on an outcrop photograph, and all features greater than 30 cm in size are represented.

The outcrop contains metasedimentary rocks of the Khan Formation that are bound at the top and bottom by migmatitic orthogneiss of the Abbabis Complex (Fig. 7.1C). The bounding contacts are subparallel to the layering in the supracrustal package, and are shallowly north-dipping. The mineral elongation lineation plunges down-dip to the NNE, such that the ESE-facing cliff is oriented parallel to the lineation and therefore contains the directions of maximum elongation (X) and shortening (Z), whereas the south-facing cliff is oriented normal to the lineation and contains the Y–Z plane of the strain ellipse (see below; Fig. 7.1).

7.1.1 Lithology

The Abbabis Complex rocks are comprised of several migmatitic quartzofelspathic gneisses with minor discontinuous biotite schist and amphibolite pods (Nex *et al.*, 2001; Basson & Greenway, 2004). These rocks have been extensively migmatized, and are intruded by several phases of fine- to medium-grained granite. They outcrop as smooth domes to the south and north of the metasedimentary sequence (Fig. 7.1C). The metasedimentary package has been downfolded into the Abbabis Complex during formation of the Palmenhorst Dome (Luke Longridge, personal communication, 2012). It consists of metapsammitic gneisses containing variable proportions of quartz, biotite and hornblende, interlayered with horizons of hornblende–diopside–calcite–quartz calc-silicate rocks and garnet–magnetite metapelitic schists that have a conformable stratigraphy (Figs. 7.2, 7.3 and 7.4).

The base of the package contains a 2–5 m-thick calc-silicate layer that forms the most competent lithology in the sequence and is green and black in colour. The calc-silicate (Fig. 7.5A) is predominantly coarse-grained (0.1–3 cm grain size), and is comprised of 0.1–0.5 cm green euhedral diopside crystals (50% modal abundance), 0.1–3 cm euhedral black hornblende crystals (40% modal abundance), 0.1–1 cm biotite grains which are often visible as books (5% modal abundance), 0.1–0.5 cm grains of quartz which are intergrown with hornblende and diopside, as well as occasional 3–15 cm quartz patches.

The calc-silicate is overlain by a massive, medium-grained, quartz-rich, dark-grey metapsammitic gneiss with a thickness of 10–15 m (Figs. 7.4 and 7.5B). This massive metapsammite often contains isolated, 1–3 cm stretched nodules of calc-silicate rock and is comprised of 1–2 mm subhedral grey quartz grains (85% modal abundance) and 1–3 mm biotite grains (15% modal abundance). Overlying the massive metapsammite is a thin layer of magnetite-rich semi-pelitic schist. This unit is 2–5 m thick, is fairly equigranular, and has a grain size from

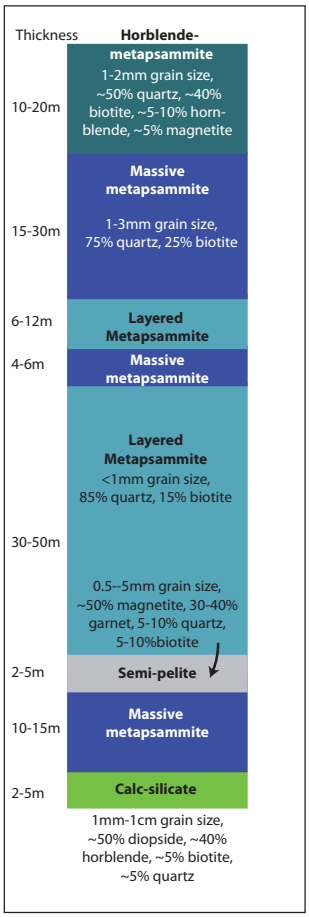

Figure 7.4: Stratigraphic column showing relative thicknesses and mineralogy of the metasediments that comprise the outcrop.

0.1–5 mm. It consists of of 30–50% magnetite, 30–40% garnet, 5–25% quartz, 5-10% biotite, with minor cordierite. This unit is not distinguished from the layered metapsammite above it on Figures 7.2 and 7.3 due to its thin and discontinuous nature, and because it preferentially weathers so that it is mostly covered by alluvium.

The main unit that comprises about half the cliff height is a well-layered, fine-grained, light-grey metapsammitic gneiss (Figs. 7.2, 7.3, 7.4 and 7.5D,E). This unit contains abundant early, stromatic leucosome that defines the layering. It is finer-grained than the massive metapsammite, with grain size <1 mm and is comprised of 70% quartz, and 30% biotite. Overlying the layered metapsammite is another 4–6 m-thick massive metapsammite unit, which is in turn overlain by another 6–12 m-thick layered metapsammite unit (Figs. 7.2, 7.3 and 7.4). The top of the package consists of a 20–30 m-thick massive metapsammite

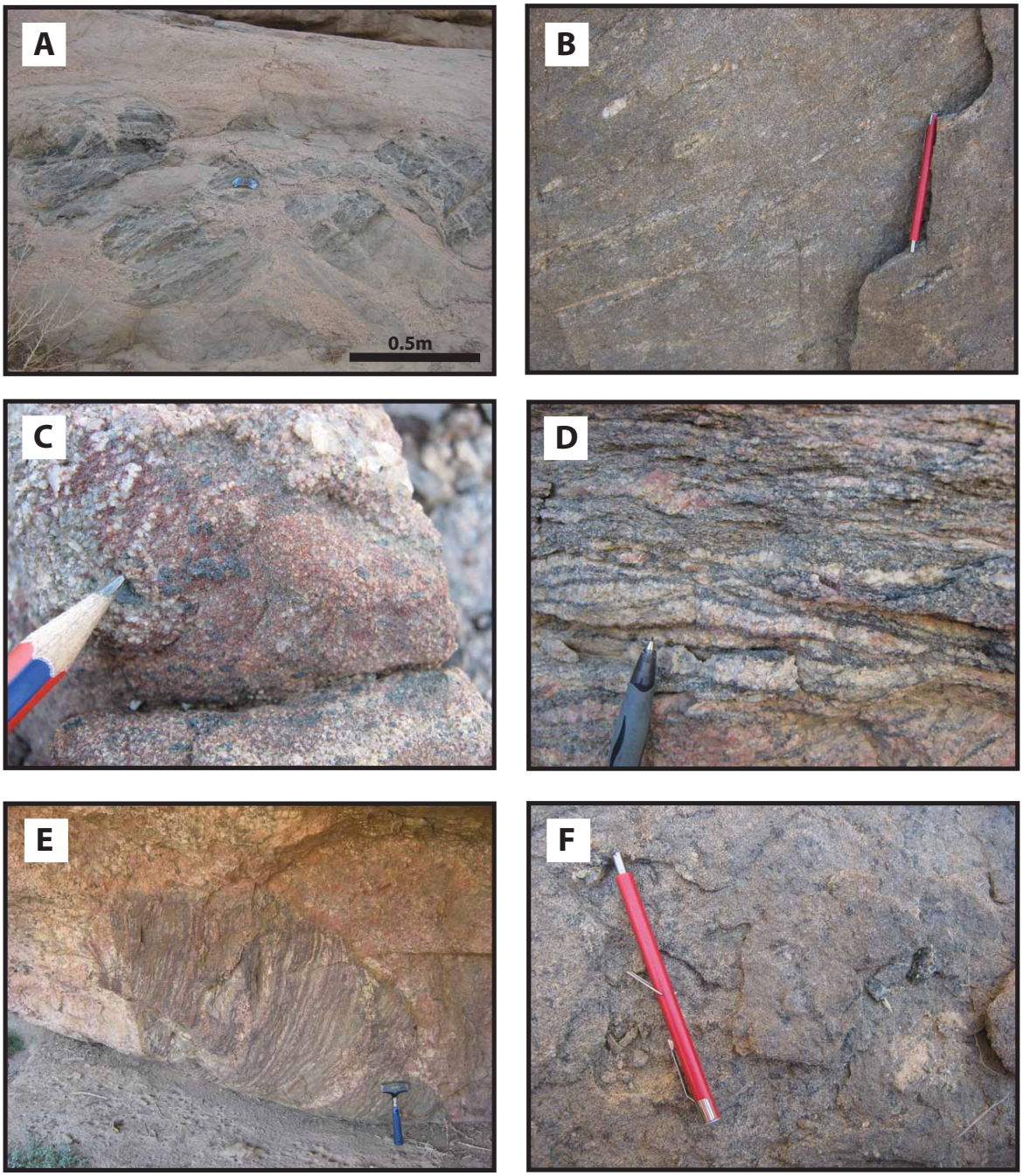

Figure 7.5: The metasediments which comprise the supracrustal package. (A) Hornblende and diopside-rich calc-silicate blocks surrounded by leucogranite. (B) Massive metapsammite with occasional calc-silicate pods. (C) Magnetite-rich semi-pelitic schist. (D) Layered metapsammitic gneiss. (E) A block of strongly layered metapsammite surrounded by leucogranite. (F) Hornblende-biotite schist containing black hornblende nodules.

unit that is overlain by a >20 m-thick, dark brown, hornblende–biotite-rich metapsammitic schist (Figs. 7.4, 7.5F). It is fairly equigranular with a grain size between 1 and 2 mm. The mineralogy includes 50% quartz, 40% biotite, 5–10% hornblende, and approximately 5% magnetite. The layer also includes fine-grained patches of hornblende and diopside and stretched calc-silicate nodules (Fig. 7.5F).

7.1.2 Intrusive Phases

Five intrusive phases are distinguished based on their mineralogy and texture, the presence or absence of planar and/or linear fabrics, and crosscutting relationships. The total intrusive phase volume comprises 32% of the outcrop, as calculated from image analysis of both cliff faces. Within the metasediments, the earliest two phases of grey and red quartz-rich granitoids (see below) are never observed to crosscut one another, and therefore their relative ages are unclear. A younger pink to white leucogranite often intrudes along the edges of the grey quartz-rich granitoid, whereas younger orange and yellow leucogranites crosscut and/or intrude along the edges of all earlier phases. The orange and yellow leucogranites are mutually crosscutting; however the orange leucogranite tends to exhibit some minor deformation as pinch-and-swell structures whereas the yellow leucogranite is undeformed. The early phases are poor in alkali feldspar whereas the later ones become progressively more enriched. Many of the intrusive bodies are composite, and bodies mapped as one phase might also contain older leucogranite phases. This variation has been distinguished where possible, but otherwise the dominant phase is the one represented on the maps (Figs. 7.2, 7.3)

Grey Quartz-Rich Granitoid

The oldest intrusive phase is a grey-white, medium-grained quartz-rich granitoid that is composed of 85–90%, 1–10 mm white and smoky quartz and 10–15 %, 1–2 mm biotite grains (Fig. 7.6A). Biotite grains in the grey quartz-rich granitoid are aligned and define a solid-state foliation that is oriented parallel to S_1. The grey quartz-rich granitoid occurs exclusively as 0.1–1 m thick, foliation-parallel boudinaged layers within the layered metasediment in the in the lower half of the cliff (Figs. 7.2 and 7.3). This phase is <1% of the outcrop volume and comprises 1–3% of the total intrusive phases in the outcrop.

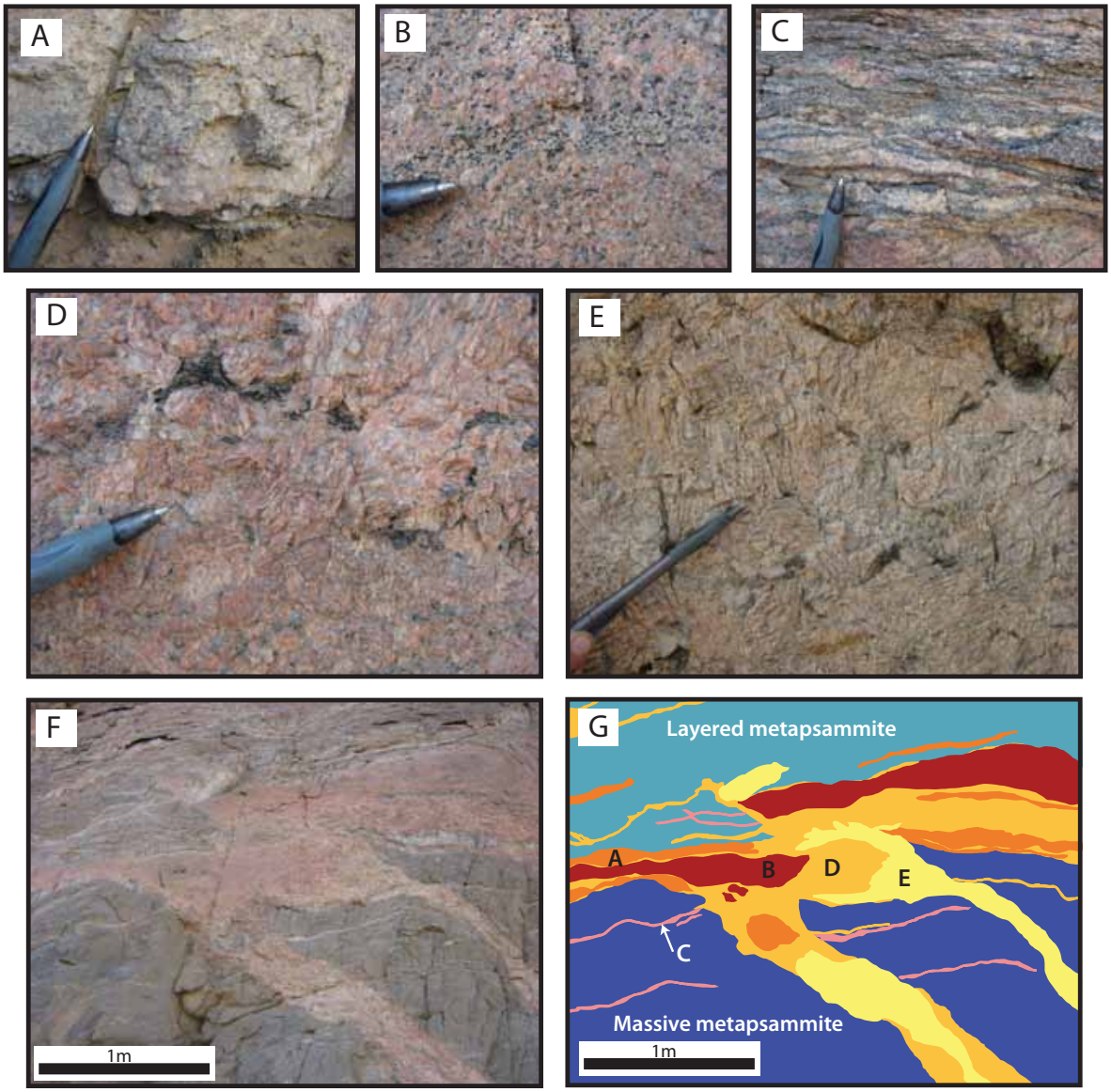

Figure 7.6: Intrusive phases in the outcrop. (a) Grey quartz-rich granitoid. (b) Red quartz-rich granitoid. (c) Light-grey metapsammite with pink and white stromatic leucogranite. (d) Orange leucogranite, showing 1 cm biotite books. (e) Yellow leucogranite, containing 1–4 cm biotite books. (f) Photograph of all five intrusive phases illustrating the relationship between them. (g) Interpretive sketch of the relationship between the five leucogranite phases in (F). The labels A to E are representative of the other photographs in this figure. The layered metapsammite contains small pink and white leucogranite that is not shown in the sketch.

Red Quartz-Rich Granitoid

The red intrusive phase (Fig. 7.6B) is the second-oldest phase identified and is grey-pink in colour, equigranular, and medium-grained. It is comprised of 70 %, 3–5 mm red-stained quartz, 20 %, 2–4 mm potassium feldspar, 5–10 %, 1–2 mm biotite grains and minor magnetite. Biotite grains are aligned and define a fabric parallel to the foliation in the surrounding metasediments. This red quartz-rich granitoid occurs as <0.5 m-thick, foliation-parallel layers that are occasionally boudinaged, or as an early boudinaged phase within thick, composite foliation-parallel dykes. This phase comprises 1–2% of the total outcrop, and 2–5% of the total intrusive phases in the outrcrop.

Pink and White Leucogranite

A third leucogranite generation occurs as medium- to coarse-grained (3–50 mm grain size), pink-red and beige-white leucogranites (Fig. 7.6C). These pink and white leucogranites are grouped as one phase as they exist in the same structures, have almost the same mineral proportions, and are distinguished mainly by red-staining of quartz in the pink leucogranite, which is absent in the white leucogranite. They are comprised of approximately 55-60 % quartz, 30 % feldspar, and 10 % biotite, and do not exhibit any alignment of minerals. These phases usually occur as thin (5–10 cm) boudinaged or finely folded stromatic stringers oriented parallel to S_0/S_1, and occasionally within crosscutting conjugate shears. They do not often occur in larger structures, with the exception of their occurrence in composite leucogranite sheets. This generation predominantly intrudes the light-grey metapsammite and is responsible for its layered nature. This phase contributes a medium volume relative to other phases. Its volume is difficult to quantify on the map scale because it mainly occurs in cm-scale stromatic layers, however it is shown to make up 3–5% of the outcrop and about 12–15% of the total intrusive phase volume.

Orange and Yellow Leucogranite

The youngest phases are the orange (Fig. 7.6D) and yellow (Fig. 7.6E) pegmatitic leucogranites. They are coarse-grained, orange-yellow in colour, and consist of 55–75 % potassic feldspar and plagioclase, 20–35 % quartz, <15 % biotite and <5 % magnetite. Feldspar occurs as large (>30 mm) crystals with interstitial quartz (∼20 mm) and large (10–50 mm) biotite books. Magnetite is found in small clusters of grains 2–20 mm in size. These two phases

are grouped together because they have mutually crosscutting relationships, exploit similar structures and have similar textures, all of which suggest that they are near-contemporaneous in age and formed under similar conditions. In places where the two phases can be distinguished, they are mapped as separate leucogranites (Figs. 7.2 and 7.3). These two phases are far more voluminous than the other leucogranites and constitute 30% of the outcrop and 75–80% of the total intrusive phase volume seen in the sections. The orange and yellow leucogranites occur in a variety of structures, and can be present as thick (>0.5 m) foliation-parallel sheets, as thin bodies within shears and tensile fractures, or as the interstitial phase cementing large rotated blocks in leucogranite-cemented breccias (see below).

7.1.3 Fabrics and Structures

The predominant fabric in the outcrop is a well-developed, shallowly NNE-dipping penetrative foliation that is oriented parallel to the macroscopic lithological layering as well as the contacts between the supracrustal rocks and the Abbabis Complex. (S_0/S_1; 040–100°/10–40°N; Fig. 7.7A). Even though the parallel orientation of the layering and the foliation might be considered to indicate a composite transposition fabric, there are no intrafolial folds or other features observed that would confirm this. This fabric is defined by the alignment of biotite and hornblende in the metapsammitic rocks. A penetrative foliation is not developed in the calc-silicate units. The foliation is associated with a weakly-developed to absent mineral elongation lineation (L_1) that plunges shallowly to the NNE, approximately down-dip to S_0/S_1 (010–050°/10–30°; Fig. 7.7A). The lineation is defined by elongate quartz grains in metapsammitic units and aligned hornblende in hornblende-rich lithologies. Elongated calc-silicate nodules in massive and hornblende metapsammitic units are aligned in the same orientation. Mesoscale folding is not observed in the sequence.

Centimetre- to metre-scale shear zones crosscut the bedding and tectonic fabric (Fig. 7.8). Individual shears are between 5 cm and several metres in length and 1 cm to 0.5 m thick and they often contain leucosome, sometimes with diffuse edges. Small centimetre-scale shears are more common than metre-scale ones. The shear zones have a normal sense of displacement, as identified from foliation drag and offset markers such as lithological layers and dykes of early intrusive phases. Typically there is little offset on these shears, usually on the order of a 1–5 cm on small shears and less than a metre on larger shears, although there are examples where the offset can reach a few metres. The shears exhibit a range of orientations,

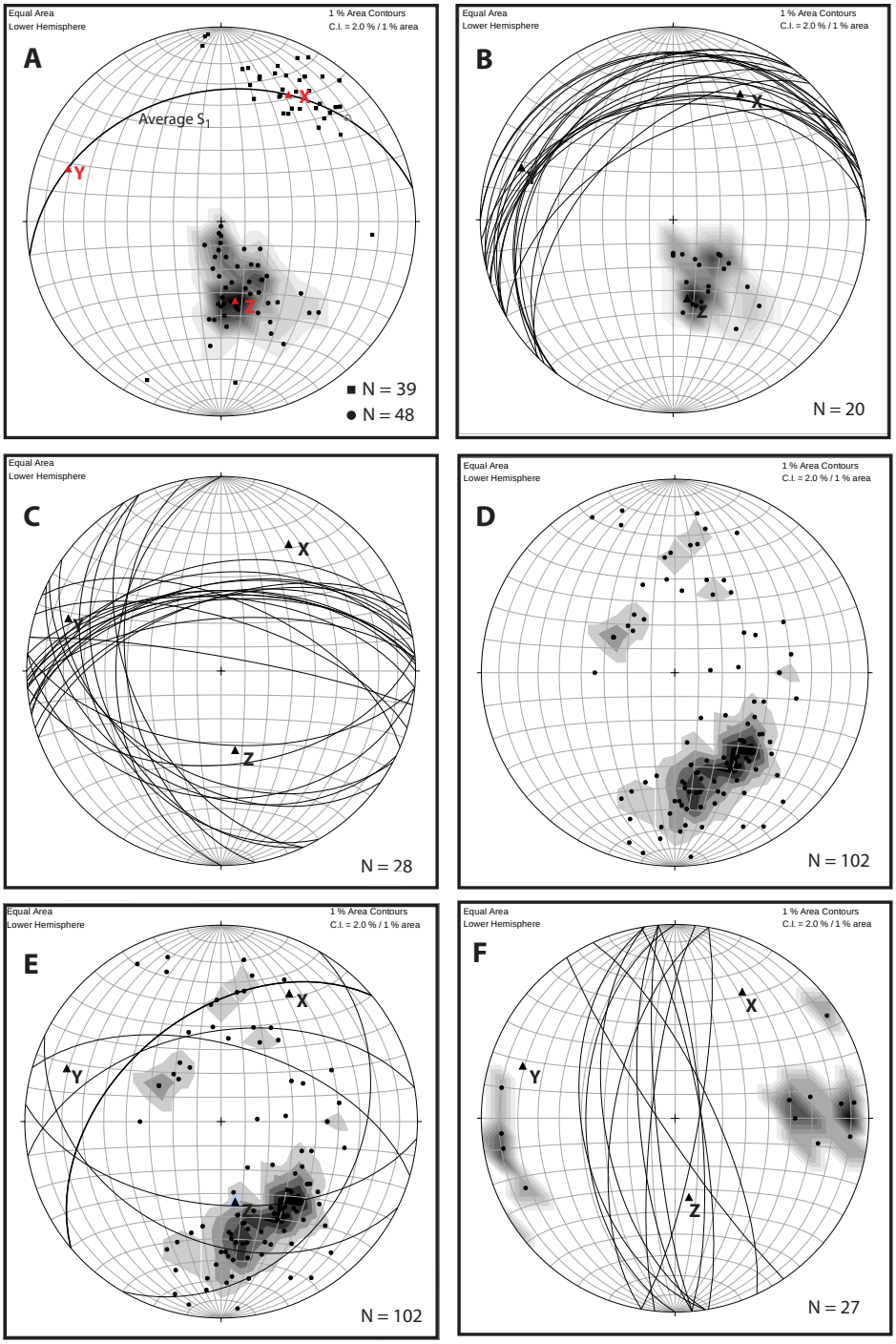

Figure 7.7: Equal area stereonets. (A) Dots represent the poles to S_1 foliation planes, and average foliation plane is shown by a black line. Squares represent L_1 mineral lineation measurements. XYZ are the orientation of the strain axes. (B) Planes and poles to planes of concordant intrusive sheets. (C) Orientations of ductile shears that do not contain leucosome. (D) Contoured poles for all non-concordant intrusive sheets showing specific clusters. (E) The thick black NW-dipping great circle represents the most common orientation of intrusive sheets. Thin lines are slightly less predominant average orientations. (F) Planes representing orientations of near-vertical planar leucogranite dykes and their contoured poles.

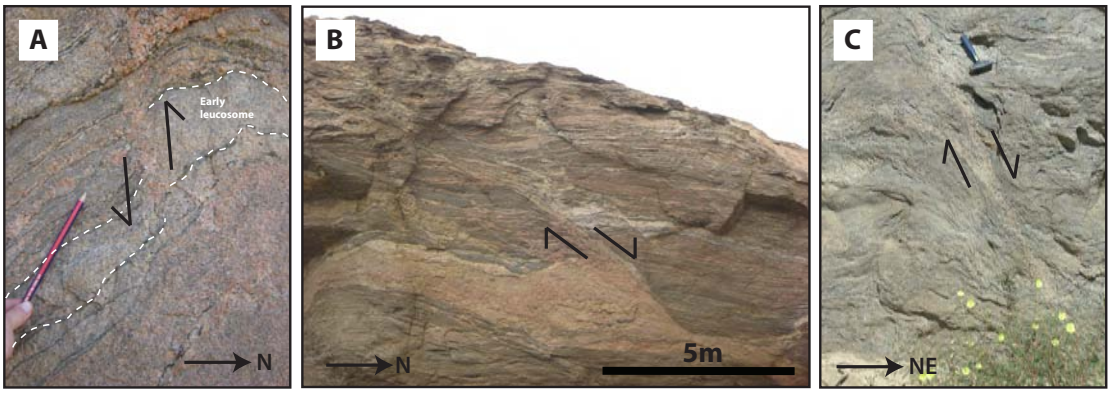

Figure 7.8: Photographs of shears. (A) Small diffuse shear with normal sense of shear. (B) Larger shear causing a pinch-and-swell structure in the leucogranite below it. (C) A diffuse leucogranite-bearing shear with normal offset.

but with dominant clusters oriented around 080/60°N, with top-to-the-north displacement, and 120-150/35-45°SW, with top-to-the-SW displacement (Fig. 7.7C). Adjacent shears often occur as conjugate pairs, and the stereonet shows that the angle between average conjugate shear planes is 80–95°. The N-dipping and SW-dipping shears are 27° and 60–70° from S_0/S_1, respectively (Fig. 7.9). Layers of massive metapsammite and calc-silicate often exhibit chocolate-tablet boudinage, with the boudin necks having a near vertical orientation perpendicular to the layering.

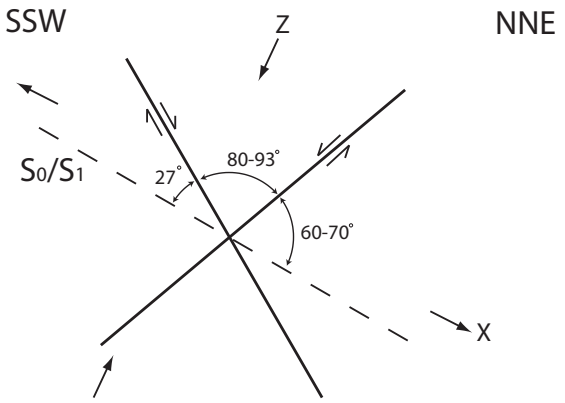

Figure 7.9: Simplified sketch in the same orientation as Fig. 7.2, showing the relationship between the conjugate shear set and S_0/S_1 and the approximate orientation of X and Z.

7.2 Former Melt-bearing Structures

The intrusive phases occur in a variety of orientations and structures, as summarised in Figure 7.10. Individual intrusive veins range from less than 1 cm to at least 3 metres in thickness and are often connected to form an intrusive network which pervades the outcrop. The intrusive structures have sharp boundaries, and can contain single or multiple phases (Fig. 7.6F,G). Within these structures older intrusive phases occur as boudins and xenoliths surrounded by younger leucogranite phases, or older phases occur as continuous layers, with younger leucogranites found along the contact between the older phase and the surrounding metasediment. Occasionally these phases are separated by biotite rims, but no phases exhibit chilled margins.

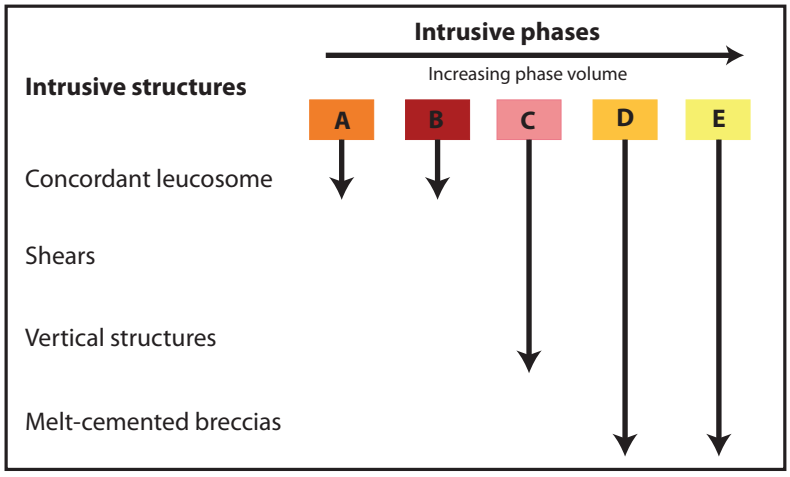

Figure 7.10: Occurrence and distribution of the various intrusive phases in different structures. (grey (A), red (B), pink and white (C), orange (D) and yellow (E)). A trend of increase in the number of intrusive structures with increasing phase volume is shown.

7.2.1 Stromatic / Concordant Leucosome

Stromatic or concordant leucosomes are oriented parallel to S_0/S_1, and are the most common intrusive structures within the metasediments. All intrusive phases occur as concordant leucosome on varying scales, and they exhibit sharp edges suggestive of injected leucosome. The early grey and red quartz-rich granitoids occur exclusively in these structures, with the grey quartz-rich granitoid forming 0.1–1 m-thick and 2–15 m long boudin trains parallel to the foliation in layered metapsammite. The red quartz-rich granitoid occurs in all metased-

iments, but is most prominent as a concordant, continuous, 0.5–1 m thick layer along the contact between layered and massive metapsammite (Figs. 7.2 and 7.3). The pink and white leucogranite occurs in thin (2–10 cm) bodies that are a few metres in length and almost exclusively developed in the layered metapsammite.

Larger and more prominent concordant leucosomes (>0.3 m) are typically composite and contain a combination of multiple intrusive phases. Orange leucogranite is the youngest and most abundant phase within them. These bodies are laterally continuous for tens of metres and are found within all rock types, but particularly within the layered metapsammite, and along contacts between different lithologies. The orientation for these structures fall in the range 040–080°/15–40°N, similar to the foliation that contains them (Fig. 7.7B).

7.2.2 Melt-filled Shears

Pre-existing, ductile shears with normal offset often contain planar leucogranite dykes, parallel to the shear surface. The leucogranite is usually in sharp contact with the surrounding metasediments, and occasionally contains small (1–5 cm) xenoliths of surrounding material. The dykes vary from several centimetres to 2–3 m thickness, and have lengths between 10 cm and 10–15 m. Grey and red quartz-rich granitoids are not found within shears, and pink and white leucogranites are only occasionally found in centimetre-scale shears (Fig. 7.10). Pink and white leucogranite in these structures is petrographically continuous with stromatic leucosome, but the structures are too small and rare to have formed an interconnected network.

Orange and yellow leucogranite are the main phases that occur as dykes within shear planes (Fig. 7.11A), although they are often composite and can contain two or more leucogranite generations usually as xenoliths of older phases. These structures tend to be connected to other leucogranite-bearing structures with petrographic continuity, indicating an interconnected network (Fig. 7.2 and 7.3). Leucogranite sheets within shear planes are most easily observed in the layered metapsammite, where they show a predominant orientation centered around 050°/45°N (Fig. 7.7D,E). A second, less predominant orientation is at 030°/30°SE. The dykes and shears in these orientations are observed as a conjugate shear pair in the field and are at approximately 100° (angle containing the downthrown block) to one other (Fig. 7.7D,E). The north-dipping and SE-dipping sets are 22° and 57° from S_0/S_1, respectively. Similar structures in massive metapsammitic units have the same, but slightly

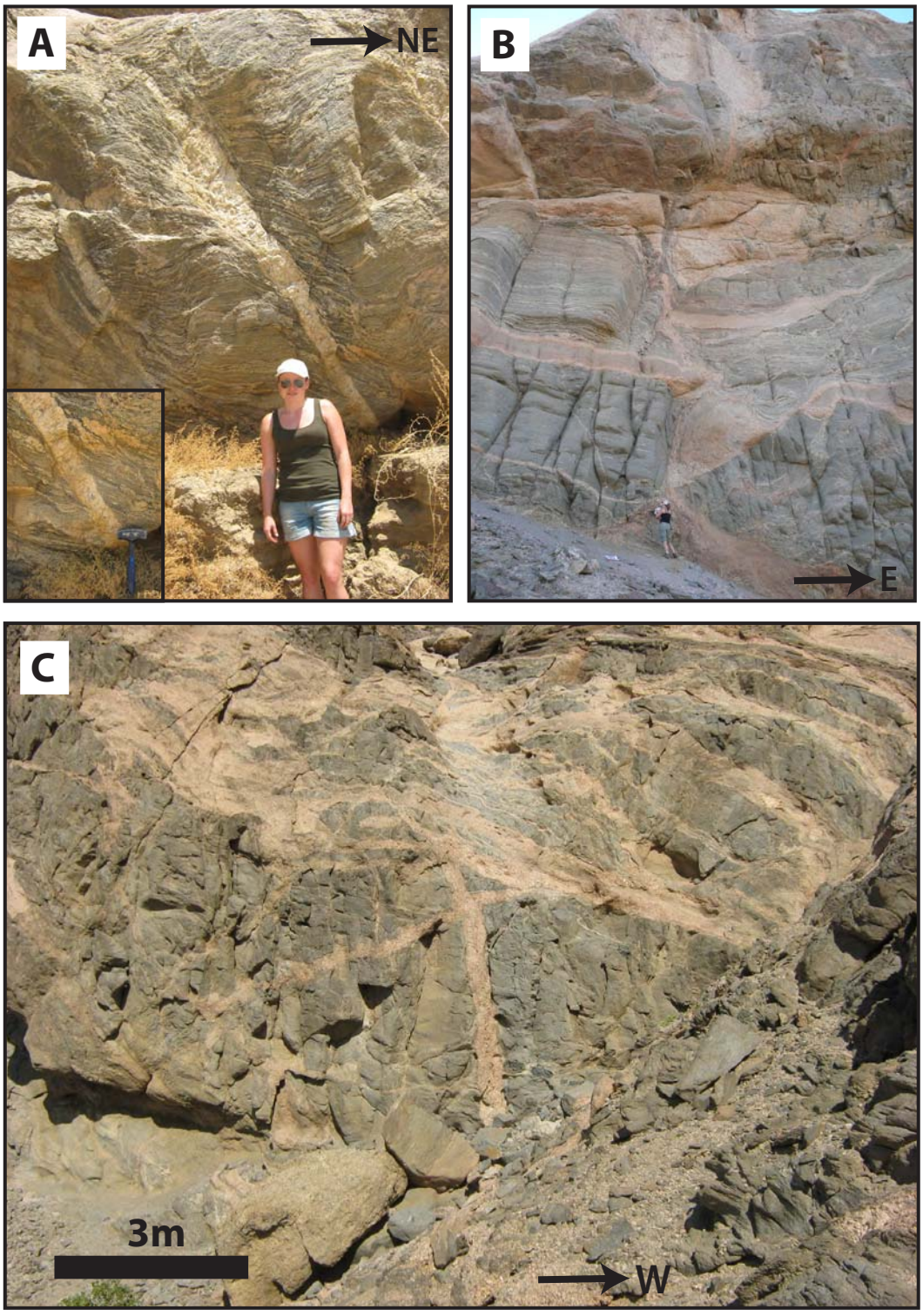

Figure 7.11: Leucogranite-filled shears. (A) A leucogranite sheet with dragged foliation on either side. Inset: Close-up photograph of the shear. (B) Large shear-bound structure on the south-facing cliff face that contains multiple leucogranite phases. (C) A set of conjugate leucogranite-filled shears in massive metapsammite.

steeper orientation (Fig. 7.11C). Along with the main conjugate set, less predominant sets of leucogranite-filled shears are oriented around 080–095°/50–55°N, with top-to-the-north displacement, and 105–115°/40–60°S, with top-to-the-south displacement (Fig. 7.7D,E). These shears are approximately 55–60° from one another (angle which contains the downthrown block) and the north-dipping set and south-dipping sets are 20–30°, and 70–85° from S_0/S_1, respectively (Fig. 7.7D,E).

7.2.3 Tensile Fractures

Leucogranite bodies that crosscut S_0/S_1 at a high angle are rare, and almost exclusively contain orange and yellow leucogranite (Fig. 7.12A,B). These structures are not composite and are best-developed in the massive metapsammite. They have sharp boundaries, have a steep to subvertical orientation, and do not show foliation drag that might indicate shearing along their edges. However, the foliation is sometimes symmetrically bent into these structures to suggest that they have collapsed and lost volume (Fig. 7.12A; Bons *et al.*, 2008). Their orientations fall within a range of 155–185°/85°E to 140–185°/50–85°W (Fig. 7.7F). Boudin necks with a similar orientation also occur within the calc-silicate, massive metapsammite, and very occasionally within the layered metapsammite (Fig. 7.12C). The vertical structures are often connected with concordant leucosome and more shallowly-oriented dykes within shear planes (Fig. 7.12C,D).

7.2.4 Pipes and Collapsed Breccias

Leucogranites also occur within subvertical, tube-like structures that are filled with leucogranite-cemented breccia (Fig. 7.13). Breccias consist of subangular blocks derived from the surrounding metasediments, but the planar and linear fabric orientations varies between blocks and is different from that in the intact supracrustal sequence, indicating that individual blocks have been rotated relative to each other (Fig. 7.13). Blocks sometimes have dragged foliation along their edges similar to dragged foliation along shears. The shape of individual blocks varies with rock type, and layered metapsammite blocks occur predominantly as diamond-shapes (Fig. 7.13B), whereas calc-silicate blocks are more rectangular, and the shape of massive metapsammite blocks is variable.

The size of the collapsed breccias is variable, from metre-sized pockets containing blocks as small as 10 cm in diameter that occur throughout the outcrop, to a 15–20 m wide

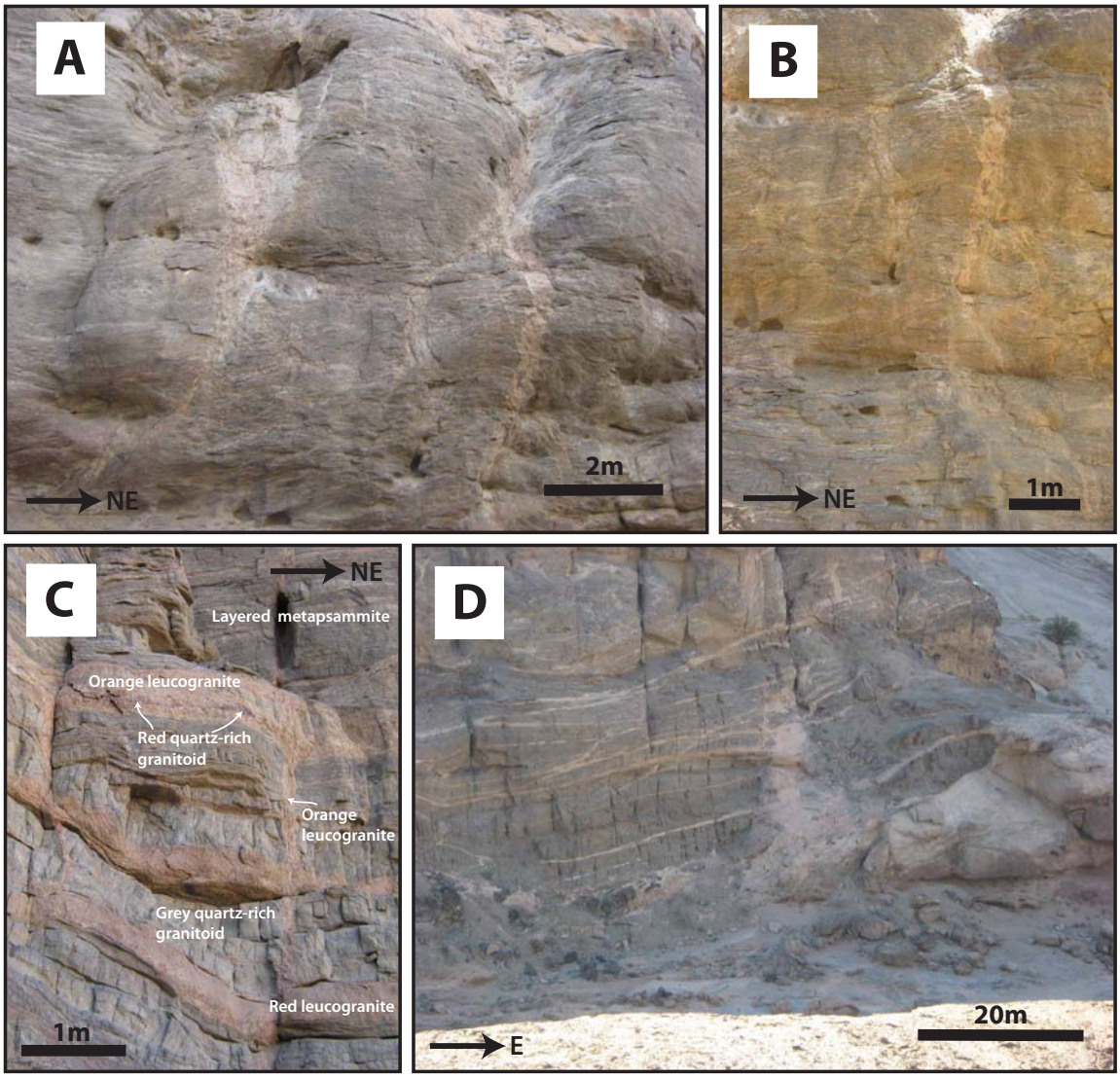

Figure 7.12: Melt-bearing tensile fractures. (A) and (B) show meso-scale vertical structures from the ESE face with the foliation deflecting into the structures. (C) Several vertical boudin necks containing orange leucogranite that are connected with orange leucogranite- and red quartz-rich granitoid-bearing concordant sheets that intrude layered metapsammite containing boudins of grey quartz-rich granitoid. (D) A large vertical structure that is petrographically continuous with several concordant sills.

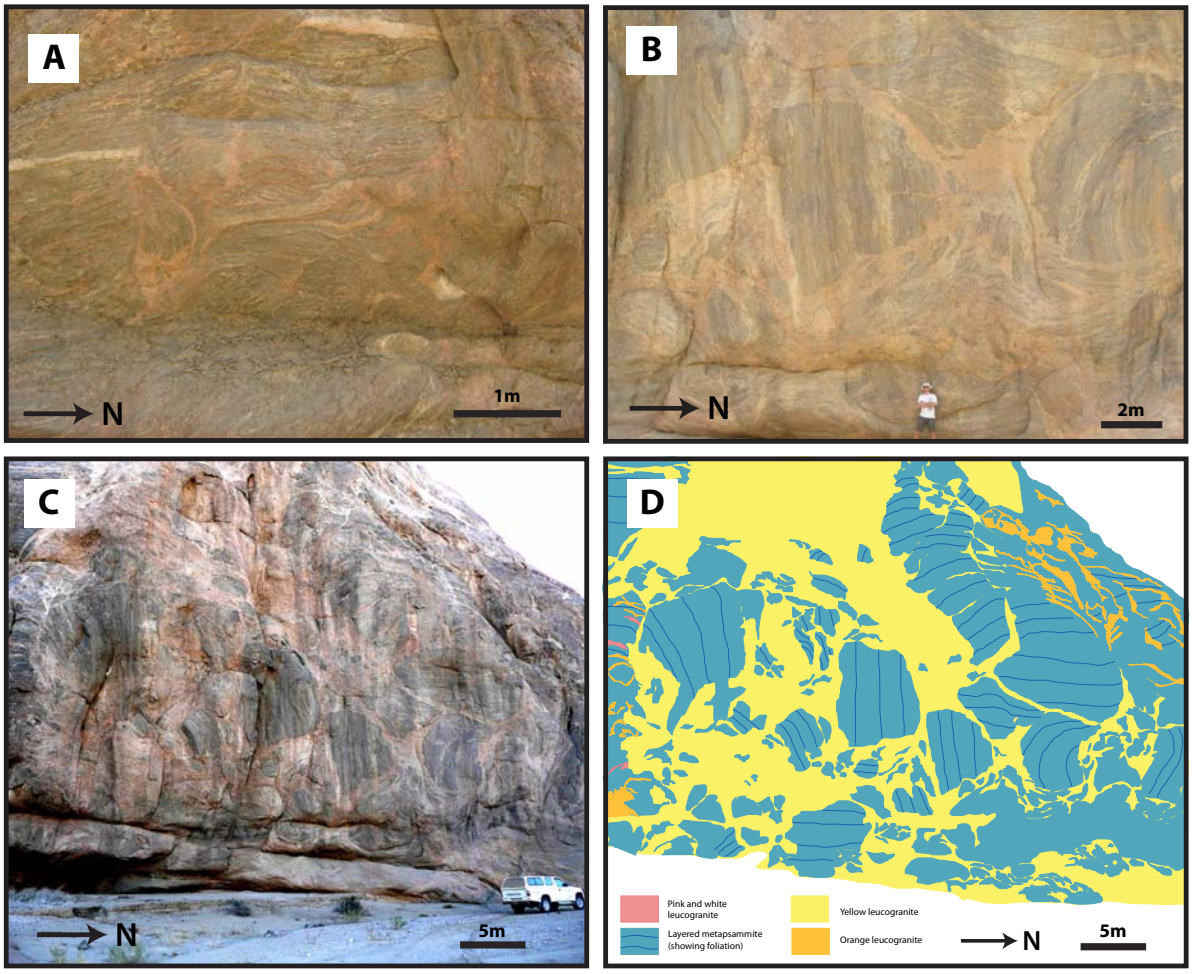

Figure 7.13: Leucogranite-cemented breccias. (A) Leucogranite-cemented breccia consisting of rotated blocks, but with a very low volume of interstitial leucogranite. (B) Leucogranite-cemented breccia with diamond-shaped rotated blocks and a higher volume of leucogranite. (C) The large breccia-filled structure in ESE-facing cliff. (D) A sketch map of (C). The black lines represent the foliation orientation in each block.

and 40–50 m high structure that contains blocks 1–15 m in diameter (Fig. 7.13C). The latter structure dominates the ESE-facing cliff (Fig. 7.2). Two other large-scale examples of these structures occur on the S-facing section (Fig. 7.3). The ratio of leucogranite to metasedimentary blocks varies between breccias, but breccias are dominantly clast-supported (Fig. 7.13A). Larger structures have a higher proportion of leucogranite than smaller structures, with leucogranite to metasediment ratios of 30–40:60–70 for larger structures compared to leucogranite to metasediment ratios of 10–20:80–90 for smaller structures. The predominant cementing phase in large structures is yellow leucogranite, whereas smaller breccia pockets contain only orange leucogranite. Older intrusive phases can be found as xenoliths within the leucogranite-cemented breccias.

7.2.5 Large Concordant Sheets

Two thick, approximately foliation-parallel continuous leucogranite sheets occur at the basal contact and near the top of the metasedimentary package. The basal sheet is 0–5 m thick and developed in the calc-silicate unit. It consists of orange and yellow leucogranite phases and contains isolated rotated prismatic blocks and boudins of calc-silicate. The sheet varies greatly in thickness along its length, and is bounded below by Abbabis Gneiss basement rocks and above by a layer of massive metapsammite (Fig. 7.3). The sheets at the bottom and top of the cliff are connected by the leucogranite networks which pervade the outcrop as well as the main leucogranite-cemented breccia on the ESE-facing cliff face, and the two large-scale vertical structures on the S-facing face. The concordant sheet at the base of the metasediments is thinner relative to elsewhere along its length when it is close to these vertical structures.

The sheet at the top of the outcrop (Fig. 7.14A) has a variable thickness of 5 –15 m and extends across the whole of the south-facing cliff (Fig. 7.3). It occurs in hornblende-metapsammite, and is bounded by a thick layer of massive metapsammite at its base. The sheet contains 2–4 m thick, 10–40 m long rafts of hornblende metapsammite that have not experienced any apparent rotation. It also contains smaller rafts, less than a metre long, which show rotated foliations. This sheet is composite (Fig. 7.14B) and contains all five intrusive phases, although it is composed predominantly of yellow and orange leucogranite (>50%), with early intrusive phases present as isolated blocks within younger leucogranite. The large sheet is connected to a vertical pipe that contains leucogranite-cemented breccia,

and has a depressed basal contact and greater thickness near the pipe (Figs. 7.3, 7.14A).

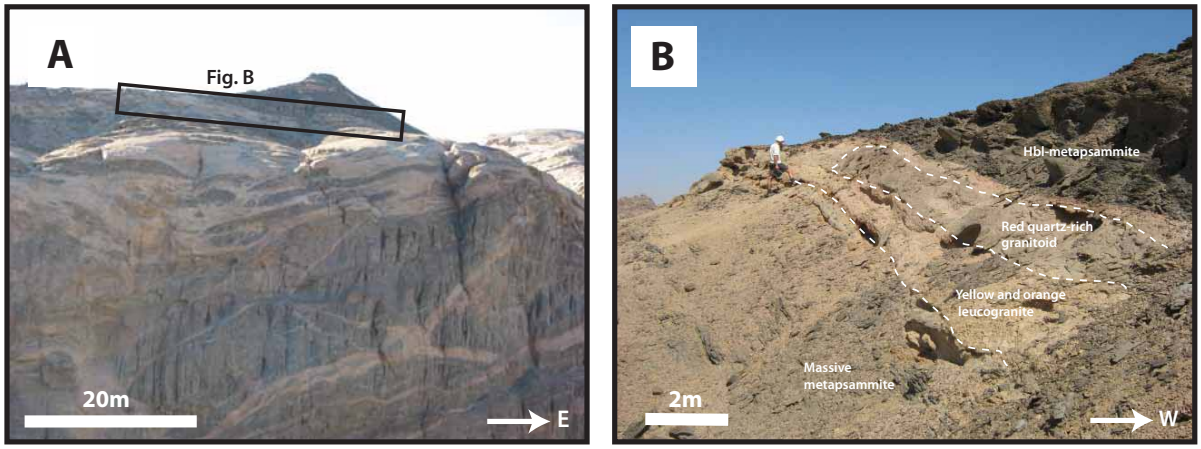

Figure 7.14: Photographs of the large concordant sheet at the top of the outcrop. (A) Thick concordant sheet which consists of leucogranite interspersed with parallel elongate rafts of metasediment (B) Composite sill of red quartz-rich granitoid and orange and yellow leucogranite that comprises the uppermost sheet shown by the black box in (A).

7.3 Structural analysis

The intensity of the penetrative foliation, compared to a relatively weakly-developed lineation suggests that the metasedimentary package predominantly experienced flattening, suggestive of close to coaxial strain, such that $X \approx Y > Z$. The shallowly NNE-plunging orientation of the weak lineation is consistent with the typical NE-SW-directed D_2 stretching seen elsewhere in the area. Assuming that S_1 and L_1 formed concurrently, the strain axes XYZ can be resolved, as shown on Figure 7.7A.

The orientations of the normal ductile shear set show apparent extension approximately NE–SW, which is consistent with the orientation of apparent extension shown by X if X>Y. The 80–95° angle between them is consistent with their origin as a conjugate shear pair in ductile rocks (Von Mises criterion for failure in ductile rocks in Twiss & Moores, 1992, p. 175). The orientations of the leucogranite-filled shears are more variable, and their orientations are more consistent with either extension in both X and Y directions (Fig. 7.16, suggesting that either both X and Y represent extension and $X \approx Y$ when they formed, or that considerable rotation of some leucogranite-filled shears has taken place since their formation. The main conjugate set that includes NW and SE-dipping shears (Set 1; Fig reffig:stereonetsE) shows

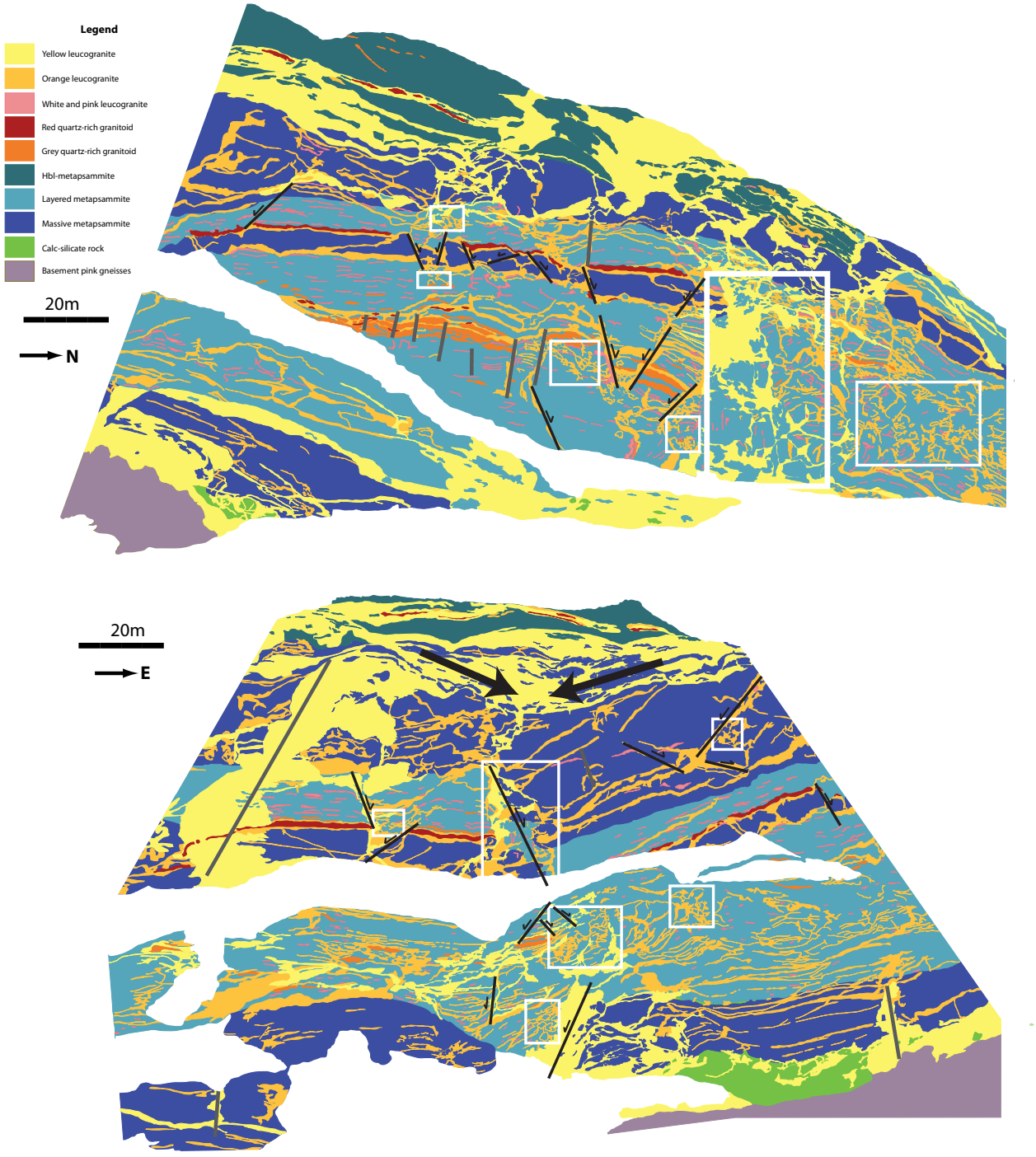

Figure 7.15: Cliff face maps for the ESE-outcrop (top) and the S-facing outcrop (bottom) showing the position of various intrusive structures. The thick grey lines denote sub-vertical structures, the black lines with arrows show shears and their normal offset, and white blocks are leucogranite-cemented breccias exhibiting block rotation. The thick black arrows show the downward collapse of the metasediments to accommodate melt in a process of mass transfer during compaction.

apparent extension approximately parallel to Y, and the subordinate sets with NNE and SSW-dipping shears (Set 2; Fig 7.7E) suggest apparent N–S to NE–SW extension which is closer to the orientations of the melt-free shears, and is more consistent with the position of X shown by the lineation.

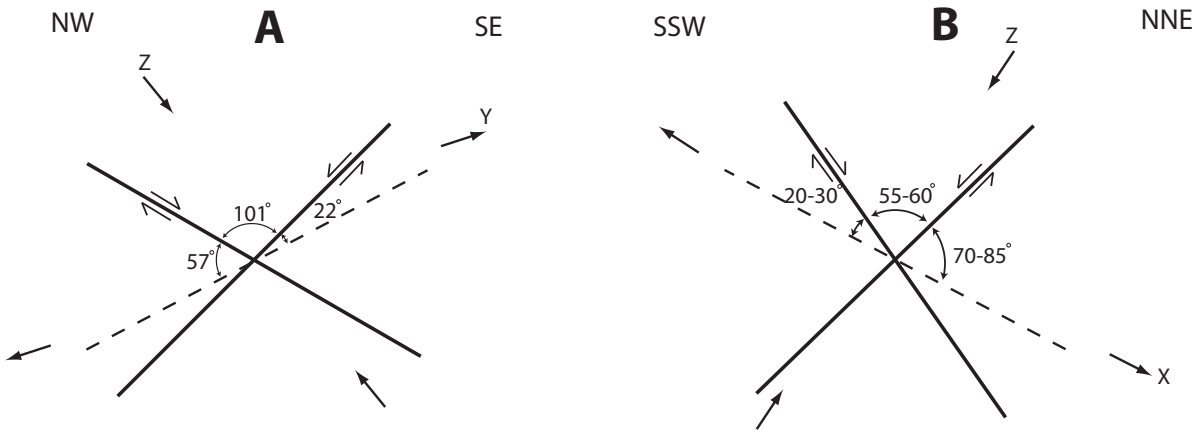

Figure 7.16: Simplified 2D sketches of the leucogranite-filled shears and their relationships to S_0/S_1. (A) Shows a simplified cross section parallel to the Y-Z plane of leucogranite-filled conjugate shear set 1 and its relationship with S_0/S_1, including Y and Z. (B) Shows a simplified cross section parallel to the X-Z plane of leucogranite-filled conjugate shear set 2 and its relationship with S_0/S_1, including X and Z.

Conjugate shears are predicted to form 45° from the plane of maximum flattening, which is approximated here to S_0/S_1. The non-melt filled shears adhere to this relationship most closely (Fig. 7.9), suggesting that they have experienced less re-orientation than the leucogranite-filled shears, and are therefore younger. Both leucogranite-filled conjugate shear sets show slightly more re-orientation away from this original relationship, and the rotation is consistent with the orientation of the strain axes (Fig. 7.16).

7.4 Melt Migration

The connectivity of the intrusive networks suggests that they are former melt pathways that connected areas of melt depletion and accumulation (Fig. 7.15). The lack of anatexis in the metasediments, and the sharp boundaries of intrusive bodies shows that all melt within the country rocks is injected. The composite nature of many structures suggests that they acted as conduits for multiple melt phases, and were likely active over a protracted period of time.

The general absence of biotite reaction rims between different intrusive phases and lack of chilled margins show that the melt phases were of similar composition and that the system remained close to the solidus while the different melt phases were injected. The presence of different intrusive phases in the same structures also suggests a long-lived and fairly constant strain regime.

The occurrence of the early intrusive phases as stromatic leucosome suggests that foliation-concordant migration is the easiest movement path for low volumes of melt. The presence of only younger phases within shear zones and vertical structures shows that at least a moderate volume of melt is required to utilize such structures, and implies that melt volume plays a role in the ability of melt to exploit discordant structures. The presence of only the highest volume intrusive phases within leucogranite-cemented breccias suggests that a large melt volume and high melt proportions is required for these to form.

The rotation of the blocks which are surrounded by leucogranite volumes too low to explain the amount of rotation they display suggests that many of these structures have lost melt before they solidified, showing that they represent effective melt-migration structures. The presence of dragged foliation and rotated blocks, together with the shape of the blocks, is consistent with the model for the formation of the leucogranite-cemented breccias described in chapter 5. The higher proportion of leucogranite within the large scale leucogranite-cemented breccia pipe on the ESE-facing cliff face (Fig. 7.15) suggests that it is in an earlier stage of collapse and has lost less melt than many of the other breccias that have lower leucogranite to metasediment ratios.

The presence of multiple intrusive phases, and the correlation between relative age of the phases and increasing degree of deformation of the various sills and dykes shows that intrusion and crystallization of each phase occurred over a protracted period of time and as the metasediment package experienced progressive deformation. The parallel alignment to S_0/S_1 of minerals within the older intrusive phases, and the chocolate-tablet boudinage of these phases is consistent with the overall coaxial strain experienced by the metasediment package. Evidence for localised shearing along shears after melt intrusion but before solidification, such as alignment of leucogranite minerals, is not present. Since younger meltless shears exist, deformation is assumed to have continued after melt presence. This is in contrast with observations of shear-zone hosted melt which usually creates weakness and localizes shearing (e.g. Davidson *et al.*, 1994), and suggests that the shear zone-hosted leucogranites crystallized fairly quickly.

Figure 7.17 shows a block diagram model describing the stepwise deformation and upward migration of progressively increasing melt volumes into and across the metasediment package. As melt migration begins, the low melt volumes and low melt pressure restrict the melt to planes of pre-existing weakness. These surfaces are predominantly bedding and foliation planes, therefore intrusive phases are predominantly stromatic (Fig. 7.17A,B). Melt in these structures crystallises to create relatively impermeable layers that have a large competency contrast with the metasediments, the contacts of which provide weak sites for later melt intrusion.

As melt volume increases, the melt can utilise additional dilational structures such as extensional shears, boudin necks (particularly in relative competent layers) and tensile fractures that form to accommodate the strain and increasing melt pressure in the progressively compacting metasediment package. These melt-filled structures are the first that allow the formation of an interconnected network. As deformation continues leucogranite-bearing structures become more abundant and interconnected and the network forms a pathway between the accumulation site along the basement-metasediment contact at the bottom to the sink/emplacement site at the top thereby drastically increasing the permeability of the metasediments and allowing for a slow emplacement of leucogranite near the top of the package. This step is represented by the orange melt phase in the outcrop (Fig. 7.17C). The figure shows the arrest of melt flow beneath a between two metasediment layers. It is speculative why the melt arrests along this interface, but is likely due to rheological contrast between the weak mica-rich schist layer above it (the top-most layer of the package - the cap layer), and the strong mica-poor metapsammite layer below it.

The presence of the youngest melt phase (yellow leucogranite) almost exclusively within vertical structures, which include dismembered older phases and rotated metasediment blocks, suggests that this phase did not migrate pervasively through the package as previous phases did. The similarity of the leucogranite-cemented breccias to hydraulic breccias, with their angular and rotated blocks, suggest that melt movement was driven by increase in melt pressure followed by a catastrophic pressure drop and implosion of metasediment blocks. The increased melt pressure drives propagation of the structures and dilation of the network so that a singular vertical migration structure containing suspended metasediment blocks forms (shown schematically on Figure 7.17D).

The increased ability for melt to move upwards due to greater connectivity, combined with the compacting force, increases the rate of melt movement through the structure upwards

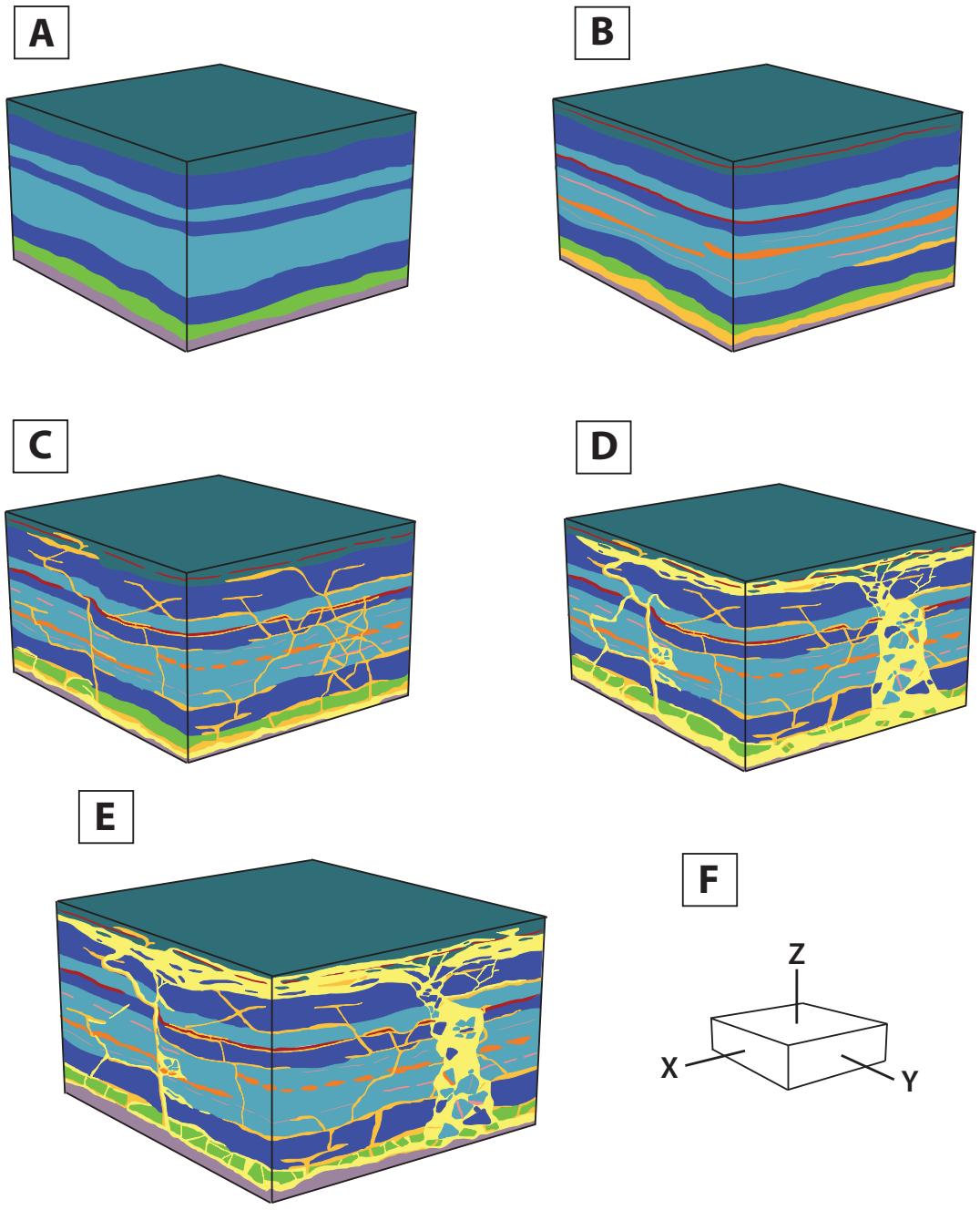

Figure 7.17: Block diagram model for melt migration across an actively compacting metasedimentary package showing migration of progressively larger volumes of melt through the metasediment (A–E). (F) shows the strain axes which are constant for each block in A–E. X $\approx$ Y $>$ Z. Note that Z-axis has been rotated to vertical for the sake of ease of representation of a flattening block.

into the metasediments above where it emplaces. Melt is also displaced upwards by sinking and compaction of metasedimentary blocks , as evidenced by the predominance of rotated blocks near the bottom of the breccia. Similar features were observed by Kisters *et al.* (1998) in breccia segregation structures where blocks of country rocks within breccia pipes were displaced downwards by several hundred metres, and were similarly interpreted to represent upwards melt movement.

If there is no melt supply from below, the melt pressure in the structure is not maintained and the structure collapses (Fig. 7.17E). Evidence for upward migration of melt, coupled to the downwards compaction of country rocks, is well-demonstrated on the south-facing cliff. The displacement of metasediment layers downward, together with the inflated concordant leucogranite sheet at the top of the cliff face and the deflated concordant sheet at the bottom of the cliff face is evidence of the mass transfer whereby melt moves upwards and metasediments move downwards (Fig. 7.15).

Chapter 8

Discussion

8.1 Controls on the Formation of Melt Channels

Processes of melt migration and ascent require the temporary creation of space within the crust to accommodate melt volumes. Unlike basaltic magma, which has a low viscosity and is hot enough to forge its own way upwards through crustal rocks (McLeod & Tait, 1999), felsic melt requires the presence of pre-existing weaknesses and local dilational sites within the crust, together with the concurrently-created pressure gradients in order to migrate. Observations that the distribution of intrusive phases, particularly leucogranite, and particularly during segregation and early migration, is related to structures and tectonic fabrics suggests that regional deformation plays a major role in providing pathways for melt migration (Brown & Solar, 1998a; Vanderhaeghe, 1999; Sawyer, 2001). There are, however less studies that focus on the smaller-scale, local strain regimes that form as a result of regional deformation, and the mechanisms behind migration through subsolidus rocks. These smaller-scale strain regimes, such as the variation in strain documented over this field area, determine the type of meso-scale structures that melt will exploit to form pervasive networks, and are arguably more important to the specific mechanics of melt ascent than overall large-scale regimes.

Similarly, the driving forces of melt movement are scale-dependent. The main force attributed to driving melt ascent is buoyancy created by the density difference between melt and the surrounding crustal rocks (Pitcher, 1979; Vanderhaeghe, 1999). Whereas it is accepted that buoyancy is the driver for melt ascent on a crustal scale, it has been argued that local pressure and hydraulic gradients formed during ongoing deformation dictate melt movement on the scale of specific melt-bearing networks (Brown, 1994; Brown & Solar, 1998a; Sawyer,

2001). Deformation can create these gradients because it is constantly creating new sites of relatively low and high pressure. Melt responds to these gradients by being pulled into, and accumulated at, sites of low pressure and being pushed out of, and extracted from, sites of high pressure. During ongoing deformation these high and low pressure sites are transient, and in this way continued melt movement is driven by, and requires, progressive deformation. This pushing and pulling of melt via pressure gradients is well described for melt segregation and initial melt movement mechanisms in anatectic rocks (Sawyer, 2001; Brown, 2007; Vanderhaeghe, 2009) but less well documented for melt migration through subsolidus rocks.

Rates of melt migration are typically difficult to quantify because estimates of time scales rely on modelling. Analogue modeling (e.g. Bons *et al.*, 2001; Barraud *et al.*, 2004; Druguet & Carreras, 2006) can be effective at demonstrating the nature and style of mechanisms, but cannot be used for estimating time scales because we cannot exactly replicate the complex systems that control melt migration, and the materials used for experiments have rheologies that deform on a human time-scale that are impossible to relate to geological-time due to scale distortion. Numerical modeling is another method used to estimate time-scales for melt migration, however, it is limited because it is theory-based, and requires inherent assumptions about melt migration processes such as a constant connectivity between source and sink, so that the rate limit is melt viscosity (e.g. Clemens, 1998). Similarly, the geometry of melt structures and networks is oversimplified, so that their effect is distorted (e.g. Weinberg, 1999). Consequently, the range of estimates span several orders of magnitude depending on the style of migration (dyking vs. diapirism vs. pervasive migration), which suggests that the mechanisms and the rates of each step in the process, particularly migration through the crust, need to be better understood before the rate of melt movement can be adequately quantified. If melt migration occurs through pervasive networks that form during ongoing deformation, similar to those observed in anatectic migmatite terrains, and melt is driven by pressure gradients created by those structures, then melt migration should occur at rates similar to the tectonic deformation rate. Previous chapters have documented various examples of the types of networks that melt exploits for migration on a meso- to large-scale, including the internal structures that create the networks, and the strain regimes in which they form (Table 8.1). Each outcrop exhibits a specific combination of local strain style and intensity, combinations of rock types, and variable intrusive phase volumes. Each of these variables, and different combinations of them, ultimately control the geometry of each melt network, with different dominant structures forming in response to the variables (Table 8.1).

Chapter	Outcrop	Outcrop Dimensions	Melt Volume	Strain Type	Strain Intensity	Strain Orientation	Rheological Contrasts	Melt batches	Network Connectivity	Net Melt Movement Direction
Ch. 3	Birkenfels	70 m × 15 m	Very low	Flattening	Low to medium	NW-SE shortening (Steep S_0/S_1)	Low	3	Low	Vertical (concordant)
Ch. 3	Swakop Pavement	50 m × 30 m	Very low	Constriction	Medium to high	NE elongation (Shallow L_1)	Low	2	High	Indistinct (concordant & discordant)
Ch. 4	Calc-silicate Outcrop	85 m × 50 m	High	Flattening	High	NW-SE shortening (Steep S_0/S_1)	High	5	High	Lateral (concordant & discordant)
Ch. 5	Etusis Pavement	30 m × 15 m	High	Plane strain	Very high	NE elongation, sub-vertical shortening (Shallow S_0/S_1)	Medium	5	Medium	Lateral (mainly concordant)
Ch. 5	High Strain Cliff	40 m × 15 m	High	Plane strain	Very high	NE elongation, sub-vertical shortening (Shallow S_0/S_1)	Low	2	High	Vertical (phase 1; discordant) & Lateral (phase 2; concordant)
Ch. 6	Fold core	400 m × 140 m	Medium	Constriction	Medium to low	NE elongation (Shallow L_1)	Low	2	Medium	Vertical (discordant)
Ch. 6	Fold limbs	200-350 m × 100-200 m	Low	Flattening	Low	NW-SE shortening (Steep S_0/S_1)	Low	2	Low	Vertical (concordant)
Ch. 7	Metasediment package	150 m × 110 m × 80 m	High	Flattening	High	Vertical shortening (Shallow S_0/S_1)	Medium to high	5	High	Vertical (mainly discordant)

Table 8.1: Table summarising and comparing the key features of each studied outcrop.

The effect and relative importance of these variables is different for each outcrop, and shows that there is no one criterion that controls the process. Rather, it suggests that migration is achieved by melt exploiting whichever structures are most accommodating in terms of the weakness of the structure and the local hydraulic gradients. These structures are not only controlled by deformation, but also by rheological contrasts between different lithologies, as well as the volume of melt present.

8.1.1 Rheological contrasts

The rheological contrasts displayed in several outcrops (Table 8.1) show that relatively competent lithologies are preferential sites of melt accumulation on various scales, such as the calc-silicate layers in chapters 4 and 7. Consequently, outcrops with high rheological contrasts tend to preserve larger volumes of intrusive phases (Table 8.1). Kisters *et al.* (1998); Brown & Solar (1999) have shown that in anatectic migmatites, melt preferentially segregates into more competent rock units, because competency contrasts allow for preferential brittle fracturing in the more competent layers, thereby allowing them to be sites of relatively low pressure.

In the subsolidus rocks we observe that melt tends to accumulate in the competent layers and similarly attribute it to strain partitioning around the competent layers where less competent lithologies respond to deformation by flowing viscously, while more competent lithologies fracture, creating dilatant sites such as interboudin spaces, tensile fractures or extensional shear fractures (Twiss & Moores, 1992, p. 37, 284, 361–363,).

The calc-silicate outcrop discussed in chapter 4 represents an example of migration together with emplacement, and shows the effectiveness of boudin neck structures at creating dilatant sites which form either discordant conduits on a mesoscale, or sites of emplacement on a large scale. These are similar to melt-filled boudin necks described by other workers in anatectic migmatites (Sawyer, 2001; Vanderhaeghe, 2009; Kisters *et al.*, 2009), and are likely created by similar mechanisms as described above. Here the competency contrast between different lithological layers, combined with progressive flattening strain, allows for the formation of chocolate-tablet boudins, and governs the geometry of the melt networks.

The calc-silicate units tends to create sites of melt emplacement, suggesting that the local dilation forces are stronger than melt buoyancy forces, and can overcome these forces for long enough to allow melt to crystallise. However, competent units that exhibit a lower relative

competency contrast, such as the calc-silicate-bearing metapsammite in the Etusis Pavement (Chapter 5) or the massive metapsammite in the ideal crustal section (Chapter 7) appear to facilitate melt migration and transfer rather than emplacement. This would suggest that the local dilation force is not strong enough to permanently overcome melt buoyancy. Therefore, it appears that the relative competency contrast in a heterogeneous sequence can influence the strength of the local hydraulic gradient, ultimately determining whether melt utilises the permeability of the competent layers to migrate through, or be emplaced into, these rocks.

8.1.2 Strain regime and intensity

Table 8.1 shows that the strain type and its intensity play a large role in the style of network that will develop, as well as its effectiveness. The Birkenfels and Swakop River outcrops (Chapter 3) and the Fold Hinge outcrop (Chapter 6) show that melt segregation and initial migration within homogenous rocks is achieved through a mesoscale interconnected network of foliation-parallel leucosome and melt-bearing extensional shears. This kind of network and the presence of segregated leucosome in such structures in other anatectic migmatite terrains is well described, and the observations in this thesis agree with observations of segregating melt along foliation planes and within low pressure structures such as shear planes (Sawyer, 2001; Vanderhaeghe, 2009). In both chapters the dominant variable that controls the geometry of melt migration is the style, orientation and intensity of the strain regime, and how these parameters might locally fluctuate. The spatial fluctuation of the strain intensity in both the Birkenfels and Fold Hinge outcrops shows that networks form more readily in areas that experience slightly higher relative strain.

Relationships observed from table 8.1 show that purely constrictional strain regimes tend to preserve lower volume melt migration, while flattening strain and plane strain regimes preserve more variable volumes. This could either be evidence for highly effective melt migration being accommodated through areas experiencing constrictional strain, resulting in low preservation, or inability of rocks undergoing constrictional strain to accommodate melt migration. Low number of preserved melt batches in constrictional strain outcrops is suggestive of the latter.

Table 8.1 also shows that the highest preserved melt volumes are associated with the outcrops that show the highest relative strain, evidenced by larger and more abundant structures. In addition, outcrops that have a shallowly-dipping planar fabric can exhibit net melt

movement in either lateral (concordant) or vertical (discordant) directions. Outcrops with a steep planar fabric tend to show more predominant vertical melt migration (concordant), with the exception of the calc-silicate outcrop (Chapter 4), where movement is towards the boudin neck emplacement sites.

The formation of a foliation plays an important role in providing initial weak planes along which low volumes of melt can localise, which is in accordance with observations of foliation parallel segregated melt in anatectic migmatites (Vanderhaeghe, 1999; Sawyer, 2001; Marchildon & Brown, 2003). Within subsolidus rocks foliation planes provided planes of weakness that preferentially fracture allowing intrusion of melt along them. Progressive strain is also accommodated by structures such as ductile shears, which introduces strong heterogeneities in the rock strength, and provides variably oriented features that ultimately allow melt channels to intersect and form networks. The intensity of the strain regime is important because higher strain is accommodated by a larger number of structures, thus increasing the permeability of the network by increasing the number and connectivity of structures that melt can exploit.

The ability of a strain regime to create an effective melt migration network lies in its ability to create dilatant structures. Constrictional strain involves unidirectional extension and multidirectional contraction, and thus creates overall dilation in one direction. Flattening strain is composed of unidirectional contraction and multidirectional extension, and thus has a greater capacity to create dilatant structures. It follows that flattening strain regimes are therefore more capable at creating space for melt to migrate.

The fold in chapter 6 has a spatially-variable strain regime, allowing for the comparison of networks styles developed in the same rocks under a changing strain regime. It showed that the strain style and orientation plays a large role in the effectiveness of local melt migration within the fold because the intensity and orientation and type of strain regime have direct influence over the creation and locality of dilational sites, their orientation, and thus their ability to increase permeability with connectivity of structures. The presence of axial planar dykes suggests that such local strain variations can allow for dilational structures to form perpendicular to an axis of shortening in the fold hinge. Such relative variability is likely capable of creating enough dilation to allow effective melt migration, even in overall compressional settings.

8.1.3 Melt Volume

Melt volume plays an important role in the development of melt networks through melt embrittlement (see below) to create channelised melt flow in brittle structures. Table 8.1 shows that higher melt volumes are usually associated with a greater connectivity of melt-bearing structures.

Within anatectic migmatites, melt volumes are variable, but controlled by melting within the wallrocks (Marchildon & Brown, 2003). The volume of melt during melt migration through subsolidus crust is controlled by the melt supply from lower stratigraphic levels and the permeability of the rocks. In anatectic migmatites increased melt volumes also have a feedback relationship with deformation, whereby higher strain leads to localization of melt due to the production of more potential melt-bearing structures, and the increased melt volume leads to weakening which further localises deformation and results in higher strain (Brown & Solar, 1998b). The subsolidus outcrops in the high strain zone (Chapter 5) specifically show high volume migration through strongly deforming rocks, and illustrates the relationship between the dominant strain regime and the volume of melt.

The presence of collapsed, melt-cemented breccias in the high-strain cliff (Chapter 5) and idealised crustal section (Chapter 7) indicates that high volumes of melt and melt overpressure can create its own melt pathways and networks, showing that melt can play an active role in the migration process.

Arguably, one of the main roles that high melt volumes play in melt migration through subsolidus rocks, is the creation of sufficiently high melt pressures for melt embrittlement, a process which also occurs in anatectic migmatites (Brown & Solar, 1998a). Despite the variation in strain regime at different outcrops, and the predominance of different structures, the brittle nature of many melt-bearing structures in most outcrops is a recurring theme. These outcrops all show evidence of features such as tensile fractures and melt-cemented breccias that form through brittle failure, which, along with the channelised nature of the leucogranites within extensional shears, suggest that brittle deformation mechanisms occur concurrent with ongoing ductile deformation during melt migration in order to faciliate the formation of channelised melt networks which make the rocks permeable.

8.2 Melt Embrittlement

The combination of concurrently-formed ductile and brittle-looking structures in the study area suggests that both brittle and viscous deformation mechanisms operated during melt migration, but that the melt migration was facilitated mainly by brittle failure which forms channelised melt pathways. The tensile fractures and extensional shear-hosted planar dykes specifically require brittle deformation mechanisms (Fig. 8.1), whereas the concurrent ductile shears, which do not show evidence of cataclastic flow, are suggestive of more plastic deformation mechanisms. However, the sharp-boundaried shear plane parallel dykes, and foliation parallel sills also require brittle mechanisms. The peak metamorphic temperature of ∼750 °C (Ward *et al.*, 2008) experienced by these rocks is well above the normal temperature required by the quartz flow law for plastic deformation mechanisms in quartz (200–400 °C; Gleason & Tullis, 1995), and many of the structures in these rocks, such as the penetrative tectonic foliation and lineation fabrics, attest to these high temperatures.

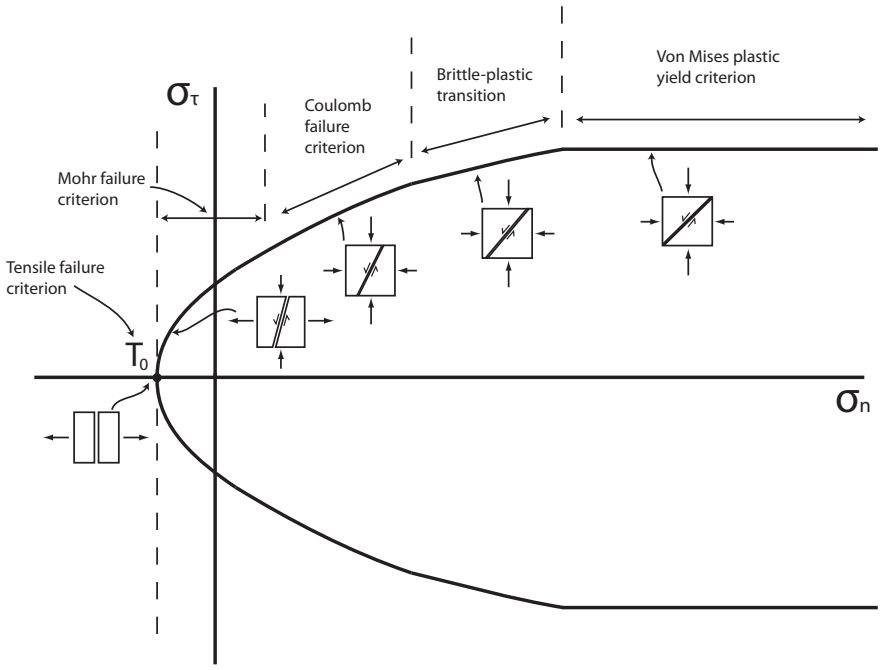

Figure 8.1: Schematic diagram of failure envelopes and related fractures showing shallowing of the dip of fractures with increasing σ_n. At a negative σ_n tensile or transitional tensile fractures form (within tensile failure criterion). Within the Coulomb failure criterion steep brittle fractures form. Less steep shear failure occurs within the brittle-plastic transition, and 45°-dipping ductile shears form within the Von Mises plastic failure criterion.

Embrittlement of high-temperature and high-pressure rocks can be achieved by an increase in strain rate or an increase in fluid pressure. In the mid- and lower-crust, the fluid pressure is likely to be close to lithostatic (i.e. P_{H_2O} is close to P_{Total}) (Fyfe *et al.*, 1978), and fluid pressure oscillates about the lithostatic because of compaction processes due to fluctuations in fluid saturation (Connolly, 1997). As melt movement by definition requires the presence of a fluid phase, it is likely that the rocks have experienced embrittlement caused by fluctuations in melt pressure. This occurs when melt pressure increases to equal lithostatic pressure and causes a drop in differential stress (Davidson *et al.*, 1994; Brown & Solar, 1998a). Melt pressure increases during accummulation when the melt cannot escape from a rock at the same rate as it is being introduced. This suggests that prior to melt embrittlement the permeability of the rock is low due to a lack of channelised melt escape pathways and networks, which require embrittlement (and thus high melt pressures) to form.

Figure 8.2 shows a schematic diagram with the maximum sustainable differential stress plotted against the depth of the crust. The intersection of Byerlee's Law (the brittle strength curve for the crust) and the Quartz Flow Law (the plastic strength curve for the crust) is often referred to as the brittle–ductile transition. However, the use of "ductile" is ambiguous because it describes mesoscopically continuous deformation which, although suggestive of plastic deformation mechanisms, can also involve brittle mechanisms such as cataclastic flow. Here, this transition is referred to as the brittle–plastic transition, and the use of the term "ductile" in this thesis is purely descriptive.

The position and shape of the plastic strength curve is dependent on composition, strain rate, and the temperature gradient in the crust and remains unchanged as melt pressure changes (Fig. 8.2). However, the position of the brittle strength curve is mostly dependent on the lithostatic pressure gradient and fluid pressure, and so it is sensitive to fluctuations in melt pressure (Davidson *et al.*, 1994; Gleason & Tullis, 1995; Brown & Solar, 1998a). With an increase in melt pressure the gradient of the brittle strength curve steepens and it intersects the plastic curve at greater depths (Fig. 8.2). The result of this is that the brittle–plastic transition is displaced to greater depths, thereby allowing for brittle deformation deeper in the crust, at conditions where deformation would normally be plastic (Fig. 8.2).

Fluctuations in melt pressure would cause the brittle–plastic transition to cyclically change position in a process where melt would build up and cause embrittlement. Sites that would fracture most readily are sites of relative weakness such as shear planes (Fig. 8.3). Tensile fractures can also form perpendicular to the maximum extension (Fig. 8.3). The melt

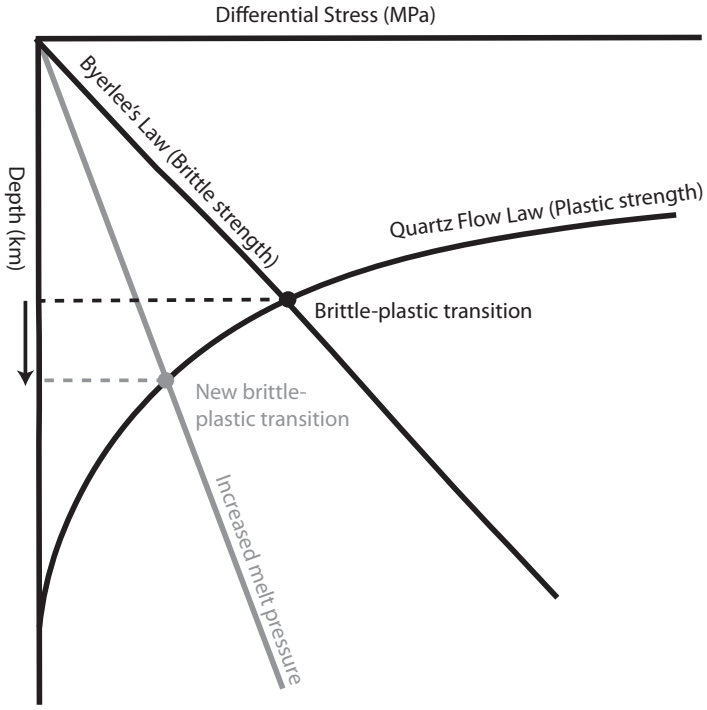

Figure 8.2: Schematic diagram showing maximum differential strength vs. depth for the crust, after Byerlee (1968). Deformation in the upper crust is dominated by brittle mechanisms governed by Byerlee's Law (brittle strength curve), and deformation in the lower crust is plastic and controlled by the Quartz Flow Law. When fluid pressure increases, differential stress decreases, and the brittle strength curve gets steeper, thereby intersecting the Quartz Flow Law at deeper crustal levels, and moving the brittle–plastic transition to a greater depth.

can then migrate away from high pressure sites via the newly-opened dilational structures. Provided that there is a constant melt supply, the fractures would remain open, otherwise fractures would close due to loss in melt pressure, and the whole process would repeat itself. During periods when the melt pressure is lower than lithostatic, which would be the predominant state of the system, plastic deformation mechanisms would predominate. This suggests that melt migration consists of multiple melt buildup and melt loss events which is consistent with the observation of multiple melt phases in most outcrops (Chapters 4, 5, and 7).

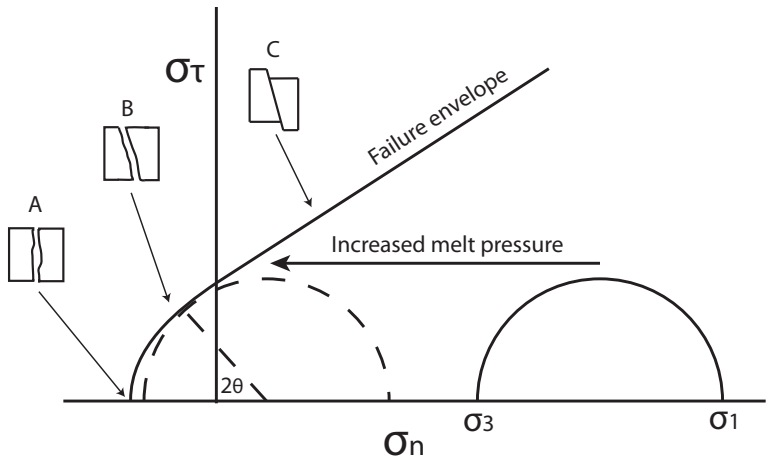

Figure 8.3: Mohr diagram showing a model for melt-enhanced embrittlement, after Davidson *et al.* (1994). As melt pressure increases there is a drop in effective normal stress and eventually the melt pressure gets sufficiently high for the Mohr circle to intersect the failure envelope. This forms tensile fractures (shown by A), dilatant-shear fractures (shown by B) or shear fractures (shown by C) depending on where the envelope is intersected.

8.3 Geometry of Melt-bearing Structures and Melt Networks

The presence of intrusive phases within any structure, brittle or ductile, implies that the structure represented a dilatant volume relative to the surrounding rocks at some point while melt was present in the system. These structures provide the sites along which mesoscale channelised flow occurs and join together to form the larger-scale pervasive networks. The structures observed here are similar to those observed in anatectic migmatites and which are interpreted to represent melt segregation and movement within the source (Sawyer, 2001; Marchildon & Brown, 2003). However, these are interpreted as channelised melt pathways which represent melt migration through rocks above the source. Subsolidus rocks have different rheologies relative to actively melting rocks, and anatectic rocks often have a diffuse presence of melt within them, which is absent in subsolidus rocks. Therefore, despite the physical similarity of melt pathways between studies of anatectic rocks and the structures from this project, the melt pathways likely form by slightly different mechanisms.

Dilational sites are created during active deformation of the crust, and the active strain regime plays an important role in determining the kinds of structures that may form, their initial orientation, as well as their potential interconnectivity (Table 8.1). However, strain

will be heterogenously distributed in any volume of rock, and so structures can be expected to locally form in different orientations. The varying predominance of different structures, and their orientation govern the geometry and connectivity (and thus permeability) of the leucogranite networks.

8.3.1 Concordant/Stromatic Leucosome

In migmatite terrains the most commonly observed leucosome orientation is parallel to bedding or a pre-existing foliation (Brown & Solar, 1999; Vanderhaeghe, 1999; Slagstad *et al.*, 2005; Weinberg & Mark, 2008; Kisters *et al.*, 2009). This is sometimes explained by preferential melting along compositional layering in anatectic migmatites (Sawyer, 2001); however, this is only true if the leucosomes are primary segregation structures. Many stromatic leucosomes, such as the ones in the field area, are clearly injected, and therefore represent planar melt migration conduits. Bedding planes are sites of weakness due to rheology contrasts between different beds, and this could explain the preference of leucosome for such sites. However, foliation planes are typically understood to represent planes of contraction (Kisters *et al.*, 2009), and therefore do not intuitively represent the most favourable orientation for leucosome intrusion. The observation of abundant foliation-parallel leucosome in the field area coupled with common observations of foliation-parallel leucosome suggests that foliation planes represent high permeability zones (Weinberg, 1999).

It is suggested that mid-crustal rocks and migmatite terrains that contain melts could have extremely low tensile strengths (1–5 MPa; Van der Molen & Paterson, 1979; Handy *et al.*, 2001; Kisters *et al.*, 2009). In addition, for foliated rocks, two different tensile strengths can be defined, depending on whether fracturing occurs oblique or parallel to layering (Cosgrove, 1997; Handy *et al.*, 2001). Foliation planes, particularly those defined by aligned platy minerals such as the biotite, represent planes of lower strength relative to the surrounding granular rock. This lower relative strength means that foliation planes represent weaker planes along which melt can preferentially intrude if the tensile strength is overcome. In addition, the orientation of the principal stress axes relative to the foliation is variable with time, and σ_1 is not necessarily normal to the foliation plane during melt intrusion.

In all outcrops the majority of intrusive phases occur as S_0/S_1-parallel leucosome. Some outcrops, such as the Etusis Pavement in Chapter 5, and the idealised crustal section in Chapter 7, show that the earlier melt phases preferentially occur as concordant leucosome

while later phases exploit discordant structures. This could suggest that either intrusion of the early intrusive phases occurred prior to, or early during deformation, when the main anisotropy in the rocks was the foliation and there were no crosscutting structures to exploit, or that low volumes of melt preferentially exploit bedding and foliation planes. Significantly, the utilisation of S_0/S_1 planes for vertical melt ascent is only effective if S_0/S_1 is steeply dipping, such as in the Birkenfels outcrop in Chapter 3 (Kisters *et al.*, 2009; McFadden *et al.*, 2010), and is not effective at moving melt upwards in the outcrops that exhibit shallowly dipping S_0/S_1 (e.g. Chapters 5 and 7).

8.3.2 Shear zones

Shear zones around the world are commonly associated with granites and leucosome, both on a large scale where granite networks are associated with deformation in crustal-scale (usually transpressional) shear zones, and on an outcrop scale where leucosome is commonly observed within compressional and/or extensional shear bands and fractures in anatectic migmatite terrains (Davidson *et al.*, 1994; Brown & Solar, 1998b; Vanderhaeghe, 1999; Marchildon & Brown, 2003; Weinberg & Mark, 2008; Weinberg & Regenauer-Lieb, 2010). The presence of melt within shear zones is generally attributed to their function as sites of reduced mean stress (Brown & Solar, 1999; Kisters *et al.*, 2009); however, extensional shears and dilatant shear fractures seem to be the most favourable shear type for melt transport (Hutton *et al.*, 1990; Brown & Solar, 1998a; Sawyer, 2001; Marchildon & Brown, 2003; Brown, 2007).

Extensional shears and dilatational shear fractures accommodate extension across the shear zone, and thus provide dilatant sites for melt (Hutton *et al.*, 1990; Brown, 2007). The presence of melt within compressional and transpressional shears is counter-intuitive since they accommodate shortening across their width. However, they do, in fact, experience extension parallel to the walls of the zone (Hudleston, 1999; Fagereng, in press). It thus follows that shear zones that accommodate either overall extension or overall compression all experience at least local extension, and thus all types of shear zones are capable of creating the dilation required to draw melt into them. In anatectic migmatites the mechanism by which melt moves into shear planes is either slow, where melt slowly drains out of wallrocks into sites of low pressure (Sawyer, 2001; Vanderhaeghe, 2009), or fast whereby melt is injected along embrittled shear planes (Davidson *et al.*, 1994).

Melt-filled shears are the predominant discordant melt-bearing structure in nearly every

outcrop of this study, and they tend to be the first discordant structure to be exploited by medium- to high-volume leucogranite phases. Shears, particularly when they occur as conjugate sets of oppositely-dipping structures, play a key role in the initial formation of the pervasive migration network by connecting previously-isolated concordant channelised structures. In chapter 3 diffuse melt-filled shears are described where small volumes of melt was likely segregated into shear planes during a slow process (e.g Sawyer, 2001). Planar, sharp-boundaried dykes within shear planes in other chapters (Chapters 4, 5. 6, 7), are more suggestive of brittle failure along the shear planes.

The channelised nature of the melt in the shears suggests that melt is localised into the shear planes by preferential fracturing of the planes during melt embrittlement rather than by percolative flow. Figure 8.4 shows that failure will preferentially occur along a pre-existing (weak) planar fabric, such as that defined by aligned platy minerals in the shear plane, because the shape and position of the failure envelope changes so that the state of stress becomes unstable (Twiss & Moores, 1992, p.180). This is because shear planes define a secondary foliation and are mechanically anisotropic. This secondary mineral alignment together with the dilation experienced by extensional shears means that they form planes of relative weakness compared with the surrounding rock. Therefore, they will preferentially fail and readily dilate during melt embrittlement so that the location and orientation of pre-existing and/or actively deforming ductile shears controls the geometry and location of these leucogranite-bearing structures. Both extensional and compressional shears provide space for melt since both experience local extension during active deformation (such as described in chapter 6); however, extensional shears offer more dilation.

Flattening strain is the most effective strain regime for the creation of extensional conjugate shears. It is a very effective strain regime for melt migration because it allows for the development and enhancement of these structures so that they form an interconnected channelised network. The style and orientation of the melt network would depend on the orientation of the flattening strain. If flattening is vertical, then the network is required for upwards migration across the flat-dipping anisotropy, and the extensional shears form the essential structure in the network (e.g. Chapter 7). In this case, flattening is vertical, and extension is horizontal, so shear offset is normal. If flattening is horizontal, then a vertical foliation results, and shears form to accommodate strain. In accordance with horizontal flattening, the shears accommodate vertical extension, and show a reverse offset. Both the foliation and shears will be favourably oriented for effective upward melt movement, and most

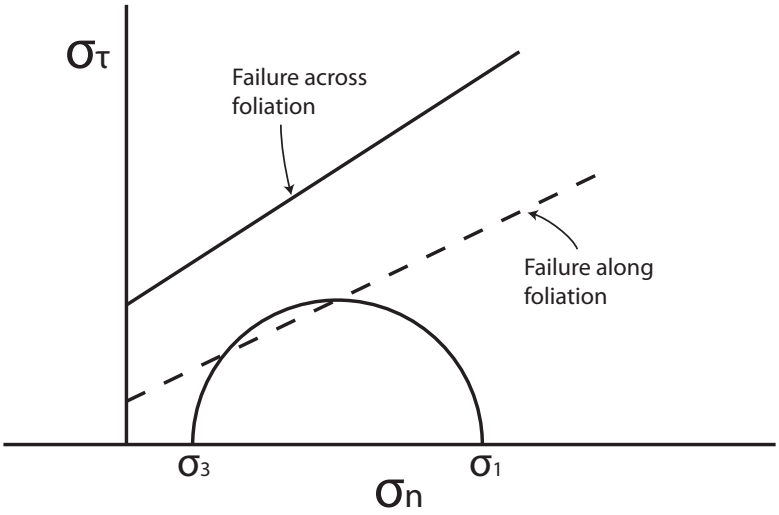

Figure 8.4: Mohr diagram showing a model for failure involving a pre-existing foliation. The solid line shows a stable state where the Mohr failure envelope for failure across a foliation does not intersect the Mohr circle. The dashed line shows an unstable state (i.e. failure) for failure along a foliation.

melt will likely be accommodated in foliation-parallel structures. Therefore, the shears are not a pre-requisite for upwards migration in this scenario, but primarily serve as connectors between the concordant structures (e.g. the Birkenfels outcrop in Chapter 3).

Melt networks consisting of conjugate shears are also described within strongly prolate environments, such as in chapters 3, 5, and 6, indicating that constrictional strain also forms localised extensional structures that can be utilised for melt migration. However, these conjugate shears do not produce very effective melt networks. The presence of melt within reverse offset shears can be attributed to the relative weakness supplied by mineral alignment coupled with the local extension within the shear zone that creates favourable dilational sites, as described above (e.g. Escher & Watterson, 1974; Hudleston, 1999).

The geometry of the conjugate shears at each outcrop is governed by the overall strain regime and the amount of deformation and re-orientation experienced subsequent to their formation. Previous chapters have discussed the significance of their geometric relationships, and the results are summarised in table 8.2. It is assumed that ductile extensional conjugate shears initiate at 90° to one another (45° from the plane of maximum compression), and that shear fractures formed within the brittle-viscous transition exhibit an acute, $< 90°$ angle between them (i.e. a steeper dip and a $>45°$ angle from the plane of maximum compression)

(Fig. 8.1, Twiss & Moores, 1992, p.175). The presence of steeply-oriented tensile fractures that are continuous with more shallowly-dipping shear fractures, such as in the Etusis Pavement and High Strain Cliff (Chapter 5) and the ideal crustal section (Chapter 7), indicates that these structures can potentially form in multiple orientations simultaneously, depending on the rheology and degree of melt embrittlement.

Chapter	Outcrop	Conjugate Angle	Predominant Strain Regime
Ch. 3	Birkenfels	90°	Flattening
Ch. 3	Swakop Pavement	40°	Constriction
Ch. 5	Etusis Pavement	105°	Plane strain
Ch. 5	High Strain Cliff	73–100°	Plane strain
Ch. 6	Fold core	140°	Constriction
Ch. 7	Metasediment package	80–105°	Flattening

Table 8.2: Table showing the angles between conjugate shear sets, measured as the angle which contains the downthrown block, in all outcrops and their predominant strain regimes. For chapter 6, the constrictional strain refers to the core of the antiform, where shears are predominant.

Shears forming in response to flattening are likely to experience subsequent re-orientation in response to progressive deformation. If the strain regime is constant, the shears will experience the same strain that created them, and will therefore flatten so that the angle which contains the downthrown block will become greater than 90°. The greater than 90° conjugate angles exhibited by all outcrops that experienced either flattening or plane strain is consistent with some re-orientation of the structures subsequent to their formation (Table 8.2; Chapters 5 and 7).

The exact timing of melt intrusion into these structures remains an open question, particularly whether it occurred prior to, and/or during and/or after their re-orientation. The presence of rare melt-free shears that show similar re-orientation to melt-filled shears (Chapters 5, 6, 7) show that shears were rotated regardless of whether they contained melt or not. Fagereng *et al.* (2010) demonstrated that shear veins prefer to utilise a pre-existing anisotropy, even if oriented at a high angle to the compressive stress, rather than forming a new structure that is more favourably oriented. Following this, shearing, dilation and melt intrusion would preferentially continue to occur on existing structures, even if they had been rotated into an unfavourable orientation. Conversely, if fracturing, melt intrusion and solidification of the

leucogranites occurred prior to re-orientation, then these granites would preferentially show folding, boudinage and the development of solid-state planar and linear fabrics. The presence of both deformed, shear-parallel dykes and planar, undeformed relatively flat-dipping dykes in these outcrops demonstrates that either situation is possible. It is likely that both occur concurrently since shear formation, re-orientation and melt intrusion is ongoing with progressive deformation.

8.3.3 Boudin Necks

Boudin necks formed by layer-parallel stretching within an overall flattening strain environment are discordant structures that allow for melt movement across relatively competent lithological layers. However, interboudin spaces are very effective at creating long-lived dilatancy, which potentially makes them sites of permanent melt emplacement rather than transient migration structures. Boudin necks have been described as sites of melt accumulation in anatectic migmatite terrains (Sawyer, 2001; Marchildon & Brown, 2003; Vanderhaeghe, 2009). Melt presence in these sites is attributed to the comptency contrast between boudinaged layers and the surrounding rock, so that more competent layers preferentially fracture. This mechanism is similar for both anatectic migmatites and the boudin neck hosted intrusive phases in the subsolidus rocks desribed here.

The calc-silicate outcrop in chapter 4 shows examples of the two different ways that boudin necks can be utilised by melt. The three large leucogranite intrusive bodies that occur along strike from one another are examples of large-scale boudin necks as accumulation and emplacement sites. Melt is drawn into these sites due to the strong dilatancy created by ongoing deformation and competency contrasts. Once melt has moved into these sites and continues to accumulate during ongoing deformation, and if the strain orientation remains relatively constant, then the pressure gradients do not change and the boudin necks cannot lose melt, causing them to become final sites of emplacement.

The smaller intrusive phase-filled boudin necks which occur within single lithological layers represent more transient accumulation sites that melt utilised as part of the pathway towards the large blow. These smaller boudin necks are sites of local dilation, and melt moves into these from the surrounding rocks. However, the overall pressure gradient created by the larger boudin necks is strong enough to remove melt from the local, transient sinks and transport it towards its ultimate sink. This indicates that boudin necks formed by active

deformation can draw melt towards them due to the pressure gradient created when they form, but require a change in strain regime or a nearby, stronger dilatant site that is in communication with (i.e. connected to) the structure in order for melt to migrate away from it. The significance of competent lithologies as part of large-scale melt migration networks is therefore their ability to create long-lived dilatancy through boudinage, allowing them to become sites of melt accumulation.

8.3.4 Tensile Fractures

Tensile fracture are described in anatectic migmatite terrains as brittle features generated by melt embrittlement that represent the beginnings of channelised melt movement out of the source rock (Vanderhaeghe, 2009; Weinberg & Regenauer-Lieb, 2010). Brittle elastic fracturing is also described as the mechanism by which dykes in the upper crust would form to facilitate melt ascent (Weinberg, 1999).

Tensile fractures, which are less common in the field area than boudin necks, occur as leucogranite-filled dykes that are near to perpendicular to the stretching direction (e.g. Chapters 5, 7). These structures are usually filled with the most voluminous melt phases, confirming that they require the highest fluid pressure and greatest degree of melt embrittlement in order to form (Figs. 8.1 and 8.3). Tensile fractures are also more predominant in outcrops that exhibit a relatively strong lineation, such as the outcrops in the high strain zone in chapter 5. This suggests that a somewhat prolate strain environment is the most favourable for their formation. Tensile fractures are usually observed to form close to normal to the apparent extension interpreted from the lineation (Chapters 5, 7).

Their occurrence in most lithologies, specifically the metapsammitic gneisses and quartzites, gives evidence that tensile fracturing is not confined to competent lithologies. Simakin & Talbot (2001) suggest that greater stresses can develop in the more viscous lithologies leading to potentially higher relative fluid pressures in these rocks compared to competent lithologies. The higher fluid pressures cause melt embrittlement (Davidson *et al.*, 1994), and the formation of tensile fractures, which is consistent with observations of vertical melt-filled fractures/dykes in regions that have undergone tensile stresses (Brown & Solar, 1998a,b). Tensile fractures are strongly dilational and make effective connections between isolated stromatic structures.

With the exception in the Fold Hinge outcrop in chapter 6, tensile fractures usually

occur in a sub-vertical orientation, and because most outcrops have a shallowly dipping anisotropy, σ_1 at the time of tensile fracture formation is probably vertical for the majority of the outcrops. This vertical orientation should make tensile fractures highly effective for the upwards migration of large volumes of magma if tensile stresses are high enough (Clemens, 1998; Weinberg, 1999). However, the predominance of conjugate melt-bearing shears as the main structures that comprise melt networks suggests that melt does not readily use tensile fractures. The likely reason is that the shear fractures are already weak and do not require very high melt pressure to open, whereas tensile fractures require the initial fracturing of relatively intact and unweakened rock at high fluid pressure (Davidson *et al.*, 1994).

Tensile fractures in these rocks often occur as isolated structures that are not connected to the rest of the melt network. They often have pointed tips and the foliation is radially deflected into them, indicating that they have lost volume and represent collapsed melt-bearing structures (Bons *et al.*, 2008). These observations would be more consistent with suggestions that they are transient and local phenomena that created and erased as melt passes through them and melt pressure within them changes (Kisters *et al.*, 2009; Weinberg & Regenauer-Lieb, 2010), and that they play a minor role in facilitating large-scale melt migration.

8.3.5 Migration networks

Melt networks are observed in anatectic migmatite terrains (Sawyer, 2001; Marchildon & Brown, 2003; Brown, 2007), and are interpreted to represent the joining of structures that have facilitated coalescence and drainage of melt from the surrounding wallrocks. It has also been suggested that these networks facilitate melt movement out of the source rock (Sawyer, 2001; Vanderhaeghe, 2009; Brown & Solar, 1998a). Here the melt networks are interpreted as interconnection between channelised melt migration pathways within subsolidus rocks that effectively increase the permeability of the otherwise impermeable rock.

The concordant sheets, shears, boudin necks and tensile fractures represent different mechanisms by which melt channels can form. For effective migration these channels have to intersect and coalesce to form continuous, high-permeability networks. These pervasive networks are the main style / mechanism by which melt ascends through the various studied outcrops, and in most cases (e.g. Chapters 4, 5, 6, 7), allows for the main direction of melt movement to be strongly discordant to the predominant planar fabrics in these rocks.

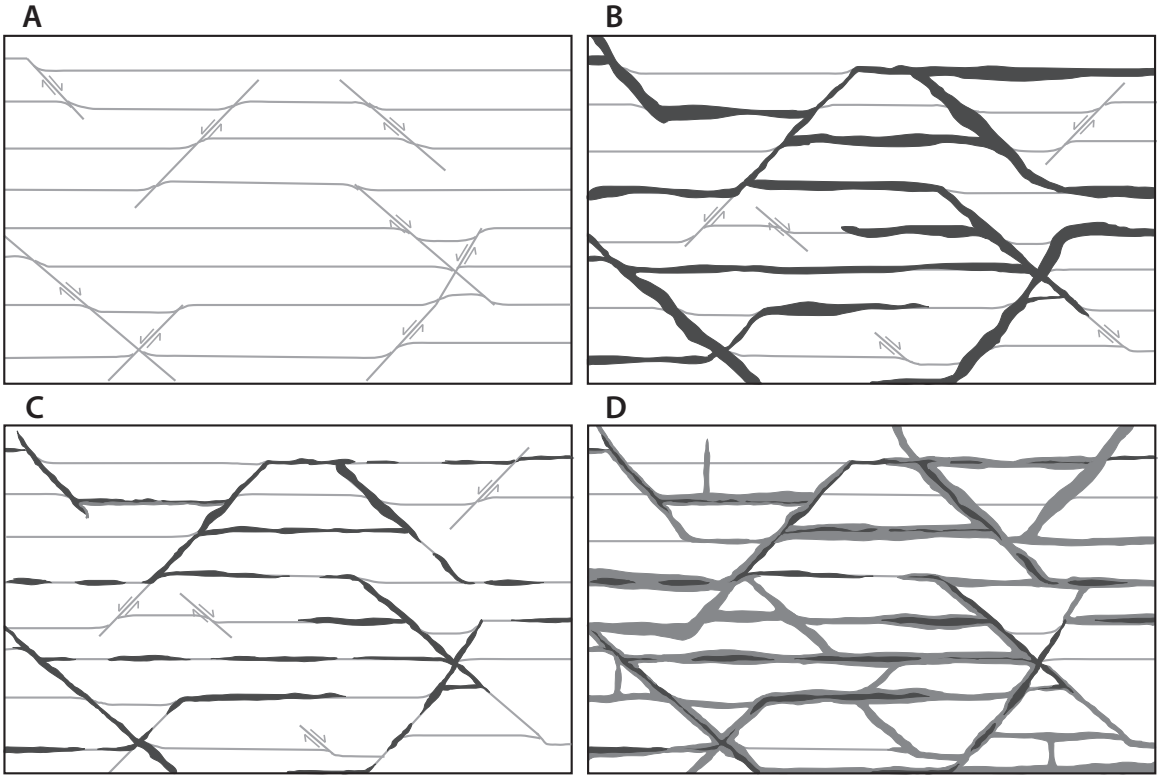

Figure 8.5: Model for the development and evolution of an idealised melt network during progressive deformation. (A) Progressive flattening forms an S_0/S_1 fabric, and is further accommodated by the formation of shear zones. (B) Melt intrudes along S_0/S_1 and shear planes, as these weak surfaces are the first to be exploited with increased melt pressure and continued deformation. This allows for channelised melt flow along interconnected structures. (C) As the melt supply dwindles and melt pressure drops, structures deflate or collapse completely, interconnectivity is lost, and any trapped melt crystallizes. (D) A second, more voluminous batch of melt utilises the pre-existing network of weak structures and granite veins and dykes, as well as new structures created by ongoing deformation and increased melt pressure to migrate through the rocks, concurrently increasing the permeability of the network.

The formation and evolution of these networks is progressive, and dependent on the interplay of tectonic deformation, which controls the formation of dilatant structures and structural weaknesses, and melt supply, which controls the degree of embrittlement. The type of strain regime plays a large role in the effectiveness and style of networks. A constrictional strain regime only provides one extension direction, and does not form a foliation. If melt volume were high in a constrictional zone, the most favourable structure forms at tensile fractures (to accommodate the strong unidirectional extension). A lack of foliation, together with parallel tensile fractures, form an environment unfavourable for setting up a network, because the probability of structures intersecting one another is low. Conjugate shears observed in outcrops that show constrictional strain regimes also rare, tend to be unfavourably oriented for upward melt movement, or show steepening into tensile fracture orientation (e.g. Etusis Pavement in chapter 5), and are thus less likely to intersect one another to form an interconnected network.

Flattening deformation is much more effective at creating melt migration networks because it provides a large array of differently oriented weak structures, such as foliation planes, conjugate shear planes, and occasional tensile fractures, that have a higher probability of intersecting one another, and thus form a more interconnected and effective network. The formation and evolution of an idealised network during flattening deformation and increasing melt supply is shown in fig. 8.5. Initial channelised structures form along pre-existing weaknesses through fracturing caused by melt embrittlement. During the early stages of deformation, and at low melt volumes, these structures are confined to bedding- and foliation-parallel orientations (Fig. 8.5A,B).

Continued deformation and increased melt pressure allows for fracturing along pre-existing and active shear planes that intersect the concordant structures and forms an initial migration network (Fig. 8.5A,B). Provided that there is a continuous supply of melt, melt pressure remains high and the network effectively accommodates upward melt movement. Since a constant melt supply is unlikely, the networks and structures deflate as melt drains out of them, and some structures will lose volume and collapse. Residual melt pockets crystallise, leaving a network of continuous weaknesses containing discontinuous and/or partially continuous granite lenses (Fig. 8.5C; Bons *et al.*, 2008).

During long-lived melt migration, multiple batches of magma will utilise the same network. A second pulse of melt may increase the melt pressure so that it becomes sufficiently high for melt embrittlement and re-fracturing to occur along the pre-existing weaknesses, such

as along solidified granite–metasediment contacts, as well as new ductile shears created by ongoing deformation. If the melt pressure is sufficiently high, tensile fractures and/or dilatant shear fractures also form and contribute greater permeability to the network (Fig. 8.5D). The network remains open and active for as long as it has a melt supply, thereafter it collapses, and may be exploited by subsequent melt batches.

Barraud *et al.* (2004) demonstrated that the melt-flow network does not need to be fully interconnected to facilitate local expulsion of melt from the rock. Thus the presence of disconnected bodies of intrusive phases within structures could also be explained by lower-volume melt migration, where the volume of melt is not sufficient to maintain a connected network, and melt could utilise the structures in a process similar to mobile hydrofracturing used to describe the formation of quartz veins (Bons, 2001), applied to melt migration by Kisters *et al.* (2009). This process facilitates migration by upward propagation of melt-filled fractures when melt pressure at the fracture tip exceeds lithostatic pressure.

The melt-filled fracture is transient because, as melt supply decreases, the lack of melt pressure at the base of the fracture cannot keep the fracture open. When lithostatic presure exceeds melt pressure, the fracture closes. The transient nature of this melt-migration structure suggests that their preservation in the rock record would be low; however, examples have been observed in the field (e.g. Kisters *et al.*, 2009) and in analogue modelling experiments (Bons *et al.*, 2001). The nature of pervasive migration is likely somewhere in between these two end members, where migration switches between full and sustained inflation of networks, and transient hydrofracturing allowing lower volumes of melt to move along pre-existing structures. Significantly, both mechanisms require interconnected weaknesses within the rock.

The progressive example discussed above explains the development and evolution of the melt network in most of the outcrops studied here, where the rates of tectonic dilation and melt supply are approximately equal, as required to sustain open networks, or the rate of dilation exceeds that of melt supply, such as when networks collapse. However, the high strain cliff in chapter 5 and the idealised crustal section in chapter 7 contain examples of the type of network and structures that form when the rate of melt supply greatly exceeds the rate of tectonic dilation.

The leucogranite-cemented breccias in these outcrops contain large rotated blocks, which requires the presence of a significantly larger volume of leucogranite than is preserved in these structures. This, together with dragged foliation along the block edges, their angularity, and

their typical diamond-shape, suggests that they form as a result of rapid inflation of melt networks comprised predominantly of melt-filled shear structures, caused by melt overpressure. Their current breccia-like state is explained by implosion of the structures during a subsequent drop in melt pressure, in a mechanism similar to the formation of quartz-cemented hydraulic breccias (e.g. implosion breccias of Sibson, 1986).

Melt overpressure is achieved by a combination of melt supply exceeding migration rate (so that a melt buildup occurs), buoyancy forces of the melt, and impermeable barriers that confine the melt. This overpressure builds until it is enough to break through the impermeable barriers, at which point a large, highly permeable network is formed and rapidly inflated. At this point, the melt volume is high enough to allow loss of cohesion of the country rocks and these are stoped and compacted downwards as melt is expelled upwards. The expulsion of melt leads to the implosion and collapse of the structure, and formation of the melt-cemented breccia. This mechanism of melt movement is similar to the fault-valve action proposed for the movement of fluids along faults (e.g. Sibson, 1992)

8.4 Driving Forces for Melt Movement

Melt ascent is traditionally understood to be driven by buoyancy forces, hydraulic gradients, and pressure gradients created during heterogenous deformation, and various authors allocate their relative contribution as driving forces differently (Sawyer, 2001; Vanderhaeghe, 2009; Brown, 2010). In some cases, buoyancy is described as the primary driving force (Clemens, 1998), while others show that local variations in differential stress can potentially generate melt pressure that may be hundreds to thousands of times greater than those due to gravitational potential (Brown *et al.*, 2011).

8.4.1 Buoyancy and Hydraulic Gradients

The traditional view is that on a crustal scale, the primary melt ascent driving force is buoyancy, created by the density contrast between melt and the surrounding rock. Hydraulic gradients form between sites of low and high fluid pressure, driving melt towards low melt pressure sites (Kisters *et al.*, 2009). Buoyancy is considered as the main crustal-scale melt ascent driving force, and is also invoked to explain vertical propagation of melt-filled dykes (Weinberg, 1999). Its role in the creating of mesoscale melt networks is small because local pressure gradients are potentially much stronger, and buoyancy forces are weak if melt

volumes are low (Weinberg, 1999).

The main role of buoyancy as a driving force on the mesoscale is its contribution to increased melt pressure, aiding in embrittlement of rocks that would otherwise be impermeable. Evidence for buoyancy-driven melt ascent is seen in the Birkenfels outcrop (Chapter 3), which shows upwards migration along steep foliation planes, and the High Strain Cliff outcrop (Chapter 5), which shows examples of failed upward migration by the younger melt phase along shear planes. Evidence for buoyancy-driven melt ascent is also seen in the Fold Hinge outcrop (Chapter 6), which shows migration towards, and emplacement within the fold hinge, and the Ideal Crustal Section (Chapter 7), which shows upwards melt movement at least partially driven by buoyancy through tensile fractures and large vertical structures in both cliff faces.

Two end-member models are proposed to describe crustal-scale melt ascent. The first defines melt migration as continuous with constantly connected melt channels through which the flow of melt is essentially unbroken, and whose structures constantly feed a growing pluton (Clemens, 1998). The predominant driving forces in such a model are buoyancy and hydraulic gradients, which passively drives melt upwards through the channels. This mechanism has the potential to be effective because it would maintain a constant hydraulic gradient between the inflated ascent structures and any melt-bearing structures in the vicinity, thus being effective melt drains for surrounding rocks. However, for this mechanism to be effective it requires constant melt pressure, and a constant supply of melt. In addition, there is little evidence for such large, isolated melt-transfer structures in the lower crust.

Since melting in the source region occurs episodically, as different minerals break down with increasing temperature, such an uninterrupted melt supply is unlikely (White *et al.*, 2004; Brown, 2007; Urtson & Soesoo, 2009), and a second melt migration end-member can be considered. It describes episodic melt ascent and accumulation whereby multiple batches of melt move through the crust in a stepwise manner, either utilising new structures, or pre-existing structures along which previous batches have already migrated (Bons *et al.*, 2001; Barraud *et al.*, 2004). Such a model suggests that melt migration is not continuous and relies on a combination of dilation, expulsion, and buoyancy.

8.4.2 Dilation

Localised dilation occurs during ongoing heterogeneous deformation and creates pressure gradients by providing low pressure sites that melt is drawn into, leading to melt depletion of the surrounding rocks. Dilation creates accumulation and/or migration sites such as boudin necks, tensile fractures and extensional shears, and can often promote emplacement of melt during periods of long-lived and unchanging dilation (e.g. Chapter 4). Dilation is largely scale-dependent, and localised dilation can also occur within overall compressional environments (e.g. extension within a compressive or transpressive shear zone as discussed above; chapter 6). Dilation alone can provide a force for melt migration, if it is transient which allows constant and dynamic change of the relative strength and location of dilational sites, forming transient pressure gradients that facilitate 'sucking' of melt through structures, such as the small-scale boudin necks in chapter 4.

8.4.3 Expulsion

Melt expulsion can result from the creation of high pressure sites by compaction and compression during progressive tectonic deformation. Experimental modeling has shown that shear-enhanced compaction leads to effective movement of melt out of the source (Cooper, 1990; Brown & Solar, 1999). This illustrates that pressure gradients can also be set up so that melt is 'pushed' away from high pressure sites. The crustal section in chapter 7, where melt is sourced from the basement rocks at a structurally lower level, shows an example of melt being expelled by compaction, whereby melt volume is translated upwards through the package, and metasediments are transferred downwards. Expulsion removes melt to sites of relative low pressure, where space has to be created to accommodate the melt volume.

8.4.4 Transient Pressure Gradients

During progressive deformation, rocks deform heterogeneously so that sites of relative high strain and low strain, and relative flattening and constriction develop (e.g. Brown & Solar, 1998a). The location and orientation of these sites change with time during progressive deformation to create transient high pressure sites from which melt is expelled and low pressure sites towards which melt is drawn. If pressure gradients are the primary driver for melt movement on the scale of mesoscopic networks, and heterogenous deformation drives the formation of pressure gradients, then sites can change from accumulation sites, to migration

pathways, to melt loss sites as deformation progresses and strain fields change. Migration likely occurs in a stepwise manner with sites alternating between periods of accumulation when strain is stable and migration when strain changes.

The two scenarios (constant versus changing strain regime) are complementary, and particularly effective if they are able to periodically switch. In fact, this switching is consistent with, and even required by, episodic and stepwise migration (e.g. Brown & Solar, 1998a; Bons *et al.*, 2001; Urtson & Soesoo, 2009). A constant strain regime allows a long-lived, stable network to be established and to allow multiple batches of melt to migrate towards accumulation sites that are favourably oriented within that strain regime. Such a scenario is illustrated by the long-lived melt networks and accumulation sites present in the calc-silicate cliff (Chapter 4) and idealised crustal section (Chapter 7). However, such a constant strain regime cannot facilitate large-scale melt migration because it has a limited pressure gradient that, if left unchanged, will cause the melt accumulation sites to become sites of melt emplacement. In order to achieve further movement, the strain regime has to change, leading to the formation of new dilation sites, with the sites of former melt accumulation becoming sites of melt loss.

The presence of multiple intrusive phases of progressively younger age within the same structures at some outcrops (e.g. Chapters 4, 5, 7) suggests that strain was relatively constant through time for those areas, and that the structures remained dilational during migration of multiple melt phases. At outcrops where the strain changes spatially and is thus more variable, such as the Birkenfels outcrop in chapter 3 and fold hinge in chapter 6, dykes typically only contain one leucogranite phase. This indicates that a changing strain regime promotes the creation of new, more favourably-oriented structures, rather than re-using pre-existing melt pathways.

8.4.5 Feedback Relationships

From the above discussion it is apparent that melt movement depends on the simultaneous availability of a melt supply, the presence of an interconnected, dilatant network of pathways, as well as a driving force. However, the synchronicity of all these criteria cannot be assumed, and it is clear from field evidence that migration does not occur constantly or continuously. If tectonic dilation occurs quicker than the rate of melt supply, then the connected network would collapse. Conversely, if tectonic dilation is slower than melt supply, melt will

accumulate against the impermeable structures. The accumulated melt can either freeze, or build the melt pressure until embrittlement leads to the creation of new channels. Brown & Solar (1999) describe a feedback mechanism between melt fraction and deformation where melt localises in high strain sites, melt presence weakens the rocks, and strain localises in high volume melt sites. Similarly, high melt fraction would increase deformation and melt-embrittlement thereby increasing localised dilation and the number of dilational sites allowing for stronger pressure gradients and faster migration, while low melt fractions would decrease the probability of melt-enhanced embrittlement, and would promote more static dilation so that rocks would have lower permeability, less dilation sites and a less complex melt network. This means that at times when the rate of tectonic dilation exceeds that of melt supply, melt movement will be restricted in favour of melt accumulation. Conversely, if melt supply exceeds the rate of tectonic dilation, migration will occur and melt will not accumulate.

The presence of structures formed through melt embrittlement, as well as the occurrence of melt-cemented breccias, shows that high melt pressure can play an active role in increasing permeability within the rocks. If melt migration was purely driven by pressure gradients created by differential stress then melt pressure should not exceed lithostatic pressure, because melt would preferentially move away from high pressure sites. However, melt preferentially moves upwards due to buoyancy forces (Clemens, 1998; Weinberg, 1999; Vanderhaeghe, 2009). If we assume that fluid pressure is close to lithostatic pressure for these rock (Fyfe *et al.*, 1978), then slight increase in melt pressure caused by buoyant melt forcing its way upward would cause melt embrittlement thus increasing the effective permeability of the rocks. Embrittlement could also occur when melt accumulation sites become overpressured due to changes in stress, and low adjacent permeability.

The relative contribution of buoyancy forces, and pressure gradients resulting from deformation, is dependent on melt volume. Buoyancy-driven movement is most effective when a large volume of melt is allowed to build up so that buoyancy stresses cause an increase in pressure, helping drive deformation and melt embrittlement. The deformation and embrittlement creates the required permeability so that melt can move upward from the high pressure site to a new accumulation site. Melt pressure then builds up at a new site and the process repeats itself. Smaller melt volumes can only migrate in channels formed along pre-existing structural weaknesses, such that they require pressure gradients formed during active deformation to facilitate movement and inhibit emplacement and freezing.

8.5 Timescales of Melt Migration

Estimating the timescales of melt migration is difficult because the speed at which melt ascends through the crust is not only dependent on the properties of the melt (e.g. viscosity), but also on a multitude of other factors such as permeability of the crust, size and shape of melt conduits, the strength of pressure gradients and the continuity of melt supply (Collins & Sawyer, 1996; Barraud *et al.*, 2004; Brown, 2007). The occurrence of structures suggestive of melt loss (Bons *et al.*, 2008; Kisters *et al.*, 2009) allude to the additional complication that it is near-impossible to quantify the volume of melt that utilises the migration networks, or how effective they are in terms of the fraction of melt transferred compared to that which crystallises in the network. Most estimates of migration timescales are inferred from either the amount of time required to fill a pluton by emplacement of multiple melt batches (e.g. Pressley & Brown, 1999), the calculated rates of ascent through vertical channelised dykes (Brown & Solar, 1998a; Clemens, 1998; Weinberg, 1999), or from rates of melting in the source (Brown, 2007).

Estimates for the timescale of melt migration are dependent on the effectiveness of the melt migration mechanism (Clemens, 1998; Brown & Solar, 1998a). Estimates of migration rates purely via dyking are likely too fast because they are only limited by melt viscosity, and assume constant migration through a crustal-scale dyke, which is inconsistent with the occurrence of pervasive networks and episodic and stepwise migration as outlined above. Using the dyking method, time estimates for migration and the filling of a pluton are as low as 1200 years (Clemens, 1998).

The rate of pervasive migration is controlled by the size and permeability of the melt network, which in turn is controlled by the number of channels, their connectivity, and their ability to prevent melt from freezing. Several workers have suggested that the rate of melt movement through a pervasive network is controlled by the deformation rate (Collins & Sawyer, 1996; Weinberg & Searle, 1998; Barraud *et al.*, 2004). This assessment is consistent with the results of this work, which show that pervasive networks are dominantly controlled by the strain regime and relative strength of the country rocks. Therefore, the rate of pervasive migration is largely controlled by the rate of tectonic deformation.

The Damara Orogen records collisional deformation lasting for at least 40 million years (c. 550–510 Ma; constrained using dating of white mica in deformation fabrics, and field relationships; Miller, 1983). Briqueu *et al.* (1980) reported a U-Pb single zircon age of 534 ±

7 Ma for early syn-metamorphic foliated red granite found in the area, and a U-Pb monazite age of 508 ± 2 Ma for the youngest sheeted leucogranites, also described by Nex *et al.* (2001). This suggests that the metasedimentary rocks that supplied melt for the Damara S-type granites were periodically melt-bearing for at least 25 million years, with the later-stage granites intruding towards the end of, and subsequent to, regional deformation. The crosscutting relationships and sharp boundaries between different intrusive phases in the same outcrop indicate that early phases cooled and crystallised before the intrusion of subsequent ones. This would indicate that temperatures in the area hovered around the leucogranite solidus during this time. In addition, the folding and boudinage of older granites show that early melts must have intruded, cooled and crystallised relatively quickly, in order to experience solid-state alignment of minerals during progressive deformation.

Specific structures within networks are likely to be more long-lived than others. The more frequent occurrence of multiple intrusive phases within stromatic layers as composite dykes, and the preferential occurrence of early melt phases as stromata (Chapters 4, 5, 6, 7) suggests that bedding and foliation planes are long-lived structures utilised by all phases throughout the melt-bearing history. Similarly, the longevity of a melt network depends on the stability of the local strain regime. Many of the outcrops examined here, such as the calc-silicate outcrop in chapter 4, the Etusis pavement in chapter 5 and the ideal crustal section in chapter 7 show evidence of long-lived networks that were exploited by multiple melt batches over a protracted period of time, likely in excess of 25 million years.

Timescale estimates for the formation of a pluton are between a few thousand years to several million years, and sheeted plutons are estimated to be closer to the order of several million years (Vanderhaeghe, 1999; Petford *et al.*, 2000; Cruden & McCaffrey, 2001; Brown, 2010), which is consistent with the 25 million year time-scale inferred from the Damara rocks. This large contrast between this estimate and the significantly faster pluton filling rate suggested by calculations from movement of melt along dykes (Clemens, 1998) suggests that migration rate is not constant with time through the crust. It is likely that during favourable stress states when channelised migration occurs, the upper limit for melt movement rate along the channel is the the melt viscosity (e.g. Clemens, 1998), however this kind of movement is punctuated by long periods during which melt is stationary. This suggests that areas that experience predominant pervasive migration (e.g. the lower crust) have slower overall migration rates than areas which experience more predominant channelised migration (e.g. the mid- to upper-crust), and that melt migration rate possibly increases with decreasing

depth in the crust, if migration becomes more channelised at higher crustal levels.

8.6 Implications for Melt Migration Through Subsolidus Rocks

Pervasive migration mechanisms are generally proposed to account for melt segregation and initial migration through migmatites experiencing active anatexis (Brown & Solar, 1998a; Sawyer, 2001; Brown, 2004). This study shows that pervasive migration is also possible in subsolidus rocks, and can be an effective migration mechanism above the source through the mid-crust.

Previously, pervasive migration was believed to be ineffective at levels in the crust above the source because melts migrating through subsolidus rocks would quickly reach their own solidus and crystallize, particularly in structures less than a few metres wide (Weinberg, 1999). However, Leitch & Weinberg (2002) showed that pervasive migration allows for effective overall heat transfer to high crustal levels due to the diffuse distribution of melt, thereby allowing for melt to remain liquid to higher crustal levels. The height above the source that melt can attain by pervasive migration before it freezes is controlled by the speed of melt production, speed of extraction, speed of transport, and the temperature and latent heat of the melt, with estimates for final melt solidus around 3–5 km above the melt source (Weinberg, 1999; Brown & Solar, 1999; Leitch & Weinberg, 2002).

This process would only occur to some height above the source and, given that plutons are fed by a few large feeder dykes at emplacement level, imply that the pervasive networks amalgamate into fewer, larger dykes before they reach a level where the melts would freeze (e.g. Weinberg, 1999). It follows that melt migration is likely a mostly pervasive process with dyke networks that occur throughout the crust. As the number and interconnectivity of dykes decrease, their size gradually increases, so that the network becomes larger and less pervasive at shallower crustal levels. Similarly, it seems probable that the rate at which melt migrates through the network increases towards shallower crustal levels, with the rate of movement being largely controlled by the rate of tectonic deformation in the lower crust, but becoming more dependent on melt viscosity at higher crustal levels.

The outcrops of the field area show that the processes and networks involved in melt movement through the metasediments are the same from the centimetre (e.g. Chapter 5) to 100m-scale (Chapter 7), suggesting that the mechanisms (but not necessarily the geometry) for the formation of melt channels and networks are somewhat scale-invariant (Marchildon

& Brown, 2003). A detailed investigation of the level of scale-invariance in the geometry of the networks is beyond the scope of this project. However, given that the mechanisms, specifically channelised migration along shear planes, are documented to operate over four orders of magnitude in this study, and that crustal-scale granites within shear zones (D'Lemos *et al.*, 1992; Brown & Solar, 1998b; Brown, 2007) form through a similar mechanism, it seems reasonable to suggest that they are scale-invariant.

The outcrops show that migration is achieved via interconnected networks that locally have different internal structures caused by local strain variations within an overall convergent and constrictional regime. Within the field area, melt transfer zones are those that show the higher relative strain and more melt-bearing structures, suggesting that migration preferentially occurs along large-scale areas of localised higher strain (Brown & Solar, 1998b,a, 1999). These areas would have a higher permeability due to the abundance of structures formed to accommodate the strain, coupled to steeper pressure gradients caused by the higher strain, making them ideal sites for voluminous melt flow.

Chapter 9

Conclusions

The outcrops investigated during this study represent a rare series of snapshots of pervasive melt migration through networked channels of melt conduits. The presence of these effective pervasive migration networks in subsolidus rocks at higher crustal levels than the melt sources supports models that suggest pervasive migration can occur in subsolidus rocks without melt freezing, due to advection of heat by the melt (e.g. Weinberg, 1999; Leitch & Weinberg, 2002).

The structure and geometry of pervasive networks, like melt segregation, is largely controlled by the local strain regime, showing that deformation plays a dominant role in the development and evolution of migration networks. Other factors affecting the internal mesoscale structure of the networks include rock rheology and rheological contrasts, and melt volume. Rheological contrasts can create barriers that hinder melt movement and enhance accumulation, but are also responsible for creating long-lived dilatant sites such as boudin necks. The main difference between channelised migration above the source and segregation within the source is the absolute requirement for embrittlement, which allows for the formation of channelised migration structures that form the networks and make otherwise impermeable rocks, permeable. Extreme melt volumes can lead to hydrofracture that greatly enhances the permeability of melt networks during periods of high melt pressure and melt oversupply.

Melt migration is driven by a combination of buoyancy forces and tectonic compaction and dilation that can expel (push) melt from compacting structures and / or draw (pull) it into dilational structures. The combination of these forces, and the specific contribution of each is highly variable. However, buoyancy is likely to play a larger role in driving melt movement during migration, relative to its role during segregation and movement in the source anatectic migmatites, because of the greater density contrast between the subsolidus

wallrocks and the melt within conduits. Heterogeneous deformation, particularly if it involves temporal strain changes, is effective at creating transient compacting and dilating structures, and pressure and hydraulic gradients between them, that allow for effective and continuous melt movement, in the same way that pressure and hydraulic gradients move melt around in the source. Melt movement is however restricted by the presence of melt conduits. Constant and uniform strain establishes stable networks that can be exploited by multiple melt batches, and long-lived dilatant structures that become melt accumulation sites, possibly evolving into emplacement sites.

The presence of multiple melt phases utilising the same structures shows that migration through subsolidus rocks is episodic and occurs in a stepwise manner, alternating between periods of accumulation and episodes of migration. Melt preferentially exploits and re-uses pre-existing pathways, unless there is a significant change in strain orientation during progressive deformation. For these examples from the Damara Orogen, available age data indicate that melt migration was long-lived, occurring episodically for at least 25 million years. This implies that pervasive migration is unlikely to be a rapid and catastrophic process, but rather suggests that it occurs at slower rates approaching that of tectonic deformation.

This project provides convincing evidence that pervasive migration is an effective mechanism for large-scale, lower- to mid-crustal melt migration above the melt source. The nature of the networks, and the alternation between accumulation and migration is controlled by existing permeability anisotropies arising from bedding, foliation, and other forms of layering coupled to structural permeability developed during progressive deformation, and networks and structures look similar to those created during segregation and melt movement in anatectic migmatites because the pathways in both instances are controlled by deformation. Progressive deformation is also responsible for creating the local pressure gradients that enable melt to be pushed or pulled through the crust, and thus aid, and can sometimes overcome buoyancy forces during migration, highlighting its fundamental influence on all aspects of the melt migration process.

References

Allibone, A. H. & Norris, R. J., 1992. Segregation of leucogranite microplutons during syn-anatectic deformation: an example from the Taylor Valley, Antarctica. *Journal of Metamorphic Geology*, **10**, 589–600.

Barraud, J., Gardien, V., Allemand, P. & Grandjean, P., 2004. Analogue models of melt-flow networks in folding migmatites. *Journal of Structural Geology*, **26**, 307–324.

Basson, I. J. & Greenway, G., 2004. The Rossing Uranium Deposit: a product of late-kinematic localization of uraniferous granites in the Central Zone of the Damara Orogen, Namibia. *Journal of African Earth Sciences*, **38**, 413–435.

Batemen, R., 1984. On the role of diapirism in the segregation, ascent and final emplacement of granitoid magmas. *Tectonophysics*, **110**, 211–231.

Benn, K., Roest, W. R., Rochette, P., Evans, N. G. & Pignotta, G. S., 1999. Geophysical and structural signatures of syntectonic batholith reconstruction: the South Mountain Batholith, Meguma Terrane, Nova Scotia. *Geophysical Journal International*, **136**, 144–158.

Bons, P. D., 2001. The formation of large quartz veins by rapid ascent of fluids in mobile hydrofractures. *Tectonophysics*, **336**, 1–17.

Bons, P. D. & van Milligen, B. P., 2004. New experiment to model self-organized critical transport and accumulation of melt and hydrocarbons from their source rock. *Geology*, **19**, 627–633.

Bons, P. D., Dougherty-Page, J. & Elburg, M. A., 2001. Stepwise accumulation and ascent of magmas. *Journal of Metamorphic Geology*, **19**, 627–633.

Bons, P. D., Druguet, E., Castaño, L.-M. & Elburg, M. A., 2008. Finding what is now not there anymore: Recognising missing fluid and magam volumes. *Geology*, **36**(11), 851–854.

Briqueu, L., Lancelot, J. R., Valois, J.-P. & Walgenwitz, F., 1980. Geochronologie U-Pb et genese d'un type mineralisation uranifere: les alaskite de Goanikontes (Namibia) et leur encaissant. *Bulletin Centrale De Recherche Exploration-Production, Elf Aquitaine*, **4**, 759–811.

Brown, K. M., Kopf, A., Underwood, M. B. & Weinberger, J. L., 2003. Compositional and fluid pressure controls on the state of stress on the Nankai subduction thrust: A weak plate boundary. *Earth and Planetary Science Letters*, **214**, 589–603.

Brown, M., 1994. The generation, segregation, ascent and emplacement of granite magma: the migmatite-to-crustally-derived granite connection in thickened orogens. *Earth Science Reviews*, **36**, 83–130.

Brown, M., 2004. The mechanism of melt extraction from the lower continental crust of orogens. *Transactions of the Royal Society of Edinburgh*, **95**, 35 – 48.

Brown, M., 2007. Crustal melting and melt extraction, ascent and emplacement in orogens: mechanisms and consequences. *Journal of the Geological Society*, **164**, 709 – 730.

Brown, M., 2010. The spatial and temporal patterning of the deep crust and implications for the process of melt extraction. *Philosophical Transactions of the Royal Society of London, Series A*, **368**, 11 – 51.

Brown, M. & Solar, G. S., 1998a. Granite ascent and emplacement during contractional deformation in convergent orogens. *Journal of Structural Geology*, **20**, 1365–1393.

Brown, M. & Solar, G. S., 1998b. Shear-zone systems and melts: feedback relations and self-organization in orogenic belts. *Journal of Structural Geology*, **20**, 211–227.

Brown, M. & Solar, G. S., 1999. The mechanism of ascent and emplacement of granite magma during transpression: a syntectonic granite paradigm. *Tectonophysics*, **312**, 1–33.

Brown, M., Korhonen, F. J. & Siddoway, C. S., 2011. Organizing melt flow through the crust. *Elements*, **7**, 261–266.

Byerlee, J. D., 1968. Brittle-ductile transition in rocks. *Journal of Geophysical Research*, **73**, p. 4741–4750.

Chiaraluce, L., Chiarabba, C., Collettini, C., Piccinini, D. & Cocco, M., 2007. Architecture and mechanics of an active low-angle normal fault: Alto Tiberina Fault, northern Apennines, Italy. *Journal of Geophysical Research*, **112**, B10310.

Clemens, J. D., 1998. Observations on the origins and ascent of granitic magmas. *Journal of the Geological Society*, **155**, 843–851.

Clemens, J. D. & Mawer, C., 1992. Granitic magma transport by fracture propagation. *Tectonophysics*, **204**, 339–360.

Clemens, J. D. & Petford, N., 1999. Granitic melt viscosity and silicic magma dynamics in contrasting tectonic settings. *Journal of the Geological Society of London*, **20**, 1057–1060.

Collins, W. J. & Sawyer, E. W., 1996. Pervasive granitoid magma transport through the lower-middle crust during non-coaxial compressional deformation. *Journal of Metamorphic Geology*, **14**, 565–579.

Connolly, J. A. D., 1997. Devolatilization-generated fluid pressure and deformation-propagated fluid flow during prograde regional metamorphism. *Journal of Geophysical Research*, **102**, 18 149–18 173.

Cooper, R. F., 1990. Differential stress-induced melt migration: an experimental approach. *Journal of Geophysical Research*, **95**, 6979–6992.

Cosgrove, J. W., 1997. The influence of mechanical anisotropy on the behaviour of the lower crust. *Tectonophysics*, **280**, 1–14.

Cruden, A. R. & McCaffrey, K. J. W., 2001. Growth of plutons by floor subsidence: implications for rates of emplacement, intrusion spacing and melt-extraction mechanisms. *Physics and Chemistry of Earth*, **26**, 303–315.

Davidson, C., Schmid, S. M. & Hollister, L. S., 1994. Role of melt during deformation in the deep crust. *Terra Nova*, **6**, 133–142.

D'Lemos, R. S., Brown, M. & Strachan, R. A., 1992. Granite magma generation, ascent and emplacement within a transpressional orogen. *Journal of the Geological Society, London*, **149**, 487–490.

Druguet, E. & Carreras, J., 2006. Analogue modelling of syntectonic leucosomes in migmatitic schists. *Journal of Structural Geology*, **28**, 1734–1747.

Escher, A. & Watterson, J., 1974. Stretching fabrics, folds and crustal shortening. *Tectonophysics*, **22**, 223–231.

Fagereng, Å., in press. On stress and strain in continuous-discontinuous shear zone undergoing simple shear and volume loss. *Journal of Structural Geology*, .

Fagereng, Å., Remitti, F. & Sibson, R. H., 2010. Shear veins observed within anisotropic fabric at high angles to the maximum compressive stress. *Nature Geoscience*, **3**, 482–485.

Fyfe, W. S., Price, N. J. & Thompson, A. B., 1978. *Fluids in the Earth's Crust*, Elsevier, Amsterdam.

Gleason, G. C. & Tullis, J., 1995. A flow law for dislocation creep of quartz aggregates determined with the molten salt cell. *Tectonophysics*, **247**, 1–23.

Handy, M. R., Mulch, A. & Rosenau, C. L., 2001. The role of fault zones and melts as agents of weakening, hardening and differentiation of the continental crust: a synthesis. In: *The Nature and Tectonic Significance of Fault Zone Weakening*, (eds Holdsworth, R. E., Strachan, R. A., Magloughlin, J. F. & Knipe, R. J.), Vol. 186, pp. 305–332. Geological Society, London Special Publications.

Henry, G., 1992. The sedimentary evolution of the Damara Sequence in the lower Khan river valley, Namibia. *Ph.D Dissertation, University of Witwatersrand, South Africa*, 218pp.

Henry, G., Clendenin, C. W., Stanistreet, I. G. & Maiden, K. J., 1990. Multiple detachment model for the early rifting stage of the Late Proterozoic Damara orogen in Namibia. *Geology*, **18**, 67–71.

Hoffman, P. F., Hawkins, D. P., Isachsen, C. E. & Bowring, S. A., 1996. Precise U-Pb zircon ages for early Damaran magmatism in the Summas Mountains and Welwitchia inlier, northern Damara Belt, Namibia. *Geological Survey of Namibia Communications*, **11**, 47–52.

Hoffmann, K.-H., Condon, D. J., Bowring, S. A. & Crowley, J. L., 2004. U-Pb zircon date from the Neoproterozoic Ghaub Formation, Namibia: constraints on Marinoan glaciation. *Geology*, **32**(9), 817–820.

Holdsworth, R. E., Butler, A. & Roberts, A. M., 1997. The recognition of reactivation during continental deformation. *Journal of the Geological Society of London*, **154**, 73–78.

Hreinsdóttir, S. & Bennett, R. A., 2009. Active aseismic creep on the Alto Tiberina low-angle normal fault, Italy. *Geology*, **37**, 683–686.

Hudleston, P., 1999. Strain compatibility and shear zones: is there a problem? *Journal of Structural Geology*, **21**, 923–932.

Hutton, D. H. W., Dempster, T. J., Brown, P. E. & Becker, S. D., 1990. A new mechanism for granite emplacement in active extensional shear zones. *Nature*, **343**, 452–455.

Jacob, R. E., 1974. Geology and metamorphic petrology of part of the Damara Orogen along the lower Swakop River, South-West Africa. *Bulletin of the Precambrian Research Unit, University of Cape Town*, **17**, 201pp.

Jacob, R. E., Corner, B. & Brynard, H. J., 1986. The regional geological and structural setting of the uraniferous granitic provinces of southern Africa. *Mineral Deposits of Southern Africa*, **2**, 1807 – 1818.

Jacob, R. E., Kröner, A. & Burger, A. J., 1978. Areal extent and first U-Pb age of the Pre-Damaran Abbabis Complex in the central Damara Belt of South West Africa (Namibia). *Geologische Rundschau*, **67**, 706–718.

John, B. E., 1988. Structural reconstruction and zonation of a tilted mid-crustal magma chamber: the felsic Chemehuevi Mountains plutonic suite. *Geology*, **16**, 613–617.

Jung, S. & Mezger, K., 2003. Petrology of basement dominated terrains: I. Regional metamorphic T-t path from U-Pb monazite and Sm-Nd garnet chronology (Central Damara orogen, Namibia). *Chemical Geology*, **198**, 223 – 247.

Jung, S., Hoernes, S. & Mezger, K., 2002. Synorogenic melting of mafic lower crust: constraints from geochronology, petrology and Sr, Nd, Pb and O isotope geochemistry of quartz diorites (Damara Orogen, Namibia). *Contributions to Mineralogy and Petrology*, **143**, 551 – 566.

Jung, S., Hoernes, S., Masberg, P. & Hoffer, E., 1999. The petrogenesis of some migmatites and granites (Central Damara Orogen, Namibia): evidence for disequilibrium melting, wall-rock contamination and crystal fractionation. *Journal of Petrology*, **40**(8), 1241–1269.

Jung, S., Mezger, K. & Hoernes, S., 2001. Trace element and isotopic (Sr, Nd, Pb, O) arguments for a mid-crustal origin of Pan-African garnet-bearing S-type granites from the Damara Orogen (Namibia). *Precambrian Research*, **110**, 325–355.

Kerrich, R. & Allison, I., 1978. Vein geometry and hydrostatics during Yellowknife mineralisation. *Canadian Journal of Earth Sciences*, **15**, 1653–1660.

Kisters, A. F. M., Gibson, R. L., Charlesworth, E. G. & Anhaeusser, C. R., 1998. The role of strain localization in the segregation and ascent of anatectic melts, Namaqualand, South Africa. *Journal of Structural Geology*, **20**, 229.

Kisters, A. F. M., Jordaan, L. S. & Neumaier, K., 2004. Thrust-related dome structures in the Karibib district and the origin of orthogonal fabric domains in the south Central Zone of the Pan-African Damara Belt, Namibia. *Precambrian Research*, **133**, 283–303.

Kisters, A. F. M., Ward, R. A., Anthonissen, C. J. & Vietze, M. E., 2009. Melt segregation and far-field melt transfer in the mid-crust. *Journal of the Geological Society, London*, **166**, 905–918.

Kröner, A., Retief, E. A., Compston, W., Jacob, R. E. & Burger, A. J., 1991. Single-grain and conventional zircon dating of remobilized basement gneisses in the central Damara belt of Namibia. *South African Journal of Geology*, **94**, 379–387.

Kukla, C., Kramm, U., Kukla, P. A. & Okrusch, M., 1991. U-Pb monazite data relating to metamorphism and granite intrusion in the northwestern Khomas Trough, Damara Orogen, Central Namibia. *Communications of the Geological Survey of Namibia*, **7**, 49–54.

Leitch, A. M. & Weinberg, R. F., 2002. Modelling granite migration by mesoscale pervasive flow. *Earth and Planetary Science Letters*, **200**, 131–146.

Marchildon, N. & Brown, M., 2003. Spatial distribution of melt-bearing structures in anatectic rocks from Southern Brittany, France: implications for melt transfer at grain- to orogen-scale. *Tectonophysics*, **364**, 215–235.

Martin, H. & Porada, H., 1977. The intracratonic branch of the Damara Orogen in South West Africa: I. Discussion of geodynamic models. *Precambrian Research*, **5**, 311–338.

Masberg, P., 2000. Garnet growth in medium pressure granulite facies metapelites from the Central Damara Orogen - igneous versus metamorphic history. *Communications of the Geological Society of Namibia*, **12**, 115–124.

McDermott, F., Harris, N. B. W. & Hawkesworth, C. J., 1996. Geochemical constraints on crustal anatexis: a case study from the Pan-African Damaran granitoids of Namibia. *Contributions to Mineralogy and Petrology*, **123**, 406–423.

McFadden, R. R., Teyssier, C., Siddoway, C. S., Whitney, D. L. & Fanning, C. M., 2010. Oblique dilation, melt transfer, and gneiss dome emplacement. *Geology*, **38**, 375–378.

McLeod, P. & Tait, S., 1999. The growth of dykes from magma chambers. *Journal of Volcanology and Geothermal Research*, **92**, 231–245.

Means, W. D., 1987. Retrodeformation of anisotropic rocks. *Geological Society of America, Abstracts with Programs*, **19**, 769.

Miller, R. M., 1983. The Pan-African Damara Orogen of South West Africa / Namibia. In: *Evolution of the Damara Orogen of South West Africa / Namibia, Special Publication 11*, (ed. Miller, R. M.), pp. 431–515. Geological Society of South Africa.

Nash, C. R., 1971. Metamorphic petrology of the SJ area, Swakopmund District, South West Africa. *Bulletin of the Precambrian Research Unit, University of Cape Town*, **9**, 77.

Nex, P. A. M., Kinnaird, J. A. & Oliver, G. J. H., 2001. Petrology, geochemistry and uranium mineralisation of the post-collisional magmatism around Goanikontes, southern Central Zone, Damara Orogen, Namibia. *Journal of African Earth Sciences*, **33**, 481 – 502.

Oliver, G. J. H., 1994. Mid-crustal detachment and domes in the Central Zone of the Damara Orogen, Namibia. *Journal of African Earth Sciences*, **19**, 331–344.

Paterson, M. S., 1995. A theory for granular flow accommodated by material transfer via an intergranular fluid. *Tectonophysics*, **245**, 135–151.

Petford, N., Cruden, A. R., McCaffrey, K. J. W. & Vigneresse, J.-L., 2000. Granite magma formation, transport and emplacement in the Earth's crust. *Nature*, **408**, 669–673.

Petford, N., Kerr, R. C. & Lister, J. R., 1993. Dike transport of granitoid magmas. *Geology*, **21**(9), 845–848.

Pitcher, W. S., 1979. The nature, ascent and emplacement of granitic magmas. *Journal of the Geological Society*, **136**, 627–662.

Poli, L. C. & Oliver, G. J. H., 2001. Constrictional deformation of the Central Zone of the Damara Orogen, Namibia. *Journal of African Earth Sciences*, **33**(2), 303–321.

Prave, A. R., 1996. Tale of three cratons: Tectonostratigraphic anatomy of the Damara orogen in northwestern Namibia and the assembly of Gondwana. *Geology*, **24**(12), 1115–1118.

Pressley, R. A. & Brown, M., 1999. The Phillips pluton, Maine, USA: evidence of heterogeneous crustal sources and implications for granite ascent and emplacement in convergent orogens. *Lithos*, **46**, 335–366.

Puhan, D., 1983. Temperature and pressure of metamorphism in the central Damara Orogen. *Special Publication Geological Society of South Africa*, **11**, 219–223.

Rushmer, T., 1991. Partial melting of two amphibolites: contrasting experimental results under fluid-absent conditions. *Contributions to Mineralogy and Petrology*, **107**, 41–59.

Sawyer, E. W., 1994. Melt segregation in the continental crust. *Geology*, **22**, 1019–1022.

Sawyer, E. W., 2001. Melt segregation in the continental crust: distribution and movement of melt in anatectic rocks. *Journal of Metamorphic Geology*, **19**, 291–309.

Sawyer, E. W. & Robin, P. Y., 1986. The subsolidus segregation of layer-parallel quartz-feldspar veins in greenschist to upper amphibolite facies metasediments. *Journal of Metamorphic Geology*, **4**, 237–260.

Sawyer, E. W., Cesare, B. & Brown, M., 2011. When the continental crust melts. *Elements*, **7**, 229–234.

Scaillet, B., Pecher, A., Rochette, P. & Champenois, M., 1995. The Gangotri granite (Garhwal Himalaya): laccolithic emplacement in an extending collisional belt. *Journal of Geophysical Research*, **B100**, 585–607.

Sibson, R. H., 1986. Brecciation processes in fault zones: Inferences from earthquake rupturing. *Pure and Applied Geophysics*, **124**(1/2), 159–175.

Sibson, R. H., 1992. Implications of fault-valve behaviour for rupture nucleation and recurrence. *Tectonophysics*, **211**, 283–293.

Simakin, A. & Talbot, C., 2001. Tectonic pumping of pervasive granitic melts. *Tectonophysics*, **332**, 387–402.

Simpson, G. D. H., 1998. Dehydration-related deformation during regional metamorphism, NW Sardinia, Italy. *Journal of Metamorphic Geology*, **16**, 457–472.

Slagstad, T., Jamieson, R. A. & Culshaw, G., 2005. Formation, crystallization, and migration of melt in the mid-orogenic crust: Musoka Domain migmatites, Grenville Province, Ontario. *Journal of Petrology*, **46**(5), 893–919.

Stevens, G., Clemens, J. D. & Droop, G. T. R., 1997. Melt production during granulite-facies anatexis: experimental data from primitive metasedimentary protoliths. *Contributions to Mineralogy and Petrology*, **128**, 352–370.

Sweeney, J. F., 1975. Diapiric granite batholiths in south-Central Maine. *American Journal of Science*, **275**, 1183–1191.

Tack, L. & Bowden, P., 1999. Post-collisional granite magmatism in the central Damaran (Pan-African) Orogenic Belt, western Namibia. *Journal of African Earth Sciences*, **28**(3), 653–674.

Twiss, R. J. & Moores, E. M., 1992. *Structural Geology*, W.H Freeman and Company, New York.

Urtson, K. & Soesoo, A., 2009. Stepwise magma migration and accumulation processes and their effect on extracted melt chemistry. *Estonian Journal of Earth Sciences*, **58**(4), 246–258.

Van der Molen, I. & Paterson, M. S., 1979. Experimental deformation of partially melted granite. *Contributions to Mineralogy and Petrology*, **70**, 299–318.

Vanderhaeghe, O., 1999. Pervasive melt migration from migmatites to leucogranite in the Shuswap metamorphic core complex, Canada: control of regional deformation. *Tectonophysics*, **312**, 35–55.

Vanderhaeghe, O., 2001. Melt segregation, pervasive melt migration and magma mobility in the continental crust: the structural record from pores to orogens. *Physics and Chemistry of Earth*, **26**(4–5), 213–223.

Vanderhaeghe, O., 2009. Migmatites, granites and orogeny: flow modes of partially-molten rocks and magmas associated with melt/solid segregation in orogenic belts. *Tectonophysics*, **477**, 119–134.

Vernon, R. H. & Paterson, S. R., 2001. Axial-surface leucosomes in anatectic migmatites. *Tectonophysics*, **335**, 183–192.

Vielzeuf, D. & Holloway, J. R., 1988. Experimental deformation of fluid-absent melting relations in the pelitic system. *Contributions to Mineralogy and Petrology*, **98**, 257–276.

Viola, G., Mancktelow, N. S. & Miller, J. A., 2006. Cyclic frictional-viscous slip oscillations along the base of an advancing nappe complex: insights into brittle-ductile nappe emplacement mechanisms from the Naukluft Nappe Complex, central Namibia. *Tectonics*, **25**. doi: 10.1029/2005TC001939.

Ward, R., Stevens, G. & Kisters, A. F. M., 2008. Fluid and deformation induced partial melting and melt volumes in low-temperature granulite-facies metasediments, Damara Belt, Namibia. *Lithos*, **105**, 253–271.

Weertman, J., 1971. Theory of water-filled crevasses in glaciers applied to vertical magma transport beneath ocean ridges. *Journal of Geophysical Research*, **76**, 1171–1183.

Weinberg, R. & Mark, G., 2008. Magma migration, folding and disagregation of migmatites in the Karakoram Shear Zone, Ladakh, NW India. *Geological Society of America Bulletin*, **120**, 994–1009.

Weinberg, R. F., 1999. Mesoscale pervasive felsic magma migration: alternatives to dyking. *Lithos*, **46**, 393 – 410.

Weinberg, R. F. & Podladchikov, Y. Y., 1994. Diapiric ascent of magmas through power law crust and mantle. *Journal of Geophysical Research*, **B99**, 9543–9559.

Weinberg, R. F. & Regenauer-Lieb, K., 2010. Ductile fractures and magma migration from the source. *Geology*, **38**(4), 363–366.

Weinberg, R. F. & Searle, M. P., 1998. The Pangong Injection Complex, India Karakoram: a case of pervasive granite flow through hot vicous crust. *Journal of the Geological Society, London*, **155**, 883–891.

Wells, M., Richards, D. L. & Volkmann, M. J., 1988. Geological map of the Damara Orogen, South West Africa/Namibia. Geological Survey, Windhoek.

White, R. W. & Powell, R., 2002. Melt loss and the preservation of granulite facies mineral assemblages. *Journal of Metamorphic Geology*, **20**, 621–632.

White, R. W., Powell, R. & Halpin, J. A., 2004. Spatially-focussed melt formation in aluminous metapelites from Broken Hill, Australia. *Journal of Metamorphic Geology*, **22**, 825–845.

White, R. W., Powell, R. & Holland, T. J. B., 2001. Calculation of partial melting equilibria in the system Na_2O–CaO–K_2O–FeO–MgO–Al_2O_3–SiO_2–H_2O (NCKFMASH). *Journal of Metamorphic Geology*, **19**, 139–153.

White, S. H., Bretan, P. G. & Rutter, E. H., 1986. Fault-zone reactivation: kinematics and mechanisms. *Philosophical Transactions of the Royal Society of London*, **A317**, 81–97.

Wickham, S. M., 1987. The segregation and emplacement of granitic magma. *Journal of the Geological Society of London*, **144**, 281–297.

Legend

- Granodiorite
- Biotite metapsammite
- Horblende - diopside calc-silicate
- Pyroxene-amphibole metapsammite
- Biotite leucogranite
- Pegmatitic leucogranite
- Schlieren pegmatite
- Pink granite

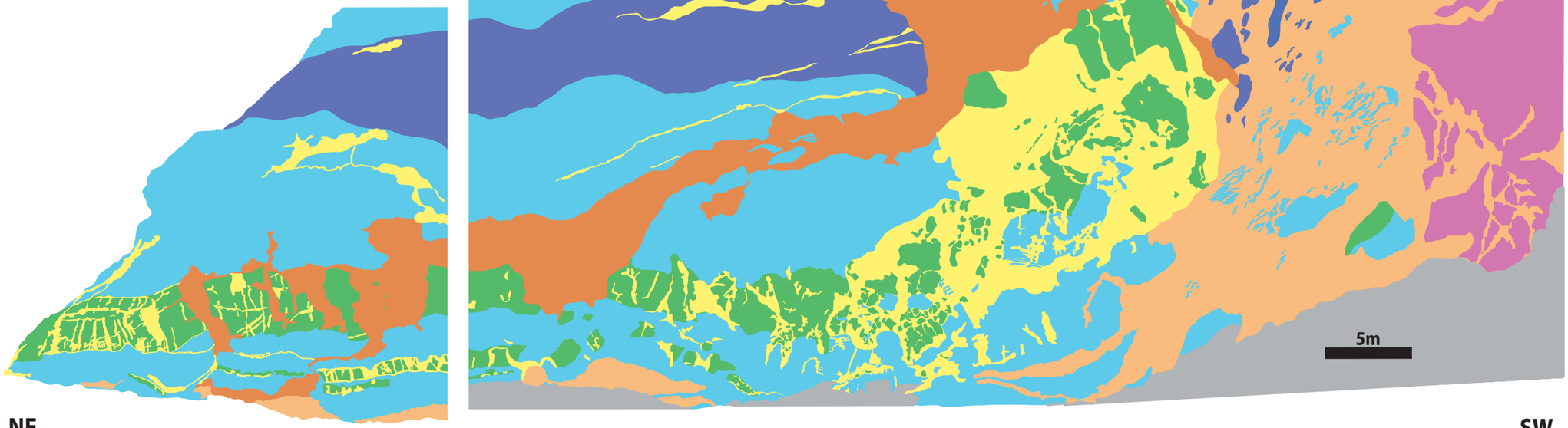

NE

SW

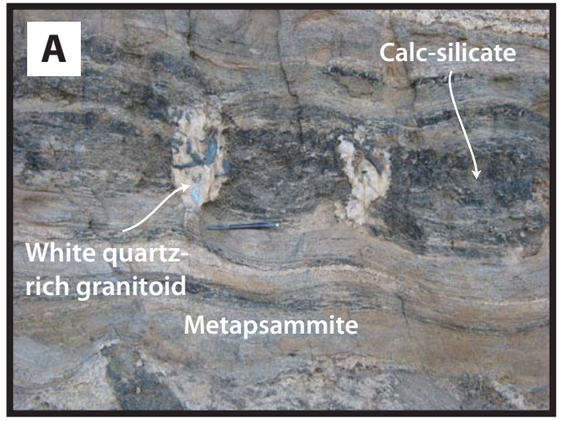
A
Calc-silicate
White quartz-
rich granitoid
Metapsammite

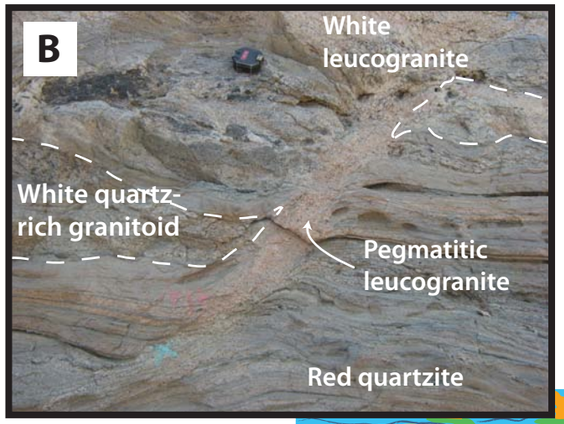
B
White
leucogranite
White quartz-
rich granitoid
Pegmatitic
leucogranite
Red quartzite

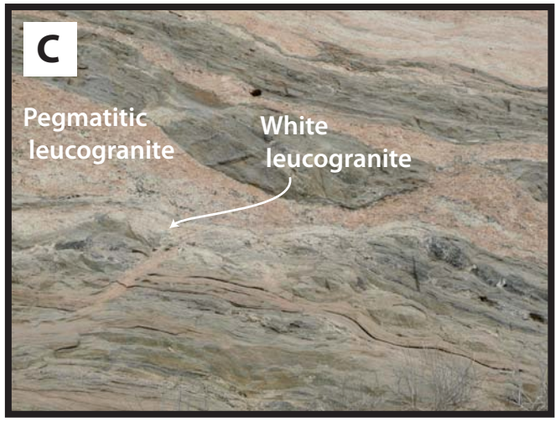
C
Pegmatitic
leucogranite
White
leucogranite


H
Blue
quartzite
White
leucogranite

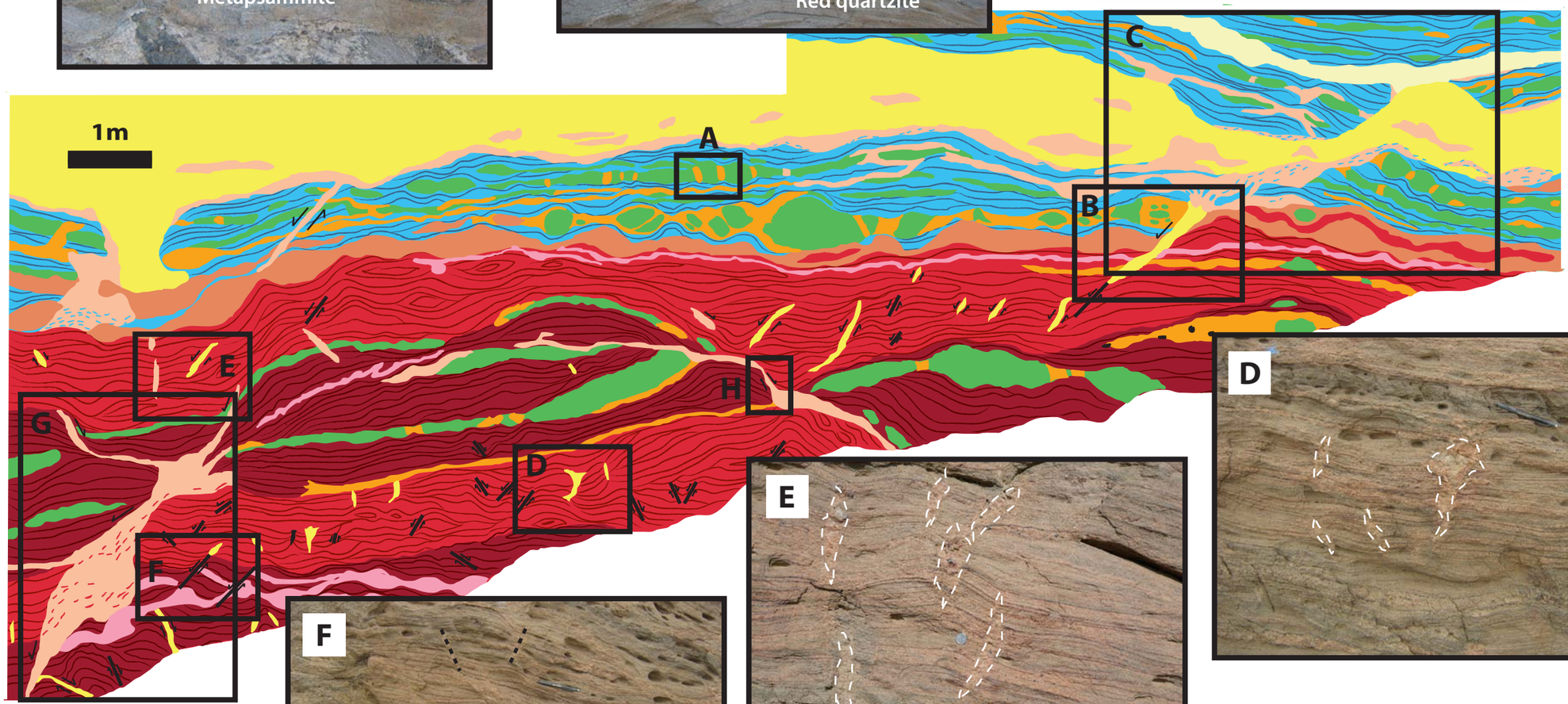
1m
A
B
C
D
E
F
G
H

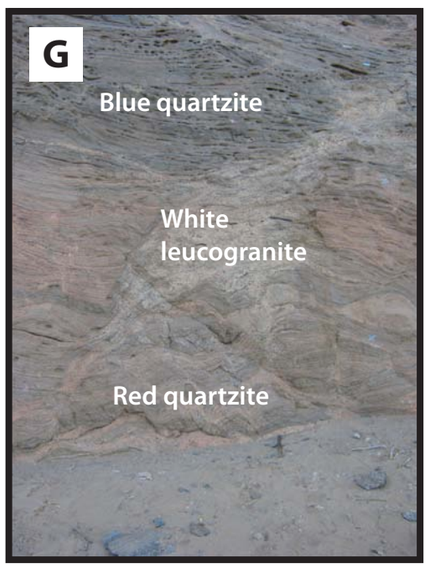
G
Blue quartzite
White
leucogranite
Red quartzite

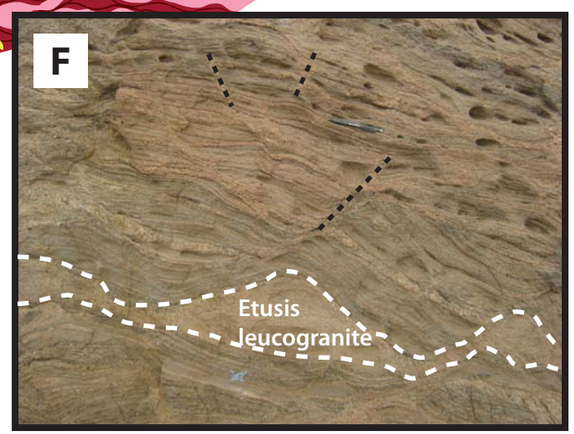
F
Etusis
Jeucogranite


E


D

Key

- Yellow leucogranite
- Orange leucogranite
- White and pink leucogranite
- Red quartz-rich granitoid
- Grey quartz-rich granitoid
- Hbl-metapsammite
- Layered metapsammite
- Massive metapsammite
- Calc-silicate rock
- Basement pink gneisses

20m

N

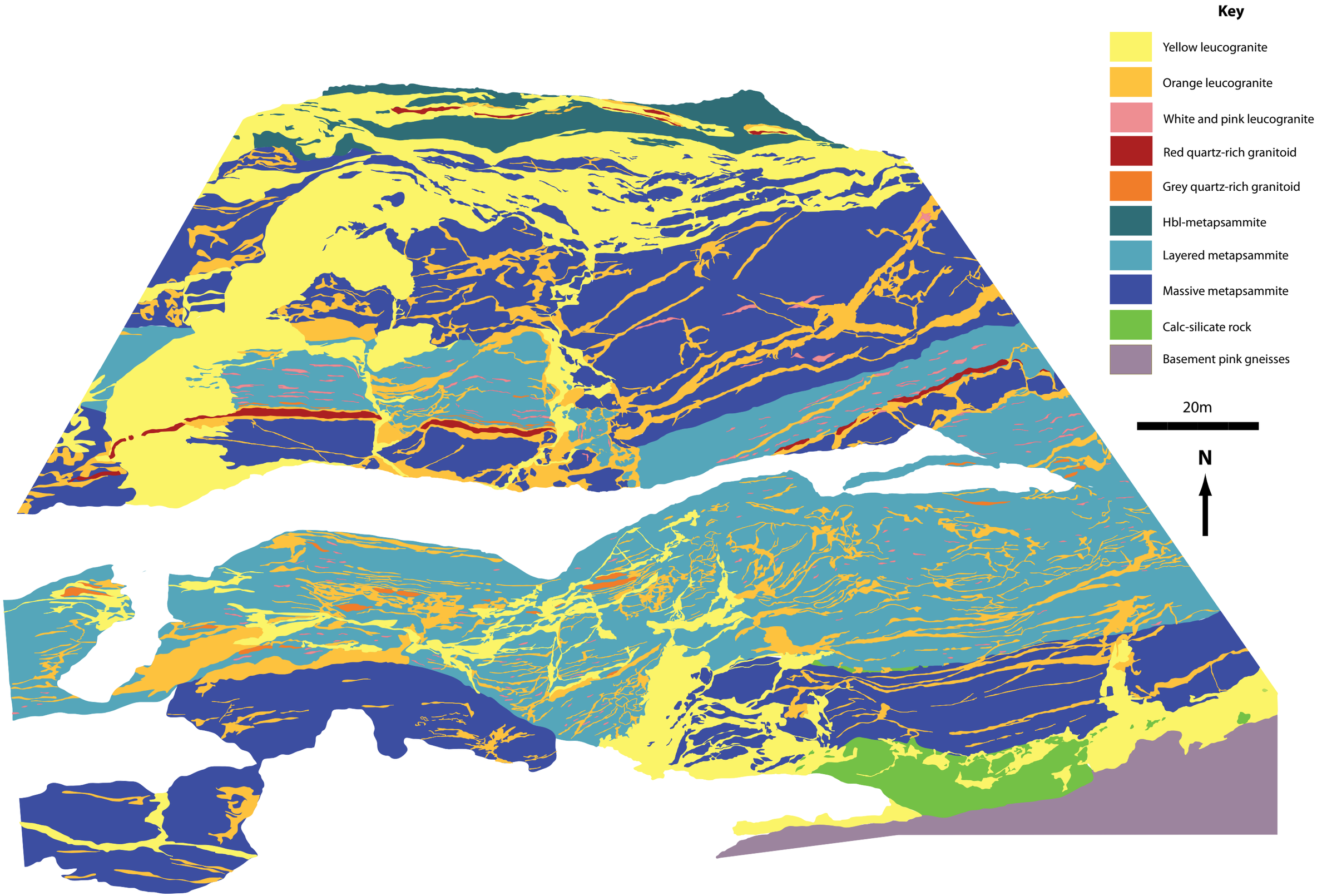
Key
Yellow leucogranite
Orange leucogranite
White and pink leucogranite
Red quartz-rich granitoid
Grey quartz-rich granitoid
Hbl-metapsammite
Layered metapsammite
Massive metapsammite
Calc-silicate rock
Basement pink gneisses
20m
N